X. Larráyoz Izcara

Characterization and Modeling of the Influence of the Ageing Treatment on the Precipitation Process and the Mechanical Behavior of the $AlSi_{10}Mg(Cu)$ Aluminum Alloy

Ph.D. Thesis

Characterization and Modeling of the Influence of the Ageing Treatment on the Precipitation Process and the Mechanical Behavior of the $AlSi_{10}Mg(Cu)$ Aluminum Alloy

Vom Promotionsausschuss der
Technischen Universität Hamburg-Harburg
zur Erlangung des akademischen Grades
Doktor-Ingenieur (Dr.-Ing.)
genehmigte Dissertation

von
Xabier Larráyoz Izcara

aus
Pamplona, Spanien

2016

Gutachter:
Prof. Dr. -Ing. Norbert Huber
Prof. Dr. rer. nat. Siegfried Schmauder

Tag der mündlichen Prüfung:
21. März 2016

Acknowledgments

I acknowledge with deep gratitude the outstanding, dedicated, and enthusiastic support of my supervisor Prof. Dr.-Ing. habil. Norbert Huber, whose valuable guidance, hints, and suggestions in many discussions significantly helped completing this work. I am also highly indebted to Prof. Dr. Andreas Schreyer and the German Engineering Materials Science Centre (GEMS) in Geesthacht (Germany), especially Dr. Peter Staron and Helmut Eckerlebe for the valuable SANS experiments performed. Without their contribution, this work would not have been possible. I want also to express my gratitude to Dr. Florian Pyczak for the TEM/HTEM analysis. It is a great pleasure for me to express my gratitude to the Helmholtz–Zentrum Geesthacht and the Technische Universität Hamburg–Harburg for giving me the chance to do my doctoral studies at these two prestigious scientific institutions.

I am also especially grateful to Prof. Dr. rer. nat. Siegfried Schmauder for accepting the proposal of being the co–advisor of this thesis and being part of the defense committee, taking the time and the interest for carefully reading this manuscript.

I would like to thank all my colleagues at Volkswagen Group Research for their interest and appreciation of my work. I am especially indebted to Alejandro Guirao for his valuable ideas and suggestions. It has been a privilege to work with him during this time. Special thanks go to Andreas Marx and Dr. Oliver Moll for their support with experiments. I would like to extend my gratitude to Dr. Sönke Schumann for the warm welcome into his group and his support.

Finally, I would like to give my thanks in all sincerity to my mother Ángela and my sister María for putting up my happy days as well as the bad ones, and my late father José for supporting me up there. And last, but most definitely not least, I would like to express my deepest thanks to Paola for her everlasting patience, love, and support.

Xabier Larráyoz Izcara

Abstract

A major objective of the current engine development projects is the downsizing of engines, which leads to more demanding specifications for the design of aluminum cylinder head castings such as higher operating temperatures or increased combustion pressures. As a result, these internal combustion engine components are subjected to more severe thermal loads related to the start–operate–stop cycles of the engine which produces low–cycle fatigue loading conditions in the material. Therefore, the initial ageing condition of the alloy as well as the subsequent thermal loading during the component service have a great impact on the cylinder head mechanical response and lifetime predictions. For this reason, mechanical models which can consider the ageing condition in the alloy are highly appreciated in this field.

A comprehensive analysis of the effect of the artificial ageing on the precipitation process of the age–hardenable $AlSi_{10}Mg(Cu)$ aluminum alloy from T6 to T7 condition and its influence on the mechanical behavior of the alloy at elevated temperatures is presented in this work, considering the influence of temperature and time ageing conditions of interest.

The influence of the artificial ageing on the material microstructure is carried out considering the most important microstructure compounds usually present in Al–Si–Mg alloy systems. A complete quantitative characterization of the Mg_2Si precipitation distributions covering a broad range of ageing conditions is obtained using the small angle neutron scattering (SANS) technique, complemented with high–resolution transmission electron microscopy (HTEM). This information is used to fit Robson's precipitation model for the prediction of the precipitation distribution as function of time and temperature. Based on the measured precipitation behavior, a sigmoidal interface energy function is added to Robson's model. As a result a unique set of modeling parameters is obtained for the whole precipitation process. Therefore, Robson's model is shown to be a powerful tool for predicting the evolution of these nanometer–scale particles in industrial and complex ageing processes.

The influence of the ageing condition on the mechanical response of the alloy to different loading

conditions is also examined. Hardness measurements and tensile tests are performed at room temperature. At higher temperatures, creep and low–cycle fatigue tests are carried out to analyze the relationship existing between the precipitation distributions and the mechanical response of the alloy. The predominant strengthening mechanism at this high temperature regime is determined from these results. The information obtained from this analysis is of great importance for the mechanical modeling using Steck's viscoplastic material model considering both isotropic and kinematic hardening. This constitutive mechanical model is further developed in this work to consider combined cyclic and relaxation loading conditions by using a unique set of modeling parameters independent of each other and of temperature. According to the results presented, Steck's model is especially useful at elevated temperatures, of interest in this work.

Finally and based on the physic principles of both precipitation and material models, Steck's material model is extended to consider the alloy ageing condition in the kinematic and isotropic hardening components. The results obtained for an intermediate overaged condition of the alloy using the extended Steck's constitutive model make this model combined with Robson's precipitation model a good approach to predict the mechanical behavior of the $AlSi_{10}Mg(Cu)$ aluminum cast alloy at high temperatures considering the potential effect of further thermal loading, which is of great interest for its industrial application in future cylinder head design projects.

Contents

List of symbols

A list of the main symbols appearing in the document is presented here:

Capital Symbols

C	Steck parameter (Eq. (6.12), Pag. 87)	(s^{-1})
$C\,(\lambda)$	Steck parameter (Eq. (7.2), Pag. 106)	(s^{-1})
D	Diffusion parameter (Eq. (4.4), Pag. 47)	$(\mathrm{m}^2\mathrm{s}^{-1})$
D_0	Diffusivity constant (Eq. (4.6), Pag. 47)	$(\mathrm{m}^2\mathrm{s}^{-1})$
E	Young modulus (Eq. (6.9), Pag. 87)	$(\mathrm{N}\,\mathrm{m}^{-2})$
G^*	Activation energy (Eq. (4.2), Pag. 46)	$(\mathrm{J}\,\mathrm{mol}^{-1})$
J	Nucleation rate (Eq. (4.3), Pag. 46)	(s^{-1})
N_0	Nucleation sites density (Eq. (4.3), Pag. 46)	(m^{-3})
Q	Activation energy (Eq. (4.3), Pag. 46)	$(\mathrm{J}\,\mathrm{mol}^{-1})$
R	Universal gas constant (Eq. (4.6), Pag. 47)	$(\mathrm{J}\,\mathrm{K}^{-1}\,\mathrm{mol}^{-1})$
R_0	Normal distribution function parameter (Eq. (3.3), Pag. 40)	(m)
R_m	Ultimate tensile strength (Eq. (5.1), Pag. 59)	$(\mathrm{N}\,\mathrm{m}^{-2})$
$R_{p,0.2\%}$	Yield strength (Eq. (5.1), Pag. 59)	$(\mathrm{N}\,\mathrm{m}^{-2})$
T	Temperature (Eq. (4.1), Pag. 46)	(K)
U_0	Activation energy (Eq. (6.12), Pag. 87)	$(\mathrm{J}\,\mathrm{mol}^{-1})$

V_a	Atomic volume (Eq. (4.1), Pag. 46)	$(\mathrm{m^3\,mol^{-1}})$

Greek Symbols

α_1	Steck parameter (Eq. (6.10), Pag. 87)	(–)
$\alpha_1(\lambda)$	Steck parameter (Eq. (7.4), Pag. 106)	(–)
α_2	Steck parameter (Eq. (6.11), Pag. 87)	(–)
$\alpha_2(\lambda)$	Steck parameter (Eq. (7.5), Pag. 106)	(–)
β_1	Steck parameter (Eq. (6.10), Pag. 87)	(–)
β_2	Steck parameter (Eq. (6.11), Pag. 87)	(–)
ΔV	Activation volume (Eq. (6.10), Pag. 87)	$(\mathrm{m^3\,mol^{-1}})$
δ_1	Steck parameter (Eq. (6.10), Pag. 87)	(–)
δ_2	Steck parameter (Eq. (6.11), Pag. 87)	(–)
$\delta_2(T,\lambda)$	Steck parameter (Eq. (7.10), Pag. 111)	(–)
$\delta_2''(\lambda)$	Steck parameter (Eq. (7.10), Pag. 111)	$(^\circ\mathrm{C}^{-1})$
$\delta_2'(\lambda)$	Steck parameter (Eq. (7.10), Pag. 111)	(–)
$\dot{\epsilon}_s$	Minimum secondary creep rate (Eq. (5.2), Pag. 60)	(s^{-1})
ϵ	Total strain (Eq. (6.2), Pag. 84)	(–)
ϵ_e	Elastic strain (Eq. (6.2), Pag. 84)	(–)
ϵ_{ie}	Inelastic strain (Eq. (6.2), Pag. 84)	(–)
ϵ_{th}	Thermal strain (Eq. (6.2), Pag. 84)	(–)
γ_1	Steck parameter (Eq. (6.13), Pag. 88)	(–)
κ	Steck parameter (Eq. (6.12), Pag. 87)	(–)
λ	Interprecipitate spacing (Eq. (5.4), Pag. 64)	(m)
σ	Interfacial energy (Eq. (4.1), Pag. 46)	$(\mathrm{J\,m^{-2}})$
σ	Stress (Eq. (6.3), Pag. 85)	$(\mathrm{N\,m^{-2}})$

σ^{eff}	Effective stress (Eq. (6.3), Pag. 85)	$(\mathrm{N\,m^{-2}})$
σ^{iso}	Isotropic stress (Eq. (6.10), Pag. 87)	$(\mathrm{N\,m^{-2}})$
σ^{iso}_{eq}	Equilibrium isotropic stress (Eq. (6.13), Pag. 88)	$(\mathrm{N\,m^{-2}})$
σ^{kin}	Kinematic stress (Eq. (6.11), Pag. 87)	$(\mathrm{N\,m^{-2}})$
σ_b	Back stress (Eq. (6.1), Pag. 82)	$(\mathrm{N\,m^{-2}})$
σ_{cr}	Applied creep stress (Eq. (5.2), Pag. 60)	$(\mathrm{N\,m^{-2}})$
σ^0_{cr}	Threshold Norton stress (Eq. (5.3), Pag. 60)	$(\mathrm{N\,m^{-2}})$
σ_N	Normal distribution function parameter (Eq. (3.3), Pag. 40)	(m)
Θ	Steck parameter (Eq. (6.12), Pag. 87)	(–)
$\Theta\,(\lambda)$	Steck parameter (Eq. (7.3), Pag. 106)	(–)

Small Symbols

c	Instantaneous concentration (Eq. (4.1), Pag. 46)	(wt%)
c^{α}_{∞}	Equilibrium concentration (Eq. (4.1), Pag. 46)	(wt%)
c^{α}_{r}	Solute concentration in the precipitate (Eq. (4.4), Pag. 47)	(wt%)
h	Planck constant (Eq. (4.3), Pag. 46)	(Js)
h_1	Steck parameter (Eq. (6.10), Pag. 87)	$(\mathrm{N\,m^{-2}})$
h_2	Steck parameter (Eq. (6.11), Pag. 87)	$(\mathrm{N\,m^{-2}})$
k	Boltzmann constant (Eq. (4.1), Pag. 46)	$(\mathrm{J\,K^{-1}})$
n	Norton stress exponent (Eq. (5.2), Pag. 60)	(–)
n_0	Precipitate density (Eq. (3.3), Pag. 40)	$(\mathrm{m^{-3}})$
n_t	True Norton stress exponent (Eq. (5.3), Pag. 60)	(–)
r	Precipitate radius (Eq. (4.4), Pag. 47)	(m)
r^*	Critical radius (Eq. (4.1), Pag. 46)	(m)
r_1	Steck parameter (Eq. (6.10), Pag. 87)	$(\mathrm{N\,m^{-2}\,s^{-1}})$

r_2	Steck parameter (Eq. (6.11), Pag. 87)	$(\mathrm{N\,m^{-2}\,s^{-1}})$
$r_2\,(\lambda)$	Steck parameter (Eq. (7.5), Pag. 106)	$(\mathrm{N\,m^{-2}\,s^{-1}})$

Chapter 1

Introduction

Among the small number of components in automotive technology such as exhaust manifolds or crankcases that are subjected to thermomechanical loads, cylinder heads belong also to this components type. These are exposed to: (i) mechanical loads resulting from the combustion cycles of the engine, (ii) thermal loads as a result of the start–operate–stop cycle of the engine.

The cylinder head is an integral component of the internal combustion engine that conveys air and gasoline to the combustion chamber and serves as a cover for the cylinders. The main function of this component is to seal cylinders properly together with the head gasket to produce enough compression in the operation of the engine. Furthermore, it also supports the different parts and channels of the cooling system.

The strength and stiffness of the cylinder head are two important requirements in the design of this component in order to distribute the gas forces acting on the head as uniformly as possible through the engine block. Besides, the independent flow of the combustion gas, the coolant, and the lubricating oil through different flowing channels leads to a complex three dimensional geometry of the component.

Different casting processes using sand molds or preferentially metal dies are used for their production. At present virtually all of the cylinder heads are cast in aluminum alloys, replacing the old and heavy gray cast iron cylinder heads. In addition to the advantage of light weight (weight reduction of 10–20 kg, i.e. at least 50 %), aluminum also provides a high thermal conductivity and some advantageous productions' requirements.

The current engine development projects show as a major objective the downsizing of engines, which leads to some additional requirements to be met by cylinder heads, such as: (i) enable further weight reduction, (ii) permit increased power densities, (iii) allow the introduction of advanced combustion systems. Thus, these requirements lead to more demanding specifications

for aluminum cylinder head castings: (i) higher operating temperatures due to higher power density requirements, (ii) higher combustion pressures, producing higher mechanical stresses on the material that combined with the thermal cycles may lead to a significant reduction in the fatigue life of the component, (iii) designs with multi–port layouts and application of advanced combustion systems, leading to even more complex geometries and thinner cooling water passages. Therefore, the combustion pressure in the next generation engines is expected to rise to 180–200 bar for compression ignition engines and to 100–120 bar for boosted spark ignition engines. The maximum combustion chamber wall temperature, usually found at the bridge between the exhaust valves, might likewise rise well over 250°C and even approach 300°C.

As a result of the increasingly more demanding combustion pressure and temperature conditions, it is of great importance that the aluminum alloys used exhibit a high strength at elevated temperatures (up to 250°C) to ensure that the engine block–cylinder head assembly can withstand the combustion and thermal forces without losing tightness in the cylinder head gasket. Furthermore, a high creep strength especially for the head gasket area is also required.

For all these reasons, the Al–Si–Mg cast alloy systems are of great interest for the production of cylinder heads. The best combination of strength and ductility are usually offered by alloys with low iron content, such as the $AlSi_7Mg_{0.3}$ alloy. Therefore, most of cylinder heads were cast in the past in primary aluminum alloys. Secondary aluminum alloys with a slightly increased impurity content resulting from the recycling process such as $AlSi_{10}Mg(Cu)$ or $AlSi_7Mg$ still provide sufficient ductility and strength at high temperatures while allowing a significant reduction of the material costs.

The age–hardenable nature of these alloys requires to carry out a heat treatment to achieve the desired strengthening degree. This heat treatment takes usually place after the casting process and is ideally performed to achieve the T6 strengthening condition. A T6 heat treatment is a precipitation process in which a fine distribution of the Mg_2Si hardening phase in the case of the Al–Si–Mg alloy system is created under specific and controlled temperature and time conditions to produce the maximum strengthening by the interaction of these precipitates with the dislocations present in the material. In the case of cylinder heads, these alloys may be subjected to some additional thermal processes during the engine's operational life as mentioned above. This might result in an additional ageing of the material. For this reason and due to the metastable condition of the Mg_2Si strengthening phases at the T6 condition, a slightly more pronounced ageing condition than the T6 state (formally T7 condition) is normally used for the heat treatment of cylinder heads.

The mechanical loads to which cylinder heads are exposed as a result of the engine's combustion cycles produce high–cycle fatigue loading conditions. However, the thermal expansion and

contraction of the material produced by the engine's start–operate–stop cycle lead to low–cycle fatigue conditions. Critical high–cycle fatigue areas are on the water jacket side of the flame deck wall because of the prevailing cyclic tensile stresses, while low–cycle fatigue may primarily cause cracks in the thin–walled valve bridge areas which are at the same time exposed to the highest temperatures within the cylinder head as can be seen in Fig. 1.1.

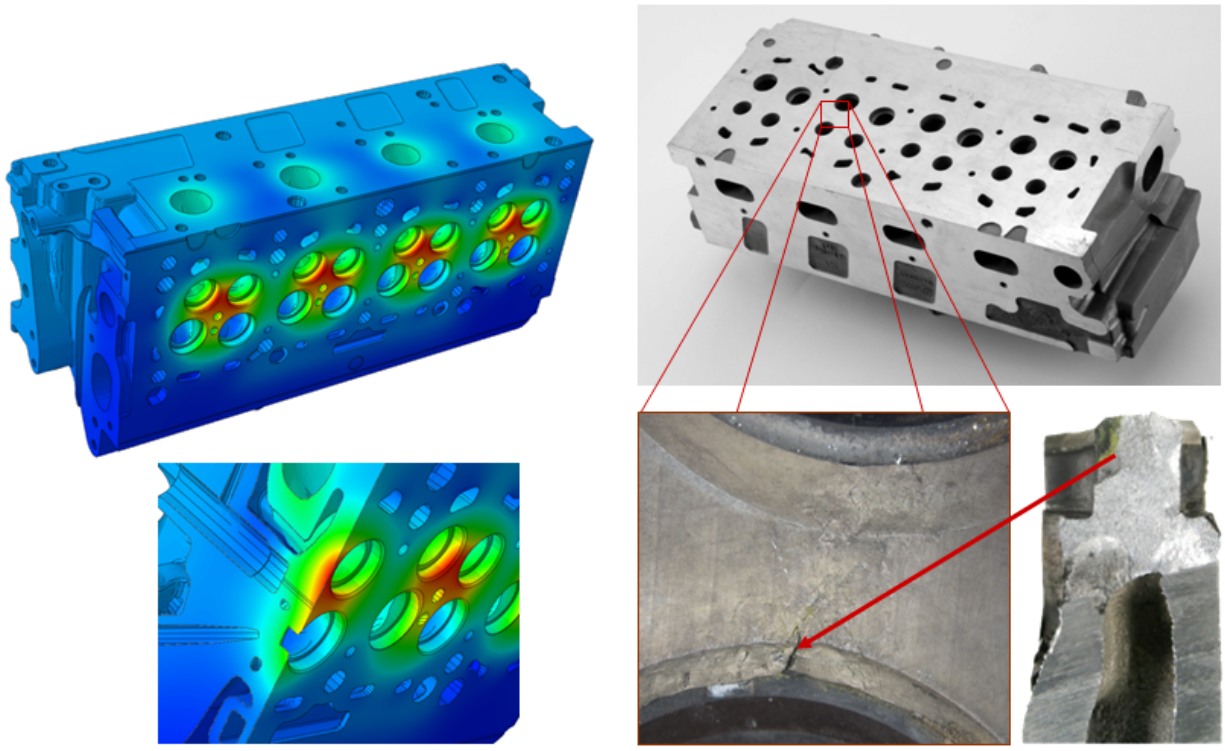

(a) (b)

Fig. 1.1: The more demanding requirements to be met by cylinder heads lead to: (a) higher temperatures during the combustion engine operation, especially in the thin–walled inlet valve bridge areas; (b) the possibility of cracks in these inlet valve areas as a result of more severe thermal loading (results of push–pull test).

The variation of mechanical properties in cylinder heads takes place during the engine's operation as a result of the high temperatures at which the component is exposed and it is not uniform throughout the component. Furthermore, the initial distribution of mechanical properties after the heat treatment are also far from being uniform in the whole cylinder head due to the massive nature and complex geometry of the component. This makes that the temperature and duration of the heat treatment have a different effect on the different parts of the cylinder head, leading to a more pronounced ageing condition of those thin–walled near–surface areas.

Thus, the initial ageing condition and the following ageing due to the engine's operation and their

effect on the strengthening degree and mechanical properties of the alloy have a great impact on the calculation of the cylinder heads fatigue life and damage location and must be considered for an integrated, robust, and successful development process of the component.

1.1 Objectives

The purpose of this work is to analyze the effect of the ageing on the precipitation process and mechanical behavior of the $AlSi_{10}Mg(Cu)$ aluminum cast alloy and determine, if possible, the relationship existing between both fields. Thus, the main objectives of the study are established as follows:

(i) The characterization and modeling of the precipitation process for different ageing states ranging from the T6 maximum strengthening towards the T7 long overaged state. The characterization of the precipitation process must provide experimental results from which valuable and statistically meaningful information on the type, shape, and distribution of the Mg_2Si precipitates can be derived. Besides, the modeling approach used must be able to predict the precipitation distribution resulting from multi–stage or complex ageing processes, such as those present in industrial applications.

(ii) The modeling of the mechanical response at high temperatures to combined low–cycle fatigue and creep loading conditions for different ageing states ranging from the T6 to the T7 condition. The constitutive mechanical model used should be based on well–founded fundamentals of metal physics for two–phase alloy systems. The model must take into account the stochastic nature of the interaction mechanisms between dislocations and precipitates. The model must likewise be able to predict the viscoplastic behavior of the alloy expected at high temperatures. All of this should be done under the premise that a unique set of model parameters corresponds to each ageing condition.

(iii) The coupling of both precipitation and material models as a result of the physics–based foundations of both approaches, so that the constitutive mechanical model can be expressed as a function of the ageing condition of the alloy. With this novel formulation, the mechanical behavior of the alloy at high temperatures resulting from any arbitrary and complex ageing process could be predicted.

In this work, the precipitation kinetics and mechanical behavior of the alloy is determined and modeled in this work assuming a T6 peak aged condition as the initial condition for further

temperature loading. This is the relevant initial state for the prediction of the local distribution of mechanical properties in cylinder heads during service. As a result, the measurement and description of the first stages of precipitation and the corresponding mechanical response of the alloy are not relevant for this work.

1.2 Work approach

A comprehensive analysis of the influence of the ageing treatment on the precipitation process and the mechanical behavior of the $AlSi_{10}Mg(Cu)$ aluminum alloy should take into account the following aspects: (i) a microstructure analysis of the precipitation process, (ii) an elasto–viscoplastic mechanical analysis of the material, . Both aspects are linked together, so that the Mg_2Si precipitation distribution formed during the ageing process together with the material behavior of the alloy given by other constituents determine the mechanical response of the material.

As mentioned previously, the T6 condition is assumed in this work as the initial ageing condition of the alloy. The subsequent ageing will alter the initial precipitation distribution, which will result in a significant variation in the initial mechanical properties of the alloy. It is of great importance for the mechanical modeling that the ageing condition remains unaltered during the experiment in those tests carried out at elevated temperatures. Only in this way the effect of mechanical loading will be correctly captured. Therefore, the work approach proposed is divided into six different stages:

(i) Analysis of the precipitation process.

(ii) Modeling of the ageing behavior of the material.

(iii) Analysis of the mechanical behavior of the alloy.

(iv) Modeling of the cyclic viscoplastic behavior of the material.

(v) Calibration of both simulation models on the basis of isothermal ageing processes and isothermal uniaxial tests.

(vi) Coupling of both precipitation and material models.

The work approach proposed is presented in graphic form in Fig. 1.2. The analysis starts with a comprehensive examination of the precipitation process occurring during the artificial ageing.

1. Introduction

The major outcome of this part is to determine which intermetallic phases and microstructure properties of the material change with the ageing condition of the alloy. The conclusions drawn from this analysis will be used not only for the modeling of the ageing process, but also for its fitting and validation. The experimental results gathered should provide meaningful statistical information to adequately characterize every ageing condition.

The influence of the ageing conditions on the mechanical behavior of the Al–Si–Mg alloy systems has been usually analyzed based on ageing curves. These curves are experimental hardness curves obtained from isothermal ageing processes covering a wide range of durations. Conclusions about the peak ageing condition and the precipitation kinetics are usually drawn from these curves [1–4].

The analysis of the mechanical behavior of the $AlSi_{10}Mg(Cu)$ alloy will be carried out in this work by performing different mechanical tests considering diverse loading conditions. This will provide not only qualitative but also quantitative information on the mechanical response of the alloy. The qualitative analysis will focus on the relationship existing between the Mg_2Si precipitation distribution and the mechanical properties of the alloy at room temperature. The quantitative analysis will contribute to determine the high temperature regime for the alloy, as well as the predominant deformation mechanism at this temperature range and the behavior of the material under low–cycle fatigue loading conditions. This information will be used for the mechanical modeling and calibration of the alloy.

Finally, the coupling of both models will be done based on the sets of parameters of the material model obtained previously for different strengthening degrees. As a result, a novel formulation of the constitutive mechanical model considering the ageing condition of the $AlSi_{10}Mg(Cu)$ alloy will be obtained.

With regard to this last point, the coupling between precipitation and constitutive mechanical models considering complex ageing processes is an issue of ongoing research. Some simple precipitation models limited to isothermal ageing treatments have been developed and coupled to the prediction of hardness for the Al–Si–Mg alloy systems [5, 6]. Assuming the hardness as a good approximation to the ageing condition, different empirical relationships between hardness and some tensile properties have been reported for a high variety of metals and alloys [7,8], also for the Al–Si–Mg alloy system [2, 9, 10]. For these alloys, different strengthening models considering the contributions of the intrinsic aluminum matrix, the solid solution strengthening, and the precipitation hardening (distinguishing between the competitive contributions of shearable and non–shearable Mg_2Si precipitates) have been also developed to predict empirically some of these tensile properties at room temperature as a result of complex ageing treatments [11–13].

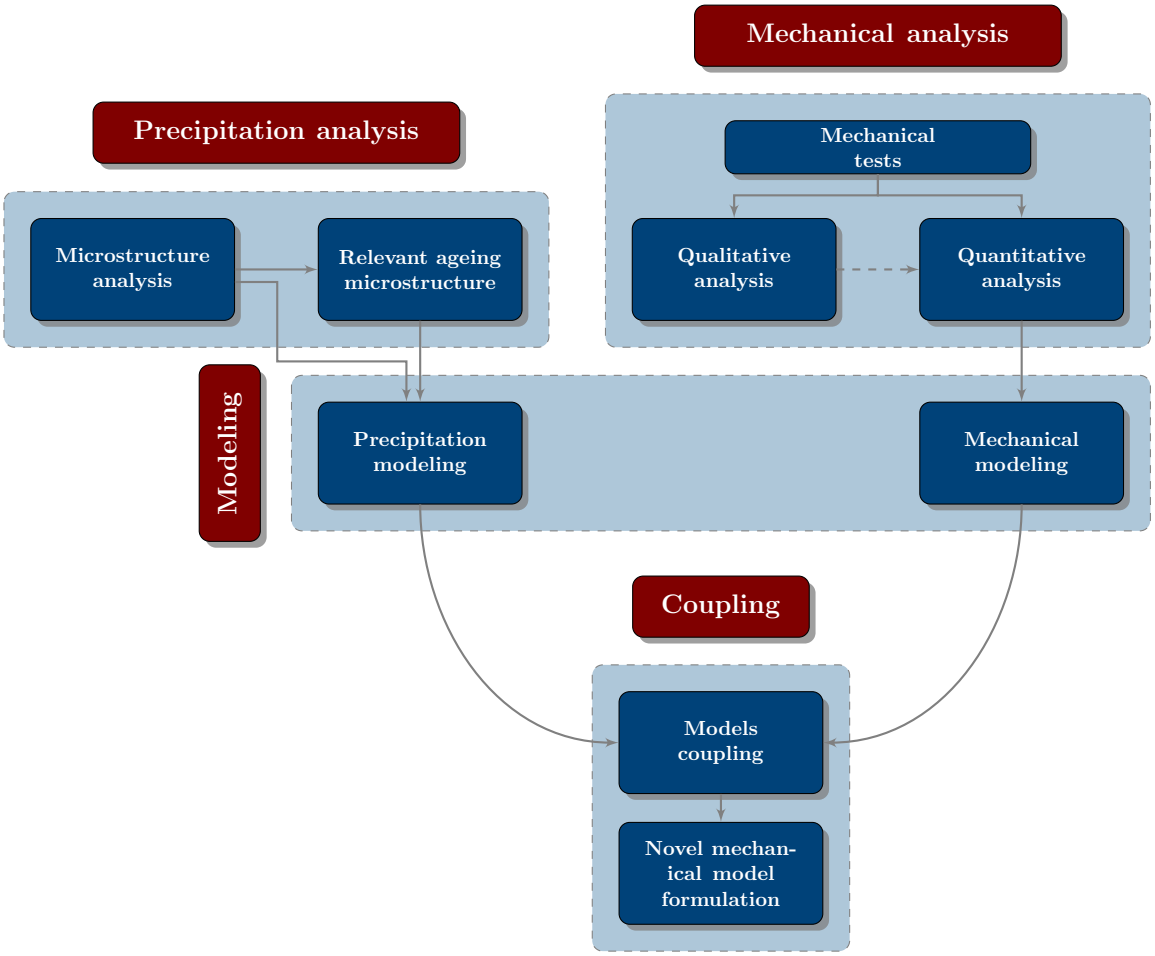

Fig. 1.2: Proposed work approach. The experimental data gathered from the precipitation analysis and the mechanical analysis will be used for the modeling of the precipitation process and mechanical behavior of the alloy, respectively. Based on the physics–based foundations of both models, the objective is to couple these two modeling approaches to consider the ageing condition of the alloy in the mechanical simulation.

1.3 Chapter overview

The theoretical fundamentals of the work are presented in Chap. 2. The different stages of the complete heat treatment usually carried out in the Al–Si–Mg alloy systems are explained in Sect. 2.1, with special focus on the artificial ageing stage and its effect on the precipitation process. Sect. 2.2 gives an overview of the different existing modeling approaches to describe the precipitation process, with special emphasis on the numerical Robson's model. The different deformation mechanisms predominant at room and high temperatures for precipitation strengthened materials are given in Sect. 2.3. This chapter ends by presenting the different constitutive approaches to describe the viscoplastic behavior of materials at high temperatures,

and by introducing the constitutive model of Steck in Sect. 2.4.

The objective of Chap. 3 is to determine those intermetallic phases and microstructure properties of the alloy changing with the ageing condition during the precipitation process. For this reason, the $AlSi_{10}Mg(Cu)$ alloy is presented in Sect. 3.1. The experimental techniques used for its microstructure study are given in Sect. 3.2. The results obtained from this analysis are shown in Sect. 3.3 and those of interest for the further development of the work are presented in Sect. 3.4.

Chap. 4 covers the modeling of the precipitation process using the numerical model of Robson. The objectives, the simplifications assumed, and the modeling approaches for the nucleation, growth, and coarsening processes are presented in Sect. 4.1. The simulation results obtained for the different ageing temperatures by using a unique set of modeling parameters are shown in Sect. 4.2.

Chap. 5 addresses the mechanical analysis of the alloy under different loading conditions at room and elevated temperatures. The influence of the ageing condition is also evaluated. After describing shortly the material preparation procedure followed in Sect. 5.1, the different mechanical tests carried out together with the intended aims are presented in Sect. 5.2. The qualitative and quantitative results gathered can be found in Sect. 5.3. Finally, the implications of this study for the modeling of the mechanical behavior of the material are presented in Sect. 5.4.

The mechanical modeling of the alloy using the constitutive viscoplastic model of Steck is presented in Chap. 6. The fundamentals of the model and its macroscopic formulation are presented in Sect. 6.1. This section also contains some further developments to predict the behavior of the alloy under low–cycle fatigue loading conditions combined with intermediate relaxation stages, as well as the parameters identification procedure followed. The simulation results for two of the four ageing conditions considered are shown in Sect. 6.2 (all simulation results for Steck's model are presented in App. B).

Finally, the challenge of coupling both models to consider the ageing condition of the alloy into its mechanical modeling is presented in Chap. 7. The fitting results of those Steck's model parameters changing with the ageing condition, with particular emphasis on the δ_2 parameter, and the resulting novel formulation of the model considering the hardening grade of the alloy can be found in Sect. 7.1. The validation of this new model formulation is presented in Sect. 7.2.

The work concludes in Chap. 8 with a detailed summary of the more relevant conclusions drawn from the results obtained.

Chapter 2

Theoretical fundamentals

The Al–Si–Mg alloy systems are of great interest for the production of different cast components in the automotive sector as explained in Chap. 1 [1]. The increasingly demanding design requirements for these components can be reached by carrying out a precipitation heat treatment, due to the age–hardenable nature of these alloys. As a result, a precipitation distribution of Mg_2Si hardening particles is formed [14–19]. This precipitation distribution determines the strengthening degree and is the main responsible of the mechanical behavior of these alloys [20–23].

The different stages of this precipitation strengthening treatment are explained in Sect. 2.1, with special emphasis on the final ageing process. The different existing modeling approaches that can be used to predict the precipitation distribution formed are presented in Sect. 2.2, focusing on Robson's model. Sect. 2.3 gives an overview of the predominant deformation mechanisms in precipitation strengthened alloys. Finally, a general review of the constitutive material models that can be applied to this study can be found in Sect. 2.4, including Steck's model.

2.1 Precipitation strengthening

The mechanical properties of most aluminum cast alloys can be greatly enhanced as required carrying out a heat treatment process. The type of process used is determined by the intended effect and depends on the alloy, and the casting method and solidification time. Stress relieving, stabilising, homogenising, soft annealing, or age–hardening are typical examples of heat treatment processes. However, the most common heat treatment for aluminum alloys is the age–hardening. The artificially aged T6, overaged T7, partially aged T64 and naturally aged T4 conditions are common heat treated states resulting from this heat treatment process.

The artificially aged T6 condition is obtained by carrying out a precipitation process at high temperatures in which a fine distribution of a hardening phase is created under specific and controlled temperature and time conditions to interact with dislocations to produce the maximum strengthening possible in the material [24, 25]. The T6 artificial ageing normally comprises three stages of treatment, starting with a solution treatment at a high temperature to create a supersaturated solid solution in the alloy. After water quenching at room temperature, this solution decomposes giving rise to a precipitation distribution of strengthening particles as homogeneous as possible during the artificial ageing process, when the solubility for one particular alloying element decreases in the solid solution. In the case of Al–Si–Mg alloy systems, after the initial formation of small clusters and GP zones, Mg_2Si precipitates nucleate first in the form of metastable and coherent β'' phases [26]. Increasing the duration of ageing towards the T6 condition, the evolution of this distribution to the metastable and semi–coherent β' phase produces the maximum strengthening of the material [26]. By further thermal loading towards the T7 overaged state, a totally incoherent distribution of the equilibrium β phase is finally obtained [26], which lowers the strength of the material as the duration of the artificial ageing increases [27]. Increasing the ageing temperature accelerates the precipitation process and produces coarser distributions [24, 25].

2.1.1 Solution heat treatment

The slow cooling rates resulting from the casting of massive Al–Si–Mg alloy components allow the Mg_2Si particles to precipitate out of solution and grow into large incoherent phases. The contribution of these particles in this as–cast structure to the strength of the alloy is irrelevant. Thus, a solution heat treatment needs to be performed first to obtain a finely dispersed Mg_2Si strengthening distribution.

The solution heat treatment is the first stage of the complete heat treatment as can be seen in Fig. 2.1. The main purpose of this stage is to dissolve the Mg_2Si particles that may result from the casting process and then bring into solution the corresponding alloying elements. During this stage, the spheroidization and coarsening of the Al–Si eutectic particles also occurs, leading to larger interparticle distances [28].

The temperature of the solution treatment should be as high as possible because solubility and speed of diffusion increase sharply with temperature. It is usually around 10°C – 15°C below the melting temperature. In case of the Al–Si–Mg alloy systems, a temperature around 530°C – 540°C close to the eutectic temperature (565°C [29]) is chosen. This temperature range for the solution treatment leads to a significant improvement of the mechanical behavior of the

Al–Si–Mg alloys compared to lower solution temperatures [28]. Nevertheless, lower solution temperatures (480°C – 490°C) can also deliver good results if a very fine grained solidification occurred as a result of a rapid cooling process.

The literature has established that the magnesium and silicon contents reach the maximum equilibrium level in the aluminum matrix according to the alloy composition within less than 1 hour of solution heat treatment [30, 31]. As well, the distribution of magnesium and silicon becomes also homogeneous within this period of time [32–34]. Nevertheless, the dissolution and homogenization of both solutes are strongly influenced by the scale of the microstructure [34].

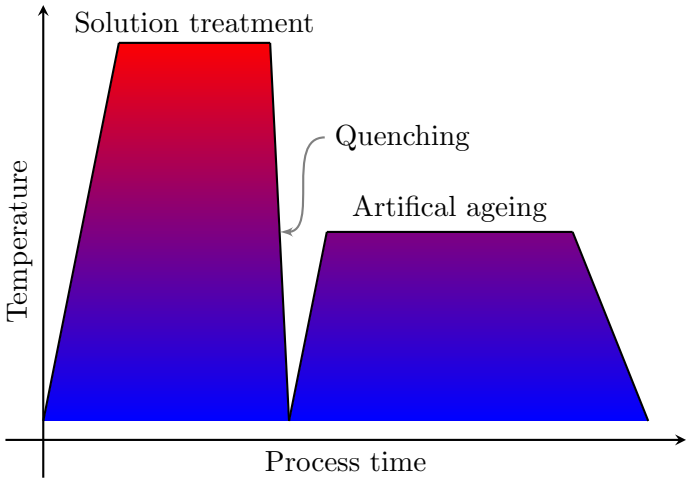

Fig. 2.1: Schematic diagram of the stages of the complete T6–T7 heat treatment: (i) the solution treatment at some temperature as close as possible to the eutectic temperature in the Al–Si–Mg alloy systems, (ii) the quenching stage where a supersaturated solid solution in the alloy is created, and (iii) the final artificial ageing where the precipitation process to strengthen the mechanical behavior towards the T6 or T7 condition of the alloy occurs.

2.1.2 Quenching

Quenching to room temperature after the solution heat treatment results in a non–equilibrium solid solution which is supersaturated, consisting of magnesium and silicon in case of Al–Si–Mg alloy systems. The rate of quenching must be sufficiently rapid to prevent the dissolved alloying elements in the aluminum solid solution from precipitating again. Water at room temperature is normally used for quenching [35]. This water bath is usually heated up to no more than 60°C to prevent the risk of forming steam bubbles. In addition, the time elapsing between the end of the solution heat treatment and the quenching operation should be as short as possible to ensure the effectiveness of the process.

This quenching operation produces large thermal gradients, which may induce large thermal stresses in the material. As a result, these stresses may cause inelastic yielding effects, which eventually will give rise to residual stresses in the component [36]. These typically remain after the following artificial ageing process, as the ageing temperature is too low to allow the stress relaxation [37]. Therefore, the water temperature can be increased for castings and alloys with a tendency to high casting or quenching stresses, but this condition will reduce the strengthening potential of the artificial ageing process.

However, the effect of residual stresses on the precipitation process in Al–Si–Mg alloy systems is usually assumed as negligible. Furthermore, the high diffusivity of both magnesium and silicon solutes into aluminum reduces considerably this potential undesirable effect [38].

Lower quenching rates in Al–Si–Mg alloys result in a partial exhaustion of the initial solid solution. This leads to the formation of small clusters of silicon and magnesium atoms or even small magnesium/silicon co–clusters homogeneously distributed in the matrix. Although these formations will be probably dissolved during the first stages of the artificial ageing, this will reduce the strengthening potential of the alloy [37].

2.1.3 Artificial ageing

The final stage of the heat treatment is the artificial ageing process. This process, typically between 120°C and 220°C for the Al–Si–Mg alloy systems, rectifies the supersaturated solid solution and produces a precipitation distribution of the strengthening phase, whose type, form, size, and density can be controlled according to the temperature and time conditions of the process.

The precipitation sequence taking place during the ageing process is well documented [26, 39, 40]. Small clusters of silicon and magnesium are firstly formed from the initial supersaturated solid solution, followed by the formation of magnesium/silicon co–clusters, which is controlled by the rate of dissolution and diffusion of magnesium atoms [26]. Other analysis report that the decomposition of matrix begins with the clustering of silicon to which secondly magnesium atoms are added [39]. Some works suggest that the initial decomposition of matrix is accompanied by the clustering of not only silicon and magnesium atom clusters, but also vacancies clusters [40].

This magnesium/silicon co–clustering can even occur at room temperature and the nature of these particles is decisive for the ability of the clusters to act as nuclei for subsequent intermediate phases. These co–clusters precede the formation of probably Guinier–Preston (GP) zones, which involve the release of foreign atoms and/or vacancies from the co–clusters [26, 40].

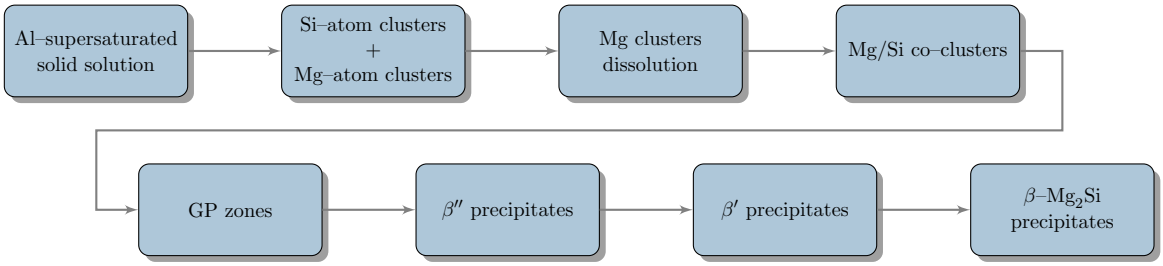

Fig. 2.2: Precipitation sequence for the Al–Si–Mg alloy systems from the first decomposition stages of the initial solid solution to the final stable and incoherent β–Mg_2Si hardening phase [26,40]. This precipitation sequence may be altered by the presence of copper as trace element [43].

By continuing ageing, the next strengthening phases which will be formed would be β'', β', and finally the β–Mg_2Si precipitates. Each of these stages is governed by its own metastable phase diagram towards the final equilibrium β–Mg_2Si phase. The degree of coherency falls as the ageing process continues towards the equilibrium β phase, which shows a complete incoherency with the surrounding aluminum matrix. The β'' is a needle–shaped precipitate presenting a monoclinic structure and it is oriented along $\langle 100 \rangle$ of the aluminum matrix [41]. The exact composition of this precipitate is not clearly defined. However, the magnesium to silicon ratio varies from 1.0 for the alloys with excess of silicon to 2.0 for the balanced alloy [26, 42, 43].

β' particles are semi–coherent precipitates with the aluminum matrix and are present in form of rods with circular cross–section whose axes are parallel to the cube matrix directions [41]. Their final rod–shaped morphology has been shown to be preceded by an initial needle–shaped form [42]. This phase is also reported to have a large length to diameter ratio and therefore exhibits a strong shape effect [39].

The β–Mg_2Si strengthening particles are the final equilibrium precipitates in the Al–Si–Mg alloy systems [26]. These precipitates show a plate–shaped morphology and an orientation along $\langle 100 \rangle$ of the aluminum matrix. The ratio of magnesium to silicon atoms in this precipitate is 2.10 and 2.13 for balanced and with excess of silicon alloys, respectively [42]. In this precipitation stage, the initial solid solution becomes depleted and subsequently the obtained precipitation distribution coarsens by competitive growth at constant volume fraction. The complete precipitation sequence is presented in graphic form in Fig. 2.2 [26, 40].

This precipitation sequence can be highly influenced by the chemical composition of the alloy as well as by the quenching and ageing conditions. Thus, an increase in the ageing temperature leads to an acceleration of the precipitation process, at the same time as it reduces the maximum strengthening potential in the material [44]. Referring to the latter and considering the industrial application of this study, the ageing temperature in this work ranges from 180°C to 300°C.

The predominant strengthening phase and the size and density of the precipitation distribution will determine the interaction mechanism of these precipitates with the dislocations present in the material. According to the first works on the comprehension of artificial ageing based on dislocations interaction mechanisms, the strengthening of an age–hardenable alloy at room temperature increases as the average dislocations internal stress increases when precipitates with respect to their localized stress fields are considered [45]. The flexibility and therefore the capacity of the dislocations to curve between precipitates is limited by their inherent line tension. Under these conditions, small precipitates are sheared by moving dislocations according to the widely known Friedel effect (see Fig. 2.3(a)) [46, 47].

However, the progressive loss of coherency strain and chemical hardening as the precipitation distribution moves towards overageing conditions usually leads to a larger interprecipitate spacing. This effect may produce an expansion of the dislocations into the region between these precipitates. If this expansion is large enough, the dislocations will again rejoin and continue moving on as described in the Orowan effect (see Fig. 2.3(b)) [47, 48].

Providing that the precipitates themselves can withstand the applied stress, the flow stress of precipitation strengthened alloys is governed entirely by the spacing between these particles. Therefore, the greatest impedance to dislocation motion and hence the maximum strengthening possible by age–hardening corresponding to the T6 condition will occur when the precipitates contained in the alloy are large enough to resist shearing by dislocations (Friedel effect) and yet are too finely spaced to be by–passed (Orowan effect).

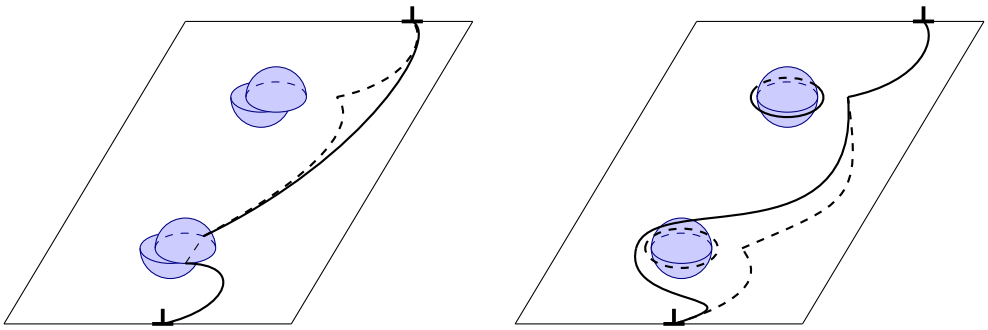

(a) (b)

Fig. 2.3: Scheme of precipitate strengthening mechanisms at room temperature based on precipitate–dislocation interactions for alloys containing small precipitates volume fractions according to the: (a) Friedel mechanism when the precipitates are coherent and small; (b) Orowan mechanism when the precipitates are incoherent and coarse [47].

Thus, the Mg_2Si precipitates in the Al–Si–Mg alloy systems are cut by moving dislocations during

the first stages of precipitation, when these particles are small, coherent, and closely spaced. Due to the inherent flexibility of the dislocations, the number of particles touched per unit length increases as the precipitates grow and become stronger. This effect produces an increase in the strengthening of the alloy. The evolution of the precipitation distribution to the metastable and semi–coherent β' phase produces the T6 maximum strengthening of the material. For a further ageing to T7, an incoherent distribution of the stable β phase is finally obtained. As a result, the precipitates strength and the interprecipitate spacing continuously increase. This allows the dislocations to bulge between the precipitates and escape without cutting them, which continuously lowers the strength of the material.

In addition to the main contribution of the precipitation distribution to the total strengthening of the alloy, the remaining solid solution of alloying elements and the intrinsic strength of the aluminum matrix contribute also to the strength of these alloys. Fig. 2.4 shows a schematic diagram of these relative contributions to the total strength of the material [5].

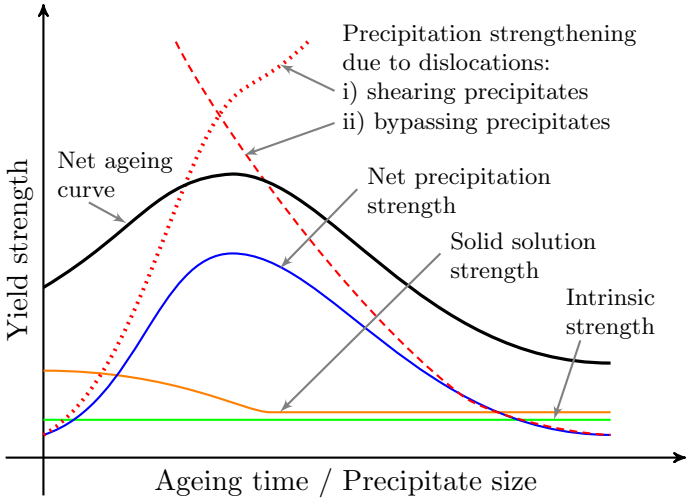

Fig. 2.4: Scheme of the relative contributions of the intrinsic matrix strength, solid solution strength, and shearable and non–shearable particles hardening to the yield strength in Al–Si–Mg alloy systems [5].

2.2 Precipitation modeling

The modeling of the precipitation process is of great interest in industrial applications for designing and optimizing complex non–isothermal ageing processes. For this purpose, different modeling approaches have been developed. These models usually take into account the most relevant features of the hardening precipitates, such as: (i) their crystallography, (ii) their

morphology, (iii) their chemical composition, (iv) their size distribution, (v) their volume fraction, and (vi) their number density [49].

In general, two groups of models can be found depending on the stages of interest of the precipitation process. These are the *early stage decomposition kinetics* models and the *classical nucleation and growth* theories [44].

The *early stage decomposition kinetics* approaches, as their name suggests, are focused on the first stages of precipitation and their objective is the modeling of the particular shape, amplitude, and spacial extension of solute fluctuations in the initial supersaturated solid solution which become critical and, hence, stable against decay. The Johnson–Mehl–Avrami model [50] or the cluster dynamic approach [51, 52] are examples of these approaches.

There are two groups of *early stage decomposition kinetics* models. One is based on *nucleation theories* while the second consider *spinoidal theories*. The nucleation theories, which can be sub–categorized into *classical* and *non–classical* theories, consider the rate of formation of stable nuclei which are usually referred to as "particles" or "droplets". These are considered as spatially localized solute rich clusters with large concentration amplitudes. The spinoidal theories describe the early stage decomposition kinetics as a function of the time evolution of the amplitude and wavelength of certain stable "homophase" fluctuations [44].

Such diffusional growth models of isolated non–interacting particles with uniform size usually does not provide a realistic description of the precipitation process beyond the nucleation stage. Furthermore, the applicability and usefulness of these methods have been reported exclusively for isothermal ageing processes [53].

Conversely, the *classical nucleation and growth* theories consider the three major physical processes involved during the whole precipitation process, that is, the nucleation, growth, and coarsening stages. Small clusters and the well–known GP zones are usually formed in the early first stages during the nucleation process. With the duration of the ageing towards the T6 condition, the nucleation process becomes exhausted and gives rise to the growth process. For a further ageing to T7, the growth stage becomes also exhausted and the coarsening process dominates the precipitation process during which the larger precipitates will grow at the expense of the smaller ones as a result of the release process of excess internal free energy according to the Gibbs–Thomson equation.

The main weakness of these approaches is that they are rather complicated in their fundamentals and require a big amount of input data for their fitting. The application of these models is thus usually limited to very specific alloy systems and precipitation processes.

According to the implementation procedure of these *classical nucleation and growth* theories for precipitation, three different approaches can be found [49]:

(i) *"Mean radius approach"*
The average size and precipitate density (number of particles per unit volume) of the precipitation distribution are considered as sufficient to describe the precipitation process. The Lifshitz–Slyozov–Wagner predicting the average particle size in the precipitation distribution during the coarsening stage is one example [54, 55]. The Langer–Schwartz [56] theory and later modified versions [57] belong also to this kind of models.

(ii) *"Euler–like multi–class approach"*
The precipitation distribution is discretized in different size classes and its time evolution is computed considering the fluxes between neighboring classes. The Kampmann–Wagner model is the classical example of this type of implementation [58]. This approach has been extensively used as basis for later models, such as the models of Myhr [59], Nicolas–Deschamps [60], or Robson [61, 62].

(iii) *"Lagrange–like multi–class approach"*
The strengthening distribution is again discretized in an appropriate number of size classes. But, the radius time evolution of the classes here is computed as a function of time. The Multi–Préci model is developed based upon this theory [63].

The three approaches lead to similar results in simple cases. However, multi–class approaches are required when more complex precipitation processes are involved. Actually, the *"Euler–like approach"* is the most appropriate option to model the precipitation process in Al–Si–Mg alloy systems. Nevertheless, this approach involves a more complex class number management.

The Kampmann–Wagner numerical model has been extensively used to model the evolution of the mechanical properties of Al–Si–Mg alloys during multi–step ageing processes [64]. Based on this numerical model, Robson developed a numerical model that considers the nucleation and growth/dissolution of the previously nucleated particles [22, 61, 62]. This simulation model is especially suitable for dilute alloy systems [61].

Based on some simplifying assumptions, Robson's model allows the prediction of the precipitation distribution in both one– and multi–stage artificial ageing processes covering a huge range of temperatures and the whole precipitation sequence from the early nucleation to the final coarsening stages attending to a unique set of model parameters [65]. In accordance to its Euler–like multi–class nature, Robson's approach divides the precipitation distribution into a series of discrete size classes. Besides, it comprises: (i) a nucleation model, which calculates the

number of new nuclei created at each time step, (ii) a growth/dissolution model, which predicts the growth/dissolution rate for every size class, and (iii) a continuity mass equation for the solutes.

A major advantage of the group of models such as Robson's approach is the possibility of predicting the growth and coarsening of the precipitates in a single distribution without considering the different strengthening phases that are present during the precipitation process [11].

The experimental information used to fit the model is of great importance for a good result. Therefore, an exhaustive quantitative characterization of the precipitation distribution should accompany the classical precipitate shape, composition, and coherency analysis [66, 67].

2.3 Deformation mechanisms

The analysis of the deformation mechanisms that take place on the microscale will contribute to understand the macroscopic behavior of the material, and also its variation when the precipitation distribution is altered. In case of aluminum alloys strengthened by age–hardening, the movement of dislocations and their interaction with the precipitation distribution are the two main microscopic mechanisms that determine their plastic deformation behavior.

The movement of dislocations and the connected plastic deformations caused by external loads are determined by two important activation mechanisms: (i) the stress activation mechanism governed by external mechanical loads, (ii) the thermal activation mechanism which supports the dislocation movements and therefore plastic deformations at elevated temperatures.

Foreign atoms, grain boundaries, and strengthening precipitates are typical obstacles on the microscopic scale that resist to the movement of dislocations in the form of barrier potentials U^*, as shown in Fig. 2.5(a). The possible position of these dislocations relative to these barrier potentials is determined by the temperature.

The effect of applying an external mechanical load can be seen in Fig. 2.5(b). The superposition of the potential U^σ coming from the external load applied changes the obstacles potentials so that the movement of dislocations in the same direction as the applied force is favored at expense of the movement in the opposite direction [68–71]. The effect of increasing temperature results similarly in a decrease of the barriers height.

But not only the obstacles present in the material contribute to these barriers potentials. The material crystalline structure and the dislocations themselves are other important contributions.

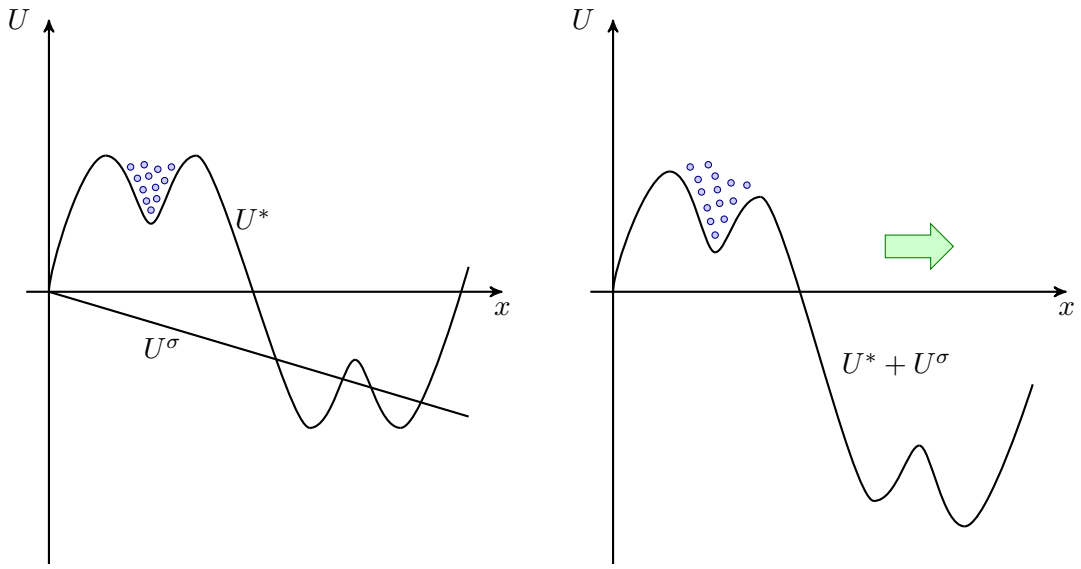

Fig. 2.5: Schematic representation of the obstacles in form of barrier potentials to be overcome for the dislocations movement referring to: (a) the possible position of dislocations relative to the barrier potentials; (b) e.g. the effect of external stress on the barrier potentials, promoting the dislocations motion in the same direction as the force applied.

With regard to the latter, new dislocations are continuously produced during plastic deformation resulting in an increasing ability of the material to deform plastically. This dislocation density increase enhances the dislocations interactions, which produce an isotropic hardening in the material.

The increase of the dislocation density together with the lattice distortions resulting from the plastic deformation produces an increase of the total elastic energy in the alloy. However, this elastic energy hampers the dislocation motion itself, which produces a kinematic hardening. This kinematic hardening is dependent on the direction of the applied stress and, in contrast to isotropic hardening, supports the dislocation motion in the opposite direction to the direction of the applied stress.

At elevated temperatures, usually above half of the material melting temperature, thermally activated reorganization processes occur in the material, which reduce the mutual influence of the lattice disturbances and result macroscopically in a recovery process [68].

The change of kinematic hardening is normally a slow process and therefore it is especially important for the deformation behavior of the alloy at both low and high temperatures. However,

the isotropic hardening changes very quickly at elevated temperatures while the response at low temperatures is similar to that experienced by the process for kinematic hardening.

The Friedel effect and the Orowan process are the predominant dislocation–precipitate interaction mechanisms in age–hardenable materials at room temperature. Both mechanisms make use of the *threshold stress* concept for the dislocation glide process at low temperatures. However, this concept cannot be applied at higher temperature ranges and the dislocation glide deformation mechanism loses its predominating significance [72].

The most important deformation mechanisms at elevated temperatures connected to the activation volume and the free activation enthalpy are given in Table 2.1 [71, 73, 74]. It is well established that at high temperatures dislocations in precipitation strengthened materials can undergo non–planar motion by climbing, which allows the dislocation segment arrested at a particle to bulge out of the slip plane and finally surmount the precipitate [47].

Mechanism	Activation Volume	Free activation enthalpy	Note
Climbing	b^3	Self–diffusion	Constant during deformation
Movement of dislocation jumps	$10 - 1000 \cdot b^3$	Crack formation or constriction	Decreasing with deformation
Slip at high temperature	$10 - 1000 \cdot b^3$	Overcoming of obstacles	–

Table 2.1: Deformation mechanisms and the corresponding activation volume (being b the Burgers vector) and free activation enthalpy at elevated temperatures ($T/T_m > 0.5$, being T_m the melting temperature) [71].

The existence of solutes and especially of precipitates usually leads also to a creep strength increase. This effect produces a roughly uniform shift of the power–law and power–law breakdown regimes to higher stresses, which suggests the convenience of using a *threshold stress for creep* concept, below which creep is assumed not to occur [72, 75, 76]. This *threshold stress for creep* is not connected to the *threshold stress* concept at low temperatures. This feature suggests that the deformation mechanism at low temperatures may not be the basis of the threshold stress at elevated temperatures.

2.4 Mechanical modeling

Simple precipitation models concerning the essential features of ageing [5, 6] or more complex strengthening models considering the contributions of the intrinsic matrix strength, the solid solution, and the strengthening distribution have been developed to predict the hardness or characteristic tensile properties at room temperature for Al–Si–Mg alloy systems [11–13].

However, more advanced and higher-performing material models are necessary when the mechanical response of the alloy under more complex loading conditions is on focus. There are two main types of material models to predict the viscoplastic behavior of two–phase metallic alloys at elevated temperatures. These are: (i) *non–constitutive* models, (ii) *constitutive* models [71].

The description of the inelastic deformation using *non–constitutive* models is done by means of different sub–models for the different deformation mechanisms considered. Each of these sub–models contains different strain–based hardening and recovery processes and is based on a kinetic law and a set of evolution processes. Models of Nix–Ilschner [77], Prinz–Argon [78], and Mugrabi [79] are some examples of this type of models.

Conversely, *constitutive* models can be distinguished by a total deformation rate definition. The description of the different deformation mechanisms is done by means of some internal variables, resulting in a unique formulation for the different deformation processes. These *constitutive* models can be sub–categorized into four different types:

(i) *Phenomenological models*
These models describe the inelastic deformation on a macroscopic scale and their constitutive equations are developed based upon experimental results. Physical observations are taken into account to select the internal variables and their number. However, the deformation mechanisms on the microscale are not considered. Miller [80, 81], Krempl [82], or Chaboche [83, 84] models are some examples.

(ii) *Rational models*
Rational models describe the inelastic behavior of a material by a set of internal variables that satisfy the general continuum mechanics and thermodynamics laws. However, these variables are averaged values and are not related to metal physics. Thus, their evolution is formulated by equations which do not consider a micromechanical background. Examples for this kind of models are the models of Haupt [85] or Lehmann [86].

(iii) *Microscopic models*
These approaches are based on dislocations motion processes. Estrin [87, 88], and

Kocks–Argon–Ashby [89] models are typical formulations. The inelastic deformation is usually described in these models by the dislocation density and the speed of dislocations motion. The difficulty of these models is to derive a macroscopic formulation and to consider effects on the mesoscopic scale such as the evolution of dislocations structures.

(iv) *Stochastic models*
Stochastic theories use the knowledge of metal physics to describe the inelastic deformation and develop the corresponding constitutive equations. The structure of the material is modeled by a distribution function. A macroscopic description can be derived by averaging the distribution function and using its mean value. Stochastic models were first introduced by Feltham [90].

The purpose of these *constitutive* models is to obtain material models of general use which can be applied under many conditions and for many materials. It is also desirable that the development of these models stays as close as possible to the physical processes in the materials. Thus, an extrapolation of the model is possible. But it has to be realized that a completely general formulation is too complicated, so that models are usually limited to a narrow range of materials.

Steck's material model is a constitutive viscoplastic model appropriate for the prediction of the mechanical behavior of two–phase alloy systems specially in the high temperature regime [68–71, 91–95]. This model belongs to the group of stochastic approaches and it has been extended to Markov chains [68, 69].

The enhanced version of the model comprises two internal variables [70]. These are: (i) the kinematic back stress σ^{kin}, (ii) the isotropic stress σ^{iso}. The model presents a large number of model parameters which are independent of temperature [70, 94, 95]. For this reason, the identification procedure followed to fit the model is of great importance.

Although efforts have been made to establish quantitatively the effect of the precipitation distribution on some mechanical properties in aluminum alloys, specially for the yield strength [12, 23, 96–99], the influence of the ageing condition on the material modeling is an issue of ongoing study. As it is based on the fundamentals of metal physics, Steck's constitutive model is an appropriate approach to describe the effect of the precipitation strengthening on the modeling of the viscoplastic response of Al–Si–Mg alloy systems at high temperatures.

Chapter 3

Microstructure characterization

A comprehensive analysis of the microstructure properties of the $AlSi_{10}Mg(Cu)$ aluminum alloy varying with the ageing condition is necessary for the modeling of the precipitation process occurring during the age–hardening treatment. The focus is on the ageing conditions ranging from the T6 to the T7 condition.

This chapter begins by presenting in Sect. 3.1 the chemical composition of the alloy as well as the material preparation procedure followed for its later microstructure analysis. This microstructure characterization involves an exhaustive analysis of the different intermetallic compounds resulting from the manufacturing process and how they are affected by the ageing process. The different investigation techniques used for this purpose are presented in Sect. 3.2. The experimental results gathered are discussed in Sect. 3.3 and summarized in Sect. 3.4. The acquired data will be used for the modeling of the precipitation process in Chap. 4.

3.1 $AlSi_{10}Mg(Cu)$ aluminum alloy

The $AlSi_{10}Mg(Cu)$ aluminum alloy is a cast alloy belonging to the Al–Si–Mg alloy systems of extended use in the automotive industry [1]. This alloy system, which contains magnesium and silicon as the major alloying elements, is usually strengthened by age–hardening. This heat treatment produces a precipitation distribution of Mg_2Si strengthening precipitates as explained in Sect. 2.1. The T6 condition corresponds to the maximum possible strengthening of the alloy and it may lead in case of the $AlSi_{10}Mg(Cu)$ alloy to an increase of the yield strength $R_{p,0.2\%}$ and the ultimate tensile strength R_m from 90 MPa and 180 MPa to 200 MPa and 240 MPa, respectively [100].

The specification for the $AlSi_{10}Mg(Cu)$ permanent mold cast alloy, solution treated, and artificial

aged is EN AC–43200 according to the DIN EN 1706 standard. It is also very common to encounter its former designation DIN 233 [100]. The very good combination of high strength, formability, corrosion resistance, good hot tearing resistance, high chemical resistance, and weldability results in a vast variety of applications for this alloy (not only cylinder heads, but also automotive cylinder blocks, car wheels, aircraft fittings, casings and other parts of compressors and pumps, ...).

3.1.1 Material composition

The chemical composition in weight percentage of the alloy is given in Table 3.1.

Si	Mg	Sr	Ti	Fe	Cu	Zn	Mn
10.0–11.0	0.35–0.50	max. 0.05	0.05–0.15	max. 0.55	max. 0.3	max. 0.3	0.2–0.5

Table 3.1: Chemical composition in weight percentage of the $AlSi_{10}Mg(Cu)$ cast alloy [101].

The Al–Si binary alloy systems present an eutectic point which results in the formation of Al–Si eutectic particles. The morphology of this Al–Si eutectic distribution is modified with the addition of chemical modifiers, such as sodium, antimony, phosphorous, or as in this case strontium [102]. The purpose of adding these modifiers is to produce a refinement in the eutectic structure, which contributes to the enhancement of the mechanical properties of Al–Si–Mg alloys, especially its ductility. Furthermore, the resulting modified eutectic contributes also during the solidification process to reduce the shrinkage factor as well as the tendency shown by the alloy to form blowholes. In addition, the rounding of the Al–Si eutectic resulting from the solution treatment produces a marked increase of the elongation at fracture. Silicon also improves the corrosion resistance, the fluidity of the molten alloy and reduces its susceptibility to hot crevicing during solidification and heating [102].

Additionally, the alloy is a hypoeutectic alloy with a higher concentration of silicon than that of the balanced silicon alloy. This feature results in a modification of the composition and density of the strengthening particles [26,42,103], but it does not alter the nature and sequence of ageing in the alloy [42]. This silicon excess accelerates and promotes the alloy ageing response by enhancing the precipitation of fine and uniformly distributed strengthening precipitates [27,104]. This results in an increase in the achieved strengthening in both naturally and artificially aged tempers, but it also produces an elongation decrease [27,105]. In addition, this silicon excess reduces the peak strength stability in overaged conditions and promotes the precipitation of free silicon particles during the latter stages of ageing. This occurs at expenses of suppresing the precipitation of

equilibrium Mg_2Si precipitates [26, 27, 106], but the contribution of these late–formed silicon particles to the total hardening is not significant [107]. The excess of this solute reduces also the ratio of magnesium to silicon in the β''–Mg_2Si strengthening phase decreasing to about 1:1 ratio [108]. However, as the precipitation process progresses towards the T7 condition, this silicon excess forces the ratio of magnesium to silicon of the β–Mg_2Si precipitates to get closer to the equilibrium value of 2:1 [27].

Magnesium is the other solute contributing to the formation of the Mg_2Si strengthening precipitates. It exhibits a high solubility in aluminum [109, 110] but decreases the ductility and fracture toughness of Al–Si–Mg alloy systems [110]. It also modifies the structure of the Al–Si eutectic, making it coarser and more heterogeneous [111]. Besides, the presence of magnesium in the alloy composition decreases its corrosion tendency.

In addition to silicon and magnesium as major alloying elements, a small content of strontium as modifier produces a modified distribution of Al–Si eutectic particles as mentioned above. Furthermore, this strontium addition enhances the form filling capability usually exhibited by Al–Si–Mg alloys due to the increased fluidity of the alloy in its molten condition. This feature is of special interest for the casting of complicated and thin–walled components.

Iron together with copper are the two main trace elements in the alloy composition coming from its secondary nature. The unavoidable presence of iron promotes the formation of intermetallic iron bearing phases, mainly the chinese–script $Al_{15}(MnFe)_3Si_2$ and $Al_8Mg_3FeSi_6$ phases, and mostly in the form of Al_5FeSi platelets [15, 112]. Iron enhances the notch effect during the casting process and produces an embrittlement in these alloys [113, 114], reducing considerably the ductility and the elongation at fracture and worsening in general the mechanical behavior of these alloys [115]. The presence of this element combined with magnesium may also have a detrimental effect on the precipitation process slowing down the process and reducing the strengthening potential [116]. Furthermore, the formation of these intermetallic phases are highly promoted by magnesium [109].

A partial dissolution of the Al_5FeSi phase may take place during the solution heat treatment occurring by its decomposition into Al_6Fe and silicon particles [15]. These silicon particles are usually brought into solution and may contribute to the formation of new silicon particles at the final precipitation stages as previously explained.

The copper content measured in the alloy in this work is lower than 0.20 wt %. The presence of copper may alter the precipitation hardening in the Al–Si–Mg systems as mentioned in Fig. 2.2 [43]. A small copper content accelerates the process kinetics and leads to finer β'' precipitation distributions [117]. Being copper a major alloying element, the lath–shaped Q' phase becomes the predominant precipitate at the T6 condition being the lath–shaped Q–$Al_5Cu_2Mg_8Si_6$

precipitate the main equilibrium phase in these cases [43]. Furthermore, the corrosion resistance as well as the thermal conductivity of these alloys are considerably reduced by the presence of this element [102]. Nevertheless, it can also prevent the alloy from ageing at room temperature [43].

3.1.2 Material preparation

The preparation of the alloy up to the artificial ageing process is done by following a common preparation procedure comprising the casting process (including the solidification stage), the solution treatment, and the quenching stage. This procedure ensures a high reproducibility of the initial supersaturated solid solution in the alloy. Thus, any changes in the microstructure properties for different ageing conditions can only be attributed to the effect of the precipitation process.

The casting process begins with the melting of the alloy at 730°C in electric furnaces, which promotes the homogenization of the different alloying elements especially of the strontium modifier. The resulting homogenized liquid metal is then poured into permanent bar metallic molds as those presented in Fig. 3.1 pre–heated at 200°C. The form of these molds prevents the casting from having macro–imperfections like pores and shrinkage cavities and also from producing residual stresses resulting from this process or the quenching. The solidification of the specimens is carried out in the molds. After staying one minute in these molds, the resulting casting is cooled down in air to room temperature. Finally, $AlSi_{10}Mg(Cu)$ bars of 270 mm in length and 23 mm in diameter are produced being the base material for the subsequent experiments and investigations.

The solution heat treatment is carried out at 535°C during 6 hours, so that the as–cast Mg_2Si particles resulting from the solidification stage are completely decomposed and dissolved into the aluminum matrix. As a result, a homogeneous solid solution of silicon and magnesium is obtained in the aluminum matrix. Actually, a solution heat treatment time of 1 hour at 538°C is enough to achieve this condition according to previous electron microprobe analysis performed for Al–Si–Mg alloy systems [30, 31].

The solutioned specimens are then quenched in water producing a non–equilibrium supersaturated solid solution of magnesium and silicon. The room temperature of the quenching water preventing the formation of steam bubbles and the bar–shaped form of the specimens guarantee a rapid cooling. As a result, a partial precipitation process during the quenching is discarded.

The final artificial ageing treatment is carried out in a separate electrical air circulation furnace. It consists of a single ageing stage at constant temperature. The temperature and time conditions

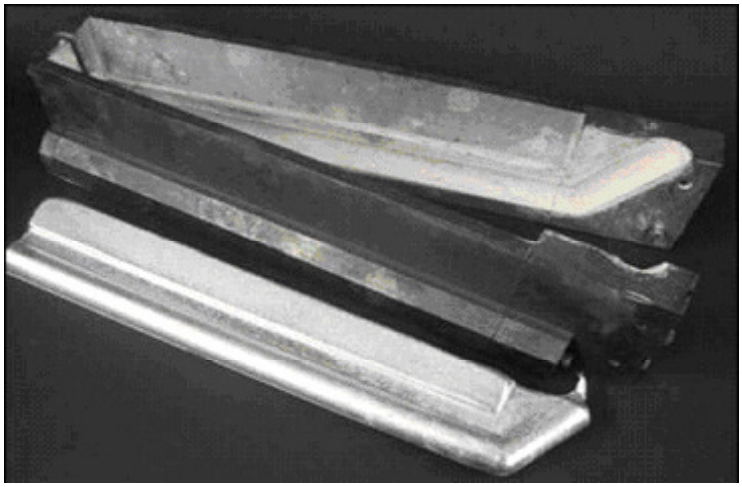

Fig. 3.1: Metallic molds used for the casting according to VDG–standard P 376. The form of the molds is especially appropriate to prevent the formation of imperfections and the appearance of residual stresses in the cast bars.

of the process are established considering both the ageing condition of interest as well as the nature of the investigations to perform. These are specified in each of the following sections.

The time elapsing between the quenching and the artificial ageing may induce the formation at room temperature of small clusters of silicon and magnesium or even very fine precipitation distributions, which lowers the strengthening potential of the material during the ageing [26]. Thus, this time is limited to a maximum of 10 minutes. The few small particles that may have been formed will be rapidly dissolved at the beginning of the artificial ageing.

3.2 Experimental fundamentals

Different investigation techniques are used for the microstructure characterization of the alloy depending on the types of intermetallics to analyze [118, 119]. The characterization of intermetallics on the micrometer scale is done using the optical microscopy utilizing visible light. The electron microscopy utilizing a beam of highly energetic electrons as excitation source is used for the investigation of the Mg_2Si strengthening precipitates on the nanometer scale as well as for the chemical analysis of the intermetallic phases. Finally, the qualitative information on the Mg_2Si precipitation distribution is gathered utilizing the neutron scattering technique.

3.2.1 Optical microscopy

Optical microscopy investigations on metals are usually carried out using reflected light due to the characteristic opacity of metals. Useful information on the morphology of particles on the micrometer scale is normally obtained. Light microscopy examinations are carried out in this work using a reflected light microscope Olympus type 41PMG3. Disc–shaped specimens of 23 mm in diameter and 10 mm in thickness are prepared for the investigations. The specimens' preparation involves mechanical grinding and polishing operations. For these investigations samples are treated at the temperatures (durations) of 210°C (0.2 h, 0.5 h, 2 h), and 280°C (0.5 h, 19 h, 69 h, 211 h). These samples are etched at the end for their grain size analysis with an acidic solution consisting of 71.4 vol % HCl, 23.8 vol % HNO_3, and 4.8 vol % HF.

3.2.2 Electron microscopy

Electron microscopy analysis utilizing a high voltage electron beam yield valuable information on the crystal structure of materials and the morphology, topology, and composition of species on the nanometer scale. Transmission electron microscopy (TEM) and scanning electron microscopy (SEM) are used here.

3.2.2.1 Transmission electron microscopy

TEM images are usually obtained in case of investigations on metals from the diffracted beam resulting from the elastically scattered electrons. TEM investigations are carried out in this work using a TEM microscope Philips type CM200 at the Helmholtz-Zentrum Geesthacht (Germany). Special purpose specimens are prepared for this analysis. Starting by cutting a disc of 2.3 mm in diameter by means of a diamond saw, the resulting disc is electrochemically grounded to a thickness in the 100 μm range using a solution of 33 vol % HNO_3 with CH_3OH at a temperature of -30°C. A voltage of 20 V is applied generating a perforation of the specimen after about one minute with an average current of 80 mA during thinning.

3.2.2.2 High resolution transmission electron microscopy

HTEM is an imaging mode of the TEM microscopy that allows the imaging of the crystallographic structure on the atomic scale. A FEI TITAN 80–300 TEM with its aberration corrected electron optics is used at the Helmholtz-Zentrum Geesthacht for this analysis. The same procedure as the

one described above for the TEM investigations is used here for the samples preparation. For this analysis specimens are treated at 210°C for 0.5 h.

3.2.2.3 Scanning electron microscopy

Contrary to the characteristic transmission of TEM, SEM images are built from the electrons interactions occurring in the surface of the specimen. Their detection ultimately provide information about the condition of the specimen surface, such as its topography and composition. SEM investigations are performed here using a Zeiss type EVO50 SEM microscope. As SEM investigations allow to characterize bulk samples up to many centimeters in size, the specimens preparation procedure coincides practically with that presented for light microscopy. Nevertheless, the preparation procedure followed here finishes with a final polishing using aluminum oxide suspension. SEM investigations are coupled with an energy dispersive X–ray spectroscopy (EDX) facility for a qualitative analysis of the chemical composition of different intermetallic phases.

3.2.3 Neutron scattering

Investigations on the precipitation kinetics of the Mg_2Si strengthening particles in Al–Si–Mg alloys are usually carried out using TEM microscopy. The focus of these studies is primarily on the first stages of nucleation and how the decomposition of the supersaturated solid solution and the formation of clusters occur [26, 39, 40]. As a result, the size, shape, and approximate composition of the Mg_2Si strengthening precipitates [119–122], as well as the precipitation sequence [26], and the strengthening mechanisms [27, 123] have been well–established in the literature. However, the influence of the ageing conditions of the age–hardening process on the formation of the precipitation distribution is not fully established [18, 20, 21]. Additionally, this experimental procedure is traditionally applied locally on a reduced material volume without a reliable statistics [52]. The analysis of a relatively large volume leading to valuable and statistically meaningful experimental information can be carried out using scattering techniques applied to synchrotron or neutrons sources [124].

The neutron scattering is an experimental technique using neutrons as excitation source. This subatomic particle shows a strong force interaction with matter in a very short–range while the magnetic interaction is weak but long–range. Thus, neutrons penetrate deeply into most materials, contrary to the reduced penetration shown by electrons limited to a very few atomic layers. This feature provides very good statistics to the experimental results obtained by using neutron scattering on the nanometer scale.

The interaction between the incident neutron beam and the material examined produces the elastic and inelastic scattering of the incident neutrons. The elastic component is used to determine the material atomic or magnetic structure while the inelastic scattering provides information on the atomic and molecular motion as well as on the magnetic and crystal field excitations. From these two types of scattering, the small angle neutron scattering (SANS) technique is based on the elastic scattering. This non–destructive experimental procedure is usually used for investigations on the matter structure providing information on the average size and particles density in the range between 1 and 100 nm. For this reason, SANS investigations allow characterizing the size distribution of the Mg_2Si strengthening precipitates in Al–Si–Mg alloy systems [18, 20, 21, 66]. SANS principles can be easily found elsewhere [125, 126].

The magnesium ans silicon solutes contributing to the Mg_2Si precipitation distribution have a similar atomic number as the aluminum matrix. This produces a very low contrast between precipitates and matrix when using X–rays as excitation source [67, 124, 127]. Therefore, small angle X–ray scattering (SAXS) is not an alternative to SANS for the characterization of the Mg_2Si precipitation distribution in this work, despite its advantages like its high resolution and the short time measurement required [128, 129].

The SANS measurements are carried out in the SANS–2 facility at the German Engineering Materials Science Center (GEMS) in Geesthacht (Germany). Before being directed to the specimen to examine, the neutrons produced in the reactor have been cooled down in the cold source and guided to the SANS facility through the curved neutron guides unit. The wavelength of the neutron beam is set by a mechanical velocity selector depending on the subject matter and nature of research. The divergence of the neutron beam is appropriately corrected by the collimation system.

The resulting collimated neutron radiation is then partially transmitted by the specimen itself, partially absorbed, and partially scattered when it strikes the material. The scattered part is detected by the small angle detector unit. This unit is inside an evacuated tube and can be positioned to a distance up to 20 m of the specimen, covering a wide range of scattering vectors q ($q = 4\pi \sin(\theta)/\lambda$, where 2θ is the scattering angle). Large scattering vectors q characteristic of very small particles are detected by small distances of the detector element and *vice versa*. Thus, the macroscopic differential cross–section calculated from the intensity measured by the detector I is [126]:

$$\frac{\mathrm{d}\Sigma}{\mathrm{d}\Omega} = \frac{I}{I_0 \cdot D \cdot \Delta\Omega \cdot T \cdot \eta} \ , \tag{3.1}$$

where I is the measured intensity flux at the detector, I_0 is the primary beam intensity flux

before being scattered, D is the sample thickness, $\Delta\Omega$ is the solid angle covered, T is the sample transmission, and η is the detector efficiency.

For these SANS investigations disc–shaped specimens of 23 mm in diameter and 3.5 mm in thickness with plain parallel faces are prepared. Thus, the substantial volume to be examined guarantees the statistical significance of the results. Furthermore, the specimens thickness prevents multiple scattering. The specimens are grounded to ensure the incidence of the neutron beam in the normal direction and are previously treated at the temperatures (durations) of 180°C (2.5 h, 3.5 h, 6 h, 18 h, 48 h, 96 h, 240 h), 210°C (0.33 h, 1 h, 3 h, 6 h, 18 h, 48 h, 162 h), 240°C (0.33 h, 3 h), and 300°C (0.33 h, 0.66 h, 1.5 h, 3 h, 6 h, 24 h). The ageing of the specimens previous to the measurements allows to use long data acquisition times of about 2.5 hours contributing to the high quality of the scattering curves.

The SANS measurements are carried out at room temperature. A neutron wavelength of 5.8 Å (wavelength spread of 10 %) and different detector distances (mostly 1 m, 4.5 m and 14.0 m) are used with appropriate collimators to cover scattering vectors q from 0.025 nm^{-1} to 3 nm^{-1} using unpolarized neutrons. The measured intensities are corrected for collecting transmission, background, and detector efficiency effects. Absolute cross–sections are obtained by calibration against a vanadium sample.

3.3 Experimental results

The experimental results gathered from the different investigations carried out on dendrite arm spacing, grain size, Al–Si euectic particles, Al_5FeSi platelets, and Mg_2Si precipitation distribution are presented in the following sections. The main purpose of these analysis is to identify those microstructure properties altered with the ageing condition of the alloy during the precipitation process.

3.3.1 Dendrite arm spacing

Most of aluminum alloy castings exhibit a dendritic solidification microstructure [113]. The experimental measurements of dendrite arm spacing (DAS) on two specimens treated to the T6 and T7 conditions are shown in Figs. 3.2(a) and 3.2(b), respectively. The temperature (duration) of ageing for the T6 specimen is 210°C (30 minutes) and 280°C (211 hours) for the T7 sample, being their average DAS measured 22.53 µm and 22.67 µm respectively. These results together with those gathered for other five ageing states given in Table 3.2 (see p.41) show that the

DAS is not affected at all by the alloy ageing condition. This agrees with previous works where DAS is reported to be mainly determined by the alloy chemical composition together with the solidification and cooling rates of the casting process [113].

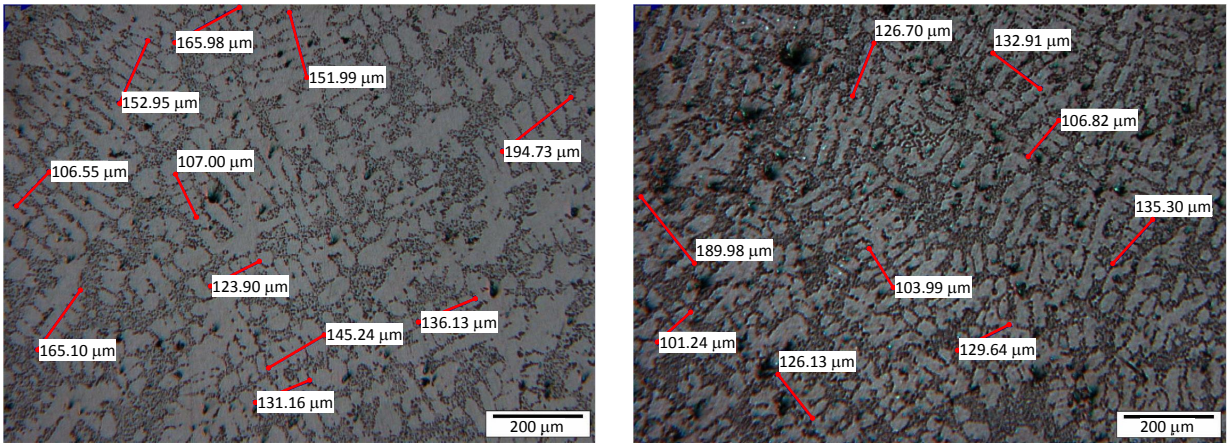

(a) (b)

Fig. 3.2: Optical micrographs showing DAS measurements in: (a) T6 condition; (b) T7 condition. DAS is not altered during the artificial ageing process.

3.3.2 Grain size

The grain boundary strengthening is one of the most common strengthening mechanisms in metals together with the precipitation hardening and is directly determined by the material average grain size. In general, the material strength is increased by reducing its grain size (Hall–Petch relationship [130]).

Grain size measurements carried out on previously etched specimens and following the linear intercept method ($\bar{D}_{grain} = L \cdot p \cdot 1000/(z \cdot V)$, being L the measurement line length, p the number of measurement lines, z the number of intercepted grains, and V the micrograph image magnification) yield the result of 1.84 mm and 2.06 mm for the same T6 and T7 ageing conditions as in Sect. 3.3.1 (see Fig. 3.3). Very similar values are obtained for all other ageing conditions as can be seen in Table 3.2 (see p.41). Therefore and similarly as with DAS, the grain size of the alloy is also unaltered during the ageing process. In fact, it is also mainly determined by the cooling rate resulting from the solidification stage during the casting [102]. Furthermore and according to the Hall–Petch relationship, these large values of grain size will reduce the contribution of the grain–boundary mechanism to the total strengthening of the alloy.

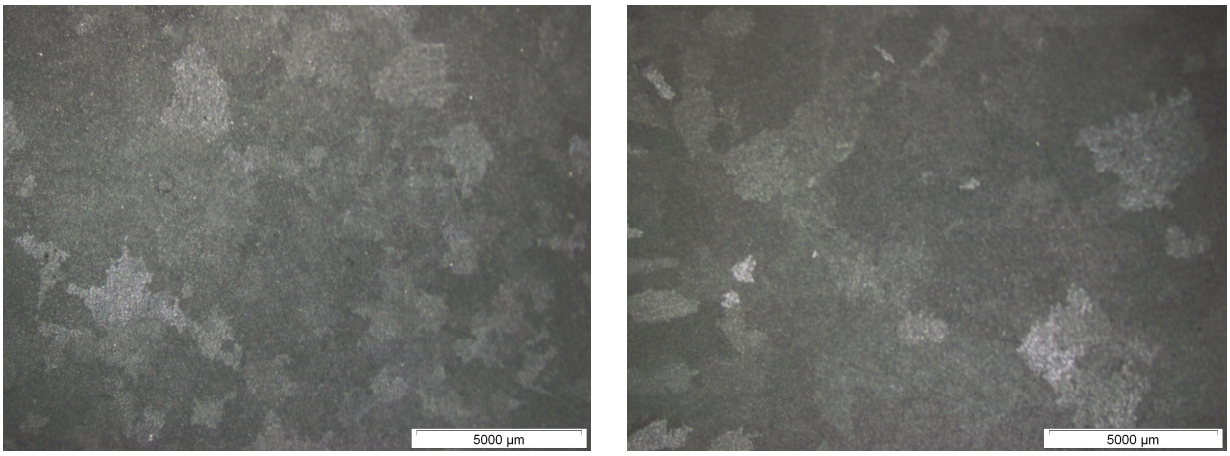

(a) (b)

Fig. 3.3: Optical micrographs showing grain sizes in: (a) T6 condition; (b) T7 condition. Grain size remains unchanged during the ageing process.

3.3.3 Al–Si eutectic particles

The Al–Si eutectic particles have also a significant contribution to the total strengthening of Al–Si–Mg alloy systems [12]. This eutectic exhibits in the as–cast condition of the $AlSi_{10}Mg(Cu)$ alloy a morphology of brittle and coarse acicular plates as shown in Fig. 3.4(a) as a result of the low cooling rates [15]. These plates act as crack initiators and will appreciably lower the alloy mechanical properties. However, the addition of strontium in the alloy chemical composition transforms this fibrous morphology into a spherical eutectic distribution during the solution treatment. The result of this *spheroidization* process is shown in Fig. 3.4(b). Additionally, the coarsening of these Al–Si particles occurs simultaneously due to the long duration of the solution treatment (Ostwald ripening).

Eutectic measurements performed on the same T6 and T7 conditions as in the preceding analysis are shown in Figs. 3.5(a) and 3.5(b) and yield an average eutectic size of 1.64 µm and 1.57 µm respectively. Besides, the roundness ratio R of these particles assumed their spheroidal shape ($R = 4A/(\pi L) \cdot 100$, being A the particle area, and L the longest distance between two points in the particle perimeter) is 80 % for both ageing conditions. Very similar results are obtained for the other five ageing conditions (see Table 3.2 in see p.41). In addition, the possible precipitation of new silicon particles during the latter stages of ageing pointed out in Sect. 3.1.1 due to the silicon excess can not be observed. Therefore, the eutectic distribution as in the case of DAS and grain size remains unchanged during the alloy ageing.

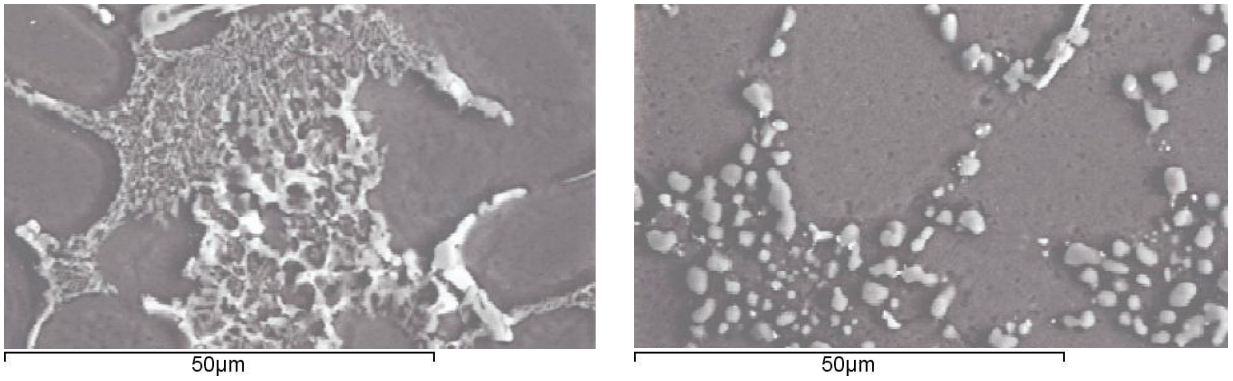

(a) (b)

Fig. 3.4: SEM micrographs showing Al–Si eutectic particles in the interdendritic area in: (a) the as–cast condition (fibrous morphology); (b) the as–quenched condition (spheroidal morphology). The solution treatment has a strong effect on the Al–Si eutectic morphology.

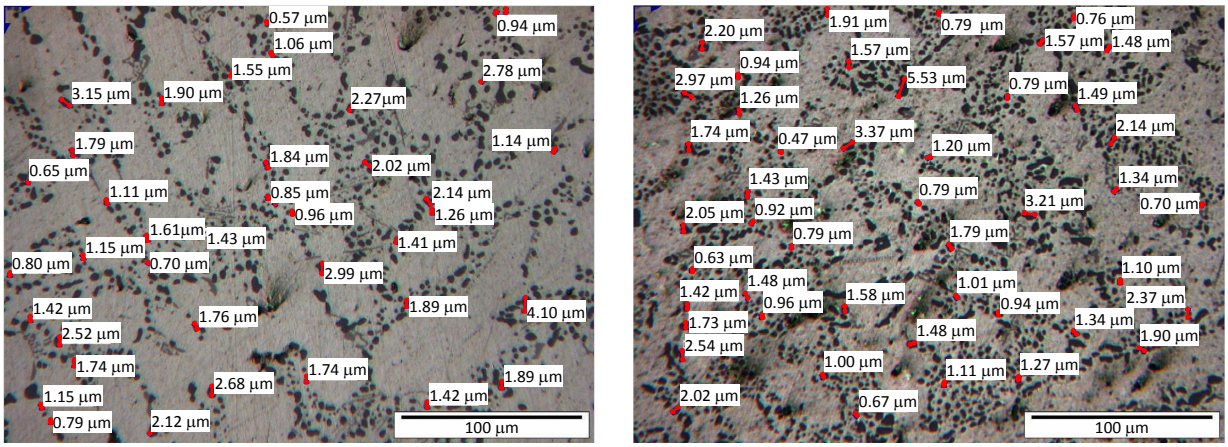

(a) (b)

Fig. 3.5: Optical micrographs showing Al–Si eutectic particle measurements in: (a) T6 condition; (b) T7 condition. The size and morphology of Al–Si eutectic particles remain unaltered during the artificial ageing process.

3.3.4 Al_5FeSi platelets

Highly faceted Al_5FeSi platelets extended even up to several millimeters long appear in the alloy (as needles in 2D sections). This brittle intermetallic compound act as stress raiser and produces a deterioration of the alloy mechanical behavior [131]. Length measurements of 2D–Al_5FeSi needles on two specimens aged to the same T6 and T7 ageing conditions are presented in Figs. 3.6(a) and 3.6(b) giving an average length of 12.00 µm and 16.22 µm. However, this difference in the average length can not be attributed to the effect of ageing conditions, but rather to the

inherent difficulty of finding the right position of the platelets longitudinal section for their measurement. This feature produces a significant scattering in the experimental results as can be seen in Table 3.2 (see p.41). Besides, the large slenderness ratio exhibited by the needles suggests rapid cooling rates during the casting due to using metal dies. In addition, the solidification and cooling of the castings in radial direction also determines the platelets aligning in this direction. Therefore, the change in length of these needles is completely random as a result of the difficulties encountered during the measurement and is not due to the effect of the ageing condition on this microstructure compound.

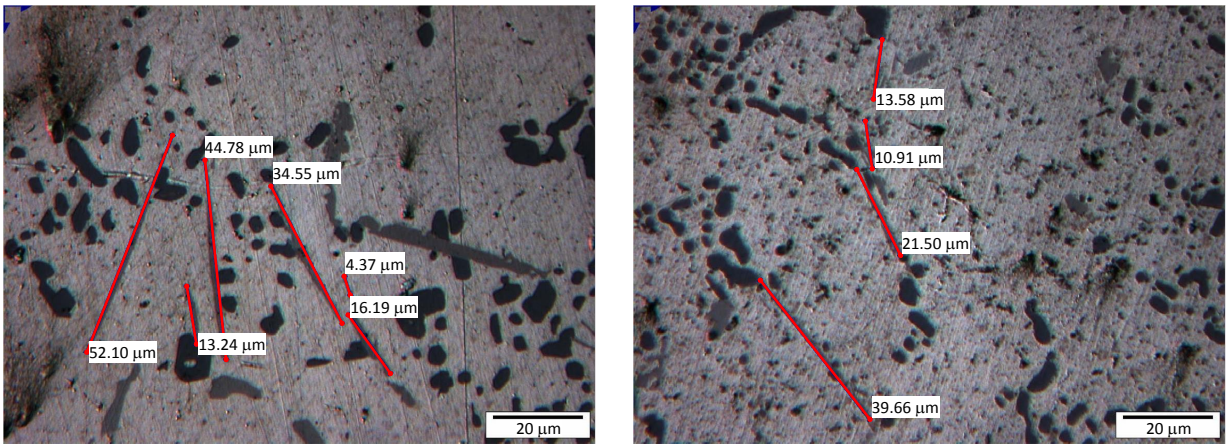

(a) (b)

Fig. 3.6: Optical micrographs showing Al_5FeSi platelets (2D–needles) length measurements in: (a) T6 condition; (b) T7 condition. The results scattering is quite pronounced.

Chinese–script $Al_{15}(MnFe)_3Si_2$ and $Al_8Mg_3FeSi_6$ intermetallics are seldom found. This confirms the decomposition of these phases due to the long duration of the solution treatment producing very fine iron rich precipitates, probably of the Al_5FeSi phase [15], and also enhancing the precipitation process because more magnesium is released into solution [27]. In addition, the possible presence of Al_6Fe intermetallics is not detected, discarding a partial decomposition of the Al_5FeSi phase also in the solution heat treatment.

3.3.5 Mg_2Si strengthening precipitates

The strengthening of the Al–Si–Mg alloy systems is mainly due to the formation of a Mg_2Si precipitation distribution during the ageing process, usually carried out at high temperatures (artificial ageing) [15–18]. The information gathered from the SANS measurements and the HTEM images provides a good basis for a complete quantitative characterization of this strengthening distribution.

However, the presence of Mg_2Si particles in the alloy does not imply an automatic strengthening increase. As an example of this, Fig. 3.7 shows the $AlSi_{10}Mg(Cu)$ alloy microstructure in the as–cast condition comprising the aluminum matrix and a secondary phase consisting of two different intermetallic compounds. These are the fibrous silicon particles distributed both inside grains and at grain boundaries and the coarse Mg_2Si particles precipitated along grain boundaries, resulting from a slow cooling rate despite the metal molds used for the casting [132]. The unrefined morphology of the Al–Si eutectic particles and the initial coarse Mg_2Si particles do not contribute to improve substantially the alloy mechanical properties. Thus, producing the appropriate Mg_2Si precipitation distribution is necessary for a significant contribution of the precipitation hardening mechanism to the total material strengthening.

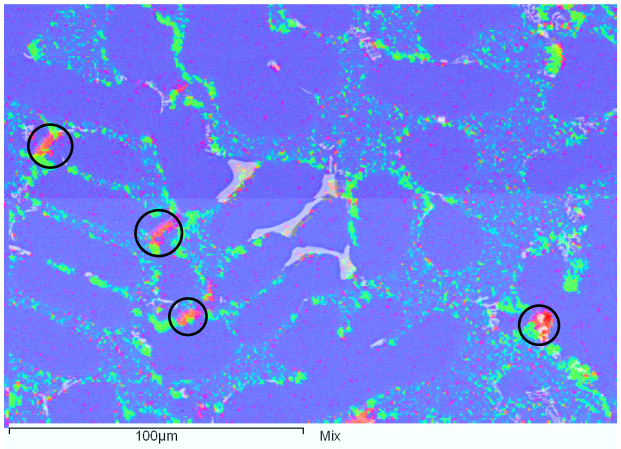

Fig. 3.7: SEM micrograph showing the alloying and trace elements mapping in the as–cast condition of the alloy. Coarse Mg_2Si precipitates are found in the interdendritic area.

3.3.5.1 TEM/HTEM Results

TEM/HTEM investigations are performed to determine the dominating precipitate phase and its shape and coherency in the alloy T6 condition as well as the preferred sites for the nucleation of new Mg_2Si precipitates.

For these investigations specimens are slightly tilted to record all micrographs along the $\langle 001 \rangle$ zone axis of the aluminum matrix, in agreement with previously reported analyses of Mg_2Si precipitates [26]. HTEM micrographs of the aluminum matrix show the expected atomic arrangement under this zone axis. This is a cubic lattice of atoms within the fcc aluminum. Fourier transformation of the micrographs gives maxima that reassemble the diffraction pattern of an unordered fcc crystal in the $\langle 001 \rangle$ orientation.

Many small rod–shaped precipitates with a radius in the 5 to 10 nm range can be found in the T6 condition. Two phase contrast images of Mg_2Si strengthening precipitates are shown in atomic resolution in Fig. 3.8(a). In this figure, a diffraction contrast showing distortion of the aluminum matrix is visible when an objective aperture is applied. Nevertheless, this distortion contrast cannot directly be related to the precipitates.

Higher magnification images of these precipitates reveal an atomic structure which corresponds to the thermodynamic metastable β' precipitate phase. This feature together with the rod shape of the precipitates suggests that the copper content in the alloy, limited to a maximum of 0.3 % (Table 3.1) and in this work lower than 0.2 %, is not large enough to promote the precipitation of Q–$Al_5Cu_2Mg_8Si_6$ precipitates and alter the precipitation sequence of the Al–Si–Mg system in agreement with the assumption made in Sect. 3.1.1.

However, the ultimate conclusion on the predominant strengthening phase could only be drawn from simulations of the HTEM pictures. It is striking that the precipitates are not aligned with the atomic {001} layers of the aluminum matrix; rather, they deviated by approximately 10° as shown in Fig. 3.8(b), indicating that these precipitates were not fully coherent with the surrounding matrix, as is expected from metastable β'–Mg_2Si phases. However, the resolution is not sufficient to determine the continuity of the atomic layers at the interface. The precipitates and dislocations cannot be clearly correlated, implying that the nucleation of the precipitates takes place homogeneously throughout the aluminum matrix.

3.3.5.2 SANS Results

The neutron scattering cross–sections for the four ageing temperatures 180°C, 210°C, 240°C and 300°C for different ageing times are presented in Fig. 3.9. These values agree with previous SANS investigations also performed for similar Al–Si–Mg alloy systems [18]. The scattering intensity curves exhibit the typical shoulder contribution at intermediate scattering vectors q of a unique distribution of strengthening precipitates of nanometer–scale (basically, β'– and β–Mg_2Si precipitates according to previous results and the alloy precipitation kinetics [26,39,40]) for every ageing temperature with no cross–over at large scattering vectors q.

At all of the ageing temperatures, the scattering curves show a constant background using a large scattering vector q. For small scattering vectors q, larger structures, such as primary precipitates, inclusions, dispersoids, and grain boundaries contribute to the effect with a q^{-4}–tail in the visible q–range. Thus, the scattering curve corresponding to the initial supersaturated solid solution in the as–quenched condition should comprise a straight line with a q^{-4} contribution at small scattering vectors q together with the constant background at large scattering vectors q.

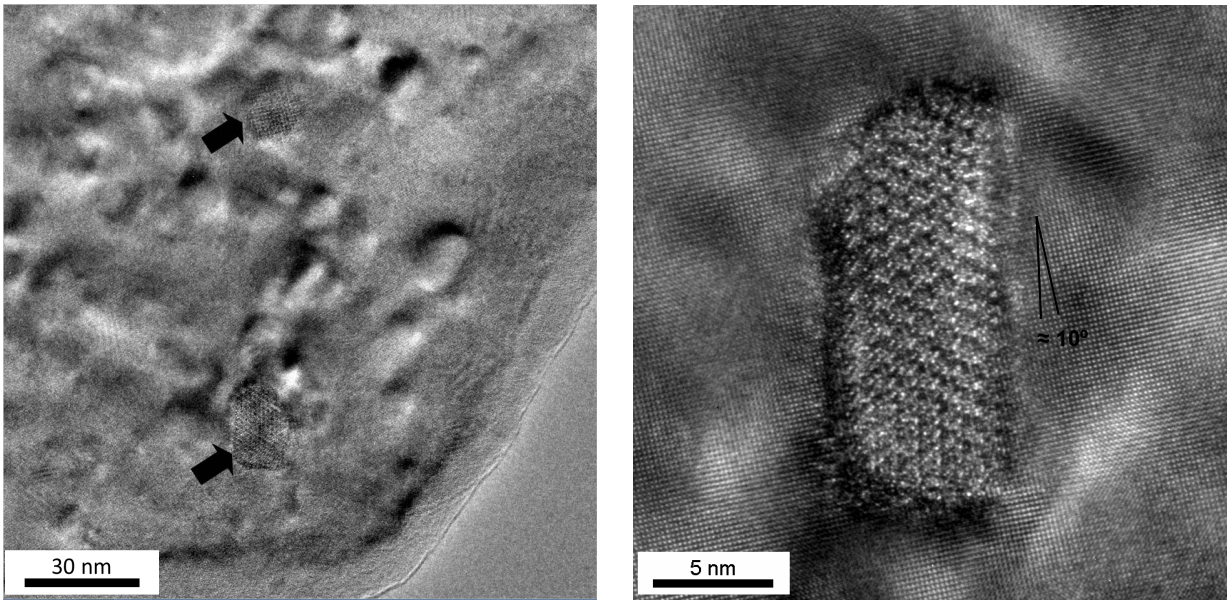

(a) (b)

Fig. 3.8: HTEM atomic resolution filtered micrographs of: (a) two semi–coherent β'–Mg_2Si precipitates; (b) a semi–coherent β'–Mg_2Si precipitate showing a deviation of approximately 10° with respect to the atomic {001} layers of the aluminum matrix.

As the ageing time period is extended, the shift of the characteristic shoulder to smaller scattering vector q ranges confirms that growth and coarsening of the Mg_2Si strengthening precipitates are taking place during the artificial ageing stage.

3.3.5.3 Analysis of the precipitation distribution of Mg_2Si strengthening precipitates

The measured scattering curves should be further analyzed in terms of the size and fraction of precipitates to quantify the effect of the ageing condition on the strengthening precipitation distribution. The local monodisperse approximation is adopted for the treatment of interparticle interference because the neutron scattering cross–sections show the characteristic shoulder caused by a high particle number density in the nanometer range [14]. The precipitates are assumed to have a rod–like shape, which was confirmed by the HTEM images previously presented. In this approximation, the scattering cross–section of a dispersion of precipitate particles can be described by Eq. (3.2):

$$\frac{\mathrm{d}\Sigma}{\mathrm{d}\Omega}(q) = (\Delta\eta)^2 \cdot \int_0^\infty n(R)\, V(R)^2\, F(q,R)^2\, S(q,R,f) \cdot \mathrm{d}R \;, \tag{3.2}$$

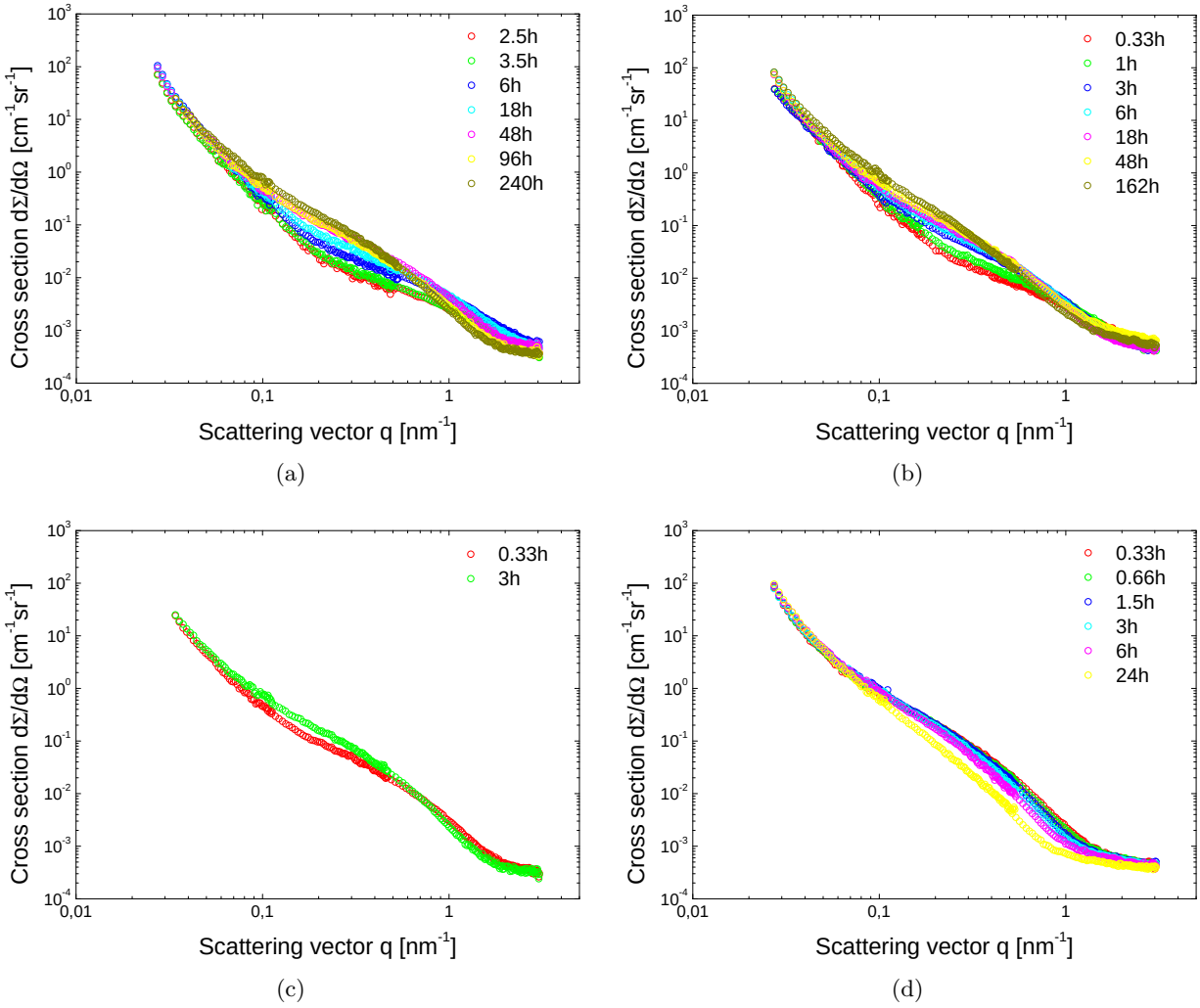

Fig. 3.9: SANS scattering curves obtained from $AlSi_{10}Mg(Cu)$ samples artificial aged at: (a) 180°C for 2.5 h, 3.5 h, 6 h, 18 h, 48 h, 96 h and, 240 h; (b) 210°C for 0.33 h, 1 h, 3 h, 6 h, 18 h, 48 h and 162 h; (c) 240°C for 0.33 h and 3 h; (d) 300°C for 0.33 h, 0.66 h, 1.5 h, 3 h, 6 h and 24 h.

where $\mathrm{d}\Sigma/\mathrm{d}\Omega$ is the macroscopic differential scattering cross–section (Eq. (3.1)), $\Delta\eta$ is the difference in the scattering length densities between particle and matrix, $n\,(R)\,\mathrm{d}R$ is the unknown size precipitation distribution, $V\,(R)$ is the particle volume, $F\,(q,R)$ is the particle form factor, and $S\,(q,R,f)$ is the structure factor describing the interparticle interference effect [128].

The resulting precipitation size distribution $n\,(R)$ is then approximated by a normal distribution function of the radius R:

$$n\left(R\right) = \frac{n_0}{\sqrt{2\pi}\sigma_N} \cdot \exp\left(-\frac{\left(R - R_0\right)^2}{2\sigma_N^2}\right) \ . \tag{3.3}$$

According to Eq. (3.3), the maximum and width of the distribution function, R_0 and σ_N, respectively, and the total density n_0 of the particles contained in the precipitation distributions at the different ageing states are determined by fitting every scattering curve calculated by Eq. (3.2) to the corresponding measured scattering curves shown in Fig. 3.9 using the least–squares procedure. This method is automatically computed using software developed by the GEMS Center.

3.4 Concluding remarks

This chapter addresses the analysis of the effect of the ageing process on the microstructure of the alloy and its precipitation kinetics, focusing on the ageing conditions ranging from the T6 to the T7 conditions. For this reason, various microstructure compounds are analyzed for determining first which of them are affected by this process, and then analyze in more detail the effect of the temperature and duration of the process.

The DAS, the grain size, the Al–Si eutectic particles, the Al_5FeSi platelets, and the Mg_2Si strengthening precipitates are examined. Of all of them, only the latter compound significantly changes with the alloy ageing condition and is altered with the ageing process. The variation in the results obtained for the Al_5FeSi platelets are due to the difficulties found for their measurements. The results of these unaltered microstructure compounds obtained for the seven ageing states considered between the T6 and T7 conditions are presented in Table 3.2.

These results does not necessarily mean that these compounds remaining unaltered during the ageing process do not contribute to the total strengthening of the alloy. For instance, the effect of DAS on the mechanical properties of Al–Si–Mg alloy systems is also a matter of study [133]. Rather, their contribution to the alloy strengthening for the overaged conditions considered in this work remain also constant, likely contributing to the intrinsic strength of the matrix.

A comprehensive characterization of the Mg_2Si precipitates is obtained by combining the results obtained from the TEM/HTEM images with the SANS experimental curves. The most notable aspect of the SANS results is their quality, providing meaningful statistics. The characteristic shoulder in these curves moving towards smaller scattering vectors q as the alloy overaged condition is more pronounced indicates a larger precipitates mean size, as expected. As a result,

Ageing conditions		Hardness	DAS	Grain size	Al–Si eutectic	Al_5FeSi
T_{ageing}	t_{ageing}					
°C	h		µm	mm	µm	µm
210	0.2	119.4	22.90	1.98	1.63	24.34
210	0.5	124.8	22.53	1.84	1.64	12.00
210	2.0	108.2	19.81	2.16	1.70	6.13
280	0.5	84.0	21.02	2.06	1.53	18.16
280	19.0	63.7	22.36	2.92	1.55	8.48
280	69.0	56.1	22.76	2.14	1.79	9.81
280	211.0	50.1	22.67	2.06	1.57	16.22

Table 3.2: Results of unaltered microstructure compounds obtained for seven ageing states ranging from the T6 to the T7 condition. The ageing conditions used for the ageing process and the corresponding Brinell hardness values are included.

a large number of scattering curves is obtained for different overaged conditions of the alloy, considering four different temperatures and varying ageing times. The HTEM images gathered for the T6 condition confirm the presence of rod–shaped β' as the most common strengthening phase and discard other types of hardening particles (mainly Q–$Al_5Cu_2Mg_8Si_6$).

These experimental curves are further analyzed to obtain the corresponding Mg_2Si precipitation distributions, assuming a normal distribution. The resulting mean size R_0 and density of precipitates n_0 for each precipitation distribution together with the corresponding ageing conditions and Brinell hardness value are given in Table 3.3. On the basis of these results, higher ageing temperatures produce coarser precipitation distributions with a lower precipitates density.

This extensive and complete characterization of the precipitation kinetics of the alloy is a good base for the modeling of the precipitation process with sufficient statistical significance. Thus, the further development of the work will focus on modeling the effect of the temperature and duration of the ageing process on the precipitation process of the alloy. A major application of the resulting model would be to predict the effect of non–idealities and more real–life ageing conditions, like complex non–isothermal ageing processes also considering the heating and cooling stages.

Ageing conditions		Hardness	Average size	Precipitate density
T_{ageing}	t_{ageing}			
°C	h		nm	m^{-3}
180	2.5	126.4	1.31	$4.03 \cdot 10^{23}$
180	3.5	125.5	1.35	$6.78 \cdot 10^{23}$
180	6.0	122.1	1.40	$4.16 \cdot 10^{23}$
180	18.0	111.4	1.98	$1.30 \cdot 10^{23}$
180	48.0	100.9	3.03	$6.30 \cdot 10^{22}$
180	96.0	94.5	3.83	$2.04 \cdot 10^{22}$
180	240.0	86.7	5.05	$1.13 \cdot 10^{22}$
180	504.0	77.3	6.17	$6.32 \cdot 10^{21}$
210	0.33	123.6	1.36	$6.29 \cdot 10^{22}$
210	1.0	122.6	2.10	$7.91 \cdot 10^{22}$
210	3.0	105.2	2.94	$4.49 \cdot 10^{22}$
210	6.0	99.1	3.32	$3.34 \cdot 10^{22}$
210	18.0	90.6	4.00	$1.61 \cdot 10^{22}$
210	162.0	77.5	7.53	$3.73 \cdot 10^{21}$
210	504.0	69.1	11.31	$7.23 \cdot 10^{20}$
240	0.67	95.7	3.42	$2.24 \cdot 10^{22}$
240	9.0	84.6	5.15	$5.67 \cdot 10^{21}$
300	0.33	83.9	5.94	$4.26 \cdot 10^{21}$
300	0.67	77.5	6.37	$3.14 \cdot 10^{21}$
300	1.5	73.1	7.16	$1.85 \cdot 10^{21}$
300	3.0	68.0	7.66	$1.29 \cdot 10^{21}$
300	6.0	64.1	9.49	$1.05 \cdot 10^{21}$
300	24.0	56.7	14.49	$4.62 \cdot 10^{20}$

Table 3.3: Results obtained from the further analysis of the experimental SANS curves shown in Fig. 3.9.

Chapter 4

Precipitation modeling

The microstructure analysis performed shows that the only microstructure compound altered during the ageing process is the Mg_2Si strengthening precipitation distribution. However, despite the successful characterization of these precipitation distributions for a wide range of ageing states, the effect of the ageing conditions on these distributions cannot be quantitatively predicted so far.

By the following, the numerical Robson's precipitation model is used for the prediction of the precipitation distribution as function of time and temperature ageing conditions. The model and its mathematical formulation are first presented in Sect. 4.1. Its calibration is done from the SANS measured scattering curves analyzed in terms of size and density of precipitates presented in Sect. 3.4. Finally, the simulation results using a unique set of modeling parameters are presented in Sect. 4.2

4.1 Robson's model

Robson's model is a precipitation model developed on the basis of the classical nucleation and growth theories governed by diffusion processes [22,61,62,65,134,135]. One strength of the model is that a unique precipitate size distribution is considered to collect the different strengthening phases formed during the whole precipitation process [65]. Besides, the application of the model can be extended to predict the precipitation process in more complex multi–stage thermal processes, and moreover, by using a unique set of modeling parameters.

4.1.1 Problem description and modeling objectives

The prediction of the Mg_2Si precipitate size distributions formed during the alloy ageing process is done here by using Robson's model. Based on the Kampmann–Wagner approach [44, 58], this numerical model is especially suitable for dilute alloy systems [61] considering the nucleation process and the growth/dissolution of the previously nucleated particles. It consists of the three following components:

(i) A nucleation model which computes the number of new precipitate nuclei formed at every time step and that become part of the strengthening distribution.

(ii) A growth/dissolution[1] rate approach for the previously nucleated particles to model the growth or coarsening processes at the intermediate and final precipitation stages.

(iii) A mass continuity equation of the solutes involved in the precipitation kinetics.

The application of the model requires some simplifying assumptions. These are:

(i) Thermodynamically stable strengthening precipitates are formed according to their stoichiometric composition. Spherical–shaped precipitates with uniform thermodynamic properties are also assumed.

(ii) The nucleation of new precipitates is homogeneous within the matrix.

(iii) The growth and coarsening of the strengthening particles are diffusion–controlled processes in which solutes diffuse to the interface between the precipitates and the matrix.

These assumptions lead to the major advantage of Robson's model. This is the possibility of predicting the growth and coarsening of the Mg_2Si precipitates in a single distribution without considering the different strengthening phases obtained during the precipitation sequence. The consideration of the precipitate curvature in the local composition at the interface between precipitates and matrix through the Gibbs–Thomson equation makes the introduction of different size distributions for the different β''–, β'– and the β–Mg_2Si phases no longer necessary [136]. Furthermore, the possible interactions between the different strengthening phases are also neglected.

[1] In the following, the term "growth" is used tacitly to refer to either the growth or dissolution processes.

Additionally, for the application of the model on Al–Si–Mg alloy systems, it is assumed in this work that:

(i) Mg_2Si particles are the only strengthening phase in the alloy.

(ii) These particles are the only precipitate in which magnesium is significantly soluble.

(iii) Nucleation of Mg_2Si precipitates is homogeneous within the aluminum matrix [12] and it depends only on the local instantaneous concentration of magnesium in the matrix. As well, magnesium and silicon are homogeneously distributed in the matrix during the whole ageing treatment.

(iv) Magnesium is the limiting reagent for forming the Mg_2Si precipitates and all the magnesium content in the alloy (Table 3.1) is released into solution in the solution heat treatment coming from the dissolution of the as–cast Mg_2Si particles and from the partial dissolution of other intermetallics, as described in Sect. 3.3.4.

(v) Because the diffusivity of magnesium and silicon solutes is similar at high temperatures [137], the solid solubility limits are obtained directly from a simple quasi–binary Al–Mg_2Si alloy system [60].

4.1.2 Mathematical modeling

As belonging to the group of *classical nucleation and growth* theories, the focus of Robson's model is on the modeling of the nucleation and growth processes. Besides, the principle of mass conservation ensures the mass continuity of the solutes during the precipitation process.

4.1.2.1 Nucleation

An appropriate modeling of the nucleation process comprises the calculation of the critical radius r^* of the new precipitate nuclei for every new time step and the total number of these nuclei to precipitate with this critical radius. A nucleation rate J expression is usually used to compute the latter magnitude.

The critical radius r^* of the particles nucleated in every new step is calculated using the Gibbs–Thomson equation in the singular case in which the concentration gradient at the interface between matrix and precipitates is exactly zero ($r = r^*$) [58], according to:

$$r^* = \frac{2\sigma V_a}{kT \ln \frac{c}{c_\infty^\alpha}} \ . \tag{4.1}$$

In Eq. (4.1) σ is the interfacial energy between the aluminum matrix and the Mg_2Si particles in this work, V_a is the atomic volume of magnesium, k is the Boltzmann constant, T is the ageing temperature, c is the instantaneous concentration of magnesium in the matrix, and c_∞^α is the concentration of magnesium in the matrix in equilibrium with Mg_2Si precipitates assuming a planar interface.

From the calculated value of critical radius r^*, the activation energy G^* required for the nucleation of new precipitates of the calculated size is computed according to [61]:

$$G^* = \frac{4}{3}\pi r^{*2} \cdot \sigma \ . \tag{4.2}$$

Adding the activation energy G^* to the activation energy for the diffusion of magnesium in aluminum Q, the steady–state nucleation rate J during artificial ageing, neglecting the incubation period, is calculated by [138]:

$$J = N_0 \cdot \frac{kT}{h} \cdot \exp\left(-\frac{G^* + Q}{kT}\right) \ , \tag{4.3}$$

where N_0 is the number density of nucleation sites, and h is the Planck constant. In the case of homogeneous nucleation, the parameter N_0 is computed as the number of magnesium atoms per unit volume [139].

The critical size r^* calculated at every time step depends on the temperature of the process, leading to larger critical radius as the ageing temperature increases. According to Eq. (4.1) and the assumed simplifications, it depends also in this work on the equilibrium magnesium solute content at the interface between the precipitate and the matrix. In fact, the driving force for the nucleation process is the instantaneous concentration of magnesium c in the matrix. Thus, this precipitation stage becomes exhausted when the magnesium concentration is close to the equilibrium concentration c_∞^α at the corresponding temperature.

4.1.2.2 Growth

The growth process arises as the first nuclei have already nucleated and it becomes increasingly important as the initial supersaturated solid solution becomes depleted. Furthermore, the growth and coarsening stages of the precipitation sequence are predicted in Robson's model using the same modeling approach, as it does not distinguish between both processes.

Similarly to the nucleation phenomenon, the growth rate $\mathrm{d}r/\mathrm{d}t$ of the previously formed precipitates is calculated by assuming a diffusion–controlled process in the case of spherical precipitates according to Eq. (4.4) [136]. This expression can be positive or negative, which requires the consideration of both growth and dissolution rates. At each calculation step, those precipitates larger than the calculated critical radius r^* will grow while the smaller particles will shrink, corresponding to [56, 58]:

$$\frac{\mathrm{d}r}{\mathrm{d}t} = \frac{D}{r} \cdot \frac{c - c_r^\alpha}{c^{\alpha'} - c_r^\alpha} \ , \tag{4.4}$$

where D is the diffusion coefficient, in this work, of magnesium in aluminum at a defined temperature, r is the discrete precipitate radius, c_r^α is the concentration of magnesium in the matrix at the interface, and $c^{\alpha'}$ is the concentration of magnesium in the Mg_2Si precipitate. The parameter c_r^α is calculated for every particle radius from the generalized Gibbs–Thompson equation:

$$c_r^\alpha = c_\infty^\alpha \cdot \exp\left(\frac{2\sigma V_a}{kT} \cdot \frac{1}{r}\right) \ . \tag{4.5}$$

Finally, the dependence of the diffusion parameter D on the ageing temperature T is expressed according to the following Arrhenius–type equation:

$$D = D_0 \cdot \exp\left(-\frac{Q}{RT}\right) \ , \tag{4.6}$$

being D_0 the diffusivity constant of magnesium in aluminum and R the universal gas constant.

The dispersion of the Mg_2Si strengthening precipitates is sufficiently dilute so that each of them can be considered in practice as isolated. This makes Eq. (4.4) applicable to this alloy system [61].

In case of alloys with a high volume fraction of precipitates, interactions between them become important and Eq. (4.4) is no longer valid for modeling the coarsening process.

It is clear that the thermal stability of the precipitates depends on the changes in temperature during the ageing process. Thus, in the case of a non–isothermal ageing process, an increase in temperature leads to the dissolution of existing precipitates. Additionally, a decrease in the ageing temperature induces successive nucleation, growth, and coarsening of the precipitates. However, none of these phenomena occurs in these conditions because a single step ageing process at constant temperature is used.

Fig. 4.1 provides a schematic view of the calculation procedure implemented for Robson's model. The strengthening Mg_2Si nanometer–scale particles created during ageing are supposed to cover the radius size range between 1 Å at nucleation and 1 μm for the long overaged precipitates at long ageing times [20]. This radius size range has been divided into three hundred different classes using a logarithmic scale, thereby achieving a highly accurate tracking of the small precipitates, similar to previous implementations of Robson's model [22, 62, 135].

At each calculation step, the number of new nucleated precipitates of critical radius r^* given by Eq. (4.1) is calculated from Eq. (4.3). Simultaneously, the growth for every size class is computed using Eq. (4.4). The nucleation rate J will determine when the growth stage and the coarsening process are taking place. A great nucleation rate indicates that the growth process dominates the precipitation process. As this nucleation rate closely approximates to zero, the coarsening stage becomes more important and larger precipitates will grow at the expense of small ones through a diffusion process. At the end of the step, the size distribution is reorganized according to the calculated growth rates, while the new Mg_2Si nuclei are placed in the corresponding size class. Then, the remaining magnesium concentration c is updated considering the solute content involved in the nucleation of new precipitates and in the growth of the already existing Mg_2Si precipitates.

4.1.3 Material parameters

The modeling parameters of the precipitation model which are calculated from the physical properties of the alloy, precipitate, and solute are given in Table 4.1. As assumed in the simplifications made for modeling of the process, the concentration of magnesium c_{ini} in the matrix at the as–quenched condition coincides with the total concentration of magnesium in the alloy. This together with the alloy density $\rho_{AlSi_{10}Mg(Cu)}$ are the only two parameters determined from laboratory measurements.

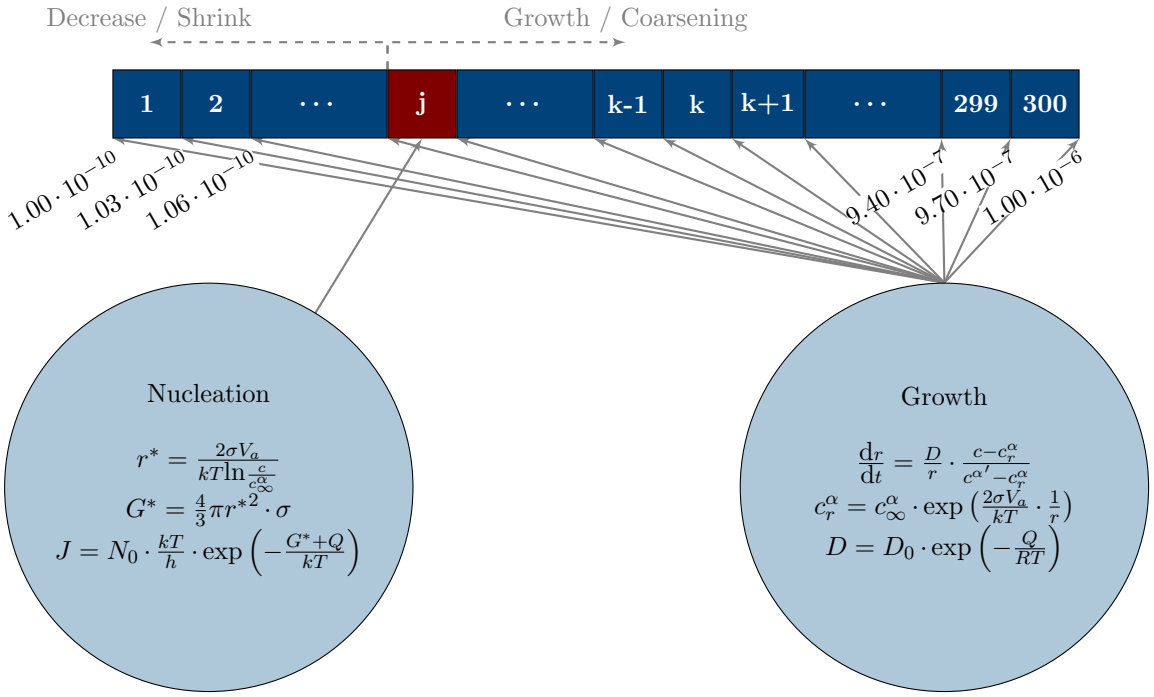

Fig. 4.1: Implementation of Robson's numerical model for the prediction of the Mg_2Si precipitation distribution in the alloy. The size distribution comprises 300 classes in the range between 0.1 nm and 1 μm. At each calculation step dt, the new nuclei formed are computed from the nucleation rate J and placed in the size class given by the critical radius r^* (j–class in the figure). In addition, the growth rate $\mathrm{d}r/\mathrm{d}t$ for all the class boundaries is computed and the precipitates already collected in the distribution are reorganized accordingly. Those classes with a larger size than the critical radius will grow, while those with a smaller size will shrink.

The two remaining parameters, the interfacial energy σ and the diffusivity constant D_0 will be fitted using the experimental SANS data. The interfacial energy σ usually depends on the size of the precipitates [61]. However, this parameter is typically assumed as constant in the existing modeling approaches [44, 58, 61, 135].

4.1.3.1 Solubility

The results of the precipitation model are usually highly sensitive to the equilibrium concentration of the solute in the matrix c_∞^α, which affects directly to the computation of the critical radius r^* (Eq. (4.1)) and the growth rate $\mathrm{d}r/\mathrm{d}t$ (Eq. (4.5)). According to the model assumptions made, the concentration of magnesium in the matrix in equilibrium with precipitates c_∞^α is calculated here from the quasi–binary Al–Mg_2Si alloy system using the magnesium solute concentration as the standard reference for the solid solubility [29, 60]. Table 4.2 gives the calculated equilibrium

Parameter	Value	Units
N_0	$2.024 \cdot 10^{24}$	part/m^3
Q	133	kJ/mol
V_a	$3.95 \cdot 10^{-5}$	m^3/mol
c_{ini}	0.41	wt %
$c^{\alpha'}$	63.4	wt %
$\rho_{\mathrm{AlSi_{10}Mg(Cu)}}$	2753	kg/m^3
ρ_{Mg_2Si}	1900	kg/m^3

Table 4.1: Alloy, precipitate, and solute properties used in the implementation of the Robson's model. The interfacial energy σ function and the diffusivity constant D_0 are calibrated using the SANS data.

magnesium concentration c^{α}_{∞} at each temperature, while the concentration at intermediate temperatures is obtained by linear interpolation.

Temperature	c^{α}_{∞}
K	wt %
453	0.1358
473	0.1585
513	0.1885
573	0.2328
673	0.3549

Table 4.2: The equilibrium concentration c^{α}_{∞} of magnesium in the matrix in equilibrium with Mg_2Si precipitates for the temperature range of interest.

4.2 Simulation results

The simulation results using Robson's model are presented in Figs. 4.2(a) and 4.2(b) for the mean radius and the particle density of the Mg_2Si strengthening distributions. Three different ageing temperatures 180°C, 210°C, and 300°C are considered. Although the simulation of the first precipitation stages is necessary for the model, only results after 100 s are shown, after which experimental data are available. These data correspond to the results of the further analysis of the SANS curves in terms of the size and fraction of precipitates. A good agreement for each

individual temperature is achieved by simultaneous calibration of the interfacial energy σ and the diffusion constant D.

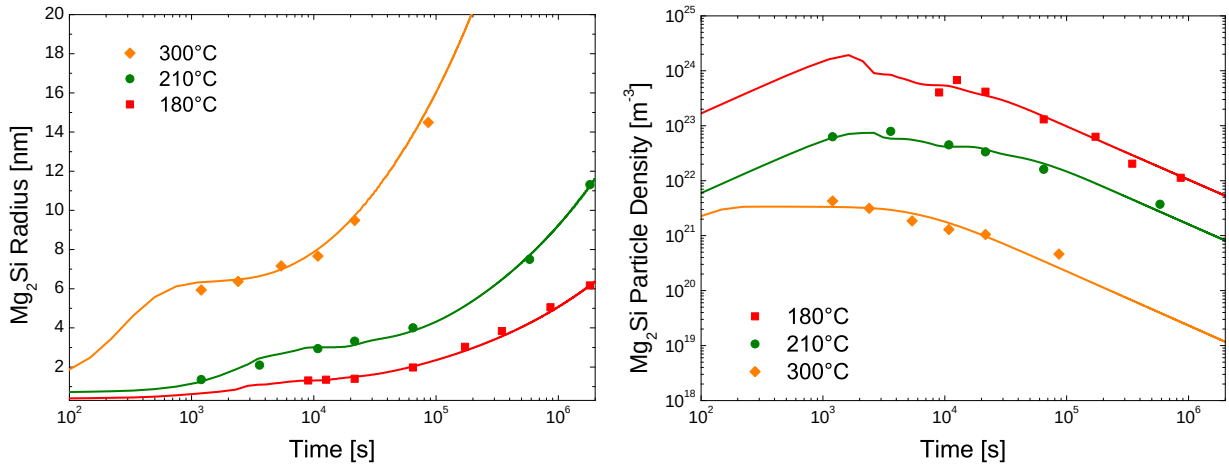

(a) (b)

Fig. 4.2: Results of SANS measurements and simulations using Robson's model for three different ageing temperatures 180°C, 210°C, and 300°C referring to: (a) precipitate average size; (b) particle density. Curves correspond to predictions, while symbols represent experimental data.

The fitted values for the interfacial energy σ at each temperature is given in Table 4.3 and agree with previous experimental work for Al–Si–Mg alloy systems [140]. Fitting the obtained values for the diffusion constant D as function of temperature according to Eq. (4.6) yields a diffusivity constant $D_0 = 9.81 \cdot 10^{-5}$ m^2/s for the activation energy Q given in Table 4.1. This value is very similar to previously reported values obtained from experimental measurements ($D_0 = 10.6 \cdot 10^{-5}$ m^2/s) [137].

Temperature	σ
K	J/mol
453	0.020
483	0.029
573	0.031

Table 4.3: Interfacial energy σ values obtained for every temperature by fitting the SANS data.

At the early stages of precipitation, the Mg_2Si precipitation distributions show a nearly constant mean size while the particle density grow in a logarithmic manner. This indicates that the nucleation of new precipitate nuclei of a few nanometers is occuring. After some time, the

precipitates density stops to grow and reaches its maximum value, while the precipitates mean radius significantly grow. This becomes more evident at higher temperatures. This is the result of the end of the precipitation process, which gives rise to the growth process of the existing precipitates at expense of the remaining magnesium in solid solution. According to the premise that the maximum strengthening due to the precipitation hardening mechanism is given by a high density of sufficient large precipitates, this point of the ageing process provides the T6 maximum strengthening to the material. For a further ageing to T7, the solid solution becomes exhausted of magnesium ($c \approx c_{\infty}^{\alpha}$ at the temperature considered) and the precipitates continue growing, but in this case at expense of the existing particles which explains the decrease of the distributions density. Therefore, the diffusion–controlled coarsening process takes place, which produces a decrease in the material strengthening.

The comparison of Fig. 4.2(a) and Fig. 4.2(b) shows the typical effect of higher ageing temperatures producing coarser size distributions of Mg_2Si strengthening precipitates at a lower density. This is mainly the reason for greater T6 maximum strengthening conditions at lower ageing temperatures. Fig. 4.2 furthermore shows that at low ageing temperatures, there is no plateau in the growth of the precipitate mean radius when the Mg_2Si particle density reaches its maximum value, in contrast to predictions at higher temperatures. This singular feature is the consequence of a significant overlap between nucleation and coarsening, while for higher temperatures, the transition from nucleation to coarsening is more distinct. This phenomenon results from a low interfacial energy σ parameter that dominates in the class range of the majority of the strengthening precipitate distribution.

The double log–scale graph in Fig. 4.3 shows that the slope of all of the precipitate mean radius curves for the long ageing times is approximately 1/3, indicating that particle coarsening by the well–known Ostwald ripening mechanism dominates [141]. This confirms that large precipitates coarsen in the overageing process at the expense of the small ones when the matrix is depleted of the limiting solute. Thus, the overall energy in the material is reduced by a diffusion–driven process. This observation agrees well with the Lifshitz–Slyozov–Wagner (LSW) theory, which uses a kinetic equation appropriate for an infinitely dilute array of spherical particles in a stress–free matrix that predicts that the mean particle radius will increase as a power function of the ageing time raised to 1/3 [54, 142].

The governing driving force for coarsening is the difference between the matrix concentration in the vicinity of small and large particles, which leads to diffusion flux of the solute atoms from smaller particles to larger ones [143]. This phenomenon is caused by the Gibbs–Thomson effect included in Robson's model, which changes the phase equilibrium between the precipitates and the matrix and also increases the solute concentration around small particles due to the interfacial

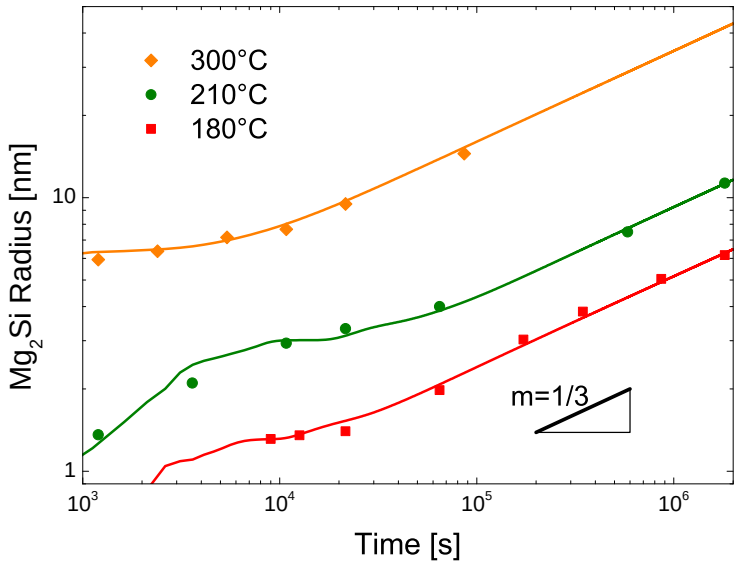

Fig. 4.3: Evolution of the Mg_2Si precipitate mean size at 180°C, 210°C, and 300°C for long durations of the ageing process during which the Ostwald ripening coarsening process occurs. Curves correspond to predictions, while symbols represent experimental data.

curvature.

4.2.1 Interfacial energy σ

A well–known feature of the classical nucleation theory is the high sensitivity of the critical radius r^* and hence the nucleation rate J to the interfacial energy σ [61]. Furthermore, this material parameter is rather difficult to be directly measured from experimental results and is usually assumed as size independent for the modeling of the precipitation process [44, 58, 61, 135].

However, this assumption is not consistent when the whole precipitation process is considered because the precipitates coarsening is usually accompanied by a loss of coherency in the matrix and an interfacial energy increase is expected [65, 144]. This increase goes from a lower value for small coherent particles to a higher value for larger incoherent particles [145]. Some approximations have been already successfully implemented in which this model parameter is piecewise linearly dependent on the precipitates' size [65]. However, the applications of these approximations are reduced to very narrow and specific ranges of precipitate size and do not extend to the whole precipitation strengthening treatment.

In this work, the interfacial energy σ is formulated as a function of the precipitate size by a sigmoidal function [145]. The resulting interfacial energy function $\sigma(r)$ is shown in Fig. 4.4 and is given by the expression:

$$\sigma(r) = A + \frac{K - A}{(1 + Q \cdot \exp(-B \cdot (r - M)))^{1/\nu}} , \tag{4.7}$$

where $A = 0.020$ J/m^2 is the lower asymptote, $K = 0.033$ J/m^2 is the upper asymptote, $Q = 45.0$ is fitted according to the value of $\sigma(0)$, $B = 8.75 \cdot 10^9$ m^{-1} is the growth rate, and $M = 8.0 \cdot 10^{-11}$ m is the radius of maximum growth if $Q = \nu$. Parameter $\nu = 0.59$ denotes the place where maximum growth occurs. From the proposed function, it is clear that the nucleation of small precipitates is promoted in terms of energy efficiency in the alloy, which also agrees with the total coherency exhibited by these small particles.

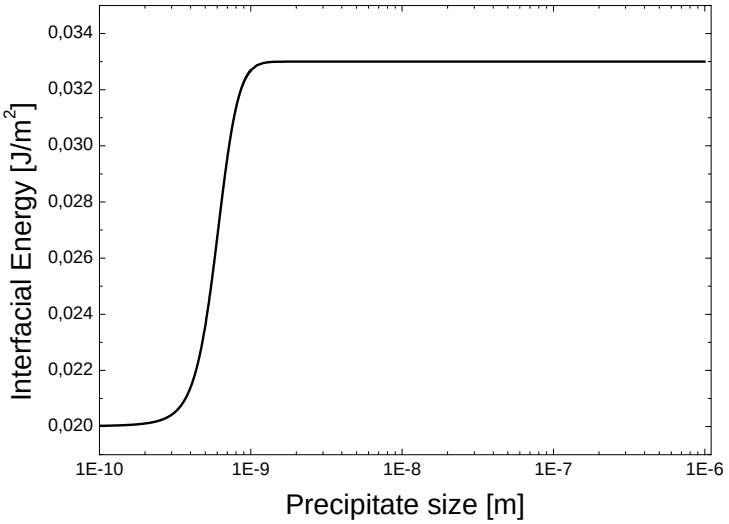

Fig. 4.4: Interfacial energy as a function of the precipitate size $\sigma(r)$ using a sigmoidal approximation.

In the assumptions made for Robson's model, the Mg_2Si strengthening precipitates are assumed to be spherical, which does not fully agree with the conclusions drawn from HTEM images in Sect. 3.3.5. Therefore the parameters of the sigmoidal function in Eq. (4.7) implicitly reflect not only the change of the interface energy but also the change of the particles' geometry in a phenomenological way.

The simulation results obtained with the Robson's model using now a unique set of parameters with the new definition of the interfacial energy $\sigma(r)$ are given in Fig 4.5. These results are very similar to the simulations shown in Fig. 4.2. The introduced interfacial energy function smooths the peaks of the precipitate density curves where the transformation of the peak hardening β'–Mg_2Si precipitates into the incoherent β phase occurs. Additionally, the precipitation distribution at 240°C is also shown as model validation using a unique set of model parameters.

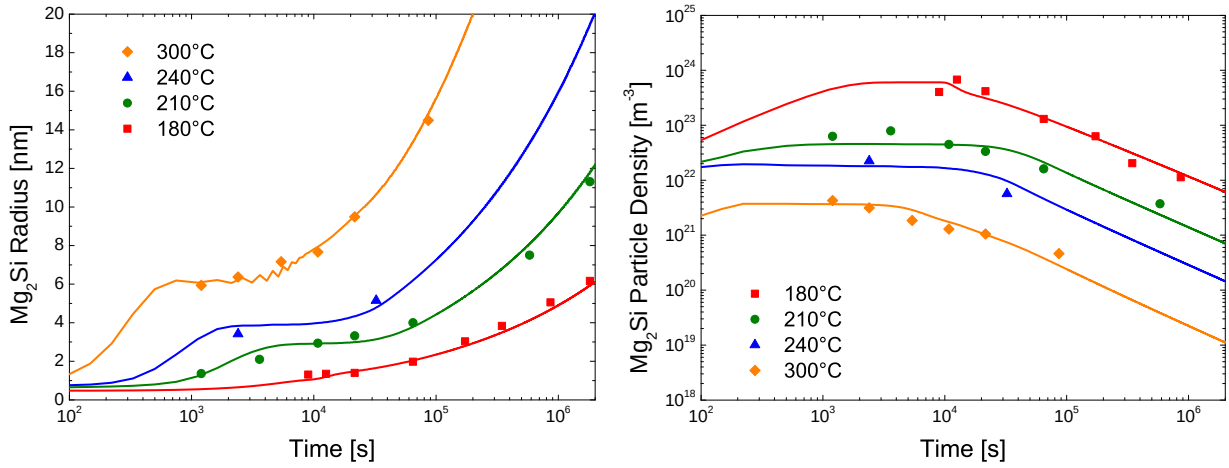

(a) (b)

Fig. 4.5: Simulations using modified Robson's model with the sigmoidal function for the interfacial energy σ for the four ageing temperatures 180°C, 210°C, 240°C (validation), and 300°C referring to: (a) precipitate mean size; (b) precipitate density. Curves correspond to predictions, while symbols represent experimental data.

Chapter 5

Mechanical characterization

An exhaustive analysis of the mechanical behavior of the alloy under different loading conditions considering a wide range of hardening grades is necessary for its mechanical modeling and to determine the effect of the ageing condition on it. As in the case of the microstructure characterization, the ageing states of interest range from the T6 to the T7 condition.

This chapter begins by describing briefly in Sect. 5.1 the material preparation procedure followed and presenting the different tests carried out as well as their purpose in Sect. 5.2. The experimental results gathered are presented in Sect. 5.3 providing very useful qualitative and quantitative information necessary for the further development of the work. Finally, the concluding remarks of the analysis are given in Sect. 5.4. A careful design of the experimental loading conditions will be shown in Chap. 6 to be of great importance for the mechanical modeling of the alloy.

5.1 Material preparation

The preparation procedure of the alloy is the same as that presented in Sect. 3.1.2 consisting of the casting of bars of 270 mm in length and 23 mm in diameter using pre–heated permanent molds and imposing a slow cooling stage. This is followed by a solution heat treatment at 535°C during 6 hours which ends by quenching the cast bars in water at room temperature.

The temperature and duration of the final ageing process is also determined according to the purpose of the test to perform and considering the ageing condition of interest. Besides, the ageing treatment is also carried out here in an one–stage process at constant temperature ranging usually from 180°C to 300°C.

5.2 Experimental fundamentals

The objective of this part of the work is to evaluate the effect of the ageing condition on the mechanical response of the alloy by means of its Mg_2Si strengthening precipitate distribution, if any, as well as to determine its mechanical bahavior at high temperatures establishing this range of temperature.

For these purposes, hardness and tensile tests are performed to determine the effect of the Mg_2Si strengthening distribution on the alloy mechanical response. Creep and low–cycle fatigue tests at elevated temperatures will provide additional information on the dominant deformation mechanism in this temperature range and will also contribute to determine the high temperature regime of the alloy.

5.2.1 Hardness testing

Hardness is usually used for a rapid estimation of the hardening grade of age–hardenable materials and to determine the effect of ageing temperature and process duration on the material strengthening [7]. This non–destructive test has also been applied with the same objectives to Al–Si–Mg alloy systems [3, 5, 6, 64, 146].

Brinell hardness tests are performed in this work to obtain the *ageing curves* at 180°C, 210°C, 240°C, and 300°C from which the effect of temperature and ageing time on the alloy strengthening due to the precipitation hardening mechanism can be estimated (see Fig. 2.4). The Brinell hardness is calculated as the total test load applied P divided by the surface area of the indentation, where D is the diameter of the hardened steel or carbide ball used and d the indentation diameter, as:

$$\mathrm{HB} = \frac{P}{(\pi D/2) \cdot \left(D - \sqrt{D^2 - d^2}\right)} \,. \tag{5.1}$$

Brinell hardness measurements are carried out in a Zwick/Roell type ZHU 750 top universal hardness tester using a carbide ball indenter of 2.5 mm in diameter, a force of 62.5 kgf, and a test duration of 20 s. Disc–shaped specimens of 23 mm in diameter and 10 mm in thickness are prepared for these experiments. For the measurements, the samples are previously treated at the study temperatures 180°C, 210°C, 240°C, and 300°C covering a wide range of ageing conditions ranging even from the short T64 to the T7 state. The specimens are also mechanically grounded producing two plain parallel faces samples free from a fine impurity layer resulting likely from the

solution treatment. Furthermore, a minimum of five repetitions are performed on every sample to average out the effect of local inhomogeneities.

5.2.2 Tensile testing

Together with ageing curves, tensile tests have been extensively utilized to analyze the effect of the precipitation process on the mechanical behavior of Al–Si–Mg alloy systems. Furthermore, these experimental results are typically used to develop and fit strength models to predict the alloy strengthening during the ageing process considering the different contributions of the intrinsic aluminum matrix, the solid solution strengthening, and the Mg_2Si precipitation hardening distribution as explained in Sect. 1.2 [11, 12, 23, 64].

From the engineering stress–strain curves obtained, the analysis focuses in this work on the yield strength $R_{p,0.2\%}$[1] and the ultimate tensile strength R_m and how they are affected by the alloy ageing condition. The experimental results gathered will also provide information on the strain hardening behavior of the alloy.

These tests are performed at room temperature using a Zwick/Roell type Z050 universal tensile testing machine. Cylindrical samples of 6 mm in diameter, 30 mm in gauge length, and 60 mm in total length are prepared according to the geometry shown in Fig. 5.1. The $AlSi_{10}Mg(Cu)$ bars from which the specimens are produced are previously treated at 210°C or 240°C. As in the case of hardness measurements, different process times are used to cover a wide range of ageing conditions from short to long ageing processes.

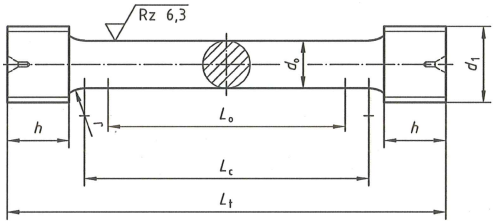

Fig. 5.1: Samples geometry used for tensile tests.

5.2.3 Creep testing

Creep tests are usually perform to investigate the plastic deformation of materials at elevated temperatures subjected to a constant loading stress, typically above 40 % of the melting

[1] *offset yield point* at 0.2 % of plastic deformation

temperature when the creep deformation becomes more evident. Once the test load is applied, three different stages can be mainly distinguished in the material time–dependent strain response. The primary stage denoted as primary creep characteristically exhibits a gradual decrease of the creep rate being the strain hardening the dominant process on the creep deformation. The secondary stage runs during the part of the curve in which the creep strain rate remains constant resulting from the balance obtained between the strain hardening rate produced by dislocations and the recovery rate. Finally, a rapid increase in the creep rate until fracture occurs in the final tertiary stage. The relation of the minimum creep rate $\dot{\epsilon}_s$ in the secondary stage with the applied stress σ_{cr} is described by the Norton equation as [72]:

$$\dot{\epsilon}_s = \frac{ADGb}{k\,T} \cdot \left(\frac{\sigma_{cr}}{G}\right)^n \quad , \tag{5.2}$$

where A is a dimensionless material characteristic constant, D is the diffusion coefficient showing an Arrhenius–type dependence on the test temperature T as that shown in Eq. (4.6), G is the material shear modulus, b is the Burgers vector size, k is the Boltzmann constant, and n is the stress exponent.

The stress exponent n is directly related to the deformation mechanism governing in the creep experiment [76]. A value of $n = 3$ is related to the viscous glide of dislocations [147, 148], $n = 5$ indicates that the dislocation climbing at high temperatures dominates [147, 148], while $n = 7$ is characteristic of the climbing process at low temperatures [149].

However, the dominant deformation mechanism in creep tests performed on precipitation strengthened alloys cannot be directly determined from the measured stress exponents n because these are significantly higher than the theoretical values. Therefore, Eq. (5.2) is modified in case of precipitation strengthened materials by means of a threshold stress σ_{cr}^0 as mentioned in Sect. 2.3 [47]. This threshold stress σ_{cr}^0 reduces the applied stress σ_{cr} and is related to the interactions that occur between precipitates and dislocations. This modification results in a decrease of the initial high stress exponents and makes possible to identify the dominant deformation mechanism directly from the new true stress exponent n_t measured [76]. The resulting modified Norton equation is [76]:

$$\dot{\epsilon}_s = \frac{ADGb}{k\,T} \cdot \left(\frac{\sigma_{cr} - \sigma_{cr}^0}{G}\right)^{n_t} \quad . \tag{5.3}$$

Different explanations are given for the origin of this threshold stress σ_{cr}^0 in the case of metallic materials. In some works, this threshold stress is identified as the Orowan stress necessary to

bow a dislocation between two particles [150] while the most plausible theories relate this stress to the additional back stress necessary to elongate the dislocation during the climbing of an obstacle [151] or as an additional stress necessary for the detaching of a dislocation after climbing over an obstacle [152].

Creep tests are performed in this work using the ATS Lever Arm Test Systems facility at the Helmholtz-Zentrum Geesthacht. The constant loading stress applied ranges from 25 MPa to 70 MPa and the test temperatures are 175°C, 200°C, 250°C, and 280°C. Therefore, these tests are carried out on prolonged overaged T7 samples at 240°C for 384 hours to prevent the potential side effect of an *in–situ* precipitation during the test. Cylindrical specimens of 8 mm in diameter, 40 mm in gauge length, and 75 mm in total length as shown in Fig. 5.2 are prepared from the treated bars.

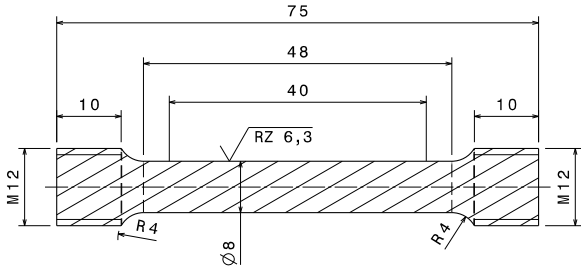

Fig. 5.2: Samples geometry used for tensile creep tests.

5.2.4 LCF testing

Low–cycle fatigue (LCF) tests are performed in this work because these are the loading conditions to which cylinder heads are subjected produced by the thermal loads resulting from the engine start–operate–stop cycles. Therefore, these strain–controlled tests are used to evaluate the mechanical behavior of the alloy at elevated temperatures under cyclic loading conditions and analyze the effect of the Mg_2Si strengthening precipitation on it. Secondly, another objective of these tests is to evaluate if the alloy mechanical behavior is determined solely by the resulting Mg_2Si precipitation distribution or if, however, the ageing process itself has also to be considered.

Uniaxial strain–controlled LCF tests with a final relaxation process at a constant temperature are performed in a MTS type 810.22 universal servo–hydraulic testing machine at the University of Applied Sciences of Regensburg. The temperature of most of these tests is 150°C (a temperature of 250°C is used for a temperature sensitivity analysis) and a constant strain amplitude of 0.45 % (0.50 % for the test at 250°C) is used. Completely reversed strain cycles under three different strain rates $\dot{\epsilon}$ of $1 \cdot 10^{-3}$ s^{-1}, $1 \cdot 10^{-4}$ s^{-1}, and $1 \cdot 10^{-5}$ s^{-1} are conducted as can be seen in

Fig. 5.3 to display the viscoplastic response of the alloy [153]. The final relaxation stage is a kind of strain–controlled creep deformation process which will lead to an equilibrium stress in the material. For this analysis focusing on the investigation of the relationship between the precipitation distribution and specific mechanical properties, a few representative points included in Fig. 5.3 are used to quantify the effect of the precipitation distribution on the main phenomena as they are visible from the determined LCF responses.

For later comparison the following stress ratios are introduced, where the index of the stress corresponds to the respective point in Fig. 5.3. For quantitative comparison of the stress level of two different materials, the stress at point 2, σ_2, will be used. The cyclic work hardening (or softening) for each material is represented by the stress ratio $\sigma^*_{cyclic} := \sigma_2/\sigma_1$, the rate sensitivity is described by the stress ratio $\sigma^*_{rate} := \sigma_4/\sigma_3$, and the effects from viscous overstress and static recovery are reflected in the stress ratio which determined from the final relaxation $\sigma^*_{relax} := \sigma_6/\sigma_5$.

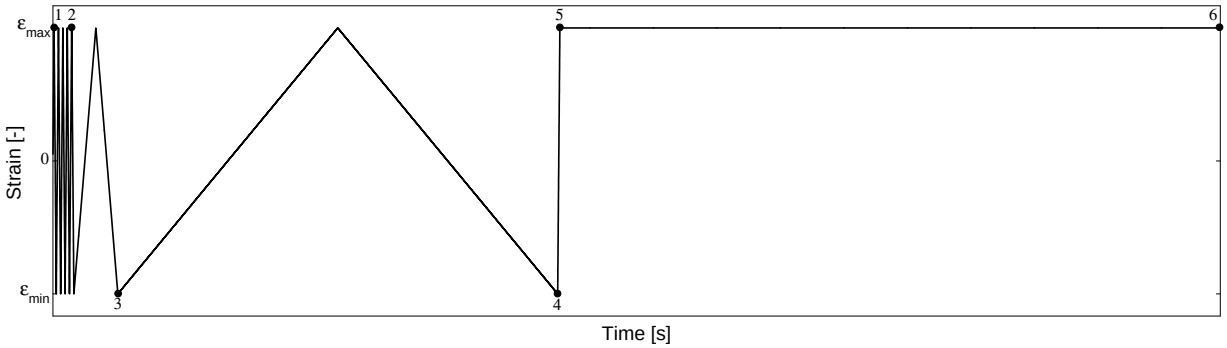

Fig. 5.3: A representative cyclic strain–controlled loading history applied for the LCF tests. Different strain rates $\dot{\epsilon}$ and a final relaxation phase are included. Two strain amplitude values of 0.45 % and 0.50 % are used.

Cylindrical specimens of 8 mm in diameter, 65 mm in gauge length, and 160 mm in total length as that shown in Fig. 5.4 are used for these LCF tests. These are also prepared from previously heat treated cast bars and this preparation procedure ends by polishing the samples, given the cyclic nature of the test.

For this analysis, three different strengthening grades AC_{I}, AC_{II}, and AC_{III} are tested corresponding to the Brinell hardness values $\mathrm{HB}_{AC_{\mathrm{I}}}$=90, $\mathrm{HB}_{AC_{\mathrm{II}}}$=80, and $\mathrm{HB}_{AC_{\mathrm{III}}}$=70. The ageing conditions to obtain these grades are determined from the experimental ageing curves at 210°C and 240°C (see Fig. 5.5). These are given in Table 5.1. An additional hardening grade AC_0 ($\mathrm{HB}_{\mathrm{ref}}$=106) close to the T6 condition is also prepared to evaluate the effect of the test temperature on the experimental results.

T_{ageing}	Hardening grades			
	AC_0–HB_{ref}=106	AC_I–HB_{AC_I}=90	AC_{II}–$HB_{AC_{II}}$=80	AC_{III}–$HB_{AC_{III}}$=70
210°C	2	41	96	400
240°C	—	2.5	14	90

Table 5.1: Duration in hours of the artificial ageing process depending on the ageing temperature T_{ageing} for the four selected heat–treated states.

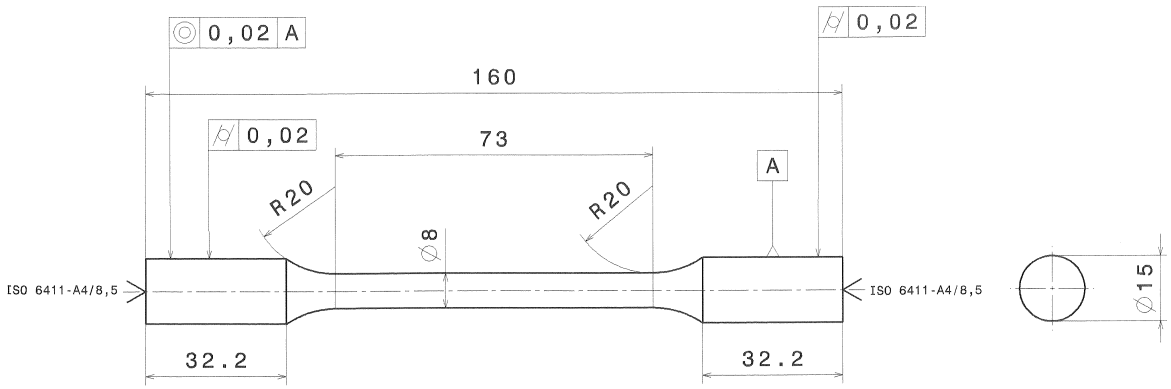

Fig. 5.4: Geometry of LCF test specimens used for the mechanical characterization.

5.3 Experimental results

The experimental results obtained are presented here in two sections according to their significance for the further development of the work. The purpose of Sect. 5.3.1 is to discuss the uniqueness of the relationship existing between the Mg_2Si precipitation distribution and those mechanical properties obtained from tests at room temperature. From these first remarks, the conclusions drawn are extrapolated to the alloy mechanical behavior at higher temperatures based on the results gathered from the creep and LCF tests in Sect. 5.3.2. The conclusions of this second part together with the analyzed results will provide relevant information for the mechanical modeling of the alloy addressed in Chap. 6.

The analysis of the relationship existing between the precipitation distribution and the alloy mechanical behavior is done taking as reference the interprecipitate spacing λ of the strengthening distributions. This parameter is computed from the total density and the mean radius of a given particle distribution based on the Wigner–Seitz radius approximation assuming a homogeneous distribution of the system, which is in agreement with the simplifications made in Sect. 4.1.1. In this study, the mean radius of the particles is neglected for the computation of this parameter

because the mean size of the Mg_2Si precipitates is significantly smaller than the spacing between them. The interprecipitate spacing λ is thus calculated as follows:

$$\lambda = 2 \cdot \left(\frac{3}{4\pi n} \right)^{1/3} , \tag{5.4}$$

where n is the total particle density.

5.3.1 Qualitative analysis

The main purpose of this section is to find out the relationship existing between the Mg_2Si precipitation distribution and the mechanical behavior of the alloy at room temperature based on the experimental results obtained from the hardness and tensile tests performed. Although experimental data for the early precipitation stages are also available, the focus of this part is on the precipitation stages ranging from the T6 to the T7 conditions.

5.3.1.1 Hardness testing

The ageing curves obtained for the four temperatures 180°C, 210°C, 240°C, and 300°C are presented in Fig. 5.5(a). Measurements also for the underaged T64 condition at the lower ageing temperatures of 180°C and 210°C are carried out. However, only the overageing tails of the curves at 240°C and 300°C are available due the high ageing temperatures. The T6 maximum strengthening for each temperature is determined from the experimental hardness peaks. Compared to the higher temperatures, the peaks of the ageing curves at lower temperatures occur after a longer heat treatment, because lower ageing temperatures produce finer and more dense distributions of the Mg_2Si strengthening precipitates.

Conversely, at all temperatures the hardness falls off beyond the peaks giving rise to the coarsening stage of the precipitation process. This effect is more pronounced at higher temperatures. Furthermore, an equilibrium hardness value of approximately HB≈46.5 is achieved at 300°C after an ageing duration of 200 h. By reaching this value, the contribution of the precipitation hardening mechanism to the total strengthening of the alloy is negligible, resulting it basically from the contributions of the intrinsic matrix strength and the remaining solid solution (see Fig. 2.4). As shown in Fig. 5.5(b), the effect of the overageing time on the hardness can be empirically represented by a logarithmic fit (solid curves) of the form:

$$HBW = A + B \cdot \log\left(t + C\right) , \tag{5.5}$$

where t is the duration in hours of the ageing and A, B, and C are the fit parameters provided in Table 5.2.

T_{ageing} [°C]	A [HBW]	B [HBW]	C [–]
180	151.77	−12.06	7.87
210	116.35	−7.73	0.11
240	96.24	−6.02	−0.18
300	73.48	−5.29	−0.12

Table 5.2: Sets of parameters for the logarithmic fit of the ageing curves at room temperature using Eq. (5.5). Fitting parameters A and B are given in units of Brinell hardness.

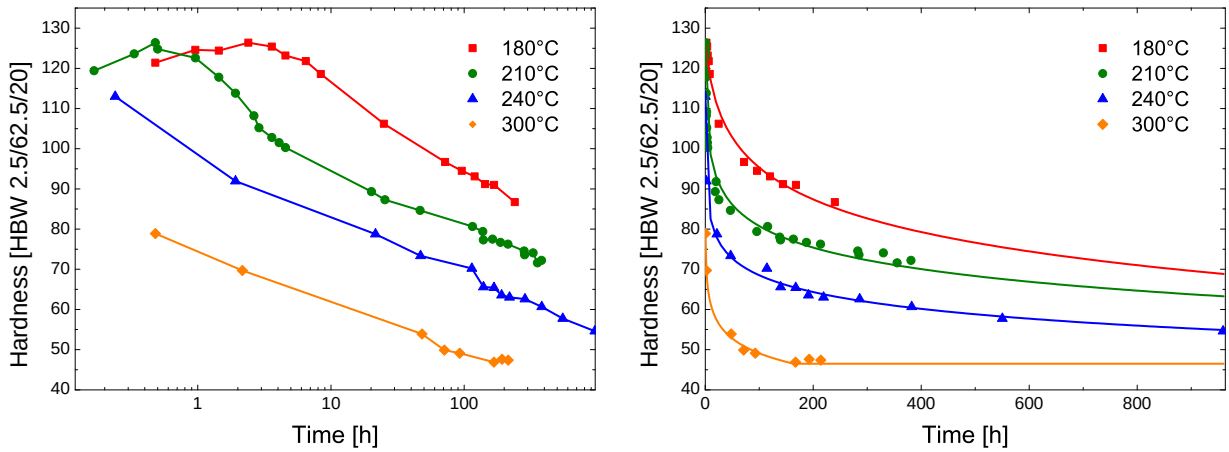

Fig. 5.5: Ageing curves at 180°C, 210°C, 240°C, and 300°C (curves at 180°C and 210°C are extrapolated): (a) considering both the underageing and the overageing stages (x-axis is plotted on a log-scale); (b) exclusively considering the overageing stage. The logarithmic fits are included as solid curves.

Overageing stage

Using Eq. (5.5), the hardness at each ageing temperature is plotted in Fig. 5.6 against the predicted interparticle spacing λ, which is calculated according to Eq. (5.4) from the simulation results for the precipitation distribution. The presented results refer to ageing temperatures of 180°C, 210°C, and 300°C. The displayed data points for 240°C refer again to the experimentally measured validation data obtained from the SANS measurements and the hardness tests of specimens aged at 240°C.

The total density of the Mg_2Si precipitation distributions decreases for longer overageing processes leading to an increasingly larger interprecipitate spacing λ. Therefore, the hardness shows a decreasing logarithmic relationship with the interprecipitate spacing λ during the overageing stage. As a reference, the relationship obtained from the numerical model of Shercliff–Ashby developed for isothermal processes is also plotted in Fig. 5.6 [5, 6]. Further details on the model ans its application to the $AlSi_{10}Mg(Cu)$ alloy can be found in App. A. This numerical model is also fitted using the further analyzed results obtained from the SANS scattering curves taking as starting set of modeling parameters that reported for the 6082 aluminum alloy [5]. The resulting model parameters obtained from the reported calibration procedure for this model are given in Table 5.3. As observed in Fig. A.1, only the contribution of the non–shearable precipitates to the total alloy strength changes during the overageing process as $\Delta\sigma_B = c \cdot G \cdot \mathbf{b}/\lambda$ (being c a constant, G the shear modulus, and $\mathbf{b}$ the Burgers vector). Thus and using the model parameters given in Table 5.3, the decrease in the strengthening grade of the alloy predicted by this model exhibits the inverse proportionality with the interprecipitate spacing λ shown in Fig. 5.6. This relationship shows a more rapid decrease than that obtained in this work from Robson's model, which has been already reported by comparing with experimental results [5].

		Parameter	Value	Units
σ_i	–	Intrinsic hardness	32	HBW
σ_q	–	As–quenched hardness	75	HBW
Q_A	–	Activation energy for ageing	$133 \cdot 10^3$	J/mol
T_c	–	Transition temperature	230	°C
T_s	–	Metastable solvus temperature	282	°C
T_e	–	Phase boundary solvus temperature	565	°C
Q_s	–	Solvus boundary enthalpy	$30 \cdot 10^3$	J/mol
Q_e	–	Phase boundary enthalpy	$30 \cdot 10^3$	J/mol
$(S_0)_{max}$	–	Strength parameter (below T_c)	94	HBW
$(S_{0c})_{max}$	–	Strength parameter (aboce T_c)	80	HBW
P_p	–	Peak temperature–corrected time (below T_c)	$10.24 \cdot 10^{-15}$	s/K
P_{pc}	–	Peak temperature–corrected time (above T_c)	$9.40 \cdot 10^{-14}$	s/K
K_I	–	Constant relating τ_1 to t_p	0.5	–

Table 5.3: Alloy properties and model parameters used in the implementation of Shercliff–Ashby model for the prediction of the ageing curves of the $AlSi_{10}Mg(Cu)$ alloy (see App. A).

The overall behavior which is found for all four temperatures indicates that – within some

scatter – there exists an one–to–one relationship between the hardness and the interprecipitate spacing λ. This result indicates that the interprecipitate spacing λ might be a suitable parameter for predicting the mechanical behavior of the $AlSi_{10}Mg(Cu)$ alloy in the overaged state.

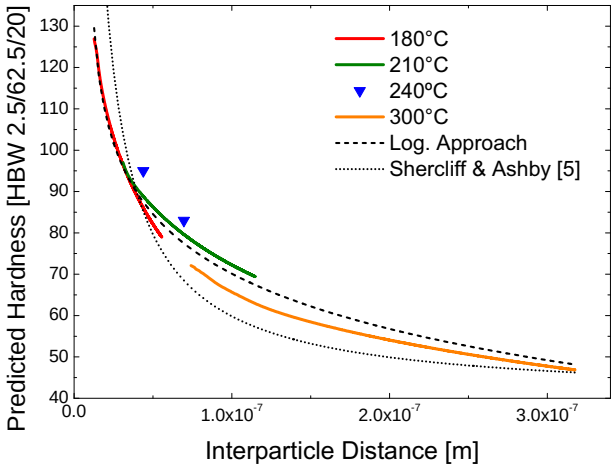

Fig. 5.6: Relationship between hardness and Mg_2Si interprecipitate spacing λ for the overageing stage. Results are shown for ageing temperatures of 180°C, 210°C, and 300°C. The input data at 240°C are derived from the SANS measurements given in Fig. 4.2 [19] and the hardness measurements. The relationship obtained using Shercliff–Ashby model [5, 6] is also included.

Effect of pre–ageing time

The elapsing time between the quenching and the artificial ageing of the alloy may alter the precipitation process, as mentioned in Sect. 3.1.2. For this reason, this time is limited in this work to a maximum of 10 minutes. As an example, the Brinell hardness of the alloy increases from 72.0 in the as–quenched condition to 93.0 after 24 hours of natural ageing at room temperature as can be seen in Fig. 5.7. This hardness increase is likely due to the partial decomposition of the supersaturated solid solution and the formation of silicon and magnesium clusters and small magnesium/silicon co–clusters producing some strength in the alloy as these clusters grow. Nevertheless, this strengthening increase is limited in time to a few hours because the diffusion processes for the growth of clusters are very slow at room temperature.

This partial decomposition of the initial solid solution is reversible and the small clusters formed can be dissolved again with a slight temperature increase, which actually occurs in the heating of the material up to the ageing temperature. However, this energy contribution is not sufficient to produce a full rehomogenization of those magnesium and silicon atoms involved and the precipitation process during the artificial ageing will be altered [154].

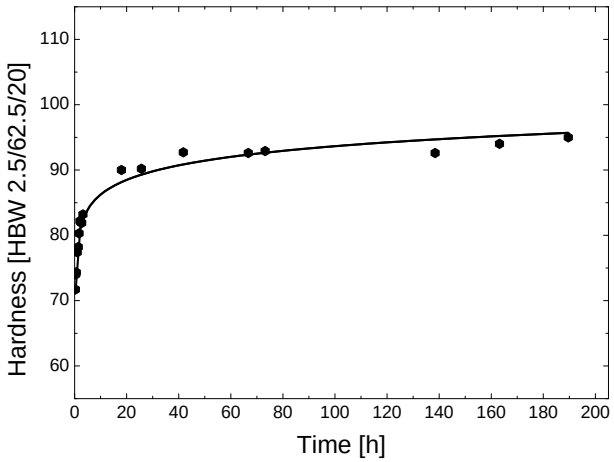

Fig. 5.7: Ageing curve at room temperature (natural ageing). The alloy exhibits a rapid increase in the total strength during the first ageing hours as a result of the partial decomposition of the initial solid solution.

5.3.1.2 Tensile testing

The effect of the precipitation process on the mechanical behavior of the alloy can be qualitatively measured from the engineering stress–strain curves presented in Fig. 5.8 corresponding to different ageing conditions obtained at 210°C but with different process durations. In this analysis, both underaged and overaged conditions of the alloy are considered.

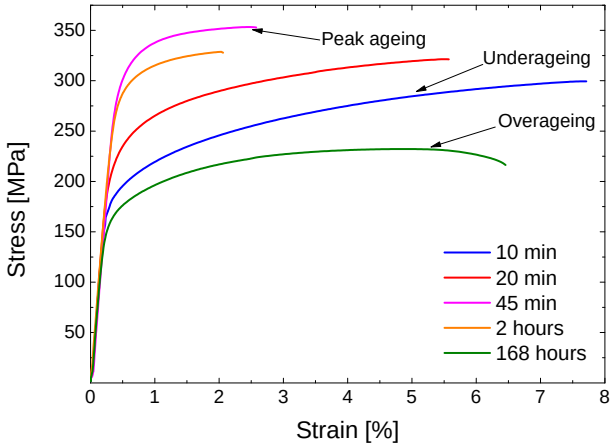

Fig. 5.8: Evolution of the mechanical response of the alloy to tension tests obtained from samples aged at 210°C with different ageing times ranging from the underaged T64 to the overaged T7 condition.

Thus, the alloy exhibits a great strain hardening and ductile behavior after a short ageing process. With the duration of ageing towards the T6 maximum strengthening condition, the precipitation produces a significant increase in the total strengthening of the alloy while reducing its fracture

strain as a result of a fine and high density distribution of Mg_2Si strengthening precipitates that limits the free motion of dislocations in the alloy. Finally, by further ageing to T7 the coarsening of this distribution reduces significantly the contribution of the precipitation hardening mechanism to the total strength of the alloy.

Yield strength and ultimate tensile strength

The effect of the precipitation process on the alloy mechanical response to tensile tests focusing on its T7 condition is further analyzed in terms of the experimental yield strength $R_{p,0.2\%}$, and ultimate tensile strength R_m.

Both tensile properties are plotted in Fig. 5.9 against the predicted interprecipitate spacing λ, which is calculated from Robson's model results. As observed for the hardness in the T7 overageing condition of the alloy, both tensile properties show also a logarithmic relationship with the predicted interprecipitate spacing λ. Therefore, a direct proportionality can also be established between the hardness and these tension mechanical properties as proposed for similar Al–Si–Mg alloy systems [9].

The yield stress $R_{p,0.2\%}$ and the ultimate tensile stress R_m are, thus, also appropriate quantitative indicators of the overaged condition of the $AlSi_{10}Mg(Cu)$ aluminum alloy. The lower the value of both mechanical properties, the more pronounced is the overaged condition. This indicates, as in the case of hardness, that both tensile properties are determined within the overaged condition of the alloy univocally by the Mg_2Si precipitation distribution.

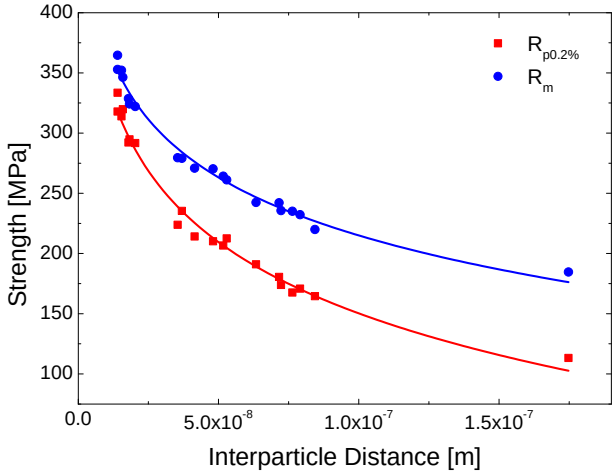

Fig. 5.9: Relationships obtained for the yield strength $R_{p,0.2\%}$ and the ultimate tensile strength R_m with the simulated Mg_2Si interprecipitate spacing λ applicable during the overageing process.

The linear relationship obtained between the hardness and the ultimate tensile strength can be extended to the first stages of precipitation covering the whole artificial ageing treatment. Conversely, that obtained for the yield strength is only applicable for the final overaged condition. As an example, the experimental stress–strain curves obtained for two specimens aged at 210°C but with different process durations such that the measured hardness coincides well in both cases (HBW≈120) are given in Fig. 5.10. Although the ultimate tensile strength in both samples is comparable, the yield strength is significantly different. The curve showing a stronger strain hardening behavior is obtained from a specimen aged only for 15 minutes (underaged condition) while the second curve exhibiting a larger yield strength results from an artificial ageing of 1 hour (overaged condition, see Fig. 5.5(a)). This result emphasizes the limitations of the hardness measurements to estimate the ageing condition of the alloy when the whole ageing process is considered. Besides, the overaged specimen shows surprisingly a greater strengthening, which is likely due to the remaining density of semi–coherent β'–Mg_2Si precipitates contributing to a larger extent to the total alloy strength. In addition, the overaged sample exhibits a lower failure strain probably caused by more dislocation tangles and a greater dislocation concentration in front of the coarser β–Mg_2Si phase [24, 155].

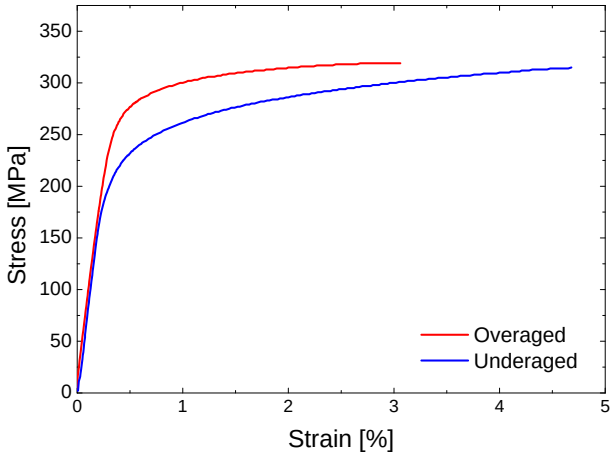

Fig. 5.10: Experimental stress–strain curves obtained from underaged and overaged samples, both having the same hardness (HBW≈120).

The different mechanical response in Fig. 5.10 is a direct consequence of the different interaction mechanisms occurring between dislocations and Mg_2Si precipitates. The fine Mg_2Si precipitates typical in underaged samples are cut by moving dislocations according to the Friedel effect. The shearing process is the dominant interaction mechanism for these conditions. However, the bowing out of dislocations between the typical coarser particles present in overaged conditions and based on the Orowan mechanism governs the interactions between both compounds [24]. The specimen aged for 15 minutes displays a Mg_2Si precipitate distribution with an equivalent mean

radius of 1.12 nm and a total particle density of $4.12 \cdot 10^4$ μm^{-3}, while for the overaged specimen the mean size increases to 2.55 nm at almost the same precipitate density (Fig. 4.2). Therefore, the Wigner–Seitz approximation used for calculating the interprecipitate spacing λ (Eq. 5.4) is not sufficient to determine the ageing condition and in such cases the full Mg_2Si strengthening distribution must be considered.

5.3.2 Quantitative analysis

The range of application of the relationships obtained in Sect. 5.3.1 between the mechanical properties and the Mg_2Si precipitation distribution expressed in terms of its interprecipitate spacing λ is extended in this section to the experimental results gathered at higher temperatures from the creep and LCF tests. Once proven this extension, relevant information for the mechanical modeling of the alloy behavior like its high temperature regime and the dominant deformation mechanism in this temperature range will be extracted from these results.

5.3.2.1 Creep testing

The minimum creep rate $\dot{\epsilon}_s$ obtained from the secondary stage of the creep tests against the corresponding applied stresses are plotted in Fig. 5.11(a). As expected, the creep rate $\dot{\epsilon}_s$ increases with the applied stress as well as with the temperature of the test.

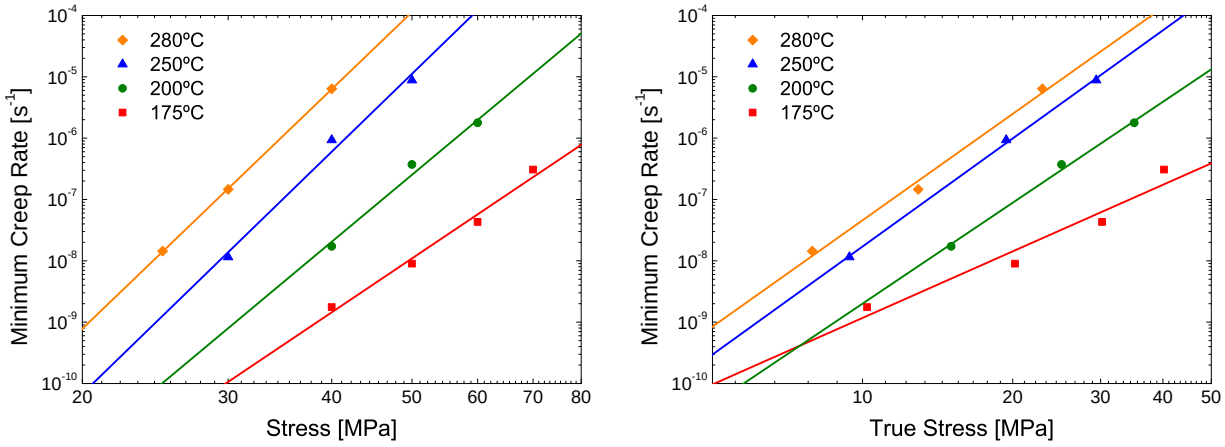

(a) (b)

Fig. 5.11: Minimum secondary creep rates $\dot{\epsilon}_s$ obtained from the creep tests carried out at 175°C, 200°C, 250°C, and 280°C using: (a) the Norton expression given by Eq. (5.2); (b) the modified Norton approach given by Eq. (5.3).

Fig. 5.11(a) is obtained by applying the Norton equation given by Eq. (5.2) to provide the relationship existing between the secondary creep rate $\dot{\epsilon}_s$ and the applied load σ_{cr}. The stress exponent n at each temperature is determined from the resulting slope of the double logarithmic plot of the minimum creep rate $\dot{\epsilon}_s$ against the applied load σ_{cr} [76]. The stress exponents gathered at each temperature are presented in Table 5.4 and as expected, these are too high (ranging from 9 to 13) to determine the deformation mechanism occurring. Therefore, the modified Norton equation including a threshold stress σ_{cr}^0 is considered to overcome this issue.

Temperature / °C	n	σ_{cr}^0 / MPa	n_t
175	9.07	29.79	3.60
200	11.28	24.95	5.46
250	13.11	20.59	5.85
280	12.98	17.07	5.76

Table 5.4: Results for the stress exponent n obtained from Norton equation, and for the threshold stress σ_{cr}^0 and true stress exponent n_t obtained from the modified Norton equation for the four creep temperatures 175°C, 200°C, 250°C, and 280°C.

Using this modified approach, the determination of the threshold stress is done on the basis of the same double logarithmic plot of the minimum creep rate against the applied stress. A minimum creep rate $\dot{\epsilon}_s$ of $1 \cdot 10^{-10}$ s^{-1} is assumed as the lowest strain rate that can be measured when creep occurs [156]. The extrapolation of the double logarithmic fitted curves to this assumed lowest strain rate measurable provides the threshold stress σ_{cr}^0 at each temperature [76]. Thus, the true Norton stress exponent n_t can be calculated by applying to Eq. (5.3) the same procedure described above for the stress exponents n. The results for the threshold stress σ_{cr}^0 and the true Norton stress exponents n_t are given in Table 5.4. By considering σ_{cr}^0, the measured true stress exponents n_t are considerably reduced (see Fig. 5.11(b)).

The deformation mechanism for the overaged condition of the alloy at high temperatures is thus determined from the experimental true Norton stress exponents n_t obtained. Thus, the dominant deformation mechanism at 175°C is the viscous glide of dislocations ($n_t = 3$) while the deformation for temperatures above 200°C occurs by climbing of dislocations over the Mg_2Si strengthening precipitates ($n_t = 5$). From these results, the start of the high temperature regime of the alloy can also be established at this temperature (200°C). Altogether, this information is very useful for the modeling of the alloy mechanical behavior (Chap. 6).

5.3.2.2 LCF testing

Ageing condition AC_{I}

The predicted initial size distributions of Mg_2Si strengthening precipitates for the ageing condition AC_{I} obtained from ageing processes at 210°C and 240°C (see Table 5.1) are shown in Fig. 5.12(a). These two distributions differ notably from each other, as is the case with the final distributions after the LCF tests performed at 150°C and presented in Fig. 5.12(b). Nevertheless, from the comparison of Figs. 5.12(a) and 5.12(b), the effect of a possible *in–situ* precipitation process resulting from the relatively high temperature of the test is discarded. The measured stress–time responses of the two samples obtained for the high strain rate cycles are shown in Fig. 5.12(c). The entire stress–time responses are given in Fig. 5.12(d).

The wider shape of the Mg_2Si strengthening distribution together with the larger mean particle size indicates a more pronounced overaged condition for the specimen aged at 210°C. As a result, a lower strengthening in the mechanical behavior of this sample is observed as expected compared to the results obtained for the specimen aged at 240°C (see Figs. 5.12(a) and 5.12(b)). Although in agreement with the conclusions drawn previously, this result is necessary but not sufficient to confirm the one–to–one relationship existing between the Mg_2Si strengthening distribution and the mechanical behavior of the alloy. Besides, the ageing conditions for this hardening grade are not properly chosen and this underlines the lack of precision of the hardness for determining the ageing state, especially for those close to the peak–aged condition. Instead, the full precipitation distribution should have been considered for a more accurate estimation.

Ageing condition AC_{II}

The experimental and simulation results obtained for the hardening grade AC_{II} are presented in Fig. 5.13. Conversely to ageing condition AC_{I}, the precipitation distributions for both samples are certainly very similar (see Figs. 5.13(a) and 5.13(b)). The mechanical response to the LCF test obtained for both samples is plotted in Figs. 5.13(c) and 5.13(d). Both graphs show nearly identical behavior for both specimens, which is the direct consequence of the strong agreement of the underlying precipitation distributions.

The results obtained for this ageing condition are in line with that presented for AC_{I}. Therefore, and in agreement with the previous analysis made for the hardness and tensile tests, the response of the $AlSi_{10}Mg(Cu)$ alloy under LCF loading conditions is also determined by the size distribution

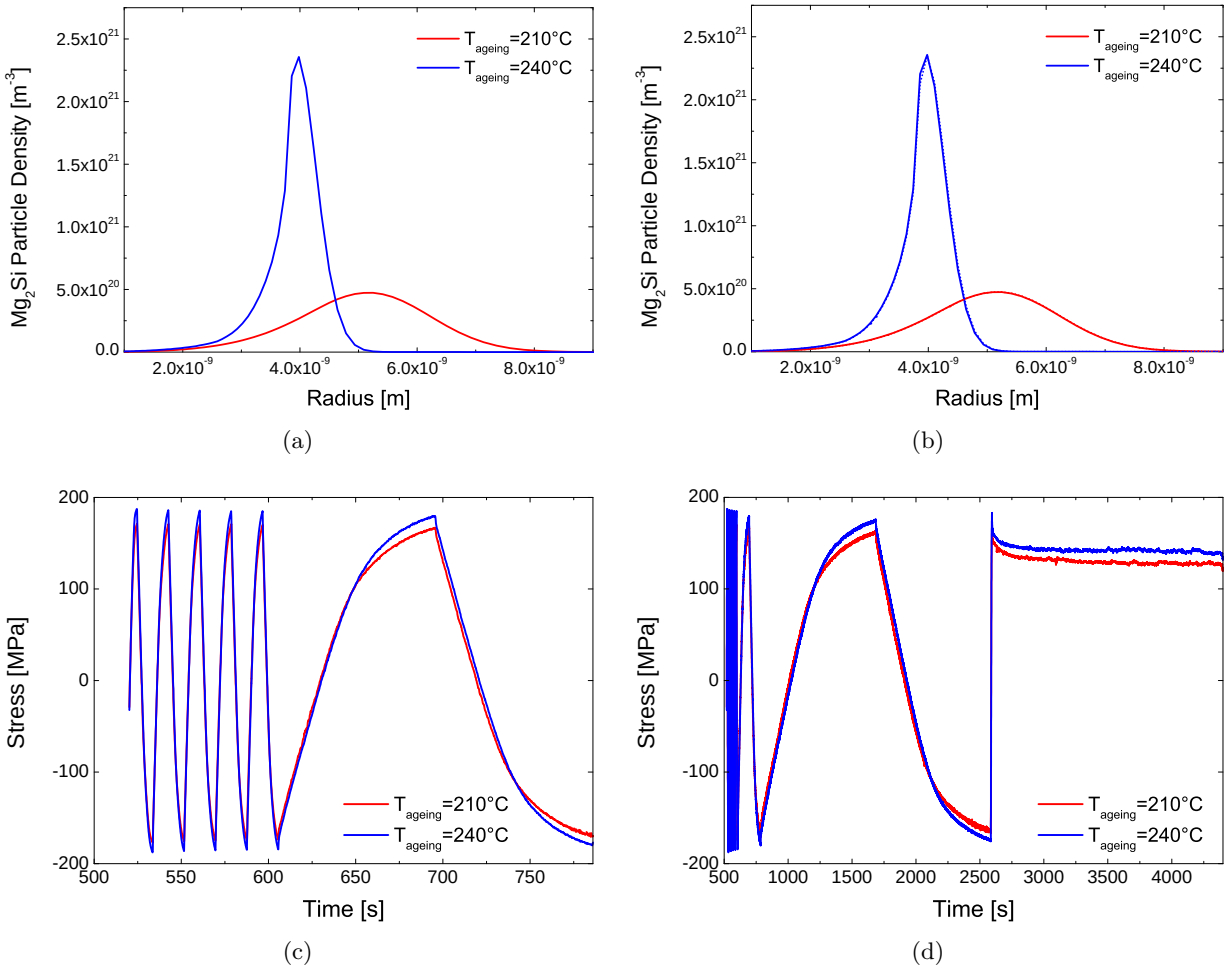

Fig. 5.12: Results for ageing condition AC_{I} obtained from samples treated at 210°C (41 hours) and 240°C (2.5 hours): (a) predicted Mg_2Si precipitation distributions after ageing; (b) Mg_2Si precipitation distributions after testing; (c) response to the high strain rate cycles of the LCF test performed at 150°C; (d) entire response to the LCF test.

of Mg_2Si strengthening precipitates. This is confirmed by additional experiments and simulations for the additional hardening grade AC_{III} presented below.

Ageing condition AC_{III}

Fig. 5.14 is another example of the relationship exiting between the Mg_2Si precipitation distribution and the alloy mechanical behavior obtained under LCF loading conditions, in this case, for a more pronounced overaged condition. The strengthening distributions are very similar for both samples and this leads again to nearly identical mechanical responses. Table 5.5

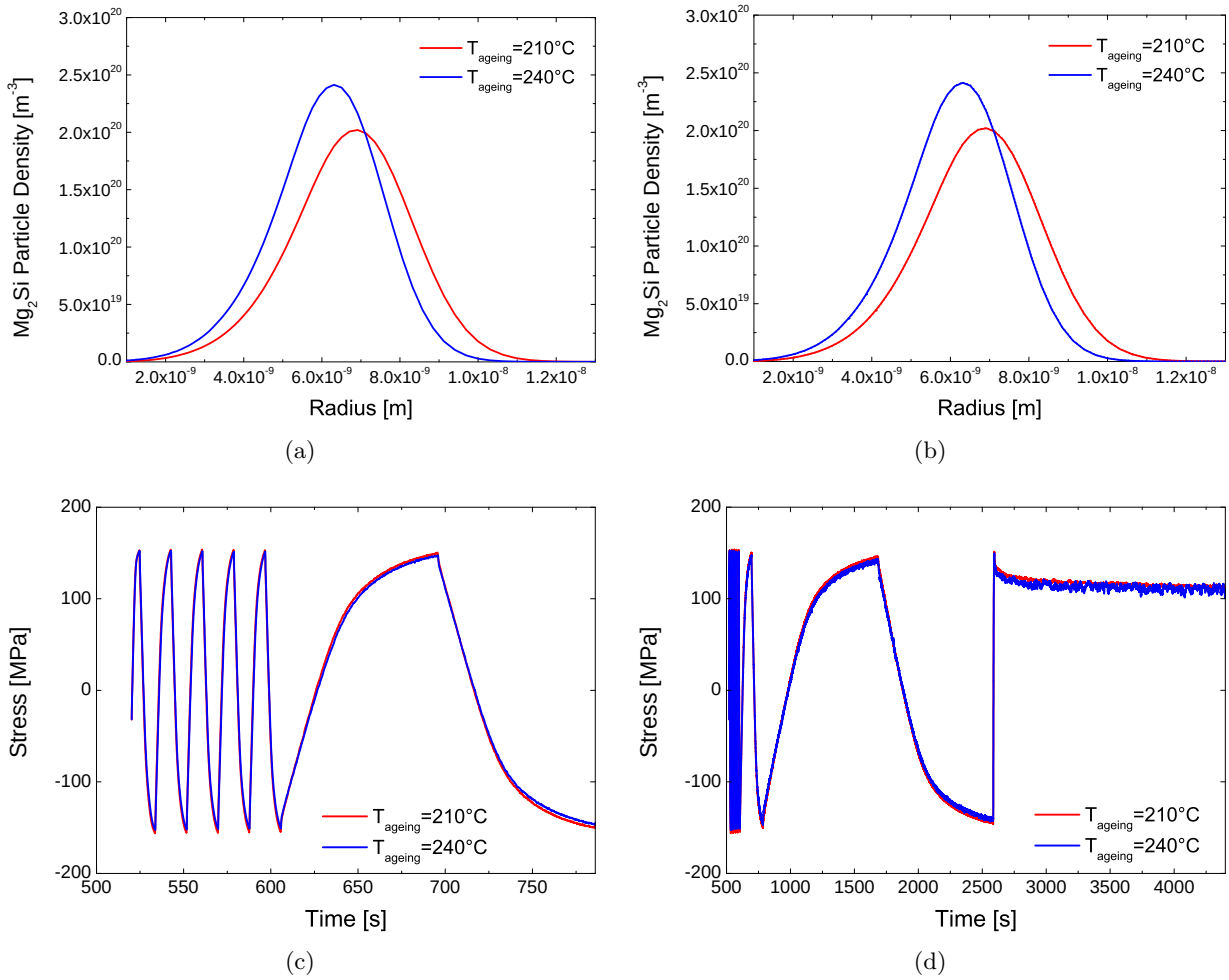

Fig. 5.13: Results for ageing condition AC_{II} obtained from samples treated at 210°C (96 hours) and 240°C (14 hours): (a) predicted Mg_2Si precipitation distributions after ageing; (b) Mg_2Si precipitation distributions after testing; (c) response to the high strain rate cycles of the LCF test performed at 150°C; (d) entire response to the LCF test.

summarizes the results for the stress–points 1 to 6, as introduced in Sect. 5.2.4.

The most relevant features of the LCF tests for the three pairs of hardening grades are given in Table 5.5. As expected, the results for each hardening grade are practically identical. The hardening grade HB_1 exhibits the maximum strengthening according to σ_2, as a result of the fine and high density precipitation distribution promoting its interaction with dislocations. The strength decrease for the most overaged condition is noticeable. Nevertheless, none of the specimens shows the typical cyclic work hardening of such alloys, likely due to he high temperatures and the overaged condition of the alloy (σ^*_{cyclic}). Furthermore, there is also no notable strain rate sensitivity for any hardening grade, probably due to the overaged condition

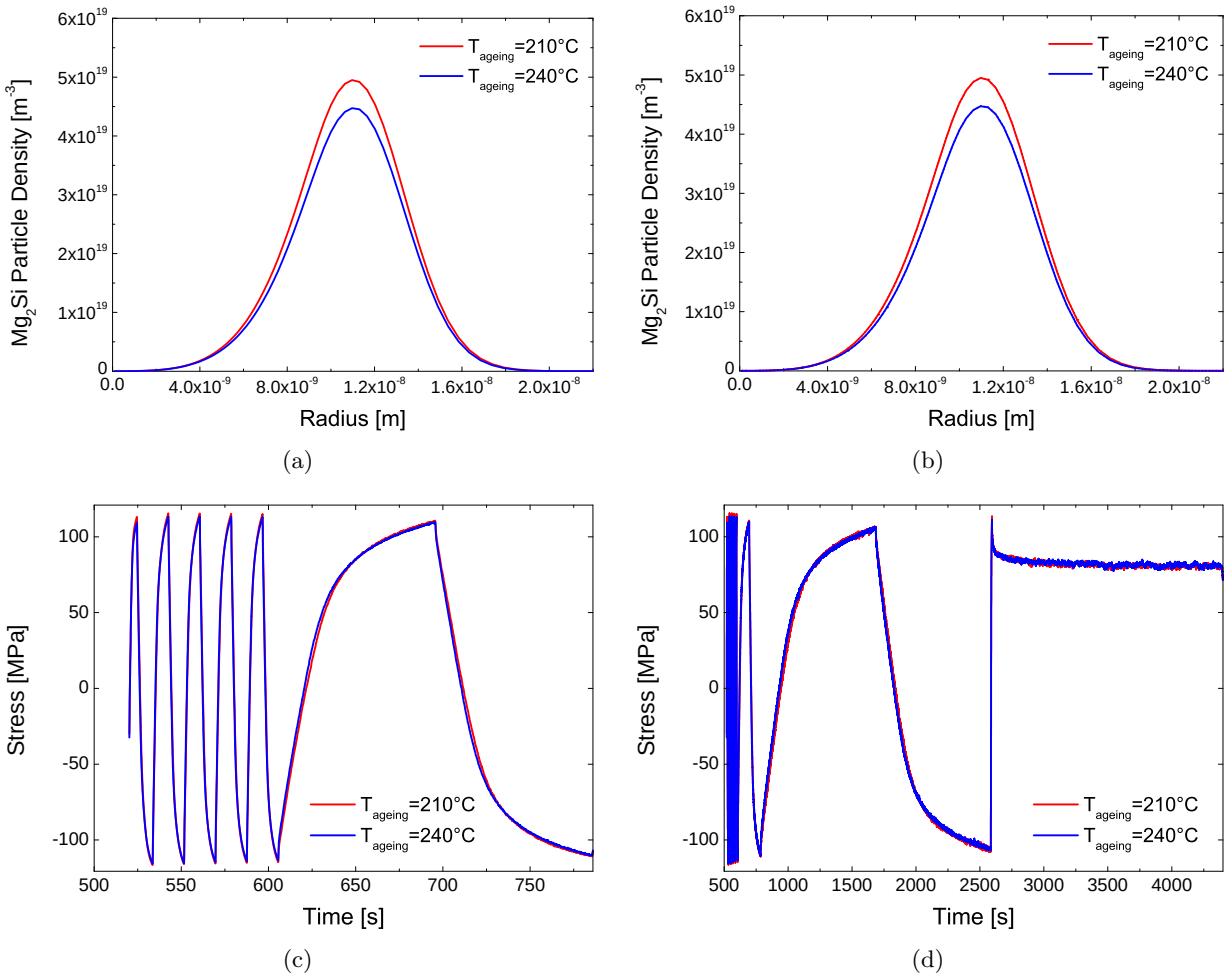

Fig. 5.14: Results for ageing condition AC_{III} obtained from samples treated at 210°C (400 hours) and 240°C (90 hours): (a) predicted Mg_2Si precipitation distributions after ageing; (b) Mg_2Si precipitation distributions after testing; (c) response to the high strain rate cycles of the LCF test performed at 150°C; (d) entire response to the LCF test.

and the coarse precipitation distributions of the three hardening grades (σ^*_{rate}). Finally, the static recovery during the final relaxation stage becomes more significant as the alloy overaged condition is more pronounced due to the lower hardening grade (σ^*_{relax}).

Effect of test temperature

A too prolonged exposure of the alloy to high temperatures may distort the Mg_2Si precipitation distribution resulting from the ageing process and therefore alter *in–situ* its mechanical response. In this respect, the time elapsed for the test setup (including the heating up of the samples) may

	T [°C]	σ_2 [MPa]	σ^*_{cyclic} [–]	σ^*_{rate} [–]	σ^*_{relax} [–]
HB_1	210	170.0	0.992	0.964	0.754
HB_1	240	185.1	0.988	0.972	0.766
HB_2	210	153.0	1.000	0.965	0.751
HB_2	240	151.6	0.993	0.964	0.742
HB_3	210	115.0	1.016	0.966	0.705
HB_3	240	113.0	1.033	0.964	0.727

Table 5.5: Comparison of the characteristic stress values determined from the LCF experiments for the different heat treatments, representing the absolute stress level, the effect of cyclic work hardening/softening, rate sensitivity, and viscosity/static recovery.

also have a great impact. This effect can be especially critical in those ageing conditions close to the T6 maximum strengthening condition.

The effect of long duration and temperature experimental conditions on the microstructure and, consequently, on the mechanical response of the alloy is analyzed in Fig. 5.15, which is based on the results from two LCF tests performed at 150°C and 250°C for the AC_0 condition. The initial precipitation distribution is plotted in Fig. 5.15(a). The corresponding experimental stress–time response to the LCF test carried out at 150°C is shown in Fig. 5.15(c). The final strengthening distribution after the test is also included in Fig. 5.15(a) and practically coincides with the initial distribution. However, in the case of the LCF test at 250°C, the strengthening distribution shape changes until the end of the test being at the end characteristic of a more pronounced overaged condition (Fig. 5.15(b)). This difference observed in the strengthening distributions shows that an *in–situ* precipitation process occurs in the alloy as a result of the prolonged exposure to 250°C. The effect of this change in the strengthening distribution on the alloy mechanical response is presented in Fig. 5.15(d), where a slight cyclic softening instead of the typical cyclic hardening (Fig. 5.15(c)) is observed.

The effect of elevated temperatures on this alloy is especially strong due mainly to the high diffusion coefficient of magnesium in aluminum but also to the high sensitivity of Mg_2Si precipitates to temperature changes [137, 157]. So much so, that the precipitation kinetics is significantly accelerated at 250°C. A rapid partial dissolution of the initial strengthening distribution occurs until the instantaneous concentration of magnesium in the matrix c matches the equilibrium concentration c^{α}_{∞}. This phenomenon can be observed in Fig. 5.15(b) from the intermediate distribution obtained after heating the specimen to 250°C and before the start of the test. During the test, the precipitation distribution coarsens rapidly becoming wider and moving to larger size classes. The incorporation of the effect of temperature on the mechanical

response can therefore be very important for both the preliminary preparation stage and the test itself. Therefore, some precipitation model like that of Robson can be very useful to predict this effect.

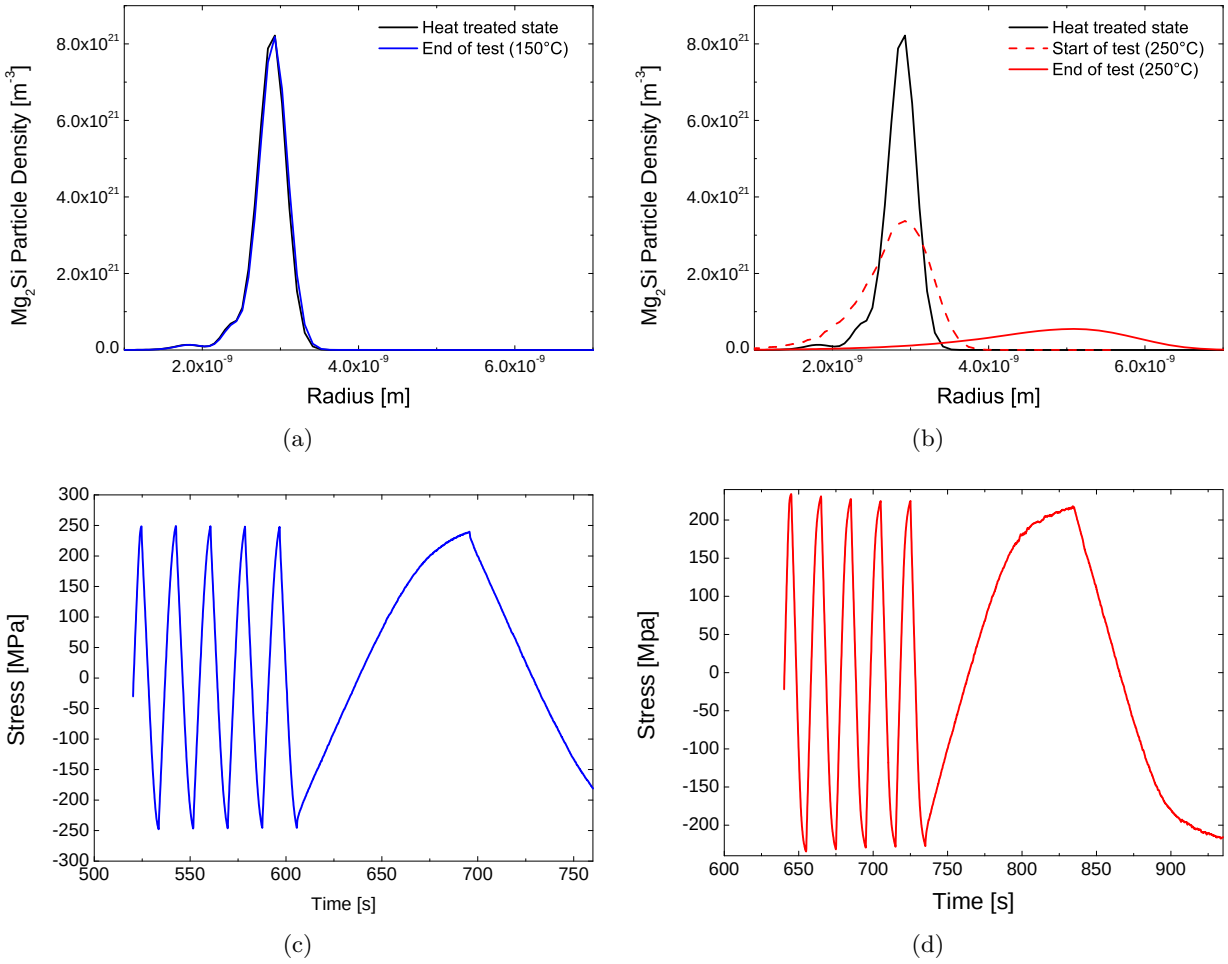

Fig. 5.15: Influence of the testing temperature on the Mg_2Si precipitation distributions and the mechanical response of the alloy: (a) predicted Mg_2Si strengthening distributions at the initial ageing state and after the test at 150°C; (b) predicted Mg_2Si strengthening distributions at the initial ageing state, before, and after the test at 250°C; (c) experimental response to the high strain rate cycles of the LCF test at 150°C; (d) experimental response to the high strain rate cycles of the LCF test at 250°C.

The strain amplitudes used for the LCF tests are different for the 150°C (0.45 %) and the 250°C (0.50 %) conditions. Therefore, the experimental stress–time responses cannot be compared quantitatively. The alloy shows at 150°C an initial strengthening during the first cycles probably produced by a low initial defect density [158]. Nevertheless, this phenomenon rapidly saturates due likely to the early development of stable dislocations substructures resulting from these fully reversed cycles [159]. Conversely, the gradual but not pronounced cyclic softening

observed at 250°C (Fig. 5.15(d)) is caused by the partial dissolution of the initial precipitate distribution and the coarsening of the remaining Mg_2Si strengthening particles, accompanied by the transformation of the semi–coherent β' to the incoherent β phase.

Severe plastic deformation usually promotes changes in the post–deformation ageing kinetics by accelerating the precipitation sequence and reducing the total volume fraction of strengthening phase. The increased defect density in the crystal structure during the plastic loading typically enhances the diffusion of the solutes contributing to the strengthening phase and to the thermodynamic equilibrium β–Mg_2Si phase [160]. However, this effect is not considered here in agreement with previous works [159]. In fact, the high temperatures and the low strain amplitudes of the LCF tests together with the strengthening distribution characteristic of overaged conditions indicate that the dominating deformation mechanism is the dislocation climb in which dislocations are deformed around precipitates [47]. Additionally, the remaining solid solution of magnesium in the matrix is low enough to discard the formation of new Mg_2Si precipitate nuclei due to the deformation process. Furthermore, the coarsening process occurring during the overageing stage is mainly governed by diffusion mechanisms [19].

5.4 Concluding remarks

The effect of the Mg_2Si strengthening distribution on the mechanical properties of the alloy in a T6–T7 heat–treated condition is analyzed in this chapter. The main purpose of this investigation is to determine if the mechanical behavior of such an alloy is determined by the shape of the precipitation distribution. For this reason, the response of the alloy to various tests of different kind and complexity is examined. These are, from least to most complex: hardness, tensile tests at room temperature, and LCF tests at higher temperatures combining the effects of nonlinear work hardening, strain rate sensitivity, and relaxation stages.

The ageing curves are the typical procedure to show the effect of the artificial ageing on the hardening grade of age–hardenable alloys for different ageing temperatures. By further analyzing these curves, a unique logarithmic relationship is found out between the hardness and the interprecipitate spacing λ of the precipitation distributions. Thus, lower hardness typical of more pronounced overaged conditions are related to larger interprecipitate spacings, as corresponds to coarser precipitation distributions. These strengthening distributions are a more accurate reference than the typical hardness for estimating the alloy ageing condition.

Similarly, the yield strength $R_{p,0.2\%}$ and ultimate tensile strength R_m obtained from the tensile tests are also uniquely determined by the Mg_2Si strengthening distribution and exhibit a

logarithmic decrease with the interprecipitate spacing λ. Nevertheless, an extension to the whole ageing process considering the first precipitation stages is not straight forward and would require considering the complete precipitation distribution.

Finally, the same conclusions can also be drawn for the response of the alloy to the complex LCF loading history used in this work at elevated temperatures. Once again, the mechanical behavior of the alloy is determined by the precipitation distribution, and small differences in these are reflected in the experimental curves of the tests. This supports the inaccuracy of hardness to determine the alloy ageing condition. Furthermore, the three hardening grades show different strength levels (σ_2) and relaxation behavior (σ^*_{relax}). However, there is no cyclic work hardening (σ^*_{cyclic}) and strain rate sensitivity (σ^*_{rate}) for any hardening grade.

Additionally to this analysis, the dislocation climbing is the governing deformation mechanism at high temperatures (above 200°C for this alloy) according to the results obtained from the creep tests analyzed by using the modified Norton equation suitable for precipitation strengthened materials.

All these results indicate that the Mg_2Si precipitation distribution reveals itself as sufficient for predicting the mechanical behavior of the alloy. In this sense, the ageing process itself is found out to be a means, but the mechanical behavior is certainly determined by the resulting Mg_2Si precipitation distribution. Based on this observation, Robson's model which allows predicting the size distribution of strengthening precipitates also for non–isothermal temperature histories, as they are present during the operation of components, represents a very powerful tool.

Despite this, the Mg_2Si precipitation distribution is not the only strengthening mechanism in the alloy. The remaining solid solution and the intrinsic strength of the matrix also contribute to the total strengthening of the alloy. However, and according to the simulation results obtained from the Shercliff–Ashby model, these latter remain approximately constant for the overaged condition of the alloy of interest for this work.

The further development of the work will focus on establishing a one–to–one relationship between the precipitation distribution and the material parameters in the evolution equations of a constitutive model predicting the nonlinear work hardening behavior and the time dependent behavior of the material. The identification of such a relationship is the missing link towards a scale bridging approach from the simulation of the precipitation distribution to the macroscopic constitutive behavior.

Chapter 6

Mechanical modeling

The thermal loads resulting from the start–operate–stop cycle of combustion engines and acting on their cylinder heads can be synthesized as low cycle fatigue conditions as that used in Chap. 5 for the mechanical characterization of the alloy. For this reason and considering the application of this project, the mechanical modeling of the alloy is accomplished by using these strain–controlled tests.

By the following, the constitutive Steck's material model is used in this work to simulate the mechanical behavior of the alloy, focusing on its high temperatures regime and only considering its overageing condition. The model and the mathematical approach implemented in this work are first presented in Sect. 6.1. For its calibration, four different ageing states within the T7 overageing condition are used. Finally and for reasons of simplicity and readability, the simulation results obtained for two of these conditions are presented in Sect. 6.2, while a survey of the results for the four states is given in App. B.

6.1 Steck's model

The Steck's constitutive mechanical model is a unified stochastic model especially useful to simulate the response of metallic materials under monotonic and cyclic inelastic deformation conditions [161]. Obtained by applying the Markov–chains methodology, it has been developed to consider applications at the whole range of temperatures. However, the model is especially appropriate to cover the high temperature plasticity and creep of metals [162], exhibiting a high–quality fitting to experimental tests [163]. Furthermore, this can be accomplished by using a unique and temperature independent set of modeling parameters.

6.1.1 Problem description and modeling objectives

Plasticity at elevated temperatures for stress ranges of technical interest is typically attributed to the movements of dislocations in the material [162]. The structure of the material acting against these movements is truly important for the plasticity modeling [162] and makes the formulation of the model on the microscopic scale particularly useful. Furthermore, the modeling of all of these as stochastic processes is meaningful, due to the stochastic nature of these microscopic processes.

In case of precipitate strengthened alloys, the free motion of dislocations in the material is usually hindered by two different types of obstacles. These are:

(i) The long–range obstacles comprising the dislocation structures resulting from the plastic deformation produced in the material [164].

(ii) The short–range obstacles produced by point defects such as foreign atoms, nucleated precipitates, or forest dislocations [162, 164].

For overcoming these obstacles, the dislocations require some additional energy which is typically provided by two different activation mechanisms as shown in Fig. 2.5. These are:

(i) The mechanical activation mechanism resulting from the external loading of the material.

(ii) The thermal activation mechanism that supports the motion of dislocations at high temperatures.

The mechanical activation mechanism is necessary to overcome those long–range stresses produced by the dislocation structures formed in the material while the thermal activation mechanism is usually enough for surmounting those energy barriers produced by point defects. The mechanical activation mechanism is usually based on the *effective stress* σ^{eff} concept acting on dislocations given by:

$$\sigma^{eff} = \sigma - \sigma_b \ , \tag{6.1}$$

where σ is the applied stress and σ_b is the so–called *back stress*. The build–up of internal back stress σ_b results from the formation of complex dislocation substructures produced during the plastic deformation of the material, like cells and dislocation pile–ups. It is usually related to

the stored elastic energy in the material and exhibits a significant statistical variation in its magnitude, spatial extent, and kinetics.

The modeling of these two types of obstacles hindering the free motion of dislocations in the $AlSi_{10}Mg(Cu)$ alloy and the corresponding two activation mechanisms necessary to overcome these energy barriers is accomplished in this work by using two internal stress variables of different physical nature [70]. These are:

(i) The kinematic stress σ^{kin} related to the formation of dislocation structures and their evolution as a result of the stresses imposed on the material [165].

(ii) The isotropic stress σ^{iso} that collects the effect of the isotropic short–range stresses produced by point defects and directly related to the dislocation density in the material [166].

The modeling of the mechanical behavior of the alloy is limited in this work to high temperatures. In case of deformation processes at elevated temperatures resulting from the action of monotonic external loads, the kinematic stress σ^{kin} is sufficient to describe the mechanical behavior of the material [91]. However, the isotropic stress σ^{iso} is also necessary for modeling the alloy mechanical behavior for a wider temperature range [164] or when cyclic loading conditions are considered [70]. Furthermore, the recovery mechanisms of both internal variables have a strong impact on the mechanical modeling of the alloy due the thermally activated reorganization processes occurring in the material at elevated temperatures [93].

Thus, the purpose of implementing Steck's material model in this work is the prediction of the plastic strain deformation process, the associated strain hardening, and the viscoplastic behavior of the alloy. Conversely, the expected anelasticity resulting from the reversible motion of dislocations at elevated temperatures is not considered, as it is also done for other viscoplastic material models [24].

6.1.1.1 Back stress

The effective stress σ^{eff} given by Eq. (6.1) is mainly considered for collecting the effect of dislocations motion in inelastic processes. For monotonic deformation processes, the back stress σ_b usually builds up from a small value as the strain increases producing the material hardening and then saturates. At saturation, thermal and mechanical activated processes are considered to be important recovery mechanisms.

Phenomenologically, the back stress σ_b is particularly necessary to predict specific features arising under cyclic loading conditions, like the shape of the cyclic hysteresis loops or the saturation of the cyclic peak stresses. As an example of this, the Bauschinger effect is mostly attributed to the interaction of dislocations with the internal back stress fields produced by other dislocations.

Certain features in the evolution of the back stress under cyclic and monotonic deformation processes are qualitatively common. As mentioned above, the back stress σ_b increases with the accumulated plastic strain until a saturated state is reached. As the accumulated plastic strain increases, tangled dislocation arrays, cells, and subgrains contributing to this back stress are produced. However, some important quantitative differences are found out. For this reason, the peak stress for the stabilized hysteresis loops are usually smaller than that reached during monotonic deformation processes for the same loading rate and temperature conditions. In general, the dislocations substructures resulting from cyclic deformation processes differ considerably from that obtained from monotonic loading.

6.1.2 Mathematical modeling

For infinitesimally–small deformations according to the infinitesimal strain theory, the total strain rate $\dot{\epsilon}$ at a point within a material can be considered as the linear combination of the single contributions of the elastic $\dot{\epsilon}_e$, inelastic $\dot{\epsilon}_{ie}$, and thermal $\dot{\epsilon}_{th}$[1] strain rates as [167]:

$$\dot{\epsilon} = \dot{\epsilon}_e + \dot{\epsilon}_{ie} + \dot{\epsilon}_{th} \ . \tag{6.2}$$

The inelastic deformation $\dot{\epsilon}_{ie}$ in Steck's model results from the elementary motion of the so–called *flow units*, that are directly related to the crystal lattice defects like single dislocations, dislocation packages, and grain boundaries [68–70, 92–95, 164]. These flow units perform elementary strain steps by overcoming those internal barriers or obstacles encountered during their motion. The magnitude of these barriers is highly influenced by the stress and temperature conditions to which the material is subjected as schematically shown in Fig. 2.5.

By further developing this figure, the passing of obstacles in Steck's model can be formulated as a transition probability of overcoming these energy barriers [70, 92, 164]. These barriers are the result of three energy contributions: (i) a ground level related to the free activation enthalpy of the material and calculated from the activation energy for self–diffusion U_0, (ii) the characteristic

[1] The modeling of the thermal strain rate $\dot{\epsilon}_{th}$ is not addressed in this work

strength of each specific type of obstacle and directly related to the isotropic stress σ^{iso}, (iii) the toughness of the long–range stresses resulting from the dislocation substructures present in the material. This last energy contribution reflects the effect of the effective stress σ^{eff}, and replacing the back stress σ_b by the kinematic back stress σ^{kin} according to Steck's model in Eq. (6.1), it yields:

$$\sigma^{eff} = \sigma - \sigma^{kin} \ . \tag{6.3}$$

The contribution of the effective stress σ^{eff} to the total barrier energy depends on the direction of the load applied (see Fig. 6.1), being small when the flow units motion occurs in the same direction as the external load σ applied or becoming larger otherwise.

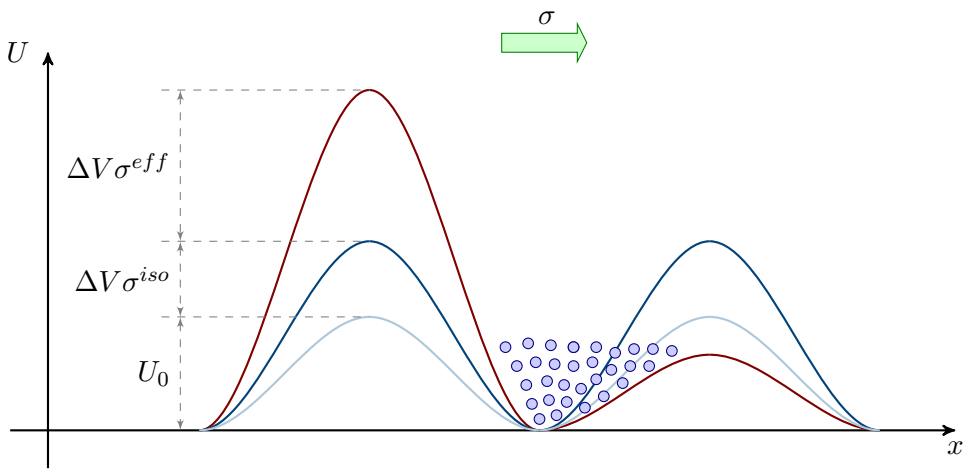

Fig. 6.1: Scheme of the relative contributions of the activation energy for self–diffusion U_0, the obstacle characteristic energy $\Delta V\sigma^{iso}$, and the long–range stresses $\Delta V\sigma^{eff}$ to the total energy barriers representing the obstacles encountered by flow units.

Thus, the gliding step probabilities of a single flow unit to pass a characteristic obstacle class of the strength σ^{iso} depending on the direction of the external load σ and assuming a Boltzmann distribution for the energy distribution of flow units [68, 70, 92, 164] are:

$$p_i^+ \sim \exp\left(-\frac{U_0 + \Delta V \sigma^{iso}}{R\,T}\right) \cdot \exp\left(\frac{\Delta V\left(\sigma - \sigma^{kin}\right)}{R\,T}\right) , \tag{6.4}$$

$$p_i^- \sim \exp\left(-\frac{U_0 + \Delta V \sigma^{iso}}{R\,T}\right) \cdot \exp\left(-\frac{\Delta V\left(\sigma - \sigma^{kin}\right)}{R\,T}\right) , \tag{6.5}$$

where p_i^+ and p_i^- are the single gliding step probabilities of a single flow unit in positive and in negative x–direction respectively, U_0 is the activation energy for self–diffusion, ΔV is the activation volume for self–diffusion, R is the gas constant, and T is the absolute temperature.

Therefore, the transition probability $H_{i,i+1}$ of passing from the obstacle class i to the next energetic class $(i+1)$ for the hardening mechanism considering both kinematic and isotropic processes is:

$$H_{i,i+1} = C_1 \cdot \delta t \cdot \left(p_i^+ - p_i^-\right) = C_1 \cdot \delta t \cdot \exp\left(-\frac{U_0 + \Delta V \sigma^{iso}}{R\,T}\right) \cdot \sinh\left(\frac{\Delta V\left|\sigma - \sigma^{kin}\right|}{R\,T}\right) . \tag{6.6}$$

Similarly, the transition probability $R_{i,i-1}$ of passing from the obstacle class i to the previous energetic class $(i-1)$ for the recovery mechanism is:

$$R_{i,i-1} = C_2 \cdot \delta t \cdot \exp\left(-\frac{U_0^* - \Delta V^* \sigma^{iso}}{R\,T}\right) , \tag{6.7}$$

where U_0^* and ΔV^* are the activation energy and the activation volume for recovery processes ($U_0^* = \alpha U_0$ and $\Delta V^* = \beta \Delta V$, being α and β material constants) [94].

Calling z_i the total number of flow units, the inelastic strain rate $\dot{\epsilon}_{ie}$ on the microscopic scale in Steck's model considering both hardening and recovery mechanisms can be calculated by:

$$\dot{\epsilon}_{ie} = C \cdot \sum_{i=1}^{\infty} z_i \cdot \exp\left(-\frac{U_0}{R\,T}\right) \cdot \sinh\left(\frac{\Delta V\left(\sigma - \sigma^{kin}\right)}{R\,T}\right) \cdot \exp\left(-\frac{\Delta V \sigma^{iso}}{R\,T}\right) , \tag{6.8}$$

Eqs. (6.4) and (6.5) refer to the probabilities of a single flow unit to overcome a determined obstacle class given by its intrinsic isotropic stress σ^{iso} under the influence of the load σ applied

and the long–range kinematic internal stresses σ^{kin}. However, the inelastic deformation observed on the macroscopic scale in the material is the result of the surmount of all possible obstacles.

Given the stochastic nature of the deformation mechanisms occurring on the microscopic scale, a discrete Markov–chain can be applied to these transition probabilities to account for the contributions of every obstacle class in the modeling of the inelastic deformation in the material [68–70, 91–95]. By applying secondly a mean value formulation, this stochastic model is further developed to obtain a unique system of non–linear differential equations on the macroscopic scale [68–70,91–95]. Thus, the resulting system of ordinary differential equations for the constitutive Steck's material model in one dimension is [70]:

$$\dot{\sigma} = E \cdot \dot{\epsilon}_e = E \cdot (\dot{\epsilon} - \dot{\epsilon}_{ie}) \ . \tag{6.9}$$

$$\begin{aligned} \dot{\sigma}^{iso} = {} & h_1 \cdot \exp\left(- (\delta_1 - 1) \cdot \frac{\Delta V \sigma^{iso}}{R\,T} \right) \cdot |\dot{\epsilon}_{ie}| \\ & - r_1 \cdot \exp\left(- \frac{\alpha_1 U_0}{R\,T} \right) \cdot \exp\left(\frac{\beta_1 \Delta V \sigma^{iso}}{R\,T} \right) \ . \end{aligned} \tag{6.10}$$

$$\begin{aligned} \dot{\sigma}^{kin} = {} & h_2 \cdot \exp\left(\frac{\Delta V \sigma^{iso}}{R\,T} \right) \cdot \exp\left(- \frac{\delta_2 \, \Delta V \sigma^{kin} \cdot \mathrm{sign}\left(\sigma^{eff}\right)}{R\,T} \right) \cdot \dot{\epsilon}_{ie} \\ & - r_2 \cdot \exp\left(- \frac{\alpha_2 U_0}{R\,T} \right) \cdot \sinh\left(\frac{\beta_2 \, \Delta V \sigma^{kin}}{R\,T} \right) \ . \end{aligned} \tag{6.11}$$

And the expression for the inelastic strain rate $\dot{\epsilon}_{ie}$ is:

$$\begin{aligned} \dot{\epsilon}_{ie} = {} & C \cdot \exp\left(- \left(1 - \frac{\alpha_1 - 1}{\kappa} \right) \cdot \frac{U_0}{R\,T} \right) \cdot \exp\left(- \Theta \frac{\Delta V \sigma^{iso}}{R\,T} \right) \\ & \cdot \left(\sinh\left(\frac{\Delta V \left| \sigma - \sigma^{kin} \right|}{R\,T} \right) \right)^{1 + \frac{1}{\kappa}} \cdot \mathrm{sign}\left(\sigma^{eff} \right) \ . \end{aligned} \tag{6.12}$$

6.1.2.1 Modifications

Steck's model has been typically implemented to predict the mechanical response of different metallic materials under creep or cyclic loading conditions separately [70, 93, 164]. However, the

response of the model to a more complex loading history combining both loading conditions such as that presented in Fig. 5.3 has not yet been addressed and may lead to some simulation difficulties if the model approach above presented is used.

In the final relaxation process ($\dot{\epsilon} = 0 \implies \dot{\epsilon}_{ie} \approx 0$), the hardening term in the isotropic stress rate expression can be neglected compared with its recovery term. Being the duration of this relaxation phase sufficiently long, the isotropic stress σ^{iso} may become negative, which is physically an inconsistency considering the relationship existing between this internal variable and the short–range stresses present in the material. Therefore, an enhancement of Steck's model and in particular of Eq. (6.10) is necessary. Thus, the recovery term of the isotropic stress rate is modified by introducing an *effective isotropic stress* concept in its thermally activated process similarly to other constitutive models [83, 84, 168, 169]. This is accomplished by entering a new modeling parameter in the recovery term called *equilibrium isotropic stress* σ_{eq}^{iso} and a new model constant γ_1. Therefore, the resulting modified expression of the isotropic stress rate is:

$$\begin{aligned} \dot{\sigma}^{iso} &= h_1 \cdot \exp\left(-(\delta_1 - 1) \cdot \frac{\Delta V \sigma^{iso}}{R\,T}\right) \cdot |\dot{\epsilon}_{ie}| \\ &\quad - r_1 \cdot \exp\left(-\frac{\gamma_1 U_0}{R\,T}\right) \cdot \sinh\left(\frac{\beta_1 \Delta V \cdot \left(\sigma^{iso} - \sigma_{eq}^{iso}\right)}{R\,T}\right) . \end{aligned} \tag{6.13}$$

A similar material parameter can be found e.g. in Chaboche model and is interpreted as the yield strength of the material [153,170]. The yield strength in metals is usually determined by the strain rate and the temperature considered [24]. Therefore, the same physical meaning is given to this new material parameter σ_{eq}^{iso} and the assumed strain rate and temperature dependencies of the parameter must be determined from the model fitting process.

These proposed modifications should be accompanied by a review of the foundations of the model at the microscopic level on the basis of metal physics, which is however out of the objectives of this work. Thus, the enhanced Steck's material model in its one–dimensional formulation is:

$$\dot{\sigma} = E \cdot \dot{\epsilon}_e = E \cdot (\dot{\epsilon} - \dot{\epsilon}_{ie}) \ . \tag{6.14}$$

$$\begin{aligned} \dot{\sigma}^{iso} &= h_1 \cdot \exp\left(-(\delta_1 - 1) \cdot \frac{\Delta V \sigma^{iso}}{R\,T}\right) \cdot |\dot{\epsilon}_{ie}| \\ &\quad - r_1 \cdot \exp\left(-\frac{\gamma_1 U_0}{R\,T}\right) \cdot \sinh\left(\frac{\beta_1 \Delta V \cdot \left(\sigma^{iso} - \sigma^{iso}_{eq}\right)}{R\,T}\right) \ . \end{aligned} \tag{6.15}$$

$$\begin{aligned} \dot{\sigma}^{kin} &= h_2 \cdot \exp\left(\frac{\Delta V \sigma^{iso}}{R\,T}\right) \cdot \exp\left(-\frac{\delta_2\ \Delta V \sigma^{kin} \cdot \mathrm{sign}\left(\sigma^{eff}\right)}{R\,T}\right) \cdot \dot{\epsilon}_{ie} \\ &\quad - r_2 \cdot \exp\left(-\frac{\alpha_2 U_0}{R\,T}\right) \cdot \sinh\left(\frac{\beta_2\ \Delta V \sigma^{kin}}{R\,T}\right) \ . \end{aligned} \tag{6.16}$$

$$\begin{aligned} \dot{\epsilon}_{ie} &= C \cdot \exp\left(-\left(1 - \frac{\alpha_1 - 1}{\kappa}\right) \cdot \frac{U_0}{R\,T}\right) \cdot \exp\left(-\Theta \frac{\Delta V \sigma^{iso}}{R\,T}\right) \\ &\quad \cdot \left(\sinh\left(\frac{\Delta V \left|\sigma - \sigma^{kin}\right|}{R\,T}\right)\right)^{1+\frac{1}{\kappa}} \cdot \mathrm{sign}\left(\sigma^{eff}\right) \ . \end{aligned} \tag{6.17}$$

The hardening terms of both isotropic and kinematic stresses are:

$$\dot{H}^{iso} = h_1 \cdot \exp\left(-(\delta_1 - 1) \cdot \frac{\Delta V \sigma^{iso}}{R\,T}\right) \cdot |\dot{\epsilon}_{ie}| \ .$$

$$\dot{H}^{kin} = h_2 \cdot \exp\left(\frac{\Delta V \sigma^{iso}}{R\,T}\right) \cdot \exp\left(-\frac{\delta_2\ \Delta V \sigma^{kin} \cdot \mathrm{sign}\left(\sigma^{eff}\right)}{R\,T}\right) \cdot \dot{\epsilon}_{ie} \ .$$

Both hardening processes are driven by the inelastic strain rate. However, while the kinematic hardening depends on the direction of the load application allowing the model to predict the material behavior under cyclic loading conditions, the isotropic hardening is not affected by the direction of the inelastic deformation rate.

Similarly, the recovery processes for both internal variables are given by:

$$\dot{R}^{iso} = r_1 \cdot \exp\left(-\frac{\gamma_1 U_0}{R\,T}\right) \cdot \sinh\left(\frac{\beta_1 \Delta V \cdot \left(\sigma^{iso} - \sigma^{iso}_{eq}\right)}{R\,T}\right) .$$

$$\dot{R}^{kin} = r_2 \cdot \exp\left(-\frac{\alpha_2 U_0}{R\,T}\right) \cdot \sinh\left(\frac{\beta_2\, \Delta V \sigma^{kin}}{R\,T}\right) .$$

Contrary to the hardening processes, the recovery terms are thermally activated and as in other constitutive approaches these processes are not governed by the inelastic strain rate.

Thus, the constitutive Steck's model presented in Eqs. (6.14), (6.15), (6.16), and (6.17) can now be used to simulate the mechanical behavior of the $AlSi_{10}Mg(Cu)$ alloy under complex loading conditions combining cyclic and relaxation processes by using a unique set of modeling parameters.

6.1.2.2 Model parameters identification procedure

The version of the Steck's model proposed in this work consists of 16 model parameters h_1, δ_1, ΔV, r_1, γ_1, U_0, β_1, h_2, δ_2, r_2, α_2, β_2, C, α_1, κ, and Θ. These are independent of each other as well as of temperature. This latter feature is a major strength of this model compared with other constitutive approaches [83, 84, 169]. Furthermore, the fitting of the equilibrium isotropic stress σ^{iso}_{eq} introduced for extending the model beyond the typical applications has also to be done determining its strain rate $\dot{\epsilon}$ and temperature T dependencies.

Given the large number of parameters, a successive calibration procedure is ideally suited to fit this model [80, 81]. By using this type of parameters estimation methods, a better understanding of the model may be gained from the calibration process. Between all of them, the Trial–and–Error method has been already used to this end in other similar constitutive models [171].

The challenge of this parameters estimation procedure lies in including different stages in the complete loading history in which only a subset of the model parameters is relevant for the modeling of the material behavior, thereby following a kind of "progressive" parameters identification procedure [167]. Among the processes that the loading history must incorporate are non–linear isotropic hardening, non–linear kinematic hardening, rate sensitivity, and thermal activated static recovery. Besides, this loading history should display and separate the viscoplastic phenomenological behavior of the alloy as well as the contributions of the isotropic and kinematic processes to the material hardening process. Therefore, the strain–controlled cyclic loading

history proposed in Fig. 5.3 covering different strain rates and incorporating a final relaxation stage appears to be a good option for the calibration of Steck's model [172]. In fact, similar experimental tests have been successfully used for the calibration of constitutive viscoplastic material models incorporating kinematic and isotropic hardening rules [153].

The details on the loading history can be found in Sect. 5.2.4. The hardening terms of the isotropic $\dot{H}^{iso}$ and kinematic $\dot{H}^{kin}$ stress rates are first calibrated from the first cycles carried out at different strain rates. The kinematic term is expected to exhibit the typical cyclic behavior resulting from cyclic loading conditions, while the isotropic stress will increase until reaching a saturation value. As a result of this isotropic stress increase, a material hardening is usually observed after performing the first cycles in most metallic materials. However, this is not the case in this work according to the LCF experimental results presented in Sect. 5.3.2.2, likely due to the faster evolution at higher temperatures of the dislocations density, related to the isotropic stress σ^{iso}, than that of the dislocations structures given by the kinematic back stress σ^{kin} [164]. For this reason, the fitting of the initial value of isotropic stress σ_0^{iso} can be relegated to second place. Furthermore, the modeling of the alloy mechanical behavior can be done as a first approximation by only considering the kinematic hardening, assuming the isotropic stress σ^{iso} as constant under pure cyclic loading conditions. From this simplification, the equilibrium isotropic stress σ_{eq}^{iso} for each strain rate is immediately obtained and the relationship between σ_{eq}^{iso} and the strain rate $\dot{\epsilon}$ and temperature T can be determined from Eq. (6.10) ($\dot{\sigma}^{iso} = 0 \implies \sigma^{iso} = \sigma_{eq}^{iso}$). Therefore, a new expression is obtained for the inelastic strain rate $\dot{\epsilon}_{ie}$ as a function of σ_{eq}^{iso}:

$$\ln\left(\dot{\epsilon}_{ie}\right) = ln\left(\frac{r_1}{h_1}\right) - \alpha_1 \frac{U_0}{R\,T} + \left(\beta_1 + \delta_1 - 1\right) \cdot \frac{\Delta V \sigma_{eq}^{iso}}{R\,T} \ . \tag{6.18}$$

Thus, Steck's model can be simplified under cyclic loading conditions to:

$$\dot{\sigma} = E \cdot \dot{\epsilon}_e = E \cdot \left(\dot{\epsilon} - \dot{\epsilon}_{ie}\right) \ . \tag{6.19}$$

$$\dot{\sigma}^{kin} = K_1 \cdot \exp\left(-\frac{\delta_2\ \Delta V \sigma^{kin} \cdot \mathrm{sign}\left(\sigma - \sigma^{kin}\right)}{R\,T}\right) \cdot \dot{\epsilon}_{ie} \ . \tag{6.20}$$

$$\dot{\epsilon}_{ie} = K_2 \cdot \exp\left(-\left(1 - \frac{\alpha_1 - 1}{\kappa}\right) \cdot \frac{U_0}{R\,T}\right) \cdot \left(\sinh\left(\frac{\Delta V \left|\sigma - \sigma^{kin}\right|}{R\,T}\right)\right)^{1+\frac{1}{\kappa}} \cdot \mathrm{sign}\left(\sigma - \sigma^{kin}\right) \ . \tag{6.21}$$

The new pre–exponential parameters K_1 and K_2 in Eq. (6.20) and Eq. (6.21) are defined as:

$$K_1 = h_2 \cdot \exp\left(\frac{\Delta V \sigma_{eq}^{iso}}{R\,T}\right) . \tag{6.22}$$

$$K_2 = C \cdot \exp\left(-\Theta \frac{\Delta V \sigma_{eq}^{iso}}{R\,T}\right) . \tag{6.23}$$

The recovery term of the kinematic stress rate $\dot{R}^{kin}$ is not included in Eq. (6.20) because the hardening component $\dot{H}^{kin}$ is much larger under fully reversed strain–controlled cycles. Hence this hardening process $\dot{H}^{kin}$ is fitted to the experimental results gathered from these first cycles.

Besides, provided that both expressions for the inelastic strain rate in Eqs. (6.18) and (6.21) are driven by the same *driving force* ($\left(\Delta V \sigma_{eq}^{iso}\right)/(R\,T)$ and $\left(\Delta V \left|\sigma - \sigma^{kin}\right|\right)/(R\,T)$), the effect of temperature on the inelastic strain rate $\dot{\epsilon}_{ie}$ is included in the reduced model by the parameter α_1. Thus, parameters K_1 and K_2 are assumed temperature independent as well as constant for every strain rate, which fully agrees with previous reported investigations of the model [94, 95].

The hardening term of the isotropic stress rate $\dot{H}^{iso}$ and the corresponding model parameters h_1 and δ_1 can be identified from the response of the material to the last half–cycle previous to the relaxation process, where the strain rate increases from $1 \cdot 10^{-5}$ s^{-1} to $1 \cdot 10^{-3}$ s^{-1}. This rapid variation will produce an increase in the isotropic stress as a result of the rapid variation of the dislocations density [164].

The final relaxation process is used for the calibration of the recovery terms $\dot{R}^{iso}$ and $\dot{R}^{kin}$. This can only be accomplished by considering one sufficiently long relaxation stage (1800 s in this work). The parameters γ_1 and α_2 reflect only the effect of temperature on the recovery process of the isotropic and kinematic stress respectively, while β_1 and β_2 determine the curvature of both internal stresses in this relaxation process. The combined contribution of both recovery processes results in an intermediate response of the material model between the borderline cases in which only one of them is active [153].

Finally, the initial values of isotropic stress σ_0^{iso} and kinematic stress σ_0^{kin} are determined from the initial stress condition of the alloy. The initial value of kinematic stress σ_0^{kin} is assumed to be zero because no significant internal dislocation substructures are produced in the alloy in the absence of inelastic deformation [71]. Conversely, according to the rapid evolution of isotropic stress in the strain–controlled cycles, the initial isotropic stress σ_0^{iso} is assumed as the equilibrium isotropic stress σ_{eq}^{iso} at the strain rate $1 \cdot 10^{-3}$ s^{-1}.

6.1.3 Material preparation and experimental tests

Four ageing conditions of the alloy ranging from the T6 maximum strengthening condition to the T7 overageing process are used for the modeling of the alloy mechanical behavior. In this context, selecting the most suited ageing states and temperature ranges for the tests is particularly important to ensure that an *in–situ* precipitation process during the test will not occur and therefore a unique set of modeling parameters for each ageing condition will be obtained.

According to the simulations of the Mg_2Si precipitation distributions, the four selected ageing conditions remain unaltered during the tests despite the high temperatures. The temperature and duration of the ageing process as well as the hardness and the mean radius, particle density, and interprecipitate spacing of the Mg_2Si precipitation distributions for the four ageing states are given in Table 6.1. Actually, the first two ageing states are the ageing conditions AC_{I}, and AC_{II} used in Sect. 5.2.4. A third strengthening grade with a hardness of HB=60 and the ageing condition corresponding to the final equilibrium hardness of HB≈46.5 according to Fig. 5.5 are additionally considered for this analysis. The preparation procedure of the samples in this case is the same as that used in Sect. 5.2.4. The Mg_2Si strengthening distributions for the four selected ageing conditions are presented in Fig. 6.2. As can be seen, the strengthening distributions become wider showing a larger mean radius with a lower particle density as the overageing process to which the alloy is subjected is more pronounced.

State	Ageing conditions		Hardness	R_0	n_0	λ
	Temperature	Time				
	°C	h		nm	m^{-3}	nm
S_{I}	240	2.5	90	3.93	$1.68 \cdot 10^{22}$	48.4
S_{II}	240	14	80	5.65	$6.02 \cdot 10^{21}$	68.2
S_{III}	240	384	60	17.70	$2.08 \cdot 10^{20}$	209.4
S_{IV}	300	168	46.5	29.36	$3.67 \cdot 10^{19}$	373.3

Table 6.1: Temperature and duration of the ageing processes as well as the hardness measurements and the mean radius, particle density, and interprecipitate spacing of the Mg_2Si strengthening distributions for the four selected heat–treated states used for the calibration of Steck's model.

The temperature of all of these tests is 200°C or higher according to the definition of the high temperature regime made from the experimental creep results. Furthermore, these tests are carried out at two different temperatures for each ageing condition for the purpose of including the effect of temperature in the model. Nevertheless, the highest temperature used for the ageing state S_{I} is limited to 225°C due to the risk of *in–situ* precipitation, while it increases to 280°C for the rest of hardening grades. Similarly, the strain amplitude for those tests carried out in the

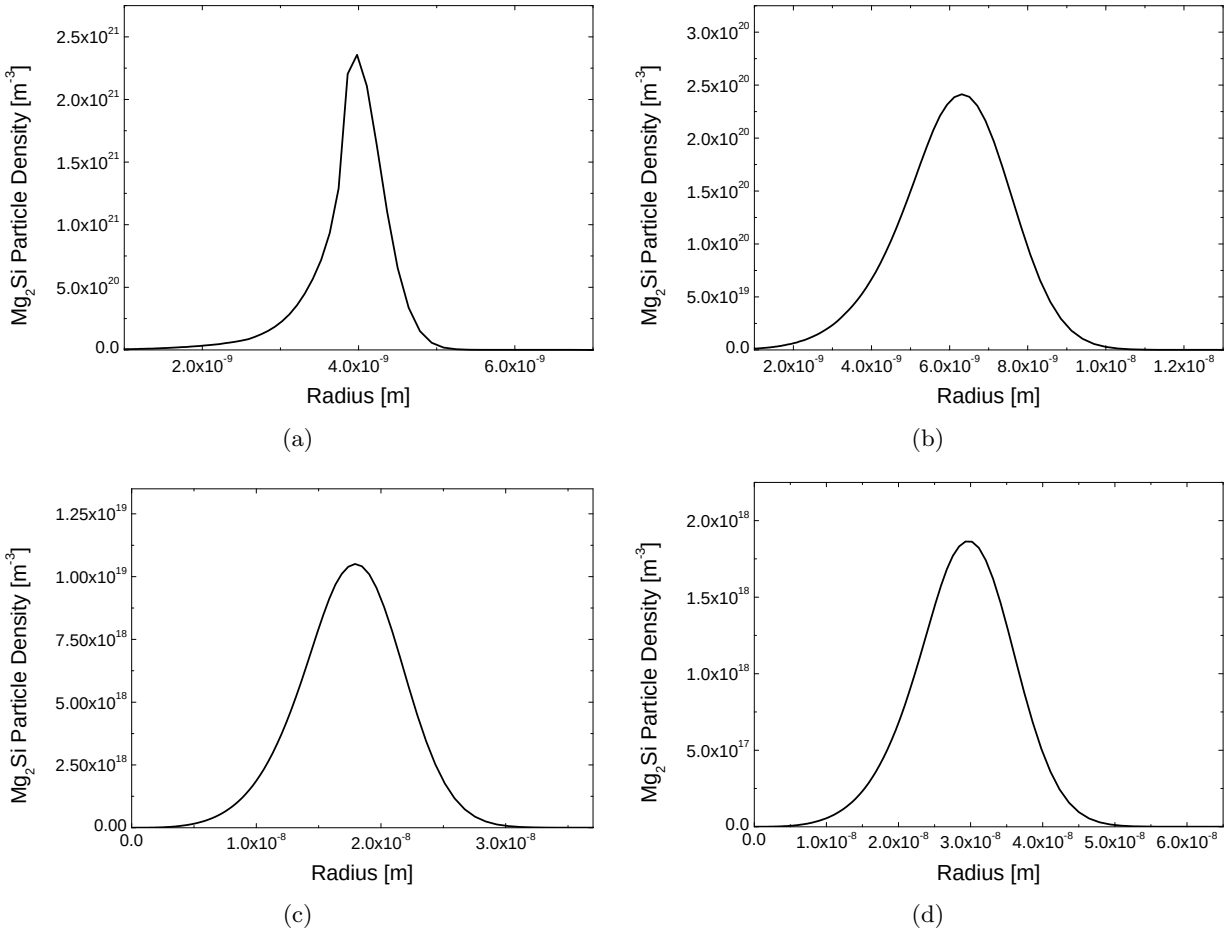

Fig. 6.2: Mg_2Si precipitation distributions obtained using Robson's model corresponding to the four hardening grades used for fitting Steck's model: (a) S_{I}; (b) S_{II}; (c) S_{III}; (d) S_{IV}.

S_{I} and S_{II} conditions is 0.45 %. It reduces to 0.25 % and 0.30 % for the S_{III} and S_{IV} ageing states.

6.1.4 Model parameters

The parameters of Steck's material model for the four ageing conditions obtained by following the successive identification procedure above proposed are given in Table 6.2. The model parameter δ_2 is a special case and is *ex–professo* not included in Table 6.2 because it will be discussed in detail in Sect. 7.1.1.

The activation energy for self–diffusion U_0 and the activation volume for self–diffusion ΔV are the only two model parameters directly taken from the literature [173]. Furthermore, the exponent κ

in Eq. (6.17) is determined from the creep tests presented in Sect. 5.3.2.1. Finally, an expression for the equilibrium isotropic stress σ_{eq}^{iso} depending on the temperature and strain rate is also obtained from the fitting procedure.

Parameter	Ageing conditions				Units
	S_{I}	S_{II}	S_{III}	S_{IV}	
C	$1.7 \cdot 10^{-4}$	$8.6 \cdot 10^{-3}$	$3.1 \cdot 10^{5}$	$3.1 \cdot 10^{7}$	1/s
α_1	1.197	1.181	1.085	1.082	–
κ	0.25	0.25	0.25	0.25	–
U_0	$140.0 \cdot 10^{3}$	$140.0 \cdot 10^{3}$	$140.0 \cdot 10^{3}$	$140.0 \cdot 10^{3}$	J/mol
Θ	329.0	321.3	295.2	237.1	–
ΔV	$13.5 \cdot 10^{-6}$	$13.5 \cdot 10^{-6}$	$13.5 \cdot 10^{-6}$	$13.5 \cdot 10^{-6}$	$\mathrm{m}^3/\mathrm{mol}$
h_1	$1.2 \cdot 10^{14}$	$1.2 \cdot 10^{14}$	$1.2 \cdot 10^{14}$	$1.2 \cdot 10^{14}$	N/m^2
δ_1	323.3	323.3	323.3	323.3	–
r_1	$7.106 \cdot 10^{-32}$	$7.106 \cdot 10^{-32}$	$7.106 \cdot 10^{-32}$	$7.106 \cdot 10^{-32}$	$\mathrm{N}/\left(\mathrm{m}^2 \cdot \mathrm{s}\right)$
γ_1	2.008	2.008	2.008	2.008	–
β_1	3581	3581	3581	3581	–
h_2	$1.52 \cdot 10^{10}$	$1.52 \cdot 10^{10}$	$1.52 \cdot 10^{10}$	$1.52 \cdot 10^{10}$	N/m^2
r_2	$8.44 \cdot 10^{6}$	$1.46 \cdot 10^{7}$	$4.58 \cdot 10^{10}$	$5.82 \cdot 10^{11}$	$\mathrm{N}/\left(\mathrm{m}^2 \cdot \mathrm{s}\right)$
α_2	0.392	0.423	0.566	0.663	–
β_2	129.65	129.65	129.65	129.65	–

Table 6.2: Model parameters used in the implementation of Steck's model. The activation energy U_0 and activation volume ΔV for self–diffusion are taken from the literature and the exponent κ is determined from the creep tests results.

6.1.4.1 Model parameters U_0 and ΔV

The activation energy for self–diffusion U_0 and the activation volume for self–diffusion ΔV in Steck's model can be well approximated by applying the results obtained from previous analysis on the effect of temperature and pressure on the high–temperature steady–state creep rate in Al–Si–Mg alloy systems.

The activation energy for creep deformation is therefore a good approximation for the activation energy for self–diffusion U_0 at elevated temperatures [168, 173–175]. Furthermore and according

to previous works, this material parameter is very similar to the activation energy for diffusion of magnesium in aluminum Q used in Robson's precipitation model [173]. Likewise, the activation volume for self–diffusion ΔV is also well approximated at elevated temperatures by the activation volume for creep deformation [173].

Referring to the activation energy for self–diffusion U_0, it can be experimentally determined from the ageing curves in Fig. 5.5 by applying the *temperature–corrected time* P concept used in Shercliff–Ashby model [5,6] (see App. A). This model variable is defined as the number of kinetic jumps taking place at time t and at temperature T ($P = t/T \cdot \exp\left(-U_0/\left(R\,T\right)\right)$) and its peak value P_p is independent of temperature. Thus, the activation energy U_0 can be determined if the duration of the ageing process producing the alloy maximum strengthening t_p for two ageing curves is known.

6.1.4.2 Model parameter κ

The parameter κ can be determined from the dominant interaction mechanism occurring between dislocations and precipitates at elevated temperatures, given the similarity between the expression of inelastic deformation rate in Eq. (6.17) and the modified Norton equation for precipitation strengthened alloys in Eq. (5.3). According to Sect. 5.3.2.1, the dominant deformation mechanism governing at elevated temperatures above 200°C in the overaged condition of the alloy is the dislocation climbing, by which dislocations bulge out of the slip plane and surmount the Mg_2Si precipitates [47, 176]. The experimentally measured true exponent n_t is 5. Therefore, the value of κ in Steck's model is 0.25.

6.1.4.3 Parameter σ_{eq}^{iso}

The equilibrium isotropic stress σ_{eq}^{iso} introduced in Eq. (6.13) for the correct prediction of the isotropic recovery process is fitted to the experimental data gathered from the LCF experiments. The resulting expression derived from Eq. (6.18) providing the relationship of this parameter with the temperature T and strain rate $\dot{\epsilon}$ is:

$$\sigma_{eq}^{iso} = \frac{R\,T}{352.3 \cdot \Delta V} \cdot \log\left(\mathrm{abs}\left(\dot{\epsilon}\right)\right) + 20.185\ . \tag{6.24}$$

As in the case of creep tests in Sect. 5.3.2.1, the assumed lowest strain rate $\dot{\epsilon}$ that can be measured is $1 \cdot 10^{-10}$ s^{-1}.

6.2 Simulation results

The simulation results using the modified Steck's model proposed in this work for the hardening grades S_{I}, and S_{IV} are presented below, as a demonstration of the agreement achieved between experiments and simulation. The results for the four ageing conditions can be found in App. B.

6.2.1 Ageing condition S_{I}

The simulation results for the hardening grade S_{I} at 200°C and 225°C are presented in Figs. 6.3(a) and 6.4(a). The results for the kinematic σ^{kin} and isotropic σ^{iso} stress are also shown in Figs. 6.3(b), 6.3(c) and in Figs. 6.4(b), 6.4(c). The strain amplitude used in these cases is 0.45 %. A good agreement for each individual temperature is achieved by calibrating the model parameter δ_2 and using the corresponding model parameters given in Table 6.2.

The kinematic stress σ^{kin} describes a stabilized hysteresis loop during the initial test cycles. This model's component is strongly dominated at high strain rates by its hardening term. However, as the alloy is subjected to lower strain rates, the recovery component becomes increasingly important. This feature is particularly evident in the unloading process of the cycles performed at the lowest strain rate immediately after the load direction change, in which the elastic component $\dot{\epsilon}_e$ practically coincides with the total strain rate $\dot{\epsilon}$. As a result, at this moment the hardening term $\dot{H}^{kin}$ can be ignored and this produces an "anelastic recovery" effect in the kinematic stress behavior.

The absence of cyclic hardening in the alloy response during the first loading cycles is supported by the nearly constant initial isotropic stress. This behavior also remains for the lower strain rates, due to the high temperature of the tests that lead to a rapid saturation of the isotropic stress. This feature supports the simplification of Steck's model at elevated temperatures to only the kinematic stress σ^{kin} under cyclic loading conditions. However, the recovery component of this hardening rule becomes more important during the relaxation process as the inelastic strain rate decreases to very low values. This underlines the importance of an appropriate design of the mechanical tests covering a wide range of loading conditions to address all phenomena incorporated in the model.

6.2.2 Ageing condition S_{IV}

The predicted response to the LCF tests at 200°C, 225°C, and 250°C obtained for the hardening grade S_{IV} by using the enhanced Steck's model are presented in Figs. 6.5(a), 6.6(a), and 6.7(a). In

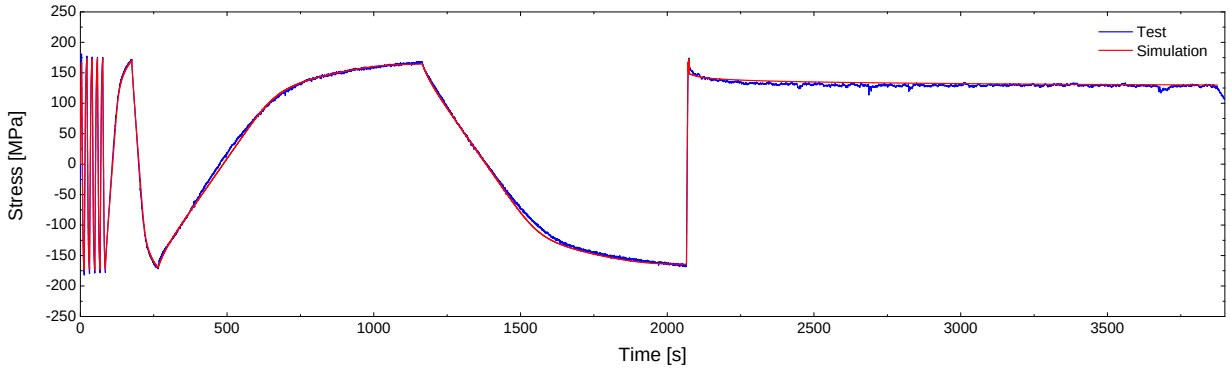

(a)

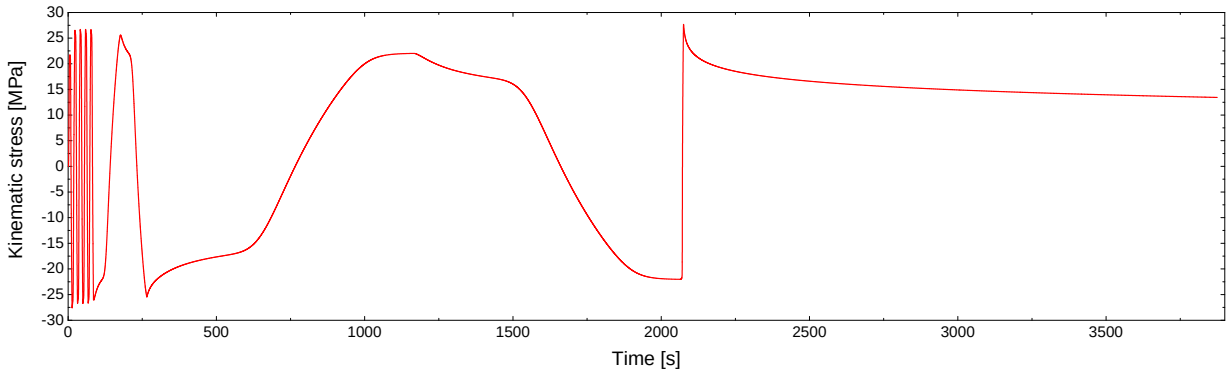

(b)

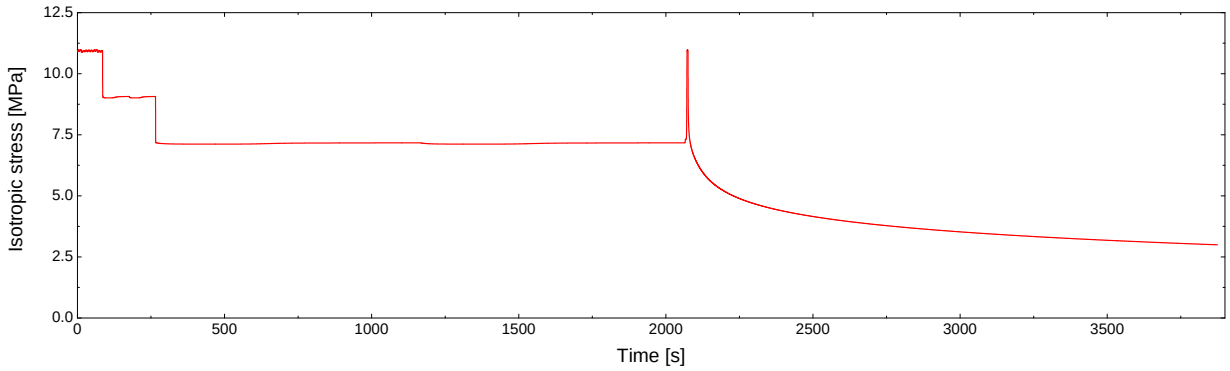

(c)

Fig. 6.3: Results of the LCF test and simulation using the modified Steck's model for the ageing condition S_{I} at 200°C referring to: (a) experimental and predicted stress σ; (b) kinematic stress σ^{kin}; (c) isotropic stress σ^{iso}.

this case, the strain amplitude used for the tests is 0.30 % and as shown for the ageing condition S_{I}, the simulation results agree very well with the experimental results by using the model parameters given in Table 6.2 and fitting the parameter δ_2 for each temperature. Although three

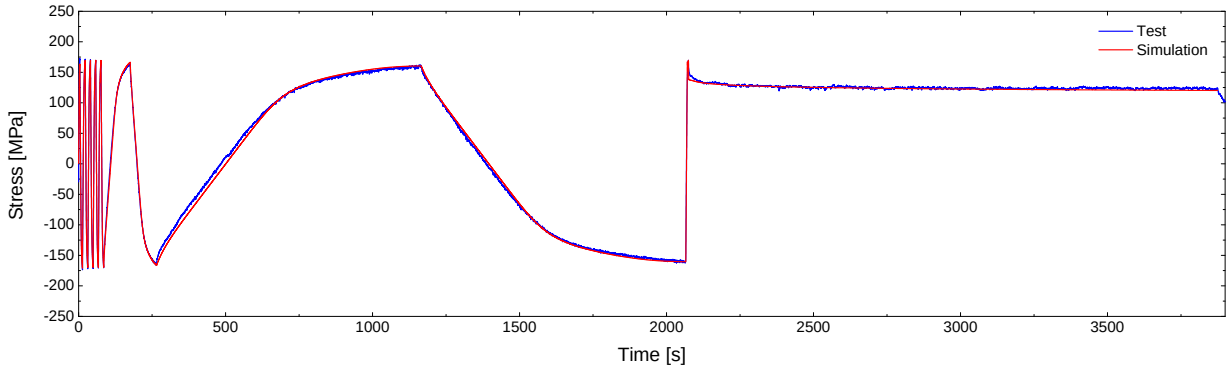

(a)

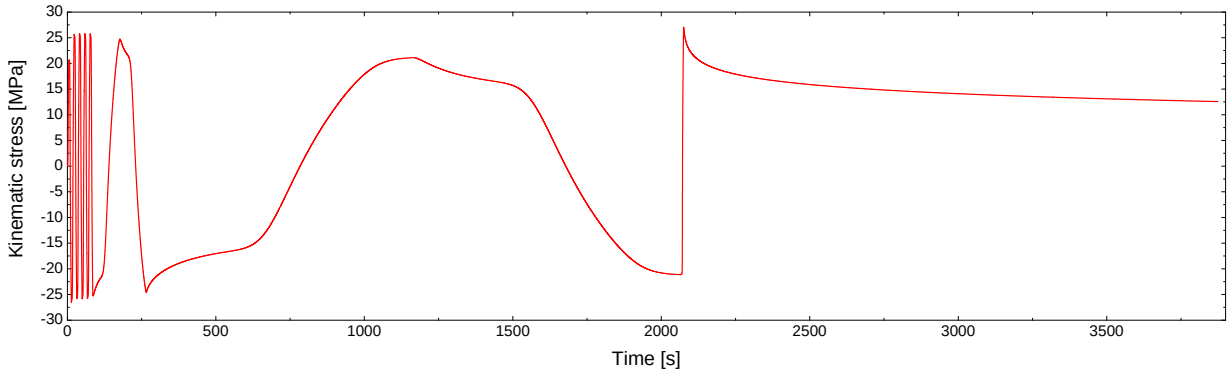

(b)

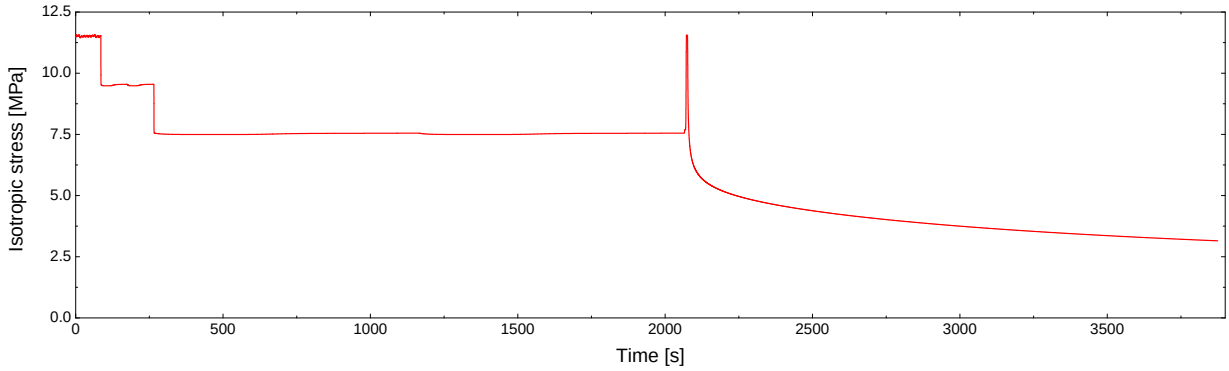

(c)

Fig. 6.4: Results of the LCF test and simulation using the modified Steck's model for the ageing condition S_{I} at 225°C referring to: (a) experimental and predicted stress σ; (b) kinematic stress σ^{kin}; (c) isotropic stress σ^{iso}.

temperatures are considered for this ageing condition, only the experimental results at 225°C, and 250°C are used for the fitting of the model, while that obtained at 200°C are used for its validation (except for δ_2). In this case, this strengthening grade can be subjected to higher

temperatures due to a more pronounced overageing condition of the alloy.

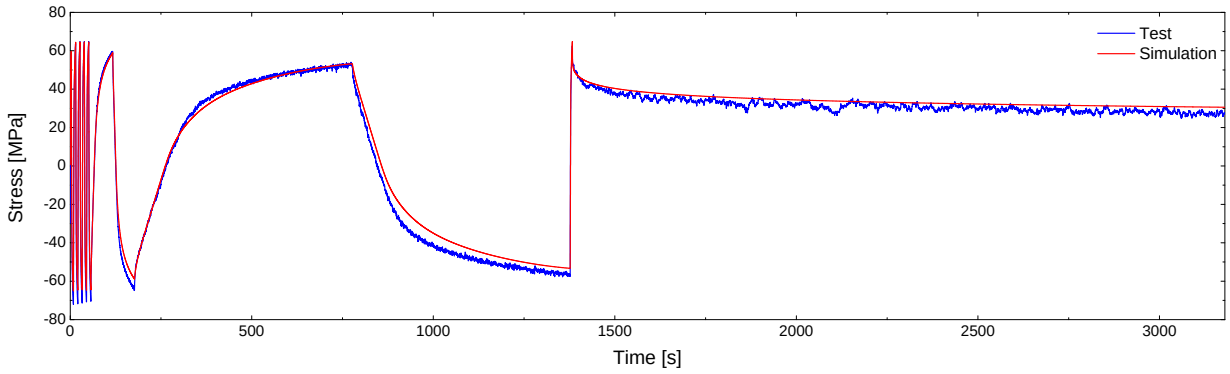

(a)

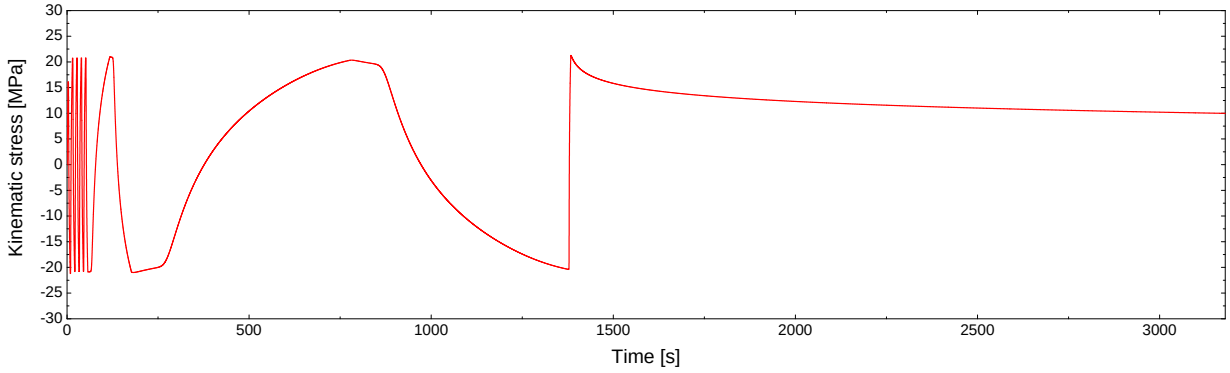

(b)

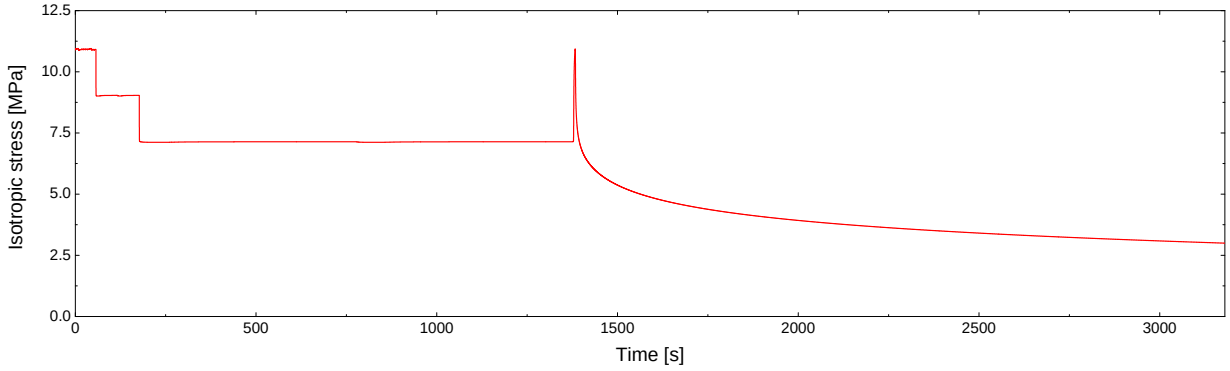

(c)

Fig. 6.5: Results of the LCF test and simulation using the modified Steck's model for the ageing condition S_{IV} at 200°C referring to: (a) experimental and predicted stress σ; (b) kinematic stress σ^{kin}; (c) isotropic stress σ^{iso}.

A slight peak tension–compression asymmetry can be seen in the response of the material (see Figs. 6.5(a), 6.6(a), and 6.7(a)), especially in the cycles conducted at the high strain rate $1 \cdot 10^{-3}$

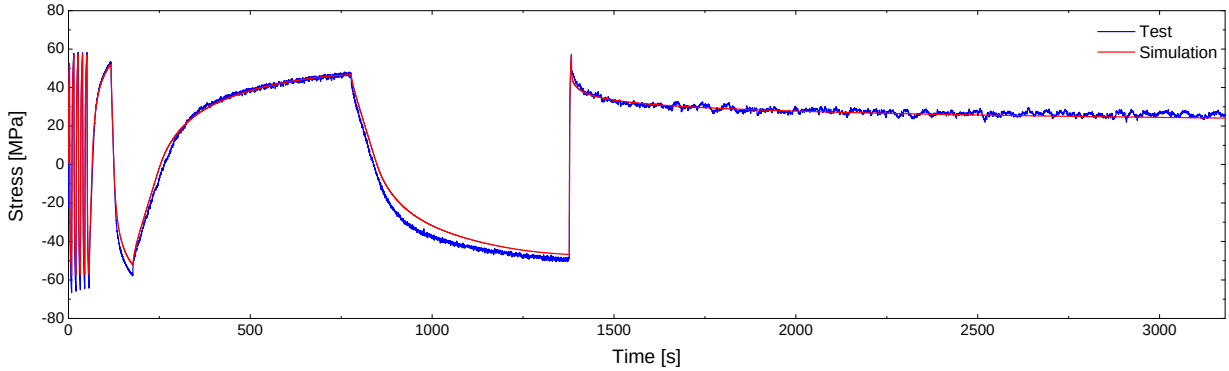

(a)

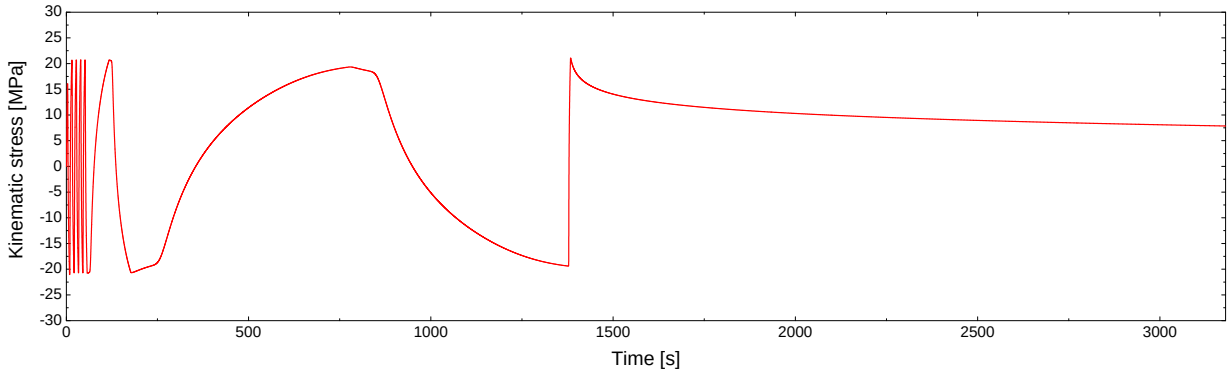

(b)

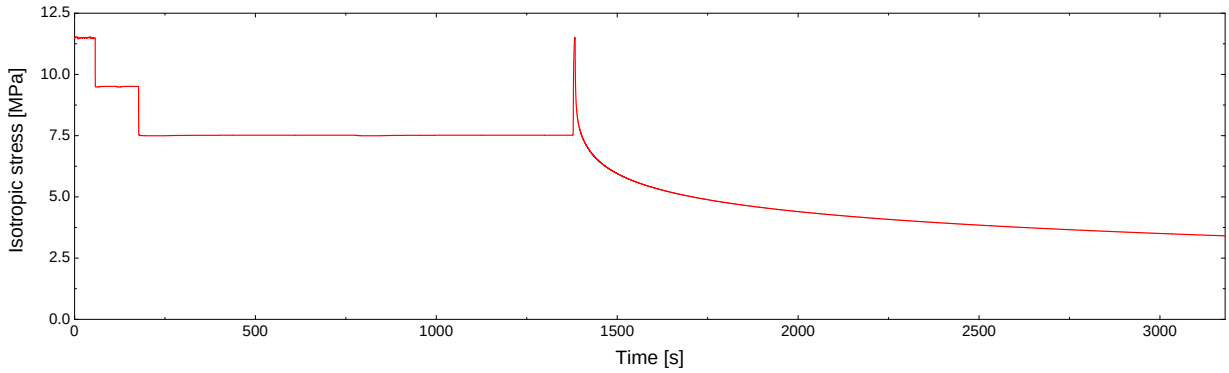

(c)

Fig. 6.6: Results of the LCF test and simulation using the modified Steck's model for the ageing condition S_{IV} at 225°C referring to: (a) experimental and predicted stress σ; (b) kinematic stress σ^{kin}; (c) isotropic stress σ^{iso}.

s^{-1}. Although being also observed for the hardening grade S_{I}, it becomes more evident for the ageing condition S_{IV}, despite being subjected to a lower strain amplitude. This is likely the result of the coarsening of the precipitation distribution producing, to a certain extent, a strain

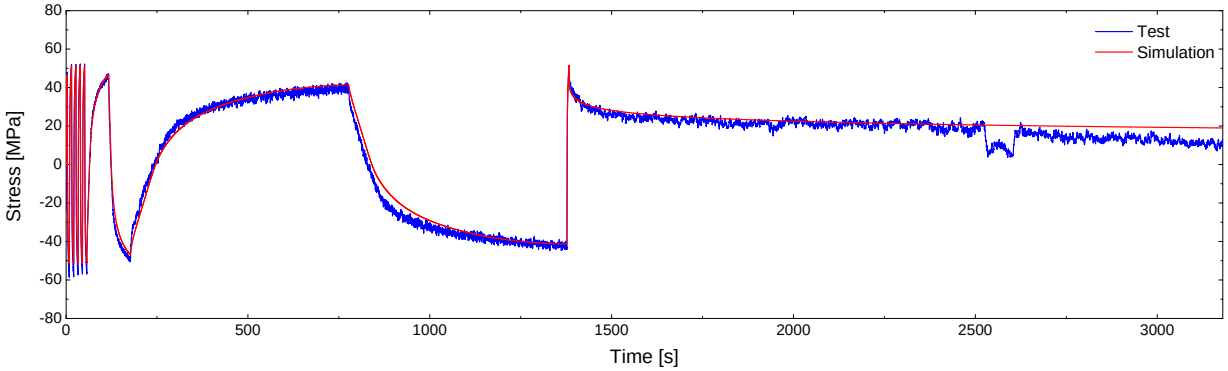

(a)

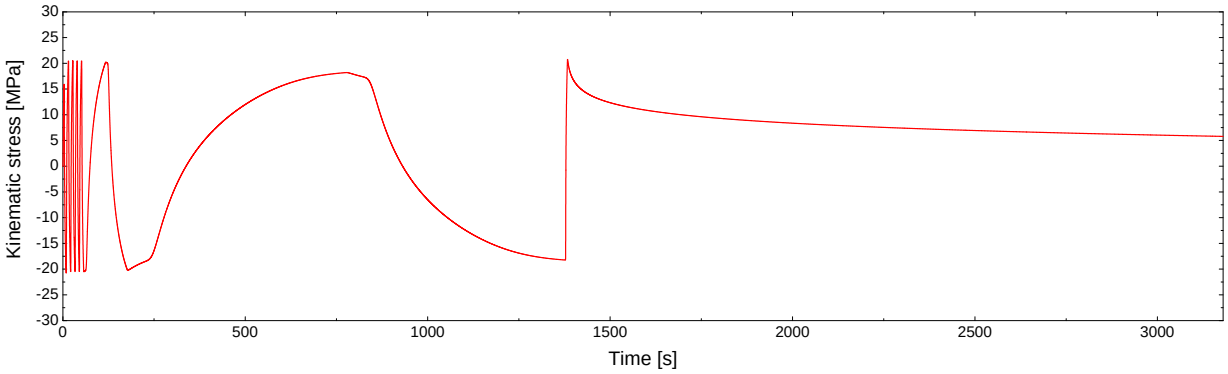

(b)

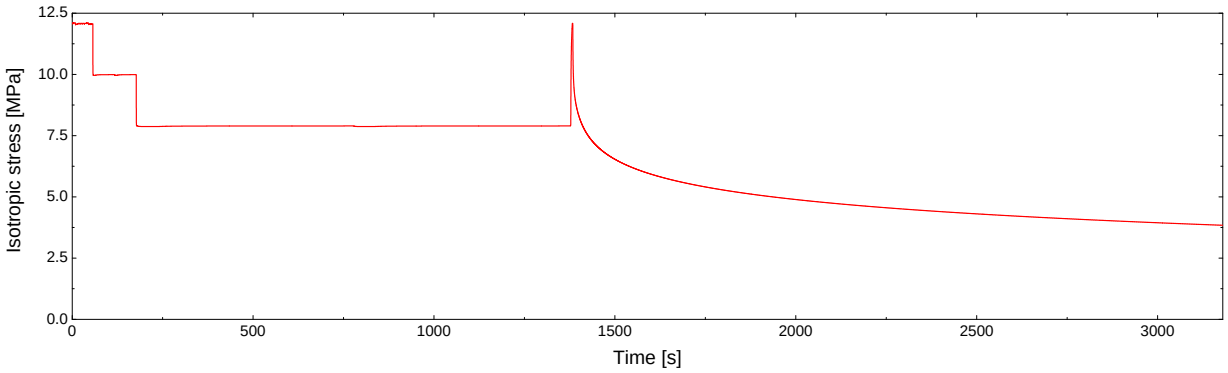

(c)

Fig. 6.7: Results of the LCF test and simulation using the modified Steck's model for the ageing condition S_{IV} at 250°C referring to: (a) experimental and predicted stress σ; (b) kinematic stress σ^{kin}; (c) isotropic stress σ^{iso}.

localization and concentration in the coarse precipitates vicinity, similarly to the way in which localized deformation produced by persistent slip bands or sheared particles also results in this effect [177].

Comparing the simulation results of kinematic stress σ^{kin} obtained for both ageing conditions, this hardening component exhibits a different behavior, in which the "anelastic recovery" effect is barely seen, mainly as a result of the lower strain amplitude used due to the lower strengthening grade of this ageing condition. However, the results for the isotropic stress σ^{iso} are very similar for both hardening grades. Attending to the relationship existing between this hardening rule and the short–range obstacles present in the material, mainly the Mg_2Si precipitates in this alloy, and given that only different hardening grades within the T7 ageing condition of the alloy have been considered here, it is to a certain extent foreseeable that the evolution of isotropic stress for different T7 ageing conditions of this alloy is the same.

Chapter 7

Coupling of precipitation and mechanical models

The coupling of precipitation models and complex constitutive material models is seldom found. This field is usually limited to simple precipitation models concerning the essential features of ageing coupled to the prediction of typical mechanical properties like hardness or yield strength like the model of Shercliff & Ashby [5,6]. These models are typically used to assess the hardening grade of these precipitation strengthened materials. However, these approaches do not consider the ageing process itself as being responsible for the formation of the strengthening distributions, i.e. the precipitation kinetics is implicitly included in the empirical models. For the same purpose, more sophisticated models consider the contribution of the precipitation distribution, among others, to the total strengthening of the material by taking into account the influence of temperature and duration of the ageing process on it [11–13].

This chapter addresses the coupling of the Robson's numerical model and the Steck's material model, given the relationships presented in Sect. 5.3 between some mechanical properties of the alloy and the Mg_2Si precipitation distribution. The physical foundations of Steck's model will facilitate this work. The information condensed from the strengthening distribution is expressed as the interprecipitate spacing λ, once demonstrated its feasibility for the T7 ageing condition of the alloy in Sect. 5.3.

The chapter begins by determining in Sect. 7.1 the dependencies of those Steck's model parameters changing with the hardening grade of the alloy. A more comprehensive analysis is done for the parameter δ_2 to eliminate its dependency on the temperature. The simulation results obtained for an intermediate hardening grade between those presented in Sect. 6.2 are presented in Sect. 7.2 and used as validation of these relationships.

7.1 Dependencies of Steck's model parameters

The physical foundations of Steck's model provide a solid basis to determine the relationship between those parameters dependent on the ageing condition of the alloy and the underlying Mg_2Si strengthening distribution. From the model parameters presented in Table 6.2 for the four ageing conditions, C, Θ, α_1, α_2, and r_2 are the five parameters that change with the alloy ageing condition. As mentioned above, the parameter δ_2 additionally exhibits a dependency on the temperature, which is the only exception and contrary to the supposed temperature independence of the parameters. These parameters only concern the expressions for inelastic strain rate $\dot{\epsilon}_{ie}$ and kinematic stress rate $\dot{\sigma}^{kin}$ (recovery term $\dot{R}^{kin}$).

The Mg_2Si precipitation distributions for the these four ageing conditions presented in Sect. 6.1.3 show an increasing mean particle size accompanied by a decreasing precipitates density as the overageing condition is more pronounced. This produces a larger spacing λ of precipitates. The five parameters C, Θ, α_1, α_2 are plotted against this interprecipitate spacing λ in Fig. 7.1.

All the five parameters exhibit a monotonic relationship with the interprecipitate spacing λ. For this reason, simple functions are fitted for each model parameter by using a least–squares procedure to obtain an empirical relationship for each one with the interprecipitate spacing. The resulting phenomenological functions with the interprecipitate spacing λ expressed in nanometers are:

$$C(\lambda) = \exp\left(-3.09 \cdot 10^{-4} \cdot \lambda^2 + 2.24 \cdot 10^{-1} \cdot \lambda - 22.10\right) \quad \left[\mathrm{s}^{-1}\right]. \tag{7.1}$$

$$\Theta(\lambda) = -2.73 \cdot 10^{-1} \cdot \lambda + 343.47 \quad [-]. \tag{7.2}$$

$$\alpha_1(\lambda) = 1.08 + 0.24 \cdot \exp\left(-1.31 \cdot 10^{-2} \cdot \lambda\right) \quad [-]. \tag{7.3}$$

$$\alpha_2(\lambda) = 8.31 \cdot 10^{-4} \cdot \lambda + 0.37 \quad [-]. \tag{7.4}$$

$$r_2(\lambda) = \exp\left(-1.19 \cdot 10^{-4} \cdot \lambda^2 + 8.71 \cdot 10^{-2} \cdot \lambda + 11.26\right) \quad \left[\mathrm{Nm}^{-2}\mathrm{s}^{-1}\right]. \tag{7.5}$$

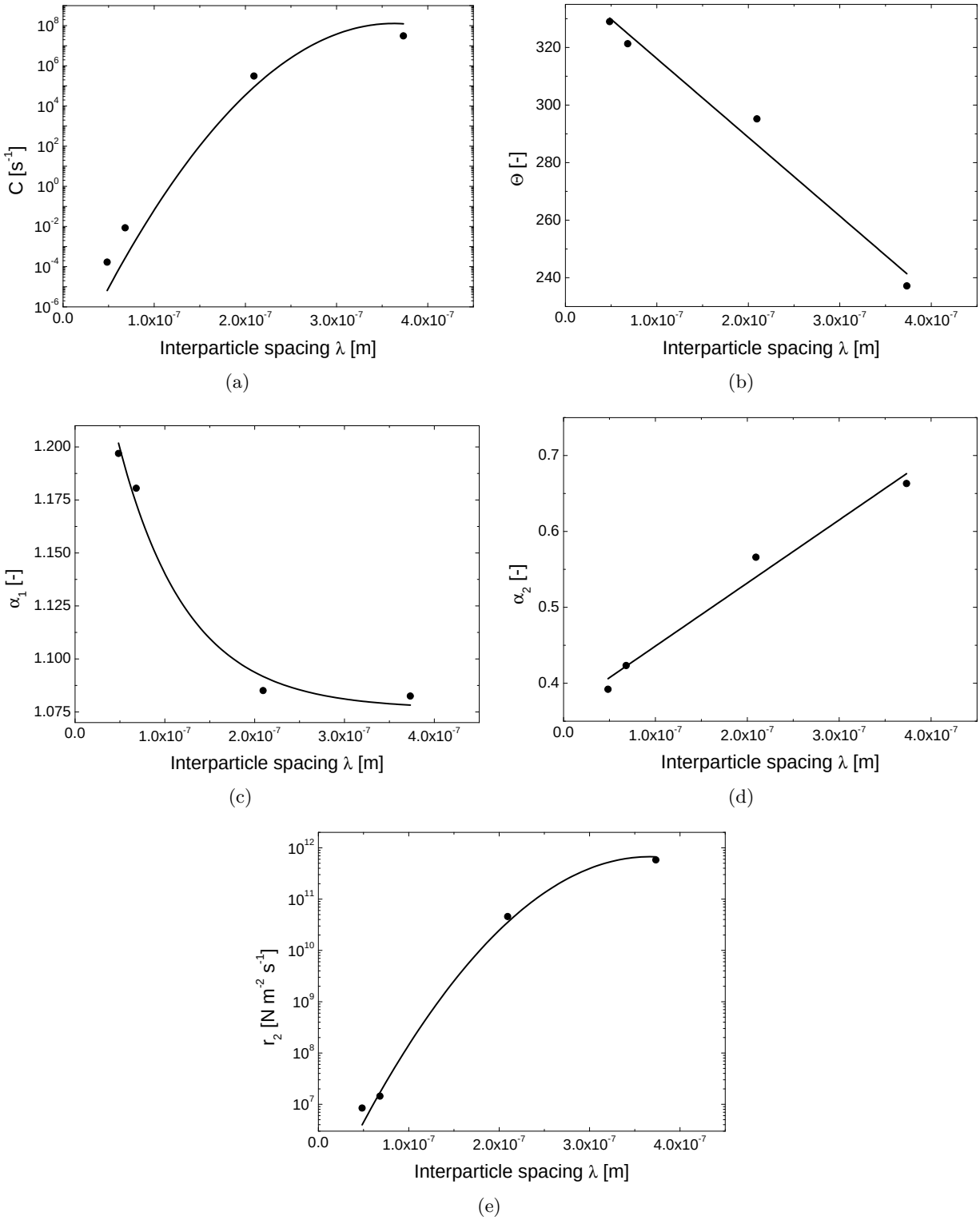

Fig. 7.1: Steck's model parameters depending on the alloy ageing condition expressed in terms of inter-precipitate spacing λ and the corresponding fitting functions: (a) C; (c) α_1; (b) Θ; (e) r_2; (d) α_2

7.1.1 Model parameter δ_2

The model parameter δ_2 concerning the kinematic hardening rate $\dot{H}^{kin}$ is *ex–professo* not included in Table 6.2 because it exhibits a double dependency on the ageing condition of the alloy and the temperature of the test, contravening the assumed temperature independence of the model parameters. The values of δ_2 for the different ageing conditions and temperatures considered are given in Table 7.1.

Temperature	Ageing conditions				Units
	S_{I}	S_{II}	S_{III}	S_{IV}	
200°C	10.0	11.1	16.6	23.0	–
225°C	13.0	14.5	–	34.0	–
250°C	–	20.0	32.0	46.5	–
280°C	–	–	39.7	–	–

Table 7.1: Values of parameter δ_2 used in the implementation of Steck's model for the modeling of the kinematic hardening.

This parameter becomes larger for higher temperatures and more pronounced overageing conditions. The accuracy of this parameter is especially important during the cyclic loading stages, in which the plastic behavior of the alloy is mainly governed by the hardening component of the kinematic stress σ^{kin} as demonstrated in Sect. 6.1. Under these loading conditions, the viscoplastic behavior of the alloy is thus strongly linked to the value of δ_2, considering the temperature independence of the parameter K_1 in the reduced version of the model. As an example, Fig. 7.2 shows the good agreement obtained in the first cycles performed at $1 \cdot 10^{-3}$ s^{-1} for the ageing conditions S_{I} and S_{IV} at 200°C and 225°C, except at the compression peaks in the state S_{IV} due to the asymmetry found in the experimental response of the alloy.

The good agreement obtained indicates that the Steck's model cannot describe the cyclic behavior of the alloy by using a unique set of parameters for each ageing condition. This parameter is plotted in Fig. 7.3(a) against the interprecipitate spacing λ for each ageing condition while the effect of temperature on the parameter is presented in Fig. 7.3(b). It shows a linear dependence with respect to the alloy ageing condition for each temperature, and besides, it is also directly proportional to the temperature of the test for each hardening grade. The dependence of this model parameter on the interprecipitate spacing λ for each temperature can be easily formulated based on a linear fitting function of the form:

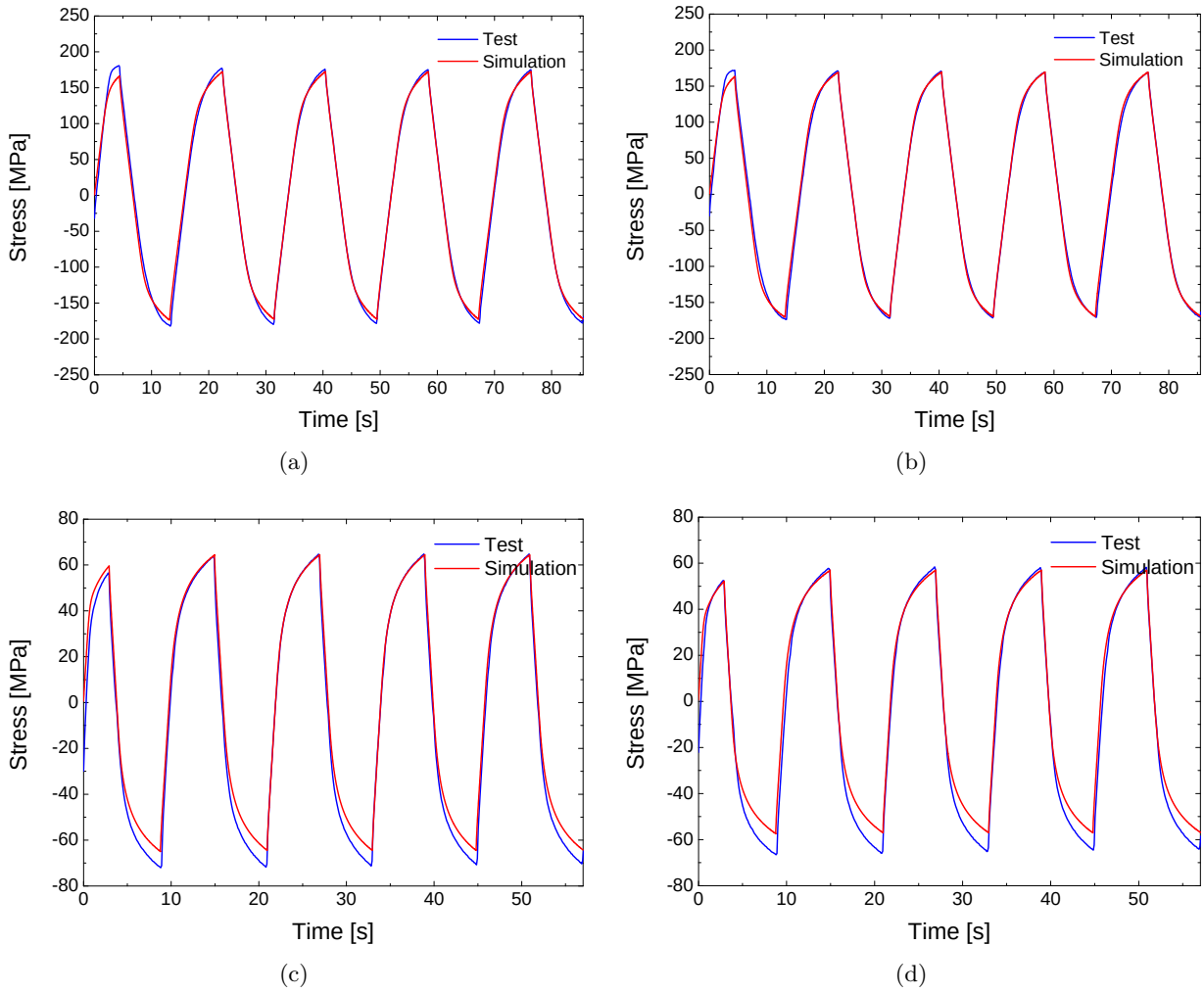

Fig. 7.2: Results of the first LCF cycles $\left(\dot{\epsilon} = 1 \cdot 10^{-3}\ \mathrm{s}^{-1}\right)$ and simulations referring to: (a) ageing condition S_{I} at 200°C; (b) ageing condition S_{I} at 225°C; (c) ageing condition S_{IV} at 200°C; (d) ageing condition S_{IV} at 225°C.

$$\delta_2\left(\lambda\right) = m \cdot \lambda + n\ , \tag{7.6}$$

where λ is the interprecipitate spacing in nanometers and m and n are the slope and the ordinate at the origin of the linear function. The m and n parameters resulting from the linear regression of δ_2 on the interprecipitate spacing λ using the least–squares procedure are given in Table 7.2.

Both parameters m and n resulting from the linear fitting exhibit in turn a temperature dependence which are also determined using a linear regression:

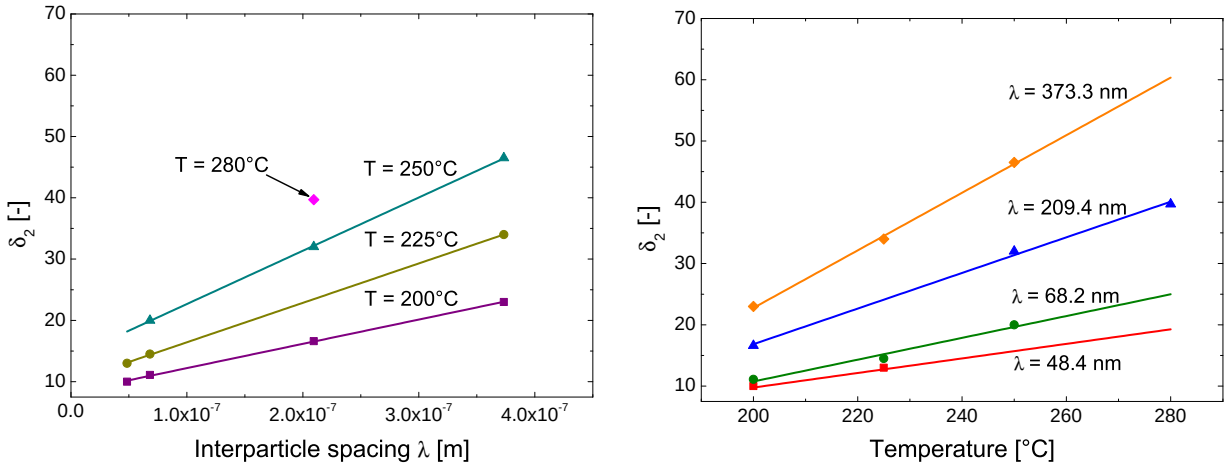

(a) (b)

Fig. 7.3: Dependence of parameter δ_2 on: (a) the interprecipitate spacing λ (ageing condition); (b) the temperature of the tests.

T	m	n
°C	nm^{-1}	–
200	0.040	8.25
225	0.064	10.00
250	0.087	13.98

Table 7.2: Results of slope m and ordinate at the origin n obtained from the linear regression for δ_2 on the interprecipitate spacing λ at 200°C, 225°C, and 250°C.

$$m\,(T) = 9.46 \cdot 10^{-4} \cdot T - 0.15 \quad \left[\mathrm{nm}^{-1}\right]. \tag{7.7}$$

$$n\,(T) = 0.11 \cdot T - 15.04 \qquad [–]\,, \tag{7.8}$$

being T the temperature in degrees Celsius.

Thus, δ_2 can be expressed as a function of temperature T and the ageing condition determined from the interprecipitate spacing λ by substituting Eqs. (7.7), and (7.8) into Eq. (7.6) as:

$$\delta_2\,(T, \lambda) = -15.04 - 0.15 \cdot \lambda + \left(0.11 + 9.46 \cdot 10^{-4} \cdot \lambda\right) \cdot T \qquad [–]\,, \tag{7.9}$$

where λ is the interprecipitate spacing in nanometers and T is the temperature in degrees

Celsius. By extending this expression to a general two–phase alloy system, δ_2 can be rewritten by introducing two new model parameters $\delta_2^{'}(\lambda)$ and $\delta_2^{''}(\lambda)$ dependent only on the ageing condition of the material as follows:

$$\delta_2(T,\lambda) = \delta_2^{'}(\lambda) + \delta_2^{''}(\lambda) \cdot T \ . \tag{7.10}$$

The temperature dependence of parameter δ_2 is now explicitly incorporated in Eq. (7.10). The mechanical modeling of other age–hardenable alloys would be very useful for the validation of this new proposed definition of δ_2. Furthermore, this should be accompanied by a thorough review of the model foundations.

7.1.2 Summary of enhanced Steck's model

An enhanced version of the Steck's constitutive model for the modeling of the mechanical behavior of the $AlSi_{10}Mg(Cu)$ alloy is proposed in this work:

$$\dot{\sigma} = E \cdot \dot{\epsilon}_e = E \cdot (\dot{\epsilon} - \dot{\epsilon}_{ie}) \ . \tag{7.11}$$

$$\begin{aligned} \dot{\sigma}^{iso} = {} & h_1 \cdot \exp\left(-(\delta_1 - 1) \cdot \frac{\Delta V \sigma^{iso}}{R\,T}\right) \cdot |\dot{\epsilon}_{ie}| \\ & - r_1 \cdot \exp\left(-\frac{\gamma_1 U_0}{R\,T}\right) \cdot \sinh\left(\frac{\beta_1 \Delta V \cdot \left(\sigma^{iso} - \sigma_{eq}^{iso}\right)}{R\,T}\right) \ . \end{aligned} \tag{7.12}$$

$$\begin{aligned} \dot{\sigma}^{kin} = {} & h_2 \cdot \exp\left(\frac{\Delta V \sigma^{iso}}{R\,T}\right) \cdot \exp\left(-\frac{\delta_2(T,\lambda)\ \Delta V \sigma^{kin} \cdot \mathrm{sign}\left(\sigma^{eff}\right)}{R\,T}\right) \cdot \dot{\epsilon}_{ie} \\ & - r_2(\lambda) \cdot \exp\left(-\frac{\alpha_2(\lambda)\, U_0}{R\,T}\right) \cdot \sinh\left(\frac{\beta_2\ \Delta V \sigma^{kin}}{R\,T}\right) \ . \end{aligned} \tag{7.13}$$

$$\begin{aligned} \dot{\epsilon}_{ie} = {} & C(\lambda) \cdot \exp\left(-\left(1 - \frac{\alpha_1(\lambda) - 1}{\kappa}\right) \cdot \frac{U_0}{R\,T}\right) \cdot \exp\left(-\Theta(\lambda)\,\frac{\Delta V \sigma^{iso}}{R\,T}\right) \\ & \cdot \left(\sinh\left(\frac{\Delta V \left|\sigma - \sigma^{kin}\right|}{R\,T}\right)\right)^{1+\frac{1}{\kappa}} \cdot \mathrm{sign}\left(\sigma^{eff}\right) \ . \end{aligned} \tag{7.14}$$

This new version of the model concerns a unique set of parameters (new definition of δ_2) and incorporates the effect of the alloy ageing condition (new expressions for parameters C, Θ, α_1, α_2, and r_2). The parameter δ_2 in Eq. (7.13) is defined as:

$$\delta_2(T,\lambda) = \delta_2^{'}(\lambda) + \delta_2^{''}(\lambda) \cdot T \ . \tag{7.15}$$

7.2 Ageing condition $S_{\text{II-III}}$

An additional hardening grade $S_{\text{II-III}}$ between the ageing conditions S_{II} and S_{III} is used in this section for the validation of the empirical relationships proposed above. The Brinell hardness of this ageing condition is $\text{HB}_{S_{\text{II-III}}}$=70. For obtaining it, the LCF samples are heat treated at 300°C for 110 minutes. The resulting Mg_2Si precipitation distribution is characterized by a mean particle radius of R_0=7.06 nm and the corresponding precipitate density is n_0=$2.45 \cdot 10^{21}$ m^{-3} (λ=92.0 nm). In this case, the test is performed at 225°C by using a strain amplitude of 0.45 %.

The model parameters for this ageing condition obtained from the empirical relationships ("Calculated") and that used for the simulation of the LCF test ("Fitted") are presented in Table 7.3. The discrepancy between both parameters sets is within reasonable limits given their own range of variation and the lack of more experimental results for a more precise model fitting.

Parameter	Calculated	Fitted	Units
C	$1.65 \cdot 10^{-2}$	$1.48 \cdot 10^{-1}$	1/s
Θ	318.3	308.1	–
α_1	1.152	1.183	–
α_2	0.446	0.4233	–
r_2	$8.57 \cdot 10^{7}$	$2.44 \cdot 10^{7}$	$\text{N}/(\text{m}^2 \cdot \text{ s})$
δ_2	15.5	16.2	–

Table 7.3: Model parameters for the ageing condition $S_{\text{II-III}}$ calculated using the empirical relationships given in Sect. 7.1 (δ_2 is computed at 225°C) and fitted to the LCF experimental results.

The experimental and simulation results for this hardening grade are shown in Fig. 7.4(a). The good results obtained for this intermediate ageing state confirm the model modifications, as well as the fitting approaches used for the parameters C, Θ, α_1, α_2, r_2, and δ_2 and their monotonic nature. Additionally, the temperature dependence of δ_2 is also demonstrated. Furthermore, these

relationships also confirm the validity of the interprecipitate spacing λ as indicator of the alloy hardening grade within its overageing condition.

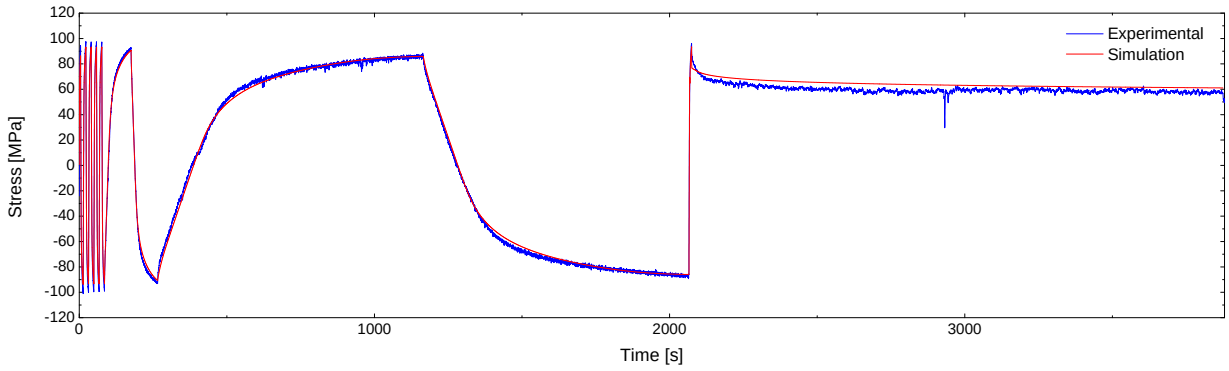

(a)

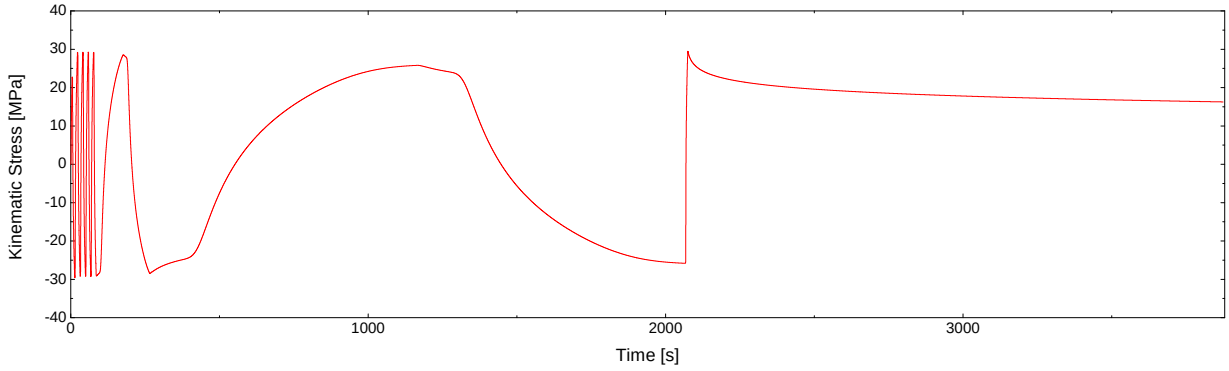

(b)

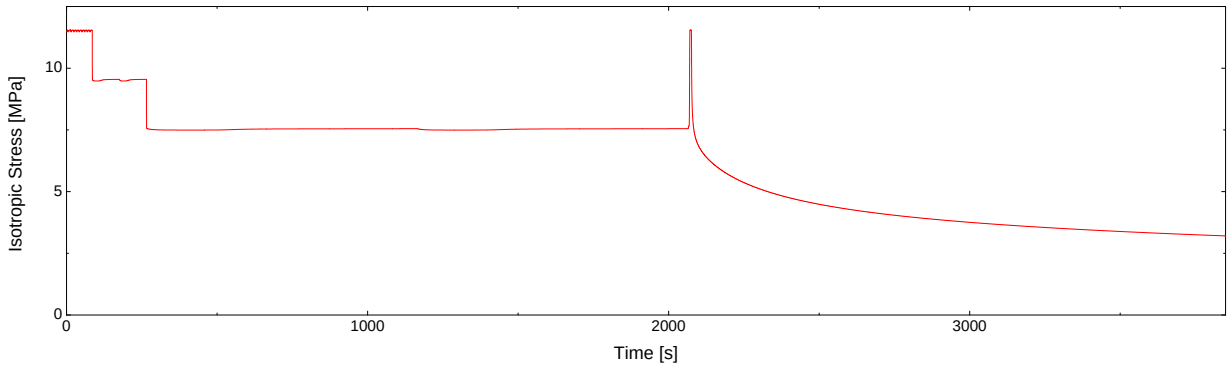

(c)

Fig. 7.4: Results of the LCF test and simulation using the modified Steck's model including the overageing condition dependence of the parameters for the ageing condition $S_{\text{II-III}}$ at 225°C referring to: (a) experimental and predicted stress σ; (b) kinematic stress σ^{kin}; (c) isotropic stress σ^{iso}.

Chapter 8

Conclusions

The main objective of this work is to characterize and predict the influence of the artificial ageing treatment on the precipitation process and the mechanical behavior of the $AlSi_{10}Mg(Cu)$ cast alloy, focusing on the ageing conditions ranging from the T6 peak aged condition to the T7 overaged state.

Therefore, the work starts with a comprehensive analysis of the precipitation kinetics of the alloy during the ageing process. The precipitation distribution consisting of the Mg_2Si hardening phase formed during the ageing process is the only microstructure compound that significantly changes with the alloy ageing condition. Besides, this is the only hardening phase in this alloy, despite the copper content in its chemical composition that could induce the precipitation of other particles. SANS and TEM (HTEM) techniques are successfully used to characterize this precipitation distribution, providing good results with meaningful statistics. Four different ageing temperatures and varying ageing times are considered for this analysis providing additionally a complete experimental base of the precipitation process. From the results obtained, the effect of higher ageing temperatures accelerates the precipitation kinetics producing coarser size distributions of Mg_2Si strengthening precipitates with a lower density.

The Robson's numerical model is used in this work for modeling the precipitation process in the alloy. The model is successfully calibrated to the measured particle radii and density distributions obtained for the Mg_2Si strengthening distributions. The interfacial energy parameter σ and the diffusivity constant D_0 are the only two parameters fitted in the model. The model shows a high sensitivity to σ and D_0. The obtained value for D_0 is similar to experimental values reported in the literature. By approximating the interfacial energy σ as a sigmoidal function of the precipitate size, the model can correctly predict the precipitation distributions for the whole temperature range with only one set of parameters.

The adapted model correctly predicts the precipitation distribution for an additional validation

case under investigation. As major outcome, the modified model can predict the precipitation distribution for a wide range of ageing temperatures and arbitrary variations of the ageing process starting from a T6 condition. These features make the model very useful for designing and optimizing complex non–isothermal artificial ageing processes, which are relevant for industrial applications as in the case of cylinder heads.

In a second step, the effect of the predicted Mg_2Si strengthening precipitates distribution on the mechanical properties of the alloy in a T6–T7 heat–treated condition is analyzed. The purpose is to demonstrate that the knowledge about the shape of the precipitation distribution is sufficient to predict the mechanical properties of such an alloy. The mechanical properties under study are at different levels of complexity: (i) hardness, (ii) tensile properties such as yield strength $R_{p,0.2\%}$ and ultimate tensile strength R_m, and (iii) effects of nonlinear isotropic and kinematic hardening, rate sensitivity, and static recovery which are determined from LCF experiments.

From the results of this analysis, the hardness at room temperature can be predicted based on the interprecipitate spacing λ calculated from the predicted precipitation distributions using the Wigner–Seitz approximation. Furthermore, a logarithmic relationship between the hardness and the interprecipitate spacing is found. Thus, larger interprecipitate spacings lead to lower hardness values and hardening grades in the alloy, which is characteristic of more pronounced overaged conditions.

Similarly, the yield strength $R_{p,0.2\%}$ and ultimate tensile strength R_m obtained from the tension tests carried out at room temperature are also uniquely determined by the strengthening distribution of Mg_2Si precipitates. Both strengths are also logarithmically dependent on the interprecipitate spacing λ throughout the entire overageing stage. However, an extension to the whole ageing process also including the first precipitation stages is not straight forward. For such predictions, the analysis of the complete size distribution is required.

Finally, the mechanical response to the LCF tests at elevated temperatures reveals that the previous conclusions can also be drawn for the relevant phenomena which determine the constitutive behavior of the material. As a "proof of concept", one test is performed at 250°C for producing an *in–situ* ageing during the test, and subsequently, altering the alloy mechanical properties. The effect produced by the high temperature used is clearly predicted by the change in the precipitation distribution and reflected in the experimental alloy mechanical response. Furthermore and likely due to the overaged condition of all the specimens, only different strength levels (σ_2) and relaxation behavior (σ^*_{relax}) are noticeable for each hardening grade. However, there is no cyclic work hardening (σ^*_{cyclic}) and strain rate sensitivity (σ^*_{rate}). Additionally, an asymmetry in the tension/compression peak stresses is observed and becomes more significant as the overageing condition is more pronounced.

In addition, the creep test results analyzed by applying the modified Norton equation indicate that the dominant deformation mechanism at elevated temperatures is the climbing of dislocations over the Mg_2Si precipitates, according to the overaged condition of the alloy. Besides, the start of the high temperature regime of the alloy is established at 200°C.

All this information supports and is used, in a third step, for modeling the mechanical behavior of the alloy at elevated temperatures by using the Steck's constitutive model. The calibration of the model is accomplished by using the mechanical response obtained for four different hardening grades within the overaged condition of the alloy to the same LCF loading history as that previously used. The different processes incorporated in this loading history make it particularly suitable for calibrating this more complex model, following a Trial–and–Error calibration procedure. By introducing a new parameter in the isotropic stress rate expression, called the equilibrium isotropic stress σ_0^{iso}, the model can successfully predict the response of the alloy to combined cyclic and relaxation loading conditions. However, this can only be accomplished by fitting the parameter δ_2 for each temperature and ageing condition, contravening the assumed temperature independence of the model parameters.

From the sets of parameters obtained for the four hardening grades, C, Θ, α_1, α_2, and r_2, besides δ_2, are the six parameters changing with the alloy ageing condition. For the first five parameters, some empirical one–to–one relationships are established for predicting the effect of the alloy ageing condition (through the interprecipitate spacing λ) on them. In case of δ_2, the temperature dependence of the parameter is found out and fixed by redefining it (new parameters $\delta_2^{'}(\lambda)$ and $\delta_2^{''}(\lambda)$). Surprisingly, none of these parameters are directly involved in the isotropic stress rate expression. Thus, the model can now correctly predict the mechanical response of the overaged condition of the alloy to combined cyclic and relaxation loading conditions by using a unique set of model parameters, and besides, considering its overaged condition. As model validation, this enhanced version of the model predicts correctly the mechanical response to the LCF loading history for an additional overaged condition.

As major outcome of this work, a scale bridging approach from the simulation of the Mg_2Si precipitation distribution resulting from the artificial ageing process to the simulation of the macroscopic constitutive behavior of the overaged condition of the $AlSi_{10}Mg(Cu)$ cast alloy predicting its nonlinear work hardening behavior and its time dependent behavior is established. This approach between both fields permits to predict the distribution of mechanical properties in heat–treated complex components, like cylinder heads. Furthermore, the effect of further ageing on the component during service as a result of the high operating temperatures on the mechanical behavior of the material can also be predicted. In this sense, the characterization and modeling of the Mg_2Si strengthening distribution is perceived as the key for the further development of the

work and the subsequent modeling of the mechanical behavior of the material under complex and real–life conditions. Thus, this work is especially useful for its industrial application for designing the heat treatment process to which complex components made of age–hardenable alloy are typically subjected and also for predicting the evolution of their mechanical performance during their service life.

Bibliography

[1] J. Thomas, L. Verger, A. Bignonnet, and E. Charkaluk, "Thermomechanical design in the automotive industry," *Fatigue & Fracture of Engineering Materials & Structures*, vol. 27, no. 10, pp. 887–895, 2003.

[2] P. Rometsch and G. Schaffer, "An age hardening model for Al-7Si-Mg casting alloys," *Materials Science & Engineering A*, vol. 325, pp. 424–434, 2002.

[3] B. Barlas, D. Ovono–Ovono, I. Guillot, and G. Cailletaud, "Ageing and fatigue behavior in cast aluminium alloys," *Materials Science Forum*, vol. 396-402, pp. 1365–1370, 2002.

[4] K. Moizumi, K. Mine, H. Tezuka, and T. Sato, "Influence of Precipitate Microstructures on Thermal Fatigue Properties of Al–Si–Mg cast alloys," *Materials Science Forum*, vol. 396-402, pp. 1371–1376, 2002.

[5] H. Shercliff and M. Ashby, "A process model for age hardening of aluminium alloys - I. The model," *Acta Metallurgica Materialia*, vol. 38, no. 10, pp. 1789–1802, 1990.

[6] H. Shercliff and M. Ashby, "A process model for age hardening of aluminium alloys - II. Applications of the model," *Acta Metallurgica Materialia*, vol. 38, no. 10, pp. 1803–1812, 1990.

[7] H. Kuhn, "Volume 2: Properties and Selection. Nonferrous Alloys and Special–Purpose Materials," in *ASM Handbook* (H. Kuhn and D. Medlin, eds.), ASM International, 2000.

[8] C.-A. Gandin, Y. Bréchet, M. Rappaz, G. Canova, M. Ashby, and H. Shercliff, "Modelling of solidification and heat treatment for the prediction of yield stress of cast alloys," *Acta Materialia*, vol. 50, no. 5, pp. 901–927, 2002.

[9] M. Tiryakioğlu and N. Alexopoulos, "The Effect of Artificial Aging on Tensile Work Hardening Characteristics of a Cast Al–7 Pct. Si–0,55 Pct. Mg (A357) Alloy," *Metallurgical and Materials Transactions A*, vol. 39, no. 11, pp. 2772–2780, 2008.

[10] G. Mrówka-Nowotnik and J. Sieniawski, "Influence of heat treatment on the microstructure and mechanical properties of 6005 and 6082 aluminium alloys," *Journal of Materials Processing Technology*, vol. 162-163, pp. 367–372, 2005.

[11] O. Myhr, O. Grong, H. Fjær, and C. Marioara, "Modelling of the microstructure and strength evolution in Al–Mg–Si alloys during multistage thermal processing," *Acta Materialia*, vol. 52, pp. 4997–5008, 2004.

[12] A. Falahati, P. Lang, M. Ahmadi, P. Warczok, E. Povoden–Karadeniz, and E. Kozeschnik, "Computer Simulationen der Ausscheidungs–Mikrostruktur– und Festigkeitsentwicklung von Al–Mg–Si Legierungen in mehrstufigen Wärmebehandlungen," in *Proceedings 6. Ranshofener Leichtmetalltage*, pp. 61–75, 2010.

[13] R. Song, G. Dhatt, and A. Cheikh, "Thermomechanical Finite Element Model of Casting Processes," *Metallurgical and Materials Transactions B*, vol. 27B, pp. 81–99, 1996.

[14] J. Pedersen, "Determination of size distribution from small–angle scattering data for systems with effective hard–sphere interactions," *Journal of Applied Crystallography*, vol. 27, pp. 595–608, 1994.

[15] M. Moustafa, F. Samuel, and H. Doty, "Effect of solution heat treatment and additives on the microstructure of Al–Si (A413.1) automotive alloys," *Journal of Materials Science*, vol. 38, pp. 4507–4522, 2003.

[16] A. Kliauga, E. Vieira, and M. Ferrante, "The influence of impurity level and tin addition on the ageing heat treatment of the 356 class alloy," *Materials Science & Engineering A*, vol. 480, pp. 5–16, 2008.

[17] R. Schiffmann, J. Haug, and J. Banhart, "Evolution of Precipitates during Age–Hardening of AW 6016 Alloy," in *9th International Conference on Aluminium Alloys*, 2004.

[18] G. Albertini, G. Caglioti, F. Fiori, and R. Pastorelli, "SANS investigation of precipitation in heat–treated AA6082 alloy," *Physica B*, vol. 276-278, pp. 921–922, 2000.

[19] X. Larráyoz Izcara, A. Guirao Blank, F. Pyczak, P. Staron, S. Schumann, and N. Huber, "Characterization and modeling of the influence of artificial ageing on the microstructural evolution of age–hardenable $AlSi_{10}Mg(Cu)$ aluminium alloys," *Materials Science & Engineering A*, vol. 610, pp. 46–53, 2014.

[20] S. Abis, A. Boeuf, R. Caciuffo, R. Fiorini, M. Magnani, S. Melone, F. Rustichelli, and M. Stefanon, "Investigation of Mg_2Si precipitation in an Al–Mg–Si alloy by small angle neutron scattering," *Journal of Nuclear Materials*, vol. 135, pp. 181–189, 1985.

[21] S. Abis, R. Caciuffo, R. Coppola, M. Magnani, F. Rustichelli, and M. Stefanon, "Small angle neutron scattering investigation of the ageing process in Al–Mg–Si alloy," *Physica B*, vol. 136, pp. 469–472, 1986.

[22] J. Robson and P. Prangnell, "Modelling Al_3Zr dispersoid precipitation in multicomponent aluminium alloys," *Materials Science & Engineering A*, vol. 352, pp. 240–250, 2003.

[23] A. Deschamps, D. Solas, and Y. Bréchet, "Modeling of Microstructure Evolution and Mechanical Properties in Age–Hardening Aluminium Alloys," in *Microstructures, Mechanical Properties and Processes – Computer Simulation and Modelling EUROMAT*, vol. 3, pp. 121–133, 1999.

[24] G. Dieter, *Mechanical Metallurgy.* 3, McGraw–Hill International Editions, 1986.

[25] D. Porter and K. Easterling, *Phase Transformations in Metals Alloys.* Chapman & Hall, 2 ed., 1993.

[26] G. Edwards, K. Stiller, G. Dunlop, and M. Couper, "The precipitation sequence in Al–Mg–Si alloys," *Acta Materialia*, vol. 46, no. 11, pp. 3893–3904, 1998.

[27] A. Gupta, D. Lloyd, and S. Court, "Precipitation hardening in Al–Mg–Si alloys with and without excess Si," *Materials Science & Engineering A*, vol. 316, pp. 11–17, 2001.

[28] G. Timelli, O. Lohne, L. Arnberg, and H. Laukli, "Effect of Solution Heat Treatments on the Microstructure and Mechanical Properties of a Die–Cast AlSi7MgMn Alloy," *Metallurgical and Materials Transactions A*, vol. 39, pp. 1747–1758, 2008.

[29] H. Hanemann and A. Schrader, "Ternäre Legierungen des Aluminiums - Beispiele für die Kristallisation Ternärer Systeme (Band III, Teil 2)," in *Atlas Metallographicus*, Verlag Stahl und Eisen, 1952.

[30] G. Ran, J. Zhou, and Q. Wang, "Precipitates and tensile fracture mechanism in a sand cast A356 aluminum alloy," *Journal of Materials Processing Technology*, vol. 207, pp. 46–52, 2008.

[31] C. Cáceres, C. Davidson, and J. Griffiths, "The deformation and fracture behaviour of an Al–Si–Mg casting alloy," *Materials Science & Engineering A*, vol. 197, pp. 171–179, 1995.

[32] D. Zhang, L. Zheng, and D. StJohn, "Effect of a short solution treatment time on microstructure and mechanical properties of modified Al–7wt.%Si–0.3wt.%Mg alloy," *Journal of Light Metals*, vol. 2, no. 1, pp. 27–36, 2002.

[33] L. Pedersen and L. Arnberg, "The effect of solution heat treatment and quenching rates on mechanical properties and microstructures in AlSiMg foundry alloys," *Metallurgical and Materials Transactions A*, vol. 32, no. 3, pp. 525–532, 2001.

[34] P. Rometsch, L. Arnberg, and D. Zhang, "Modelling Dissolution of Mg_2Si and Homogenisation in Al–Si–Mg Casting Alloys," *International Journal of Cast Metals Research*, vol. 12, pp. 1–8, 1999.

[35] W. Callister, *Materials Science and Engineering. An Introduction.* John Wiley & Sons, 7 ed., 2007.

[36] P. Li, D. Maijer, T. Lindley, and P. Lee, "Simulating the Residual Stress in an A356 Automotive Wheel ans Its Impact on Fatigue Life," *Metallurgical and Materials Transactions B*, vol. 38B, no. 4, pp. 505–515, 2007.

[37] C. Estey, S. Cockcroft, D. Maijer, and C. Hermesmann, "Constitutive behaviour of A356 during the quenching operation," *Materials Science and Engineering A*, vol. 383, pp. 245–251, 2004.

[38] J. Murken, *Mikrostrukturelle Untersuchungen zum Einfluß von Spannung und plastischer Verformung auf das Wachstum von Ausscheidungen in Al-Legierungen bei erhöhter Temperatur.* PhD thesis, Ruhr–Universität Bochum, 2002.

[39] I. Dutta and S. Allen, "A calorimetric study of precipitation in commercial aluminium alloy 6061," *Journal of Materials Science Letters*, vol. 10, pp. 323–326, 1991.

[40] L. Doan, Y. Ohmori, and K. Nakai, "Precipitation and Dissolution Reactions in a 6061 Aluminium Alloy," *Materials Transactions of the Japan Institute of Metals*, vol. 41, no. 2, pp. 300–305, 2000.

[41] S. Andersen, H. Zandbergen, J. Jansen, C. T. holt, U. Tundal, and O. Reiso, "The crystal structure of the β'' phase in Al–Mg–Si alloys," *Acta Materialia*, vol. 46, no. 9, pp. 3283–3298, 1998.

[42] N. Maruyama, R. Uemori, N. Hashimoto, M. Saga, and M. Kikuchi, "Effect of silicon addition on the composition and structure of fine–scale precipitates in Al–Mg–Si alloys," *Scripta Materialia*, vol. 36, no. 1, pp. 89–93, 1997.

[43] M. Maruyama, K. Hono, W. Miao, and D. Laughlin, "The Effect of Cu Additions on the Precipitation Kinetics in an Al–Mg–Si Alloy with Excess Si," *Metallurgical and Materials Transactions A*, vol. 32A, pp. 239–246, 2001.

[44] R. Cahn, P. Hassen, and E. Kramer, eds., *Phase Transformations in Materials*, vol. 5 of *Materials Science and Technology*. VCH Publishers, 1 ed., 1991.

[45] N. Mott and F. Nabarro, "An attempt to estimate the degree of precipitation hardening, with a simple model," *Proceedings of the Physical Society*, vol. 52, no. 1, p. 86, 1940.

[46] E. Hart, *Relations of Properties to Microstructure*. American Society for Metals, 1953.

[47] H. Mugrabi, ed., *Materials Science and Technology. A Comprehensive Treatment*, vol. 6. New York: VHC Publishers Inc., 1993.

[48] E. Orowan in *Symposium on Internal Stresses in Metals and Alloys*, (London), The Institute of Metals, 1948.

[49] M. Pérez, M. Dumont, and D. Acevedo-Reyes, "Implementation of classical nucleation and growth theories for precipitation," *Acta Materialia*, vol. 56, no. 9, pp. 2119–2132, 2008.

[50] R. Doherty, "Physical Metallurgy," ch. Diffusive Phase Transformations in the Solid State, pp. 1363–1505, New York: North–Holland, 4 ed., 1996.

[51] P. Mirold and K. Binder, "Theory for the initial stages of grain growth and unmixing kinetics of binary alloys," *Acta Metallurgica*, vol. 25, pp. 1435–1444, 1977.

[52] P. Donnadieu and A. Proult, "Cluster–based Models for the Crystal Structure of the Hardening Precipitates of Al–Mg–Si Alloys," *Materials Science Forum*, vol. 217-222, pp. 719–724, 1996.

[53] D. Bratland, O. Grong, H. Shercliff, O. Myhr, and S. T. tta, "Overview No. 124 Modelling of precipitation reactions in industrial processing," *Acta Materialia*, vol. 45, pp. 1–22, 1997.

[54] I. Lifshitz and V. Slyozov, "The Kinetics of Precipitation from Supersaturated Solid Solutions," *Journal of Physics and Chemistry of Solids*, vol. 19, no. 1-2, pp. 35–50, 1961.

[55] C. Wagner, "Theorie der Alterung von Niederschlägen duch Umlösen. (Ostwald-Reifung)," *Zeitschrift für Elektrochemie, Berichte der Bunsengesellschaft für physikalische Chemie*, vol. 65, no. 7–8, pp. 581–591, 1961.

[56] J. Langer and A. Schwartz, "Kinetics of nucleation in near–critical fluids," *Physical Review A*, vol. 21, pp. 948–958, 1980.

[57] R. Kampmann and R. Wagner, "Kinetics of precipitation in metastable binary alloys — theory and application to Cu–1.9 at % Ti and Ni–14 at % Al," in *Decomposition of Alloys: the early stages — Proc. of the 2nd Acta–Scripta Metallurgica Conference* (P. Haasen, V. Gerold, R. Wagner, and M. Ashby, eds.), pp. 91–103, Pergamon Press, 1984.

[58] R. Wagner and R. Kampmann, "Phase Transformations in Materials," in *Materials Science and Technology* (R. Cahn, P. Haasen, and E. Kramer, eds.), vol. 5, ch. Homogeneous Second Phase Precipitation, pp. 213–303, VCH, 1991.

[59] O. Myhr and O. Grong, "Modelling of non–isothermal transformations in alloys containing a particle distribution," *Acta Materialia*, vol. 48, pp. 1605–1615, 2000.

[60] M. Nicolas and A. Deschamps, "Characterisation and modelling of precipitate evolution in an Al–Zn–Mg alloy during non–isothermal heat treatments," *Acta Materialia*, vol. 51, pp. 6077–6094, 2003.

[61] J. Robson, "Modelling the overlap of nucleation, growth and coarsening during precipitation," *Acta Materialia*, vol. 52, pp. 4669–4676, 2004.

[62] J. Robson, "Modelling the evolution of particle size distribution during nucleation, growth and coarsening," *Materials Science and Technology*, vol. 20, pp. 441–448, 2004.

[63] P. Maugis and M. Gouné, "Kinetics of vanadium carbonitride precipitation in steel: A computer model," *Acta Materialia*, vol. 53, no. 12, pp. 3359–3367, 2005.

[64] O. Myhr, O. Grong, and S. Andersen, "Modelling of the Age Hardening Behaviour of Al–Mg–Si Alloys," *Acta Materialia*, vol. 49, pp. 65–75, 2001.

[65] J. Robson, M. Jones, and P. Prangnell, "Extension of the N–model to predict competing homogeneous and heterogeneous precipitation in Al–Sc alloys," *Acta Materialia*, vol. 51, pp. 1453–1469, 2003.

[66] P. Donnadieu, F. Carsughi, A. Redjaïmia, C. Diot, and G. Lapasset, "Nanoscale Hardening Precipitation in AlMgSi Alloys: a Transmission Electron Microscopy and Small–Angle Neutron Scattering Study," *Journal of Applied Crystallography*, vol. 31, pp. 212–222, 1998.

[67] A. Deschamps, "Handbook of Aluminum," vol. 2 – Alloy Production and Materials Manufacturing, ch. Analytical Techniques for Aluminum, pp. 155–192, Marcel Dekker Inc., 2003.

[68] E. Steck, "A Stochastic Model For The High Temperature Plasticity Of Metals," *International Journal of Plasticity*, vol. 1, pp. 243–258, 1985.

[69] E. Steck, "The Description of the High Temperature Plasticity of Metals by Stochastic Processes," *Res. Mechanica*, pp. 1–19, 1988.

[70] H. Schlums, *Ein stochastisches Werkstoffmodell zur Beschreibung von Kriechen und zyklischem Verhalten metallischer Werkstoffe*. PhD thesis, TU-Braunschweig, 1992.

[71] R. Gerdes, *Ein stochastisches Werkstoffmodell für das inelastische Materialverhalten metallischer Werkstoffe im Hoch- und Tieftemperaturbereich*. PhD thesis, TU-Braunschweig, 1995.

[72] M. Kassner and M. Pérez-Prado, *Fundamentals of creep in metals and alloys*. Elsevier, 1 ed., 2004.

[73] H. Conrad, "Thermally activated deformation of metals," *Journal of Metals*, vol. 16, pp. 582–588, 1964.

[74] A. Evans and R. Rawlings, "The Thermally Activated Deformation of Crystalline Materials," *physica status solidi (b)*, vol. 34, no. 1, pp. 9–31, 1969.

[75] R. Lund and W. Nix, "High temperature creep of Ni–20Cr–2ThO2 single crystals," *Acta Metallurgica*, vol. 24, pp. 469–481, 1976.

[76] H. Dieringa, N. Hort, and K. Kainer, "Investigation of minimum creep rates and stress exponents calculated from tensile and compressive creep data of magnesium alloy AE42," *Materials Science and Engineering*, vol. 510-511, pp. 382–386, 2008.

[77] K. Fuchs, J. Gibeling, and W. Nix, "Mechanical Testing for Deformation Model Development – STP 765," ch. The Role of Long–Range Internal Back Stresses in Creep of Metals, pp. 301–321, ASTM, 1982.

[78] F. Prinz and A. Argon, "The evolution of plastic resistance in large strain plastic flow of single phase subgrain forming metals," *Acta Metallurgica*, vol. 32, no. 7, pp. 1021–1028, 1984.

[79] H. Mughrabi, "Dislocation wall and cell structures and long–range internal stresses in deformed metal crystals," *Acta Metallurgica*, vol. 31, no. 9, pp. 1367–1379, 1983.

[80] A. Miller, "An Inelastic Constitutive Model for Monotonic, Cyclic and Creep Deformation: Part I — Equations Development and Analytical Procedures," *Journal of Engineering Materials and Technology*, vol. 98, pp. 97–105, 1976.

[81] A. Miller, "An Inelastic Constitutive Model for Monotonic, Cyclic and Creep Deformation: Part II — Application to Type 304 stainless Steel," *Journal of Engineering Materials and Technology*, vol. 98, pp. 107–113, 1976.

[82] E. Krempl, J. McMahon, and D. Yao, "Viscoplasticity based on overstress with a differential growth law for the equilibrium stress," *Mechanics of Materials*, vol. 5, no. 1, pp. 35–48, 1986.

[83] J. Chaboche and G. Rousselier, "On the Plastic and Viscoplastic Constitutive Equations – Part I: Rules Developed with Internal Variable Concept," *Journal of Pressure and Vessel Technology*, vol. 105, pp. 153–158, 1983.

[84] J. Chaboche and G. Rousselier, "On the Plastic and Viscoplastic Constitutive Equations – Part II: Application of Internal Variable Concept to the 316 Stainless Steel," *Journal of Pressure and Vessel Technology*, vol. 105, pp. 159–164, 1983.

[85] P. Haupt and A. Lion, "Experimental identification and mathematical modeling of viscoplastic material behavior," *Continuum Mechanics and Thermodynamics*, vol. 7, pp. 73–96, 1995.

[86] T. Lehmann, "On a Generalized Constitutive Law in Thermo–Plasticity Taking into Account Different Yield Mechanisms," *Acta Mechanica*, vol. 57, no. 1-2, pp. 1–23, 1985.

[87] Y. Estrin and H. Mecking, "A unified phenomenological description of work hardening and creep based on one–parameter model," *Acta Metallurgica*, vol. 32, no. 1, pp. 57–70, 1984.

[88] Y. Estrin, L. Tóth, A. Molinari, and Y. Bréchet, "A dislocation–based model for all hardening stages in large strain deformation," *Acta Materialia*, vol. 46, no. 15, pp. 5509–5522, 1998.

[89] H. Mecking and U. Kocks, "Kinetics of flow and strain–hardening," *Acta Metallurgica*, vol. 29, no. 11, pp. 1865–1875, 1981.

[90] P. Feltham, "A Stochastic Model of Creep," *physica status solidi (b)*, vol. 30, no. 1, pp. 135–146, 1968.

[91] R. Gerdes and F. Thielecke, "Micromechanical Development and Identification of a Stochastic Constitutive Model," *Zeitschrift für angewandte Mathematik und Mechanik*, vol. 76, pp. 587–590, 1996.

[92] H. Schlums and E. Steck, "Description of cyclic deformation processes with a stochastic model for inelastic behaviour of metals," *International Journal of Plasticity*, vol. 8, pp. 147–159, 1992.

[93] E. Steck, "Stochastic Modelling of Cyclic Deformation Processes in Metals," *Materials Science Forum*, vol. 123-125, pp. 651–660, 1993.

[94] R. Schettler-Köhler, *Entwicklung eines makroskopischen Kriechgesetzes für Metalle aus einem stochastischen Zwischemodell*. PhD thesis, TU-Braunschweig, 1985.

[95] T. Lösche, *Zur Entwicklung eines Werkstoffgesetzes für die Hochtemperatur–Plastizität über einen Markov–Prozess*. PhD thesis, TU-Braunschweig, 1984.

[96] D. Dumont, A. Deschamps, and Y. Bréchet, "On the relationship between microstructure, strength and toughness in AA7050 aluminum alloy," *Materials Science & Engineering A*, vol. 356, pp. 326–336, 2003.

[97] D. Dumont, A. Deschamps, Y. Bréchet, and C. Sigli, "Mechanical Properties / Microstructure Relationships in Aerospace Aluminium Alloys," in *Microstructures, Mechanical Properties and Processes – Computer Simulation and Modelling EUROMAT*, vol. 3, pp. 269–275, 1999.

[98] S. Esmaeli, L. Cheng, A. Deschamps, D. Lloyd, and W. Poole, "The deformation behaviour of AA6111 as a function of temperature and precipitation state," *Materials Science & Engineering A*, vol. 319-321, pp. 461–465, 2001.

[99] G. Fribourg, A. Deschamps, and Y. Bréchet, "Precipitation strengthening in AA7449 aluminium alloy: understanding the relantionship between microstructure, yield strength and strain hardening," *Materials Science Forum*, vol. 519-521, pp. 991–996, 2006.

[100] J.-G. GmbH, "Product Sheet AlSi10Mg(Cu) – VDS-Nr.: Legierung 233," 2013.

[101] V. G. Hannover, "Chemische Analyse der Gusslegierung $AlSi_{10}Mg(Cu)$," tech. rep., Volkswagen AG, 2007.

[102] "Aluminium Gußlegierungen." Vereinigung Deutscher Schmelzhütten, 1988.

[103] K. Matsuda, Y. Sakaguchi, Y. Miyata, Y. Uetani, T. Sato, A. Kamio, and S. Ikeno, "Precipitation sequence of various kinds of metastable phases in Al–1.0mass% Mg_2Si–0.4mass% Si alloy," *Journal of Materials Science*, vol. 35, no. 1, pp. 179–189, 2000.

[104] S. Ceresara, E. D. Russo, P. Fiorini, and A. Giarda, "Effect of Si Excess on the Ageing Behaviour of Al–Mg_2Si 0.8% Alloy," *Materials Science & Engineering*, vol. 5, no. 4, pp. 220–227, 1970.

[105] M. Zeren, "Effect of copper and silicon content on mechanical properties in Al–Cu–Si–Mg alloys," *Journal of Materials Processing Technology*, vol. 169, pp. 292–298, 2005.

[106] K. Matsuda, S. Tada, and S. Ikeno, "Morphology of a Planer Precipitate and its Orientation Relationship to the Matrix in an Al–1.0 mass% Mg_2Si–0.4mass% Si Alloy," *Journal of the Japan Institute of Metals*, vol. 58, pp. 252–259, 1994.

[107] A. Gupta, D. Lloyd, and S. Court, "Precipitation hardening processes in an Al–0.4%Mg–1.3%Si–0.25%Fe aluminum alloy," *Materials Science & Engineering A*, vol. 301, no. 2, pp. 140–146, 2001.

[108] M. Maruyama and K. Hono, "Pre–precipitate clusters and precipitation processes in Al–Mg–Si alloys," *Acta Materialia*, vol. 47, pp. 1537–1548, 1999.

[109] C. Cáceres, C. Davidson, J. Griffiths, and Q. Wang, "The Effect of Mg on the Microstructure and Mechanical Behavior of Al–Si–Mg Casting Alloys," *Metallurgical and Materials Transactions A*, vol. 30, pp. 2611–2618, 1999.

[110] R. Harris, S. Lipson, and H. Rosenthal, "Tensile properties of aluminum–silicon magnesium alloys and the effect of sodium modification," *American Foundry Society Transactions*, vol. 64, pp. 470–481, 1956.

[111] A. Joenoes and J. Gruzleski, "Magnesium Effects on the Microstructure of Unmodified and Modified Al–Si Alloys," *Cast Metals*, vol. 4, no. 2, pp. 62–71, 1991.

[112] M. Moustafa, "Effect of Iron Content on the Formation of β–Al_5FeSi and Porosity in Al–Si Eutectic Alloys," *Journal of Materials Processing Technology*, vol. 209, pp. 605–610, 2009.

[113] J. Davis, *Aluminum and Aluminum Alloys (American Society for Metals Specialty Handbook)*. ASM International, 1993.

[114] W. Glatt, W. Konzelmann, and E. Bruch, "Aluminium-Gußlegierungen: Sekundär–Aluminium; Qualität und Recycling," Düsseldorf: Giesserei–Verlag, 1988.

[115] Y. Tan, S. Lee, and Y. Lin, "Effects of Be and Fe Additions Microstructure and Mechanical on the Properties of A357.0 Alloys," *Metallurgical and Materials Transactions A*, vol. 26A, pp. 1195–1205, 1995.

[116] Z. Liang, C. Chang, N. Wanderka, J. Banhart, and J. Hirsch, "The Effect of Fe, Mn and Trace Elements on Precipitation in Al–Mg–Si Alloy," in *12^{th} International Conference on Aluminium Alloys*, 2010.

[117] D. Pashley, J. Rhodes, and A. Sendorek, "Delaying Ageing in Aluminum–Magnesium–Silicon Alloys: Effect on Structure and Mechanical Properties," *Journal of the Institute of Metals*, vol. 94, pp. 41–49, 1966.

[118] Y. Liu, S. Kang, and H. Kim, "The complex microstructures in an as–cast Al–Mg–Si alloy," *Materials Letters*, vol. 41, pp. 267–272, 1999.

[119] P. Donnadieu, G. Dirras, and J. Douin, "An approach of precipitate/dislocation interaction in age–hardened Al–Mg–Si alloys: measurement of the strain field around precipitates and related simulation of the dislocation propagation," *Materials Science Forum*, vol. 396-402, pp. 1019–1024, 2002.

[120] M. Tanaka and T. Warner, "Quantitative TEM study of hardening precipitates in 6XXX aluminum alloys," *La Revue de Métallurgie*, vol. 5, pp. 463–469, 2003.

[121] D. Fabregue, A. Deschamps, and M. Suery, "Microstructure of butt laser joints of aluminium alloy 6056 sheets with an AS12 filler," *Materials Science and Technology*, vol. 21, pp. 1329–1336, 2005.

[122] H. Seyedrezai, D. Grebennikov, P. Mascher, and H. Zurob, "Study of the early stages of clustering in Al–Mg–Si alloys using the electrical resistivity measurements," *Materials Science & Engineering A*, vol. 525, pp. 186–191, 2009.

[123] H. Ammar, C. Moreau, A. Samuel, F. Samuel, and H. Doty, "Influences of alloying elements, solution treatment time and quenching media on quality indices of 413–type Al–Si casting alloys," *Materials Science & Engineering A*, vol. 489, pp. 426–438, 2008.

[124] P. Staron, W. Vaidya, and M. Koçak, "Precipitates in laser beam welded aluminium alloy AA6056 butt joints studied by small–angle neutron scattering," *Materials Science & Engineering A*, vol. 525, pp. 192–199, 2009.

[125] G. Kostorz, *Physical Metallurgy*, ch. X–ray and Neutron Scattering, pp. 1115–1199. New York: North–Holland, 4 ed., 1996.

[126] G. Kostorz, "Volume 15: Neutron Scattering," in *Treatise on Materials Science and Technology*, New York: Academic Press, 1979.

[127] C. Tsao, U. Jeng, C. Chen, and T. Kuo, "Small–angle X–ray scattering study of nanostructure evolution of β'' precipitates in Al–Mg–Si alloy," *Scripta Materialia*, vol. 53, pp. 1241–1245, 2005.

[128] A. Guinier and G. Fournet, "Small Angle Scattering of X-rays," New York: Wiley, 1955.

[129] O. Glatter and O. Kratky, "Small Angle X–ray Scattering," London: Academic Press, 1982.

[130] C. Meyers, K. Hinton, and J. Chou, "Towards the Optimization of Heat–Treatment in Aluminium Alloys," *Materials Science Forum*, vol. 102-104, pp. 75–84, 1992.

[131] X. Cao and J. Campbell, "Morphology of β–Al_5SiFe Phase in Al–Si Cast Alloys," *Materials Transactions*, vol. 47, no. 5, pp. 1303–1312, 2006.

[132] E. Sakr, A. Nassar, N. Tawfik, and M. Soliman, "Study the Effect of some Metallic Additives on the Physical Properties of the Commercial Pure Aluminum Metal," *Journal of American Science*, vol. 6, pp. 239–252, 2010.

[133] B. Zhang, M. Garro, M. Leghissa, A. Giglio, and C. Tagliano, "Effect of Dendrite Arm Spacing on Mechanical Properties of Aluminum Alloy Cylinder Heads and Engine Blocks," in *SAE World Congress & Exhibition*, 2005.

[134] J. Robson, "Microstructural evolution in aluminium alloy 7050 during processing," *Materials Science & Engineering A*, vol. 382, pp. 112–121, 2004.

[135] J. Robson and P. Prangnell, "Dispersoid Precipitation and Process Modelling in Zirconium containing commercial Aluminium Alloys," *Acta Materialia*, vol. 49, pp. 599–613, 2001.

[136] H. Aaron, D. Fainstein, and G. Kotler, "Diffusion–Limited Phase Transformations: A Comparison and Critical Evaluation of the Mathematical Approximations," *Journal of Applied Physics*, vol. 41, pp. 4404–4411, 1970.

[137] S. Fujikawa, "Tracer Diffusion of Magnesium in Pseudo-Binary Al-Mg2Si Alloys," *Defect and Diffusion Forum*, vol. 143-147, pp. 403–408, 1997.

[138] J. Christian, *The Theory of Transformation in Metals and Alloys*. Pergamon, 1975.

[139] M. Stowell, "Precipitate nucleation: does capillarity theory work?," *Materials Science and Technology*, vol. 18, no. 2, pp. 139–144, 2002.

[140] A. Vasilyev, N. Kuzmin, and A. Gruzdev, "Calculation of Meta–Stable Precipitates Solvous Temperature and Modelling of Age–Hardening in Al–Mg–Si Alloys," in *Materials Sciene & Engineering Congress*, 2010.

[141] H. Gudladt, J. Lendvai, and J. Schneider, "Precipitation Strengthening and its Influence on the Mechanical Behavior of Cyclically Deformed Al-Li Alloys," *Acta Metallurgica*, vol. 37, no. 12, pp. 3327–3333, 1989.

[142] A. Baldan, "Review Progress in Ostwald ripening theories and their applications to nickel–base superalloys. Part I: Ostwald ripening theories," *Journal of Materials Science*, vol. 37, pp. 2171–2202, 2002.

[143] S. Shahandeh, H. Arami, and S. Sadrnezhaad, "Interfacial energy determination of nano-scale precipitates by CALPHAD description of Gibbs–Thomson effect," *Journal of Materials Science*, vol. 42, no. 22, pp. 9440–9446, 2007.

[144] G. Novotny and A. Ardell, "Precipitation of Al_3Sc in binary Al–Sc alloys," *Materials Science & Engineering A*, vol. 318, pp. 144–154, 2001.

[145] F. Richards, "A Flexible Growth Function for Empirical Use," *Journal of Experimental Botany*, vol. 10, pp. 290–301, 1959.

[146] L. Wu and W. Ferguson, "Modelling of Precipitation Hardening in Casting Aluminium Alloys," *Materials Science Forum*, vol. 618-619, pp. 203–206, 2009.

[147] O. Sherby and P. Burke, "Mechanical behavior of crystalline solids at elevated temperature," *Progress in Materials Science*, vol. 13, pp. 323–390, 1968.

[148] F. Mohamed, K. Park, and E. Lavernia, "Creep behavior of discontinuous SiC–Al composites," *Materials Science & Engineering A*, vol. 150, no. 1, pp. 21–35, 1992.

[149] S. Robinson and O. Sherby, "Mechanical behavior of polycrystalline tungsten at elevated temperature," *Acta Metallurgica*, vol. 17, no. 2, pp. 109–125, 1969.

[150] W. Oliver and W. Nix, "High Temperature Deformation of Oxide Dispersion Strengthened Al and Al–Mg Solid Solutions," *Acta Metallurgica*, vol. 30, no. 7, pp. 1335–1347, 1982.

[151] E. Arzt and M. Ashby, "Threshold Stresses in Materials Containing Dispersed Particles," *Scripta Metallurgica*, vol. 16, no. 11, pp. 1285–1290, 1982.

[152] E. Arzt and D. Wilkinson, "Threshold stresses for dislocation climb over hard particles: The effect of an attractive interaction," *Acta Metallurgica*, vol. 34, no. 10, pp. 1893–1898, 1986.

[153] N. Huber and C. Tsakmakis, "A Neural Network Tool for Identifying the Material Parameters of a Finite Deformation Viscoplasticity Model with Static Recovery," *Computational Methods Applied to Mechanical Engineering*, vol. 191, pp. 353–384, 2001.

[154] J. dos Santos and S. Koch, eds., *VI-IPSUS Summer School. Proceedings*, GKSS Forschungszentrum Geesthacht, 2010.

[155] H. Zhu, J. Guo, and J. Jia, "Correlation of the Aging Characteristics and Deformation Behavior of A357 Alloy," *Journal of Materials Engineering and Performance*, vol. 10, pp. 186–191, 2001.

[156] Y. Li and T. Langdon, "A Simple Procedure for Estimating Threshold Stresses in the Creep of Metal Matrix Composites," *Scripta Materialia*, vol. 36, no. 12, pp. 1457–1460, 1997.

[157] H. Rockenschaub, T. Pabel, G. Geier, and M. Hopfinger, "Beschleunigung der Auslagerungsvorgänge der Druckgusslegierung $AlSi_9Cu_3$(Fe) bei gleichzeitiger Erhöhung der statischen mechanischen Eigenschaften, Teil 1," *Druckguss–Praxis*, vol. 4, pp. 95–104, 2005.

[158] S. Suresh, *Fatigue of Materials*. Cambridge: Cambridge University Press, 2 ed., 1998.

[159] M. Jain, "TEM study of microstructure development during low–cycle fatigue of an overaged Al–Mg–Si alloy," *Journal of Materials Science*, vol. 27, pp. 399–407, 1992.

[160] L. Zhen, W. Fei, S. Kang, and H. Kim, "Precipitation behaviour of Al-Mg-Si alloys with high silicon content," *Journal of Materials Science*, vol. 32, pp. 1895–1902, 1997.

[161] N. Rohleder and F. Kollmann, "Creep experiments for parameter identification of the stochastic model of Steck with the powder metallurgical alloy AlMn10," *International Journal of Plasticity*, vol. 6, no. 1, pp. 109–122, 1990.

[162] E. Steck, R. Ritter, U. Peil, and A. Ziegenbein, *Plasticity of Metals: Experiments, Models, Computation. Collaborative Research Centres (SFB 319)*. Wiley-VCH Verlag, 2001.

[163] F. Kublik, *Vergleich zweier Werkstoffmodelle bei ein- und mehrachsigen Versuchsführungen im Hochtemperaturbereich*. PhD thesis, TU-Braunschweig, 1992.

[164] E. Steck and R. Gerdes, "Consideration of processes on the microscale of metallic materials for the development of constitutive models," *Acta Mechanica*, vol. 120, pp. 1–30, 1997.

[165] T. Hasegawa, Y. Ikeuchi, and S. Karashima, "Internal Stress and Dislocation Structure during Sigmoidal Transient Creep of a Copper–16 at.–% Aluminium Alloy," *Metal Science*, vol. 6, pp. 78–82, 1972.

[166] M. Kassner, A. Miller, and O. Sherby, "The Separate Roles of Subgrains and Forest Dislocations in the Isotropic Hardening of Type 304 Stainless Steel," *Metallurgical and Materials Transactions A*, vol. 13, pp. 1977–1986, 1982.

[167] J. Schwertel, *Modellierung des einachsigen mechanischen Verhaltens von Werkstoffen durch viskoplastische Stoffmodelle*. VDI Verlag, 1993.

[168] A. Miller, *A Unified Phenomenological Model for the Monotonic, Cylic and Creep Deformation of Strongly Work–Hardening Materials*. Stanford University, 1975.

[169] S. Bodner and Y. Partom, "Constitutive Equations for Elastic-Viscoplastic Strain-Hardening Materials," *Journal of Applied Mechanics*, vol. 42, no. 2, pp. 385–389, 1975.

[170] J. Chaboche, D. Nouailhas, P. Paulmier, and H. Policella, "Sur les problémes posés par la description des effets de rochet en plasticité et viscoplasticité cycliques," *La Recherche Aérospatiale*, vol. 1, pp. 63–79, 1989.

[171] K. Chan, S. Bodner, and U. Lindholm, "Phenomenological Modeling of Hardening and Thermal Recovery in Metals," *Journal of Engineering Materials and Technology*, vol. 110, pp. 1–8, 1988.

[172] R. Mahnken and E. Stein, "Parameter identification for viscoplastic models based on analytical derivatives of a least–squares functional and stability investigations," *International Journal of Plasticity*, vol. 12, pp. 451–479, 1996.

[173] B. Butcher, H. Hutto, and A. Ruoff, "Activation volume and energy for self–diffusion in aluminium," *Applied Physics Letters*, vol. 7, pp. 34–35, 1965.

[174] O. Sherby, J. Lytton, and J. Dorn, "Activation Energies for Creep of High–Purity Aluminium," *Acta Metallurgica*, vol. 5, pp. 219–227, 1957.

[175] R. Horiuchi and M. Otsuka, "Mechanism of High Temperature Creep of Aluminium–Magnesium Solid Solution Alloys," *Transactions of the Japan Institute of Metals*, vol. 13, pp. 284–293, 1972.

[176] H. Frost and M. Ashby, *Deformation-Mechanism Maps*. Pergamon Press, 1982.

[177] M. Mercer, S. Dickerson, and J. Gibeling, "Cyclic deformation of dispersion–strengthened aluminum alloys," *Materials Science & Engineering A*, vol. 203, pp. 46–58, 1995.

Appendix A

Shercliff–Ashby precipitation model

The model of Shercliff–Ashby is a process model developed to describe the effect of the ageing treatment on the yield strength of age–hardenable alloys, especially aluminum alloys. Despite the apparent simplicity of the model, good results have been obtained for isothermal ageing processes in some Al–Cu and Al–Si–Mg alloy systems [2, 5, 6, 146].

The model is based on simple and widely known principles of phase equilibria, coarsening processes, and dislocation–precipitate interactions. It incorporates the following components or sub–models [5]:

(i) The initial growth of a volume fraction of precipitates, and the consequent changes in the solute concentration.

(ii) The dependence of the equilibrium volume fraction of precipitates on the ageing temperature.

(iii) The coarsening of precipitates by competitive growth.

(iv) The contribution of solid solution strengthening to the yield strength;

(v) The contribution of shearable precipitates to the strength (Friedel mechanism).

(vi) The contribution of non–shearable or bypassing precipitates to the strength (Orowan mechanism).

The sub–models (i)–(iii) address the modeling of the precipitation process, while the rest of the components together with the intrinsic strength of the matrix itself form the strength model. The equations describing these sub–models are combined to obtain the process model to describe

the ageing process. Thus, the resulting expression for the overall macroscopic alloy strength σ, assuming a linear combination of the different strengthening contributions, is:

$$\sigma = \sigma_i + \Delta\sigma_{ss} + \Delta\sigma_{ppt} \ , \tag{A.1}$$

being σ_i the intrinsic strength of the matrix (alloy property), $\Delta\sigma_{ss}$ the solid solution strength, and $\Delta\sigma_{ppt}$ the net contribution of precipitation.

The *temperature–corrected time* P concept is included in this model to combine the equations of all the sub–models together to give a process model for the ageing. This parameter indicates the number of kinetic jumps that have taken place in time t and is defined as:

$$P = \frac{t}{T} \cdot \exp\left(-\frac{Q_A}{R\,T}\right) \ , \tag{A.2}$$

where T is the temperature, Q_A is the activation energy for volume diffusion, and R is the gas constant.

Precipitation strengthening

The net contribution of the precipitation strengthening from the shearing and bypassing precipitates is defined by taking the harmonic mean as:

$$\Delta\sigma_{ppt} = \left[\frac{1}{\Delta\sigma_A} + \frac{1}{\Delta\sigma_B}\right]^{-1} \ , \tag{A.3}$$

being $\Delta\sigma_A$ the contribution to strength of shearable particles, and $\Delta\sigma_B$ that of bypassing precipitates.

By defining P_p as the value of P corresponding to the ageing peak, and S_0 the maximum contribution of precipitation to the total strength denoted as "peak precipitation strength", both contributions $\Delta\sigma_A$ and $\Delta\sigma_B$ can be defined as:

$$\Delta\sigma_A = 2S_0\,(P^*)^{1/6} \ . \tag{A.4}$$

$$\Delta\sigma_B = \frac{2S_0}{(P^*)^{1/3}} \ . \tag{A.5}$$

From the definition of P, it follows that P_p is a constant for all ageing curves. By substituting

Eqs. (A.4) and (A.5) into Eq. (A.3), the resulting expression for the contribution of the precipitation strengthening mechanism is:

$$\Delta\sigma_{ppt} = \frac{2S_0\left(P^*\right)^{1/6}}{1+\left(P^*\right)^{1/2}} \ , \tag{A.6}$$

being P^* the normalized temperature–corrected time ($P^* = P/P_p$). Thus, the precipitate strength at the ageing peak ($P = P_p$) is exactly S_0. The peak precipitation strength S_0 depends on the ageing temperature due to its relationship in the model with the volume fraction of precipitates. This temperature dependence is determined as:

$$S_0^2\left(T\right) = \left(S_0\right)_{max}^2 \cdot \left[1 - \exp\left(-\frac{Q_s}{R}\cdot\left(\frac{1}{T}-\frac{1}{T_s}\right)\right)\right] \ , \tag{A.7}$$

being Q_s the free energy of solution of the solute.

The evolution of the volume fraction of precipitates throughout the ageing process also affects the contribution of precipitation to the total strength of the alloy:

$$S^2(t) = S_0^2 \cdot \left(1 - \exp\left(-\frac{t}{\tau_1}\right)\right) \tag{A.8}$$

By combining this with Eq. (A.7), the temperature dependent evolution of the precipitation contribution S is:

$$S^2\left(t,T\right) = \left(S_0\right)_{max}^2 \cdot \left[1 - \exp\left(-\frac{Q_s}{R}\cdot\left(\frac{1}{T}-\frac{1}{T_s}\right)\right)\right] \cdot \left(1 - \exp\left(-\frac{t}{\tau_1}\right)\right) \ . \tag{A.9}$$

Solid solution strengthening

The contribution of solid solution to the total strength is given by:

$$\Delta\sigma_{ss}\left(t\right) = \left[\Delta\sigma_{ss0}^{3/2} + \left(\Delta\sigma_{ssi}^{3/2} - \Delta\sigma_{ss0}^{3/2}\right)\cdot\exp\left(-\frac{t}{\tau_1}\right)\right]^{2/3} \ . \tag{A.10}$$

In Eq. (A.10), $\Delta\sigma_{ssi}$ and $\Delta\sigma_{ss0}$ are the initial and the equilibrium solid solution contributions to strength and τ_1 is a time constant defined as a fraction K_1 of the time corresponding to the peak ageing t_p ($\tau_1 = K_1 \cdot t_p = K_1 P_p T \exp\left(Q_A/\left(RT\right)\right)$) when the volume fraction and solute concentration settle to their equilibrium values.

Similarly to the precipitation strength S, the contribution of the solid solution is also dependent on the ageing temperature because it depends on the remaining amount of solute in solution. The temperature dependence of the equilibrium solid solution is:

$$(\Delta\sigma_{ss0})_T = (\sigma_q - \sigma_i) \cdot \exp\left(-\frac{2Q_s}{3R} \cdot \left(\frac{1}{T} - \frac{1}{T_s}\right)\right) \ , \tag{A.11}$$

being σ_q the alloy strength in its as–quenched condition, σ_i the above mentioned intrinsic strength of the matrix, and T_s the metastable solid solvus temperature.

From Eq. (A.11), the variation of the overaged strength in the alloy $\Delta\sigma_{oa}$ with temperature can be calculated as:

$$(\Delta\sigma_{oa})_T = \sigma_i + (\sigma_q - \sigma_i) \cdot \exp\left(-\frac{2Q_s}{3R} \cdot \left(\frac{1}{T} - \frac{1}{T_s}\right)\right) \ . \tag{A.12}$$

Further details on the sub–models of the physical model and the corresponding equations and the calibration procedure can be found in the literature [5].

Application to $AlSi_{10}Mg(Cu)$ cast alloy

The major advantage of this model is its practical application. In this sense, the calibration of the model parameters is done by using the results obtained from the experimental ageing curves. The six parameters that are calibrated from these curves are the activation energy for ageing Q_A, the peak temperature–corrected time P_p, the metastable solvus temperature T_s, the solvus enthalpy Q_s, the maximum precipitation strength at absolute zero $(S_0)_{max}$, and the constant coefficient K_1. Besides, these parameters do not change with temperature for each specific alloy.

The set of model parameters used for the modeling of the ageing process for the $AlSi_{10}Mg(Cu)$ alloy is that given in Table 5.3. This is obtained by following the calibration procedure proposed for the model and taking as base the previously reported set of parameters obtained for the alloy 6082 [5]. Comparing it to that obtained for the A356 alloy, it differs considerably despite being both alloys very similar [2]. This is likely due to the different stages of interest of the precipitation process in both studies, focusing this work on the late overageing and coarsening processes.

The contributions to the full ageing curve of the precipitation hardening due to shearable and non–shearable precipitates, solid solution strengthening, and intrinsic strength for the alloy at 180°C, 210°C, 240°C, and 300°C are presented in Fig. A.1. The predicted ageing curves agree

very good with the experimental ones. The model tends to overestimate the ageing peaks at higher temperatures. Additionally and in agreement with the conclusions drawn for Robson's model and with the experimental ageing curves, higher temperatures produce lower ageing peaks for shorter ageing times.

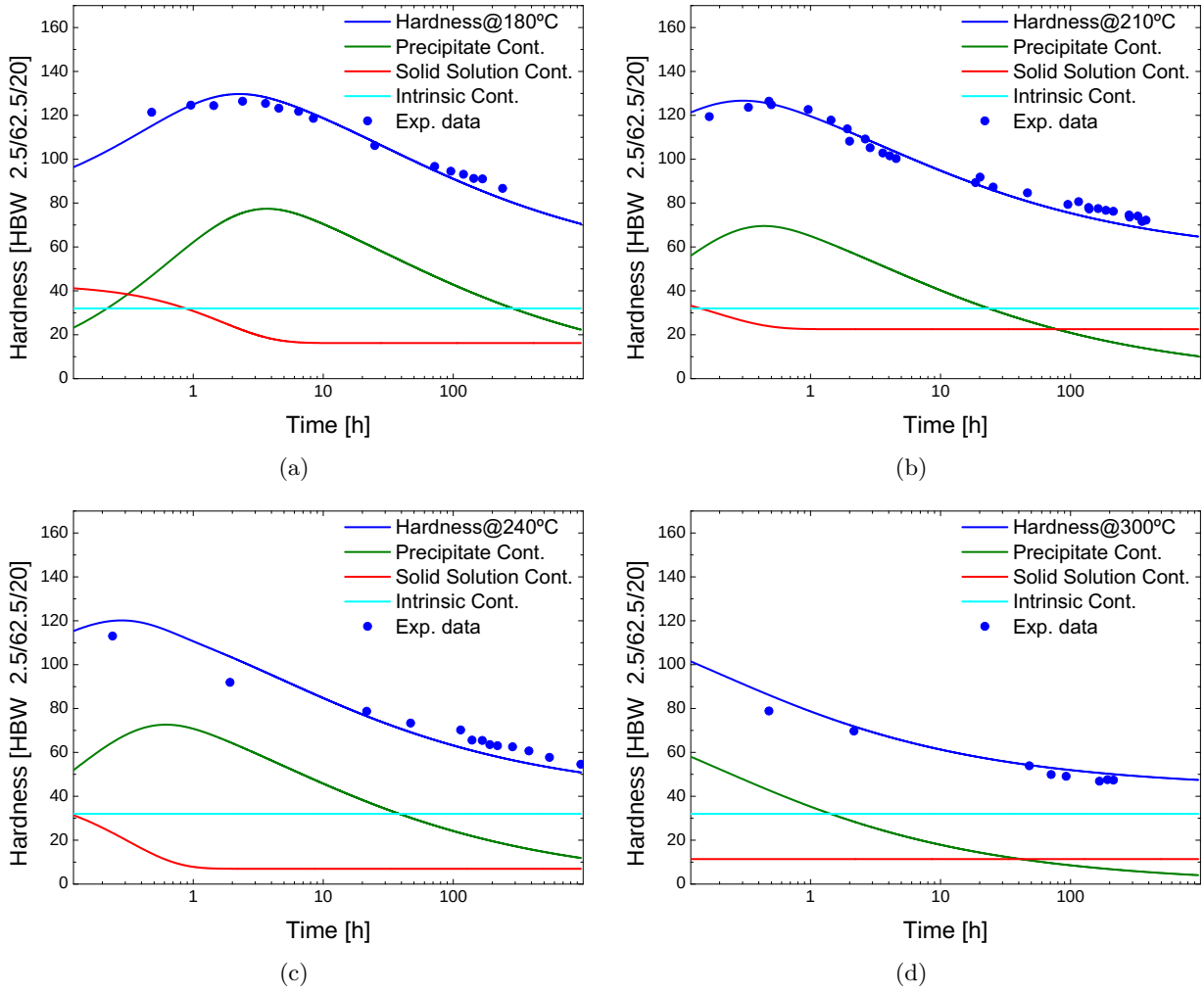

Fig. A.1: Simulation results obtained by using Shercliff–Ashby model considering the individual contributions of the precipitation distribution, remaining solid solution, ant that of the aluminum matrix for the ageing curves at: (a) at 180°C; (b) at 210°C; (c) at 240°C; (d) at 300°C.

Appendix B

Mechanical simulations

An overview of the LCF experiments and the simulation results obtained using the constitutive Steck's model and the corresponding model parameters given in Table 6.2 are presented in this appendix for the four ageing conditions S_{I}, S_{II}, S_{III}, and S_{IV} considered.

B.1 Ageing condition S_{I}

The ageing condition S_{I} is obtained by treating the alloy at 240°C for 2.5 hours, producing an interprecipitate spacing of $\lambda_{S_I} = 4.84 \cdot 10^{-8}$ m. The LCF tests are carried out at 200°C and 225°C by using a strain amplitude of 0.45 %.

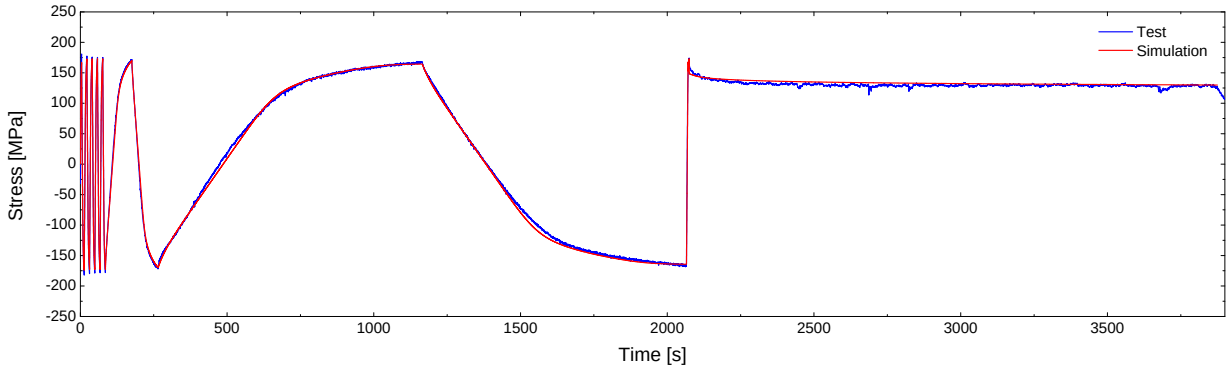

(a)

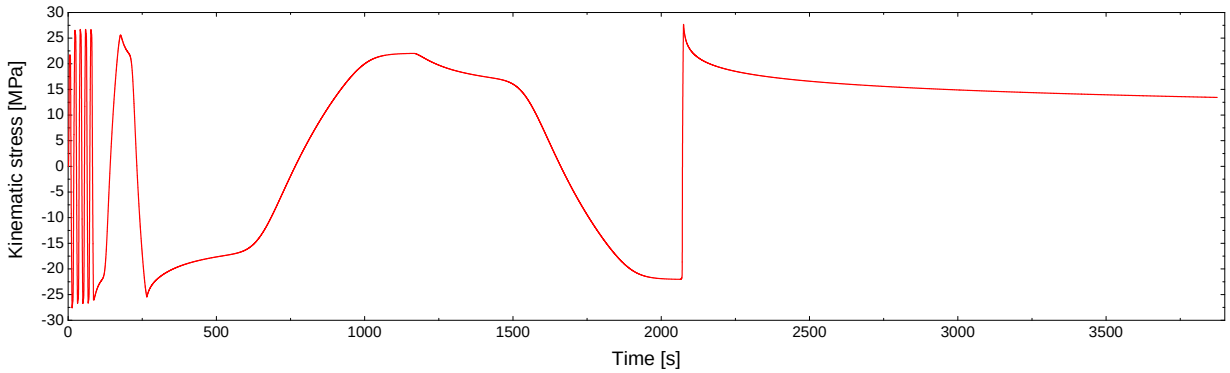

(b)

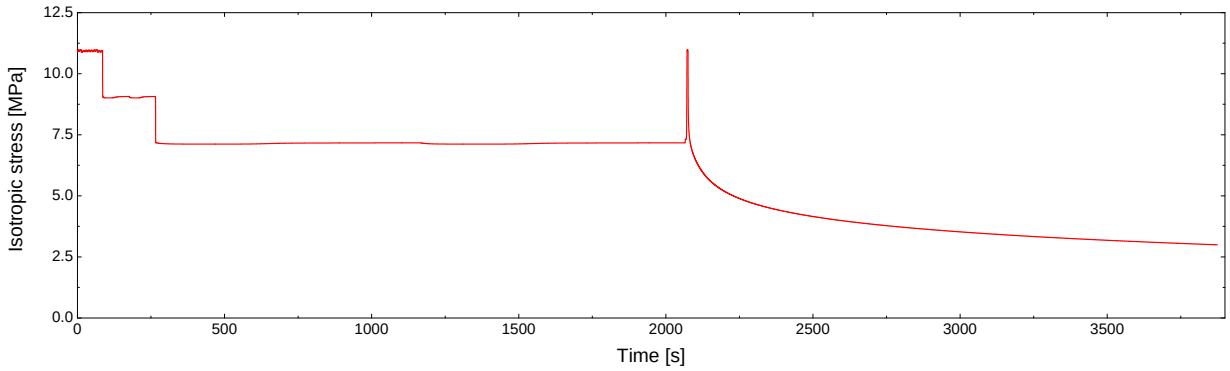

(c)

Fig. B.1: Results of the LCF test and simulation using the modified Steck's model for the ageing condition S_{I} at 200°C referring to: (a) experimental and predicted stress σ; (b) kinematic stress σ^{kin}; (c) isotropic stress σ^{iso}.

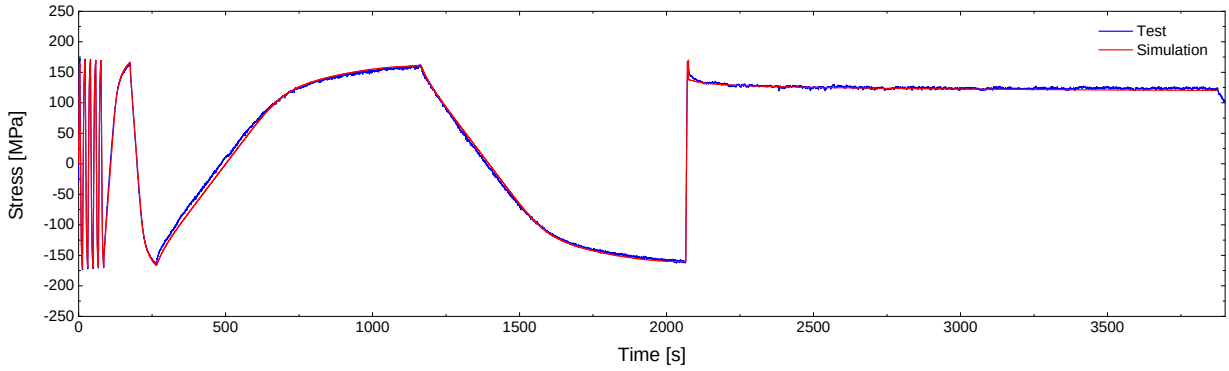

(a)

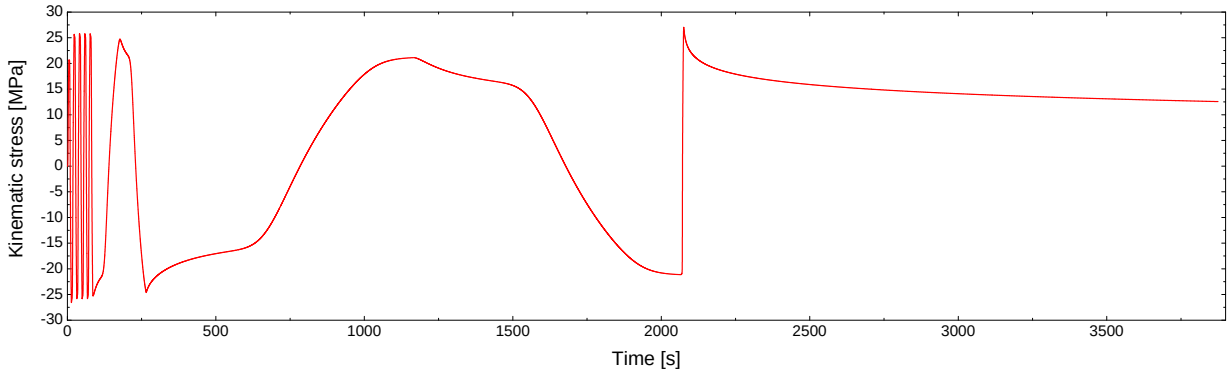

(b)

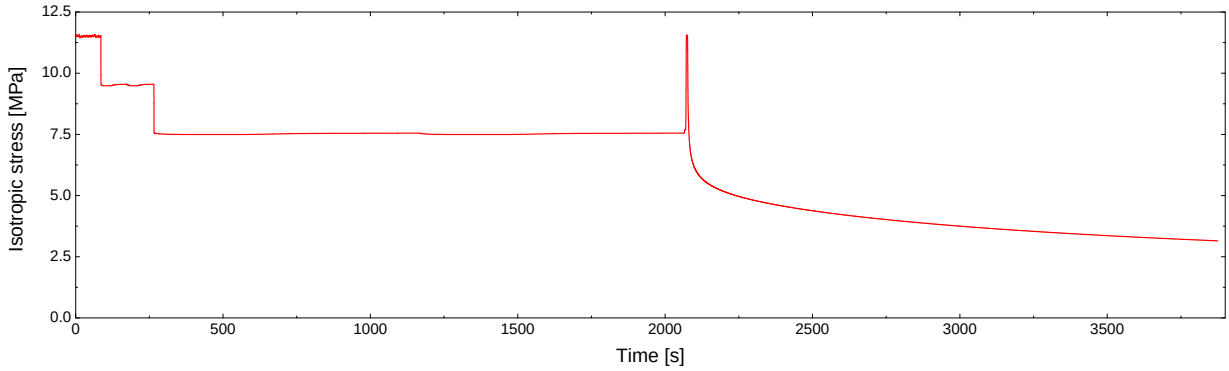

(c)

Fig. B.2: Results of the LCF test and simulation using the modified Steck's model for the ageing condition S_{I} at 225°C referring to: (a) experimental and predicted stress σ; (b) kinematic stress σ^{kin}; (c) isotropic stress σ^{iso}.

B.2 Ageing condition S_{II}

The ageing condition S_{II} is obtained by treating the alloy at 240°C for 14 hours, producing an interprecipitate spacing of $\lambda_{S_{II}} = 6.82 \cdot 10^{-8}$ m. The LCF tests are carried out at 200°C, 225°C, and 250°C by using a strain amplitude of 0.45 %.

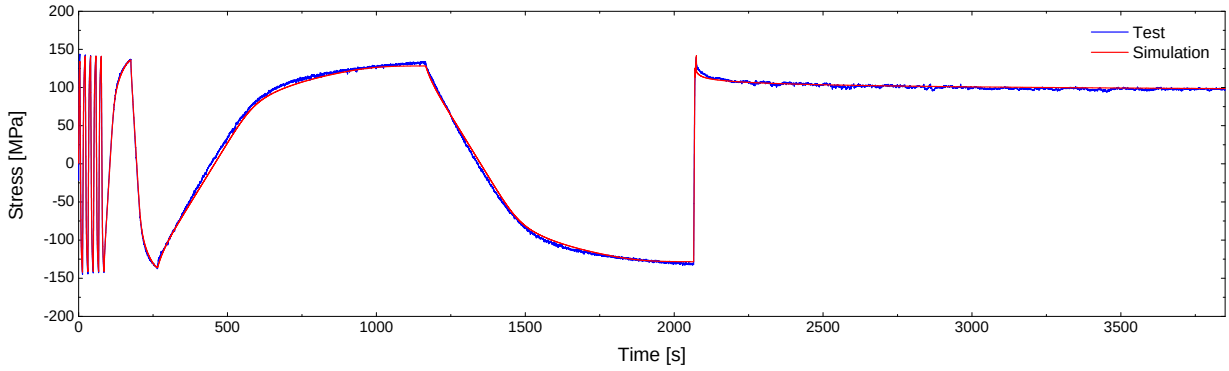

(a)

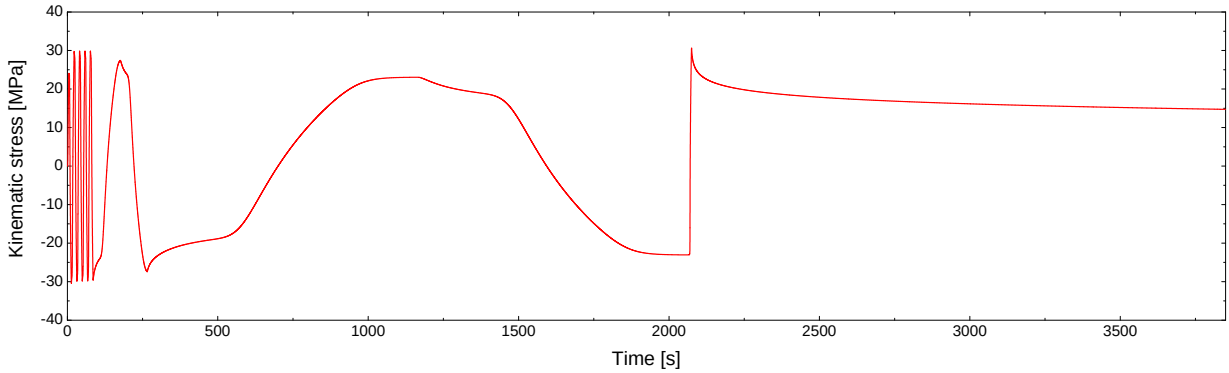

(b)

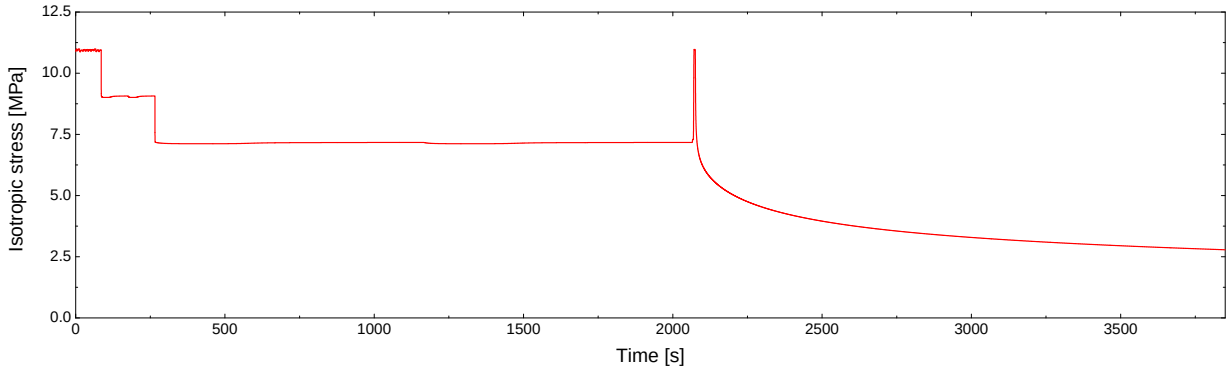

(c)

Fig. B.3: Results of the LCF test and simulation using the modified Steck's model for the ageing condition S_{II} at 200°C referring to: (a) experimental and predicted stress σ; (b) kinematic stress σ^{kin}; (c) isotropic stress σ^{iso}.

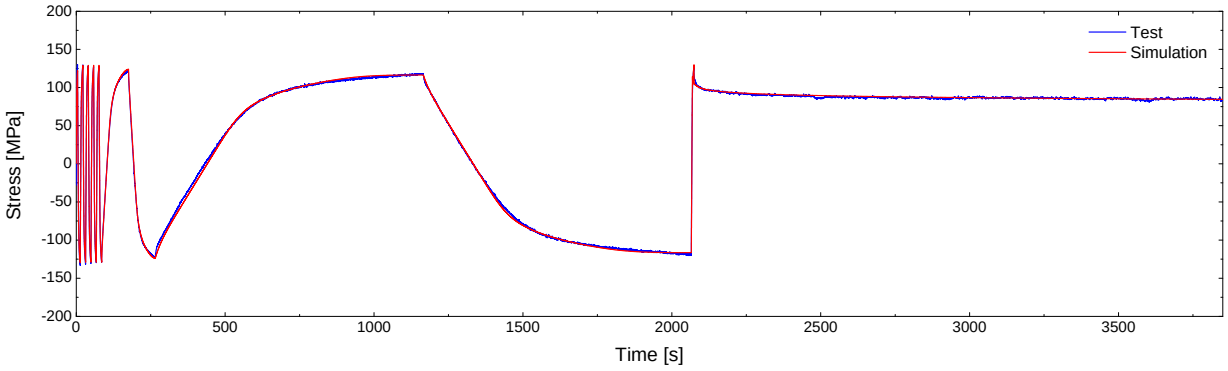

(a)

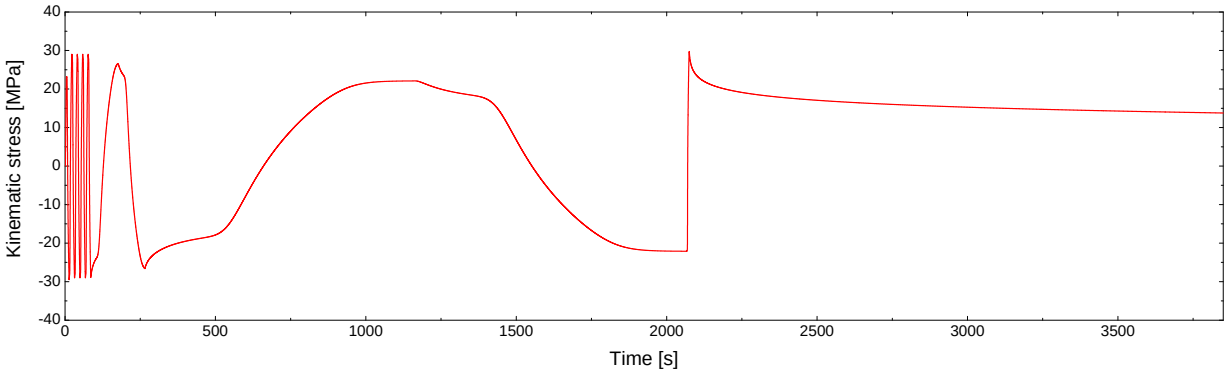

(b)

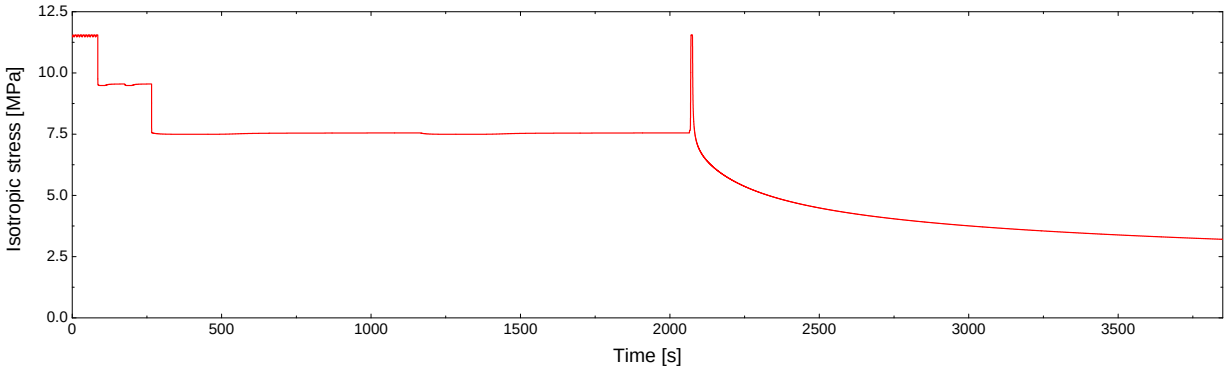

(c)

Fig. B.4: Results of the LCF test and simulation using the modified Steck's model for the ageing condition S_{II} at 225°C referring to: (a) experimental and predicted stress σ; (b) kinematic stress σ^{kin}; (c) isotropic stress σ^{iso}.

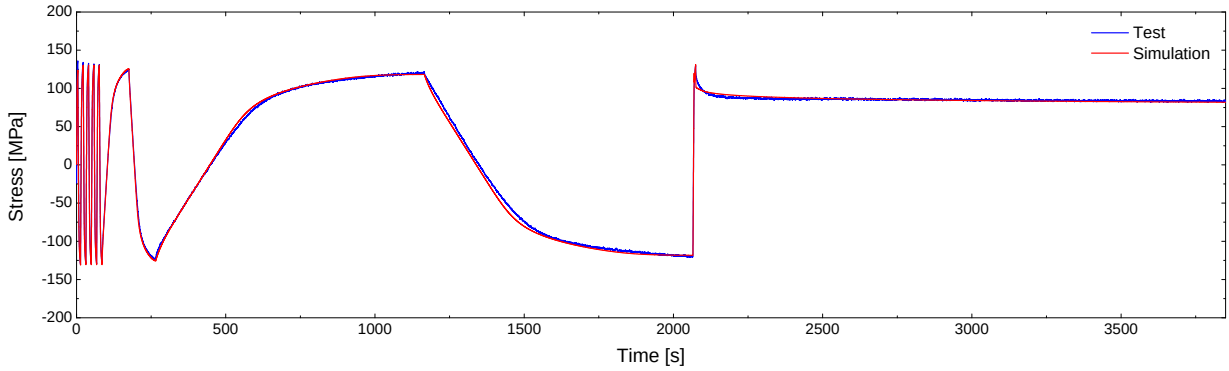

(a)

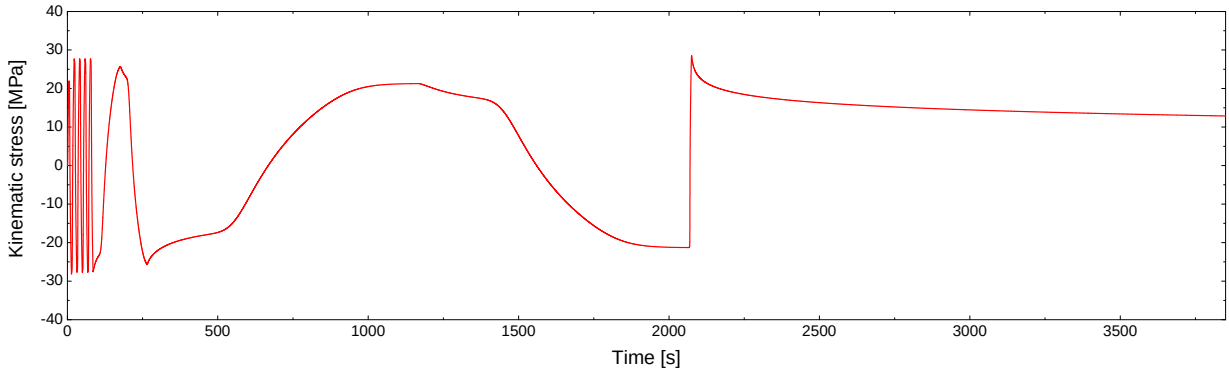

(b)

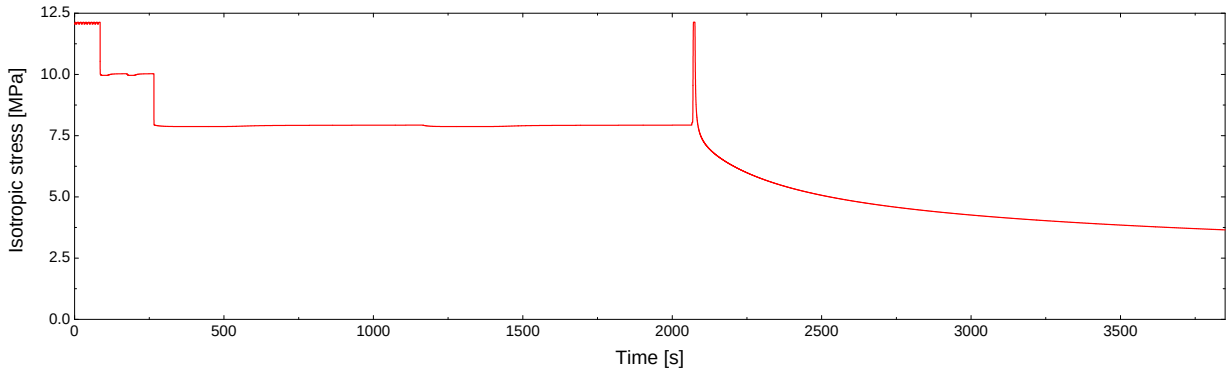

(c)

Fig. B.5: Results of the LCF test and simulation using the modified Steck's model for the ageing condition S_{II} at 250°C referring to: (a) experimental and predicted stress σ; (b) kinematic stress σ^{kin}; (c) isotropic stress σ^{iso}.

B.3 Ageing condition S_{III}

The ageing condition S_{III} is obtained by treating the alloy at 240°C for 384 hours, producing an interprecipitate spacing of $\lambda_{S_{III}} = 20.94 \cdot 10^{-8}$ m. The LCF tests are carried out at 200°C, 250°C, and 280°C by using a strain amplitude of 0.25 %.

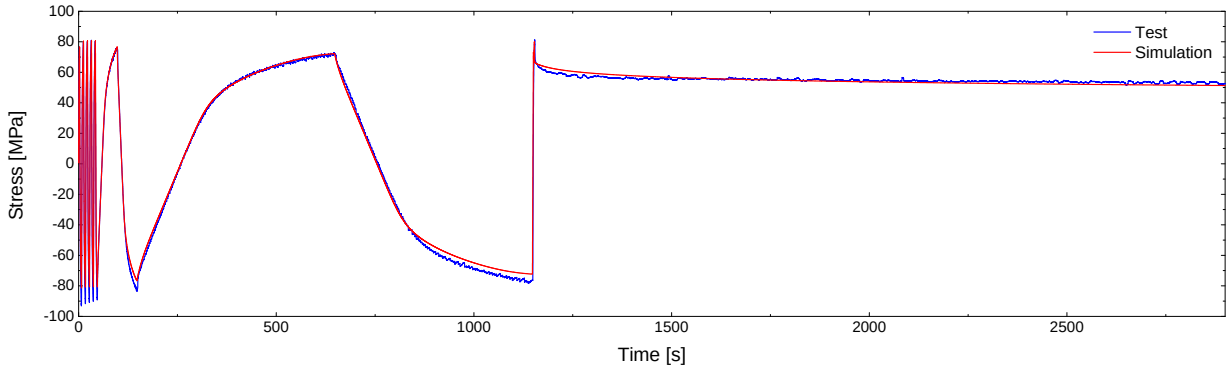

(a)

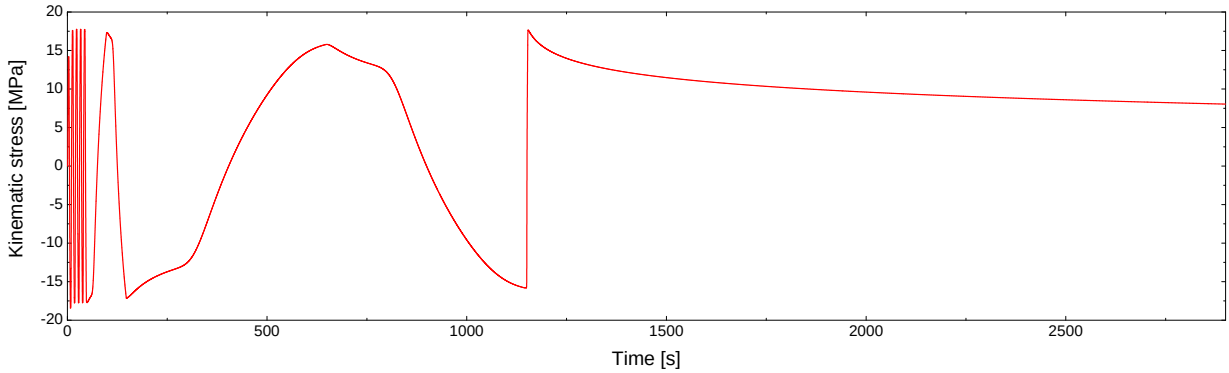

(b)

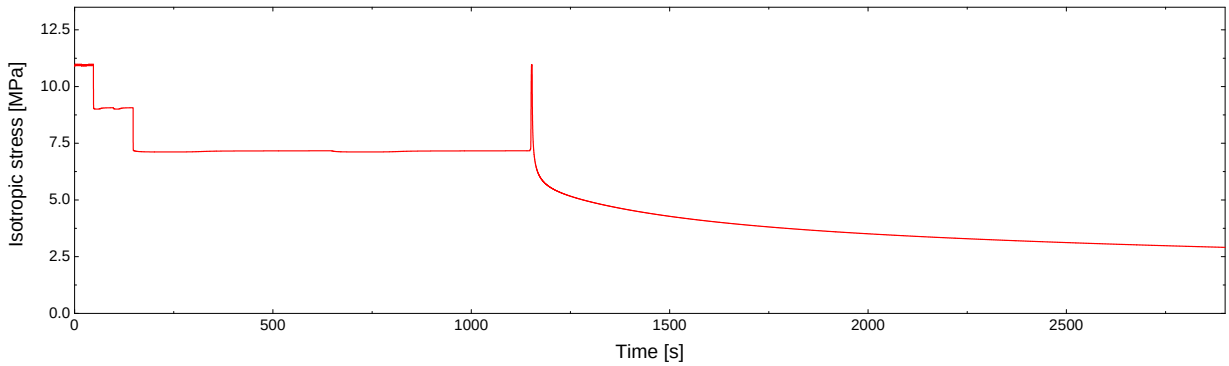

(c)

Fig. B.6: Results of the LCF test and simulation using the modified Steck's model for the ageing condition S_{III} at 200°C referring to: (a) experimental and predicted stress σ; (b) kinematic stress σ^{kin}; (c) isotropic stress σ^{iso}.

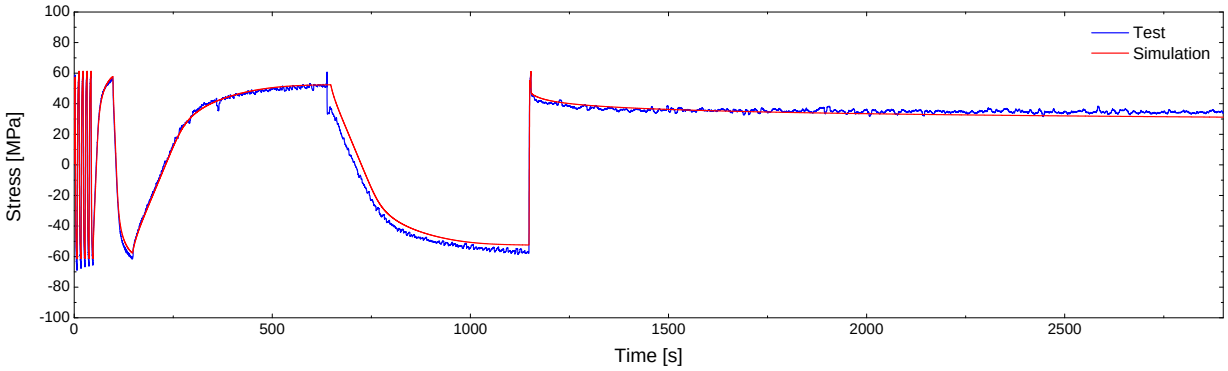

(a)

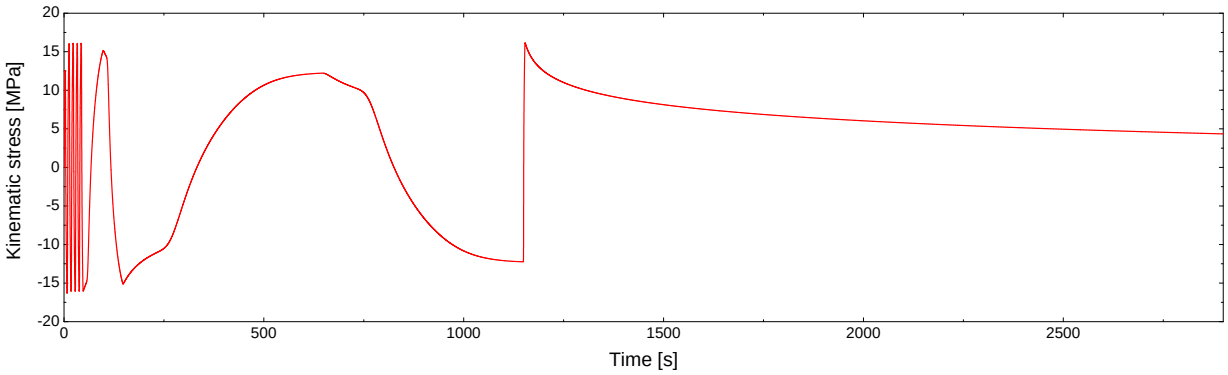

(b)

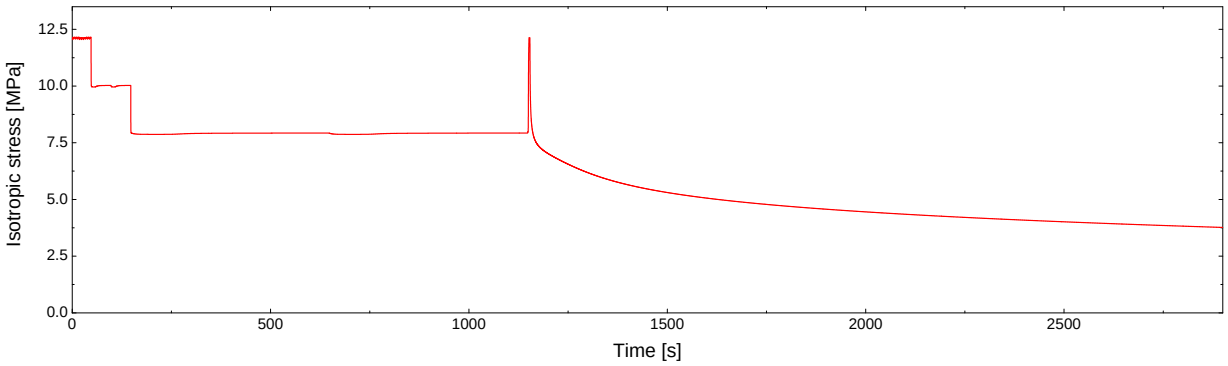

(c)

Fig. B.7: Results of the LCF test and simulation using the modified Steck's model for the ageing condition S_{III} at 250°C referring to: (a) experimental and predicted stress σ; (b) kinematic stress σ^{kin}; (c) isotropic stress σ^{iso}.

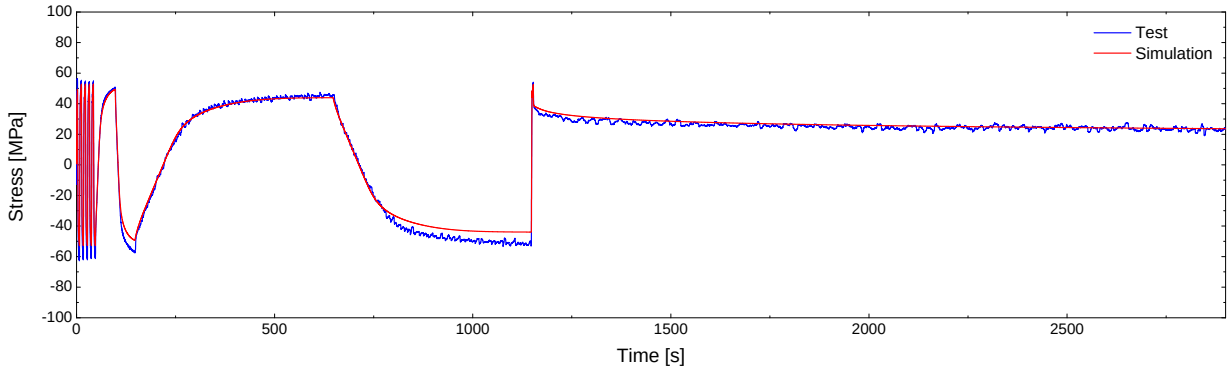

(a)

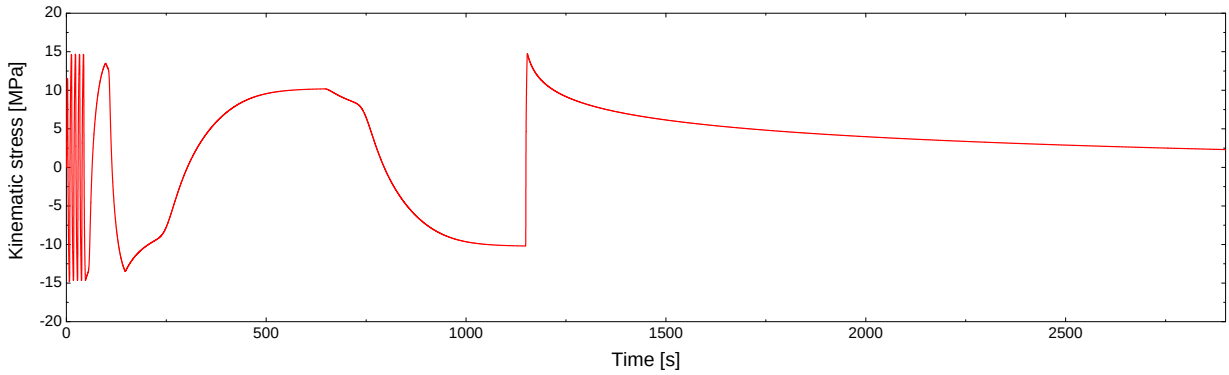

(b)

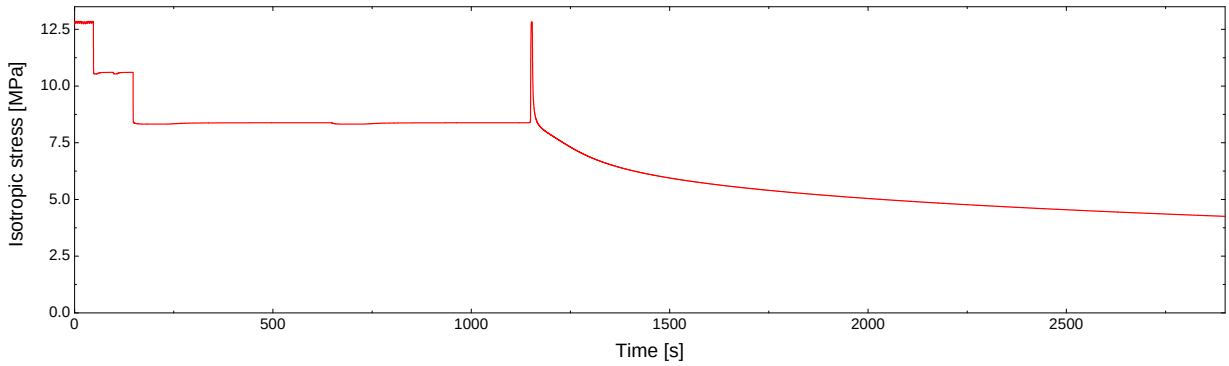

(c)

Fig. B.8: Results of the LCF test and simulation using the modified Steck's model for the ageing condition S_{III} at 280°C referring to: (a) experimental and predicted stress σ; (b) kinematic stress σ^{kin}; (c) isotropic stress σ^{iso}.

B.4 Ageing condition S_{IV}

The ageing condition S_{IV} is obtained by treating the alloy at 300°C for 168 hours, producing an interprecipitate spacing of $\lambda_{S_{IV}} = 37.33 \cdot 10^{-8}$ m. The LCF tests are carried out at 200°C, 225°C, and 250°C by using a strain amplitude of 0.30 %.

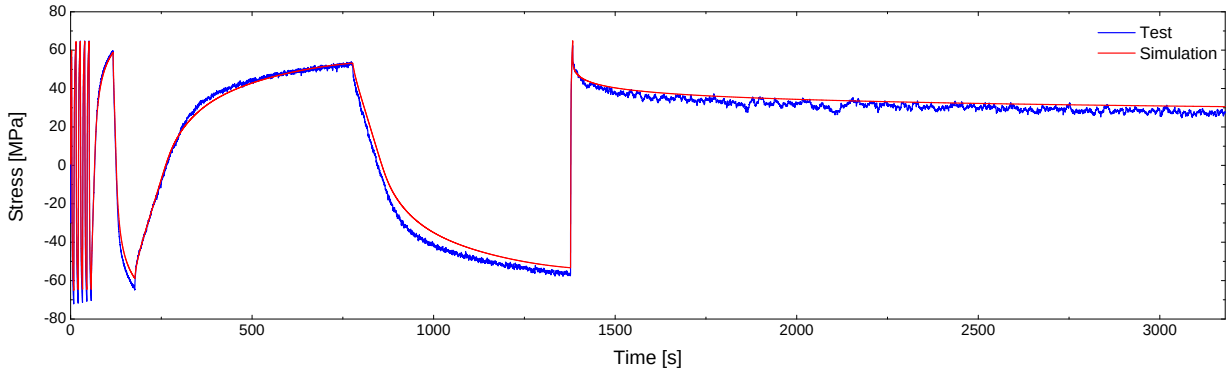

(a)

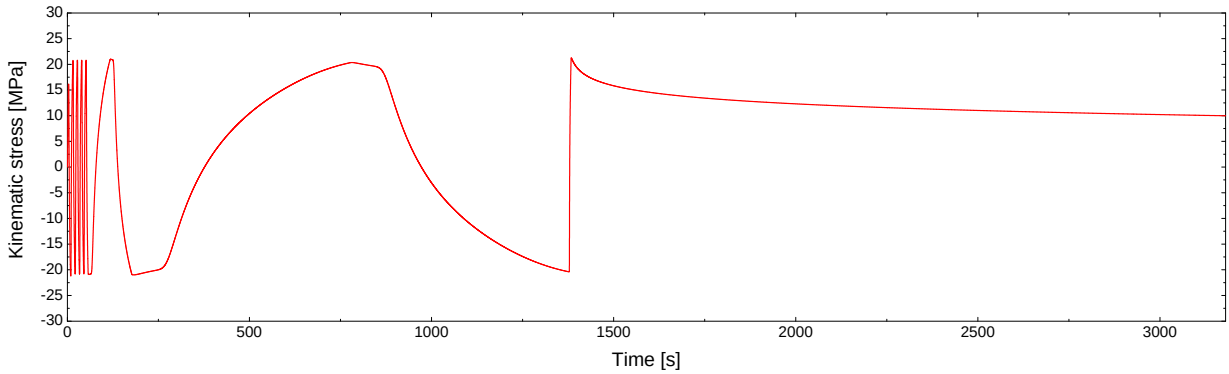

(b)

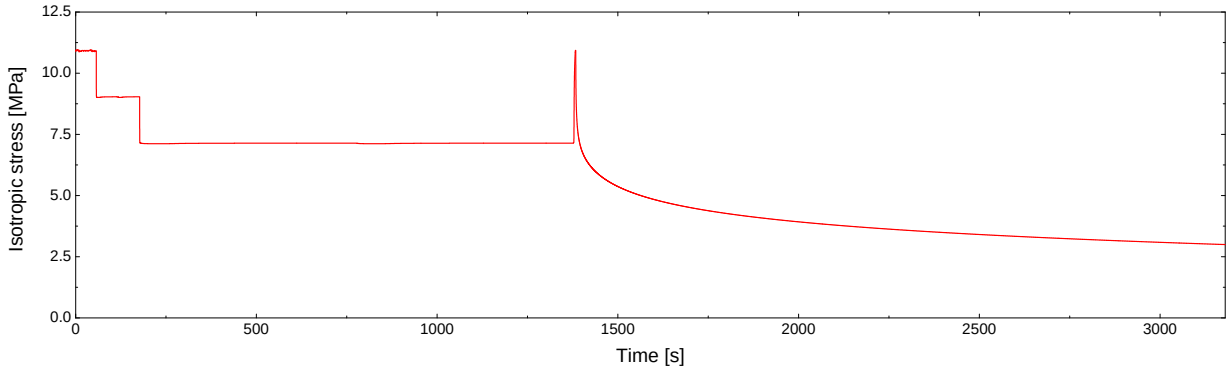

(c)

Fig. B.9: Results of the LCF test and simulation using the modified Steck's model for the ageing condition S_{IV} at 200°C referring to: (a) experimental and predicted stress σ; (b) kinematic stress σ^{kin}; (c) isotropic stress σ^{iso}.

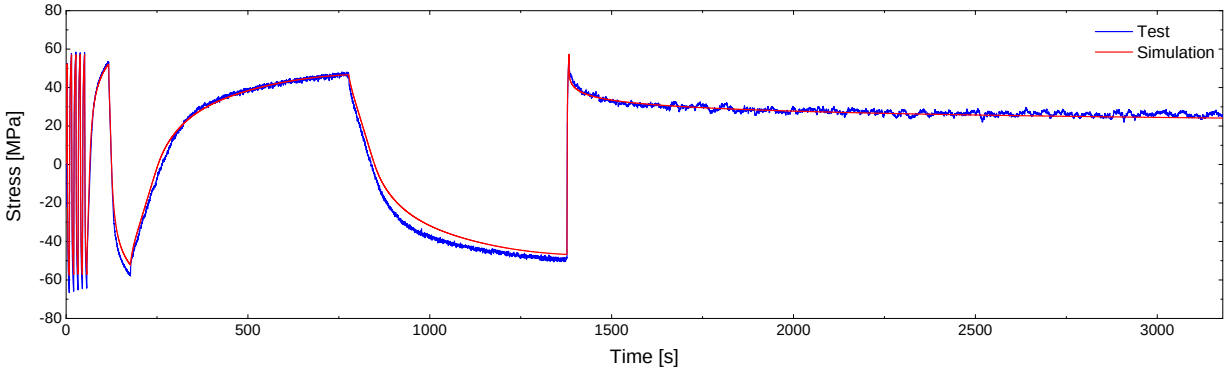

(a)

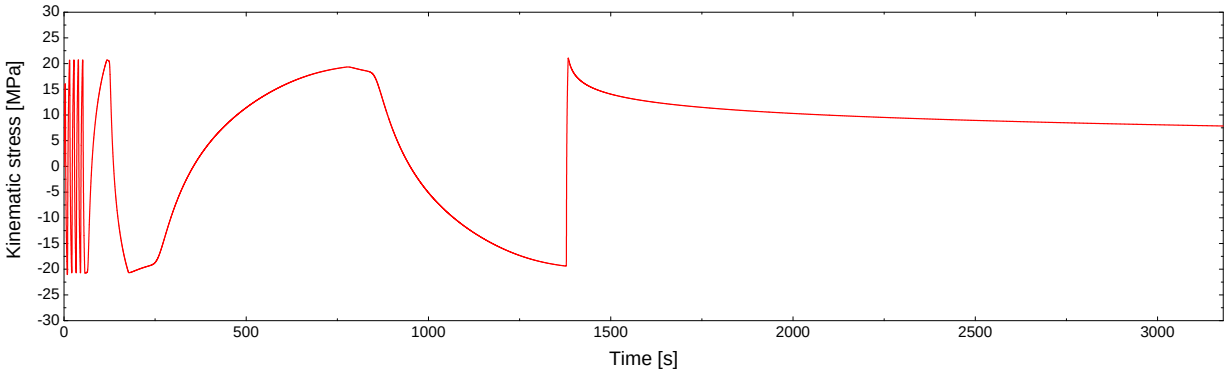

(b)

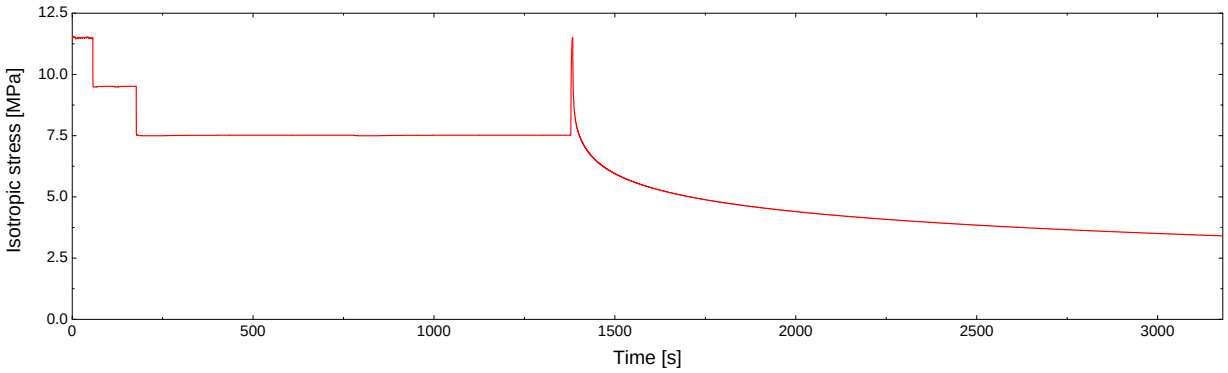

(c)

Fig. B.10: Results of the LCF test and simulation using the modified Steck's model for the ageing condition S_{IV} at 225°C referring to: (a) experimental and predicted stress σ; (b) kinematic stress σ^{kin}; (c) isotropic stress σ^{iso}.

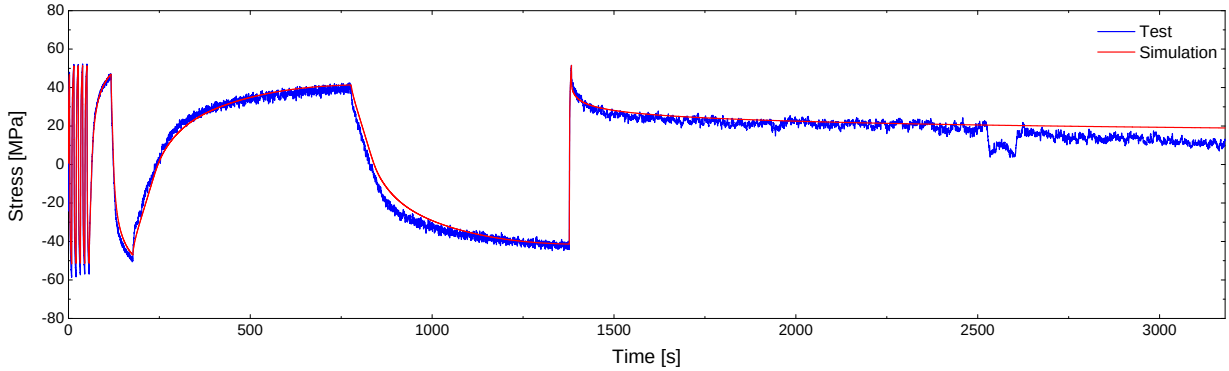

(a)

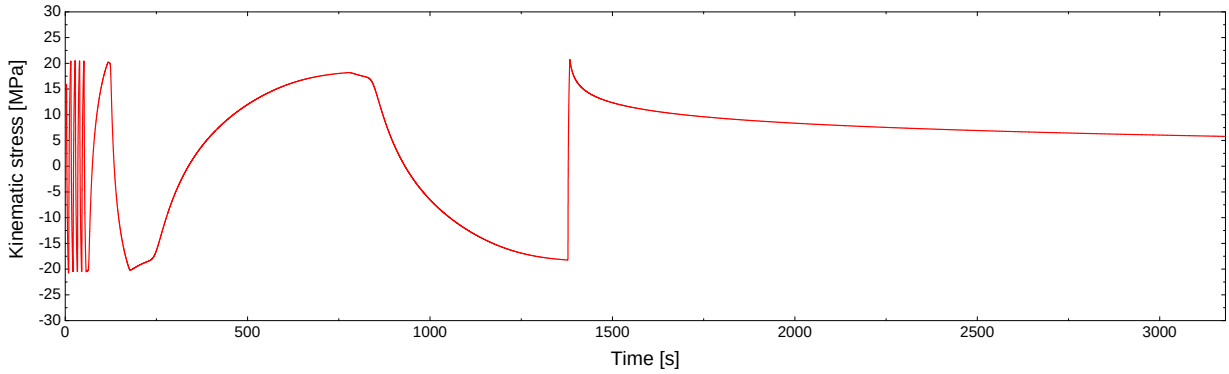

(b)

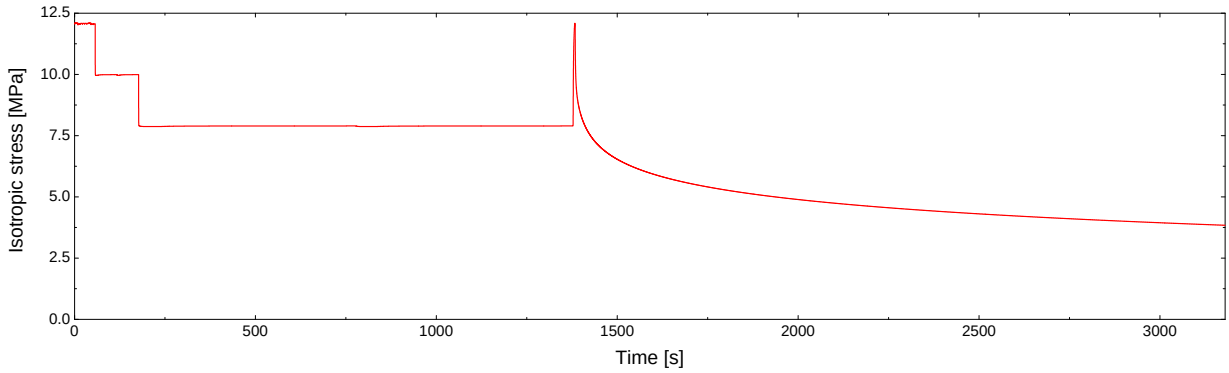

(c)

Fig. B.11: Results of the LCF test and simulation using the modified Steck's model for the ageing condition S_{IV} at 250°C referring to: (a) experimental and predicted stress σ; (b) kinematic stress σ^{kin}; (c) isotropic stress σ^{iso}.

Academic background

Xabier Larráyoz Izcara
born on November 23, 1983 in Pamplona (Spain)

Education

1989-1995	Elementary Education, *Santa Teresa School*, Pamplona (Spain)
1995-2001	Secondary Education, *Santa Teresa School*, Pamplona (Spain)
1995-2001	Baccalaureate, *Santa Teresa School*, Pamplona (Spain)
2001-2004	Basic studies in Mechanical Engineering, *Universidad Pública de Navarra*, Pamplona (Spain)
2004-2006	Main studies in Mechanical Engineering, *Universidad Pública de Navarra*, Pamplona (Spain)
2006-2007	Master Thesis, *Technische Universität Braunschweig*, Braunschweig (Germany) *New Constitutive Mechanical Model for Aluminum within the Framework of the High–Pressure Die Casting Manufacturing Process*
2008-2014	Research engineer, *Volkswagen AG*, Wolfsburg (Germany)
since 2009	extern PhD Student, *Technische Universität Hamburg–Harburg*, Hamburg (Germany) written at the Volkswagen AG, Group Research, Wolfsburg (Germany) *Characterization and Modeling of the Influence of the Ageing Treatment on the Precipitation Process and the Mechanical Behavior of the $AlSi_{10}Mg(Cu)$ Aluminum Alloy*
since 2014	Development engineer at SEAT S.A., Barcelona (Spain)

List of publications

2016 **Modeling resistance spot weld failure in martensitic boron steels using a critical J-integral fracture criterion**
ECCOMAS Congress 2016, June 7, 2016, Crete (Greece)
D. Dorribo Dorribo, P. Díez, L. Greve. I. Arias, X. Larráyoz Izcara

2015 **New modeling of structural adhesives for crash simulation using cohesive models in VPS**
ESI DACH Forum 2015, October 7, 2015, Bamberg (Germany)
X. Larráyoz, L. Greve, R. Fournier, F. Payen, W. Böhme, J. Lienhard

2015 **Characterization and modeling of structural adhesives for crash simulation**
7. crashMAT, April 22, 2015, Freiburg im Breisgau (Germany)
X. Larráyoz, L. Greve, R. Fournier, F. Payen, W. Böhme, J. Lienhard

2014 **Characterization and modeling of the influence of artificial aging on the microstructural evolution of age–hardenable $AlSi_{10}Mg(Cu)$ aluminum alloys**
Materials Science and Engineering A, vol. 610, pp. 46–53, 2014
X. Larráyoz Izcara, A. Guirao Blank, F. Pyczak, P. Staron, S. Schumann, N. Huber

2013 **Charakterisierung und Modellierung eines Plastizitätsmodells für T6 anisotropes Aluminiumblech**
VDI–Konferenz Simvec Spezial, December 11, 2013, Baden–Baden (Germany)
X. Larráyoz Izcara, R. Damink, L. Greve

2011 **How can large–scale Research Infrastructures be interesting to one of the biggest worldwide car manufacturers. The Volkswagen way**
Research Infrastructure and Structural Funds for Regional Cooperation in the Baltic Sea Region, June 21, 2011, Malmö (Sweden)
X. Larráyoz Izcara